EXPERIMENTAL AND COMPUTATIONAL STUDY OF THE INCLINED INTERFACE RICHTMYER-MESHKOV INSTABILITY

A Dissertation

by

JACOB ANDREW MCFARLAND

Submitted to the Office of Graduate Studies of
Texas A&M University
in partial fulfillment of the requirements for the degree of

DOCTOR OF PHILOSOPHY

Chair of Committee,	Devesh Ranjan
Committee Members,	Andrew Duggleby
	Eric Petersen
	Marvin Adams
	Rodney Bowersox
Head of Department,	Andreas Polycarpou

August 2013

Major Subject: Mechanical Engineering

ABSTRACT

A computational and experimental study of the Richtmyer-Meshkov instability is presented here for an inclined interface perturbation. The computational work is composed of simulation studies of the inclined interface RMI performed using the Arbitrary Lagrange Eulerian (ALE) code called ARES. These simulations covered a wide range of Mach numbers (1.2 to 3.5), gas pairs (Atwood numbers 0.23to 0.95), inclination angles (30° to 85°), and explored various perturbation types (both inclined interface and sinusoidal). The computational work included the first parametric study of the inclined interface RMI. This study yielded the first scaling method for the inclined interface RMI mixing width growth rates. It was extended to explore the effect of perturbation linearity and identified that a sharp transition in growth regimes occurs for an initial perturbation inclination angle of 75° with angles below (above) this growing faster (slower).

Finally a study of the effects of incident shock strength on the refracted shock wave perturbation decay rate is presented. This study examined how the perturbations induced on the transmitted shock front by the RMI decay with time and found that the decay rates follow a power law model, $A = B * S^E$. When the coefficients from the power law decay model were plotted versus Mach number, a distinct transition region was found which is likely a result of the post-shock heavy gas velocity transitioning from the subsonic to supersonic range.

The experimental portion of this work was conducted using the TAMUFMSTF, completed in May of 2012. This facility uses a variable inclination shock tube, with a

modular construction design for incident shock strengths of up to Mach 3.0. It employs optical systems for measuring density and velocity fields simultaneously using the planar laser induced fluorescence and particle imaging velocimetry techniques. The design and construction of this facility is reviewed in detail in chapter 4 of this work.

The initial experiments performed in the TAMUFMSTF provided the first known extensive experimental data for an inclined interface RMI. Planar laser Mie scattering images and velocity vectors were obtained for a N_2/CO_2 interface at a 60° inclination angle and an incident shock strength of Mach 1.55. These images have been compared with simulations made using the ARES codes and have been shown to have some distinct differences. Some of these differences indicate that the initial conditions in the experiments deviate from the ideal planar interface. Other differences have revealed features which have not been resolved by the simulations due to resolution limitations.

DEDICATION

To my friend, teacher, and mentor James Boyd Riddles. His encouragement and interest in my work propelled me forward through all of my education. I wish I could share with him now the work I have accomplished.

ACKNOWLEDGEMENTS

There are many people who have supported me throughout my PhD and my academic career. The effort of these people has ranged from contributing research, to providing a sounding board with which I bounced ideas from, to just being a friend and supporter of my work. I would like to acknowledge as many of these people as possible for I truly feel fortunate to have completed this work and I could not have done this without them. I must first thank my advisor, Dr. Devesh Ranjan, who has helped me develop into the researcher I am now, has given me the greatest opportunities to work with and meet other researchers and has always made sure I had the resources need to conduct the research I wanted to pursue. I would also like to thank my committee members for donating their time to review and improve my work.

I would like to thank my lab mates who I have worked with over the years and who I consider all to be good friends. Sarat Kuchibhatla has been a friend since the day I started in the shock tube and advanced mixing lab, and has always helped me to manage my stress. Bhanesh Akula has been a wise and thoughtful peer who has helped me to develop a better theoretical understanding of my research and who helped me many times with the mysteries of LabVIEW errors. Adam Martin provided much needed laughter to the lab. Adam Hartzell helped me greatly to develop the instrumentation and data acquisition system for the shock tube, and developed the basis for the LABVIEW code we use today.

There have been many undergraduate students that have worked with me but three in particular have made significant contributions to the shock tube, and have been

good friends. Peter-Kyle Koppenberger was the earliest to work in our lab and developed a design for the shock tube facility. Sterling Debner played a paramount role in constructing the shock tube and his welds hold the shock tube together, literally. Chris McDonald joined our lab when we were just starting to construct the shock tube and helped manage an ever increasingly complicated project. In the last year of my shock tube research I was fortunate to have three graduate students join the lab and multiply my previously solitary research efforts. David Reilly, Thomas Finn, and Skylar together with Chris McDonald have made sure that the tube is always running an experiment.

I was fortunate to be selected to be a part of the High Energy Density Physics summer student program at Lawrence Livermore National Laboratory (LLNL) during the summers of 2010 and 2011. Jeffrey Greenough was my mentor at LLNL and has continued to mentor me and help me to use the ARES program for new purposes. Cyrus Harrison helped me to process data from ARES code using the VisIT program, and has continued to help me trouble shoot VisIT in the time since I left LLNL. Robert Morgan and Chris Weber worked in other shock tube labs researching the RMI, and despite the fact that in some sense we were competitors, they helped me to develop my understanding of my research and listened to and critiqued my many ideas for experiments while I was at LLNL. Andrew Kessel is a computer scientist I worked with at LLNL and through his work I learned a great deal about how computers managed and processed the fluids codes that I use so often.

Before I worked at LLNL I was invited to visit Los Alamos National Laboratory (LANL) in the summer of 2009. At this time I had not even begun my research and was

very overwhelmed by the challenge that was ahead of me. Malcolm Andrews was kind enough to host me there and has continued to help my research over the years with his insightful wisdom and high research standards. I was privileged to work with two post doctoral students, Bertrand Rollin and Tie Wei, in my short visit at LANL who helped me develop my theoretical understanding of hydrodynamic instabilities. I would also like to thank the member of the LANL shock tube lab who gave me a tour of their facility long before I had plans for our own shock tube.

Many of the parts for our shock tube were donated to us by Riccardo Bonazza of the Wisconsin Shock Tube Laboratory. Riccardo has continued to provide advice to me and help me by editing papers. Mark Anderson helped me in the design phase of the shock tube by sharing with me his experience with designing components of their shock tube facility. Ricardo's students, Nich Haehn and Chris Weber, were also very helpful.

At Texas A&M there were many staff member who helped me with the design and construction of the shock tube. Johnny Halford helped me to find space for the shock tube, to find manufacturers for parts, and to design many of the parts to be fabricated easier. Layne Wylie heads the shop in the mechanical engineering department and was always willing to loan us the tools we needed to build the shock tube and provided advice to us on machining and welding. I was fortunate to learn from two professors at TAMU who made a great impact on me. Dr. Timothy Jacobs has a great passion for teaching thermodynamics that I believe I share with him. Dr. Andrew Duggleby was my professor for turbulence, and took a course which I thought was over my head and made me feel quite at ease with it. I have enjoyed numerous conversations

with both these teachers and have learned much more than course work from them. I would also like to thank my advisor from my masters work at Virginia Tech Dr. Wing Ng, and my research mentor Stephen Guillot. These people took a bet on me as an unknown undergraduate and helped me develop into a researcher.

Finally, I would like to go through and thank my friends and family that helped me become the person I am and supported me in various ways throughout my education. Ryan Breighner has been my closest friend since we were undergrads at Texas Tech, and has always driven me to keep at it as we have both pursued our doctorates. Among my family I would like to thank my sister Kate and her husband Heiko Wiggers for supporting me and providing me a retreat from my research while I was at Virginia Tech. Of course, I must thank my parents to whom I owe everything. From both of them I have inherited my abilities and my interest in the world around me. They helped to put me through my undergraduate degree and to reduce my stress and financial burden while I was at Virginia Tech. I would also like to thank my close family friend James Boyd Riddles who always took an interest in my work and wanted to know what I was doing with the shock tube and what I was teaching or learning. Boyd only got to see the shock tube once in its early stages before his death, but I know he would be so interested to see what I have done with it since then. The last person I must thank is the most important person in my life, my wife Tiffany, who has kept me sane and happy throughout all three of the degrees I have pursued. Without the happiness she creates within me I would never have lasted through my Masters degree, and would not have the motivation I have now to take on the challenges of research.

TABLE OF CONTENTS

Page

LIST OF FIGURES

Page

LIST OF TABLES

Page

1 INTRODUCTION

The National Academy of Engineering has identified "Provide Energy from Fusion" as one of the grand challenges for engineering. To meet this challenge the experiments in the National Ignition Facility (NIF) are being conducted in an attempt to show that inertial confinement fusion (ICF) could be used to supply our energy needs. NIF uses 192 laser beams to compress a fusion fuel target (of Deuterium and Tritium) and ignite it at extremely high temperatures and densities. The compression of this fuel, and therefore the energy yield of this process, is significantly hindered by the mixing of the high density fuel core with surrounding lower density materials. This mixing is generated by a family of hydrodynamic instabilities that includes the Richtmyer-Meshkov instability (RMI). The RMI is generated by the interaction of a misaligned impulsive acceleration and a density gradient created by a fluid interface. As a result of this interaction the interface begins to distort and lengthen in the direction of the impulsive acceleration. In the case of the classical RMI, the interface grows through a three stage process. During the first stage the shock wave traverses the interface and vorticity is deposited on the interface. This vorticity causes the interface amplitude to grow linearly in time. This linear growth regime is followed by a non-linear regime where the evolving structures develop small scale roll-up structures created by the formation of secondary hydrodynamic instabilities, Kelvin Helmholtz instabilities. Finally the non-linear growth decays into turbulent mixing at late times. The ability to predict and control of the mixing created by this instability is of great interest to many fields of science and engineering. The potential to predict and possibly control the

mixing of a fluid interface generated by the RMI has motivated this study. Through an integrated computation and experimental effort, the present study validates the recently developed hydrodynamic simulation package for ICF prediction and explores the turbulent mixing behavior of the RMI for a wide range of conditions.

1.1 Theory of Hydrodynamic Instabilities

The RMI [1], [2] belongs to a family of hydrodynamic instabilities that includes the Kelvin-Helmholtz [3], [4], and Rayleigh-Taylor [5], [6] instabilities (KHI and RTI). To understand the basics of the RMI a review of this family of instabilities is required. In addition, in many applications the RMI occurs concurrently with the KHI or RTI or both. A detailed review of the history of these instabilities and the associated previous work is left until section 1.4. The KHI develops at a shear layer between two fluids of equal density (no buoyancy effects). This shear creates a vortex sheet between the two fluids which if perturbed will cause the accumulation of vorticity at points along the interface and lead to the amplification of the perturbation at these points [7]. The RTI develops between two fluids of different densities where the fluids are subjected to a constant acceleration in the direction following from the heavy to the light fluid ($\nabla p \cdot \nabla \rho < 0$). A perturbation of the interface will create a pressure imbalance which will result in the creation of vorticity and amplification of the perturbation.

The growth of these instabilities can be broken down into various stages. To describe these stages it is helpful to describe the interface perturbations as a wave or sum of waves. For more complex perturbations the interface can be decomposed into a Fourier series of modes. The instabilities first start in a linear growth regime where

perturbation amplitudes are much smaller than their wavelengths ($\eta/\lambda<<0.1$). It will be seen later that in the case of the RMI there is an initial non-linear stage due to compressible effects which precedes the linear regime. As the perturbations are amplified their amplitudes begin to exceed their wavelength ($\eta/\lambda>1$) and they are considered to be in the non-linear regime. As the interface continues to grow, secondary instabilities like the KHI develop and lead to the creation of small scale vertical features in the interface. This process can be seen through the bifurcation of solutions to the Navier-Stokes equations as the flow develops into turbulence. In the final stages of growth the instability has decayed into a turbulent mixing region. As will be discussed later in respect to the RMI experiments, this turbulent mixing region does not necessarily meet the classical criteria for turbulence, i.e. the turbulence may not be isotropic.

The onset of these instabilities takes place in the linear regime and therefore the criteria for instability can be explored using the assumptions of the linear regime. A summary of the linear stability theory, as presented by Drazin and Reid [7], for this family of hydrodynamic instabilities is presented below. To develop the linearized equations of this instability, the problem is first simplified by taking the fluids to be incompressible and inviscid. The fluids have velocities U_1 and U_2, and densities ρ_1 and ρ_2. The unperturbed height of the interface is taken to be $z=0$, and the perturbed height is described by equation 1.1. Since the two fluids are each irrotational they can be described by velocity potential functions ϕ_1 and ϕ_1. The boundary conditions at $z \pm \infty$ are that the velocities remain U_1 and U_2. The boundary conditions at the interface are that the vertical velocity of the interface is the vertical velocity of the fluids (eq. 1.2), and

that the pressure is continuous (eq. 1.3). Equation 1.3 is supplemented by Bernoulli's condition (eq. 1.4) and the perturbed velocity potentials are given by equation 1.5. Linearizing these equations by neglecting the products of small terms, applying the method of normal modes (eq. 1.6) to the perturbations, and solving the system of equations gives the result in equation 1.7. When $\boldsymbol{s}$ is found to be positive and real the perturbations will grow with time. By reducing equation 1.7 a criteria for instability is found (eq. 1.8). From equation 1.8 the criteria for the KHI and RTI can be seen ($U_1 \neq U_2$ and $\rho_1 < \rho_2$). The RMI can be viewed as the impulsive limit of the RTI where the acceleration g is replaced by a step function in the stability equations.

$$z = \xi(x, y, t) \tag{1.1}$$

$$\frac{\partial \phi_i}{\partial \mathrm{z}} = \frac{\partial \xi}{\partial t} + \frac{\partial \phi_i}{\partial x}\frac{\partial \xi}{\partial x} + \frac{\partial \phi_i}{\partial y}\frac{\partial \xi}{\partial y} \ (\mathrm{at\ z} = \xi) \tag{1.2}$$

$$\rho_1\left[C_1 - \frac{1}{2}(\nabla\phi_1)^2 - \frac{\partial \phi_1}{\partial t} - gz\right] = \rho_2\left[C_2 - \frac{1}{2}(\nabla\phi_2)^2 - \frac{\partial \phi_2}{\partial t} - gz\right] (\mathrm{at\ z} = \xi) \tag{1.3}$$

$$\rho_1\left(\mathrm{C_1} - \frac{1}{2}\mathrm{U_1^2}\right) = \rho_2\left(\mathrm{C_2} - \frac{1}{2}\mathrm{U_2^2}\right) \tag{1.4}$$

$$\phi_i = \mathrm{U_i x} + \phi_\mathrm{i}' \tag{1.5}$$

$$(\xi, \varphi_1', \varphi_2') = \left(\hat{\xi}, \hat{\varphi}_1', \hat{\varphi}_2'\right)e^{i(kx+ly)+st} \tag{1.6}$$

$$s = -ik\frac{\rho_1 U_1+\rho_2 U_2}{\rho_1+\rho_2} \pm \left[\frac{k^2\rho_1\rho_2(U_1-U_2)^2}{(\rho_1+\rho_2)^2} - \frac{(k^2+l^2)^{1/2}g(\rho_1-\rho_2)}{\rho_1+\rho_2}\right]^{1/2} \quad (1.7)$$

$$(k^2+l^2)^{\frac{1}{2}}g(\rho_1-\rho_2) < k^2\rho_1\rho_2(U_1-U_2)^2 \quad (1.8)$$

These instabilities can also be explained through the vorticity equation (eq. 1.9). In the baroclinic term (eq. 1.10) of this equation it can be seen that vorticity will be generated when the pressure and density gradients are misaligned. This explains why a perturbation between the acceleration and the fluid (density) interface is necessary for the creation of the RTI and RMI and theoretically a perfectly planar interface will result in no mixing (excluding diffusion of species) in both instabilities. For the KHI there is no density gradient and so the vorticity production instead rises from the incompressible stretching /tilting term.

$$D_t\omega_i = \frac{1}{\rho^2}\varepsilon_{ijk}\partial_j(\rho)\partial_k(P) + \upsilon\partial_j\partial_j\omega_i + \omega_j\partial_j V_i - \omega_i\partial_j V_j \quad (1.9)$$

$$\frac{1}{\rho^2}\varepsilon_{ijk}\partial_j(\rho)\partial_k(P) \quad (1.10)$$

1.2 Properties of Compressible Fluids

For the KHI and RTI the effects of fluid compressibility can be neglected in most cases, but for the RMI the compressible nature of gases is of great importance and is inseparable from the formation of the instability. For this reason a brief review of the

important compressible effects in the RMI is undertaken in this section. This discussion is based on the information presented by Anderson [8].

Acoustic waves propagate through a medium at the local speed of sound (eq. 1.11). For this work the medium will be assumed to be an ideal gas (eq. 1.12) which by means of various assumptions, allows the speed of sound to be defined by equation 1.13 . Isentropic compression (expansion) waves travel at the speed of sound through a gas raising (lowering) its pressure and temperature. This change in the properties of the gas modifies its speed of sound. In the case of compression waves, the speed of sound is increased and therefore successive compression waves will travel at high speeds and catch the waves traveling in front of them. In the case of expansion waves the speed of sound is decreased and therefore the waves will travel slower leading to an expansion fan. The impulsive acceleration required for the RMI necessitates the formation of a shock wave in real compressible fluids. A shock wave can be viewed as a sheet of finite thickness, on the order of a few molecular mean free paths, over which the properties of the fluid change suddenly. These changes must satisfy the conservation equations and the second law of thermodynamics (eq. 1.14-1.17). The velocity jump created by a shock front results in a strong acceleration of the fluid medium passing through the shock.

$$a^2 = \left(\frac{\partial P}{\partial \rho}\right)_s \tag{1.11}$$

$$P = \rho RT \tag{1.12}$$

$$a = \sqrt{\gamma RT} \tag{1.13}$$

$$\rho u = const. \tag{1.14}$$

$$P + \rho u^2 = const. \tag{1.15}$$

$$h + \frac{u^2}{2} = const. \tag{1.16}$$

$$ds \geq 0 \tag{1.17}$$

The field of compressible flow can often be broken into two common view points; one where the shock front remains steady with the lab frame of reference and the fluid medium moves into the shock (steady wave motion), and one where the shock front moves with respect to the lab frame (unsteady wave motion). For the purpose of this work the unsteady wave motion point of view will be used as it is most convenient for the experiments to be described later. The formation of a shock wave is not instantaneous and requires a finite amount of time. This is because a shock front will be formed by a succession of compression waves. As the compression waves catch up to one another they form a shock front which will travel faster than the speed of sound in the unshocked fluid. In many cases these compression waves are formed by the sudden release of a volume of high pressure gas which necessitates that expansion waves propagate in the opposite direction and consume the high pressure gas (fig. 1.1). These expansion waves can be reflected back towards the shock front where they will catch up to the shock front. The intersection of the expansion waves with the shock front will reduce the shock strength and slow its velocity.

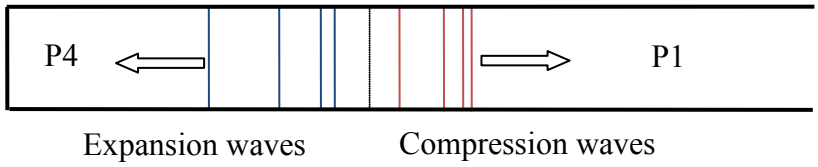

Figure 1.1: Schematic of the formation of expansion and compression waves on the sudden release of a high pressure volume of gas.

The process of compressible wave reflection is also of interest. As already mentioned, expansion waves can be reflected from a surface. In the case of a wave (compression, expansion, shock) intersecting a parallel solid surface, the wave will be reflected back in its same form. For a wave intersecting a parallel fluid boundary the process will be more complicated. To explore this interaction one must consider the acoustic impedance (eq. 1.18) of the fluids defined as the product of the gas density and speed of sound [9]. The acoustic impedance is a measure of the stiffness of a material as it is a measure of the ability of an applied pressure to impart a velocity to the material. The difference between the acoustic impedances of the fluids at the boundary (eq. 1.19) is known as the acoustic impedance mismatch (dZ). If dZ is greater than zero, the fluid boundary will reflect a like wave (shock reflects a shock, expansion reflects expansion) and the transmitted wave will be a like kind with reduced speed (incident shock is transmitted as a slower shock) (fig. 1.2). If dZ is less than zero, the interface will reflect the incident waves counterpart (shock reflects as expansion wave), and the transmitted wave will be a like kind with increased speed (incident expansion wave is transmitted as faster expansion wave) (fig. 1.2).

$$Z = \rho c \tag{1.18}$$

$$dZ = Z_1 - Z_2 \tag{1.19}$$

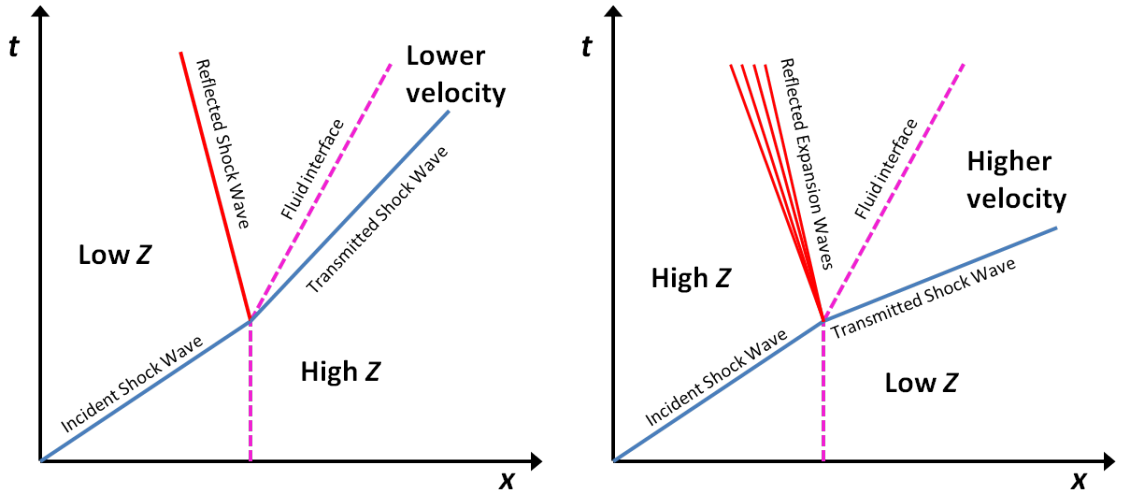

Figure 1.2: XT diagram schematics illustrating effects of acoustic impedance. Right: Shock wave transmission from low to high acoustic impedance gas. Left: Shock wave transmission from high to low acoustic impedance gas.

The case of a shock wave intersecting an oblique interface of two fluids with an acoustic impedance mismatch will generate a much more complicated set of solutions to the shock reflection problem. This type of interaction is the same as the inclined interface RMI, the study which comprises a large part of this work, and is discussed in further detail in later sections. This type of interaction can be examined by shock polar analysis as done by Jahn [10] in early experiments, explored later theoretical work by Henderson [11], and expanded on in more recent works [12], [13], [14], [15], [16]. Through shock polar analysis the deflection angles of the transmitted and reflected

waves as well as the interface can be predicted at very early times before the RMI begins developing. For the case of a fast gas resting above a slow gas (fast-slow case) at an oblique angle (fig. 1.3) it is possible that the interface could reflect an expansion wave or a shock wave depending on the incident shock strength. As shock strength increases the reflection tends towards a shock wave (fig. 1.3, Case 1) and as the inclination angle decreases the reflection tends towards an expansion wave (fig. 1.3, Case 2). For the slow-fast case the opposite is true of the trends in the reflected wave.

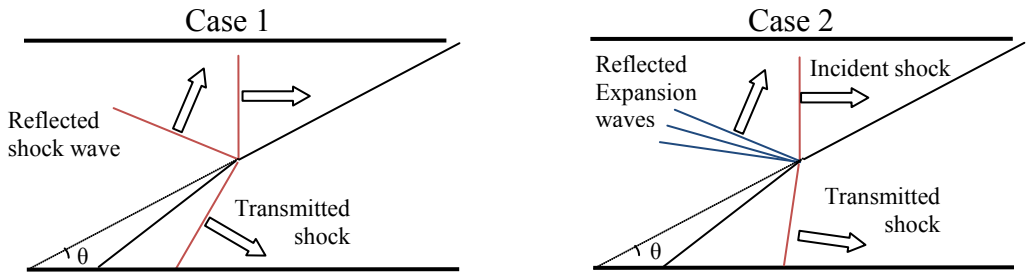

Figure 1.3: Schematic of a shock interaction with an inclined fast over slow gas interface.

1.3 Literature Review

To arrive at an understanding of the current state of research in the field of the RMI a review of the past research leading to the current work is necessary. To do this the review of previous research will be divided into two sections; theoretical works, and experimental work and simulations. These two field are not entirely separable and some overlap will exist in these sections as a result.

1.3.1 Theoretical works

As mentioned before the RMI was derived from the RTI and the work of Taylor [6]. Richtmyer [1] first examined the impulsive case of the RTI theoretically. Richtmyer derived from Taylors work (eq. 1.20) that the growth of interface perturbation amplitudes was proportional to the initial amplitude and wavelength of the perturbation, the acceleration, and the Atwood number (eq. 1.21). From this Richtmyer assumed that the compressible effects could be neglected, substituted in an impulsive acceleration of the form of a Dirac delta function, and found that the growth rate of the interface was now proportional to the velocity jump induced by the impulsive acceleration (eq. 1.22). Richtmyer performed early computational simulations for a shock wave accelerating a fluid interface with a sinusoidal perturbation and compared the calculated growth rate with his theoretical growth rate. The initial agreement between the two was not perfect but showed that at early times that the theory was reasonably accurate. The theoretical work of Richtmyer was followed up almost 10 years later by the experimental work of Meshkov [2], a Russian scientist. Meshkovs experiments were able to validate the theoretical work of Richtmyer but the experiments had many problems that resulted in more than a 10% error in growth rates when compared with theory. Meshkov added to Richtmyers work a prediction for the post shock amplitude of the interface (eq. 1.23). The experiments performed by Meshkov will be examined in detail later in the experimental works literature review section.

$$\frac{d^2\eta(t)}{dt^2} = kgA\eta(t) \tag{1.20}$$

$$A = \frac{\rho_2 - \rho_1}{\rho_2 + \rho_1} \tag{1.21}$$

$$\dot{\eta} = k[v]A\eta_0' \tag{1.22}$$

$$\eta_0' = \eta_0\left(1 - \frac{|[v]|}{w_i}\right) \tag{1.23}$$

The model presented by Richtmyer was termed the impulsive model and showed that the growth rate of interface perturbations would initially be constant with time. This model still remains an important method to calculate the growth of the instability. However, several researchers have axpanded on this model over the past 50 years. Meyer and Blewett [17] used numerical simulations to expand on Meshkovs experiments. They proposed that the average of the pre-shock and post shock amplitude (eq. 1.24) be used as well as the post shock Atwood number. The effects of compressibility were examined by Fraley [18] and found to have an important impact on the post shock perturbation amplitude. The effect of compressibility on the impulsive growth model was also examined by Wouchuck and Nishihara [19], [20], [21] who found that within a certain range, compressibility effects remained important. Vandenboomgaerde *et al.* [22] proposed a form of the impulsive model that would work for both the light over heavy gas case and the heavy over light case (eq. 1.25). The previous models only worked for the light over heavy case, because the heavy over light case would undergo a phase inversion where the perturbation would initially become

smaller, invert and then begin growing in the opposite direction of its initial amplitude. Motl *et al.* [23] proposed the addition of a growth reduction factor for a diffuse interface partially based on the work of Brouillette and Sturtevant [24].

$$\bar{\eta} = 0.5(\eta_0 + \eta_0') \tag{1.24}$$

$$\eta = k[v]0.5\dot{(}A\eta_0 + A'\eta_0') \tag{1.25}$$

The linearity of the interface perturbations has a strong effect on the validity of the impulsive growth model. The effect of nonlinearity was encountered mistakenly in Meshkovs original experiments which had nonlinear initial perturbations in some cases. These cases showed a higher level of disagreement with Richtmyers impulsive model. The effect of the nonlinearity of initial perturbations was examined later by Aleshin *et al.* [25]. The typical definition of a linear perturbation has been widely accepted to be η/λ <0.1 [26]. The effects of non-linearity have been explored in experiments as well including the work presented here. To examine the nonlinear growth models it is necessary to break the interface features into two sections; the bubble and the spike. This view point was adopted first for the RTI, and attributes the growth of the interface mixing region to a wide bubble of light fluid penetrating the heavy fluid, as a narrow spike of heavy fluid penetrates the light fluid (fig. 1.4). The growth rate of the interface can be viewed as the sum of these two growth rates where the spike grows faster than the bubble for all cases where the Atwood number is greater than zero. The linear theory was expanded with higher order terms using the method of Padé approximates by both

Zhang and Sohn [27], and Velikovich and Dimonte [28]. The resulting growth rate predicted by Zhang and Sohn shows a stall and an eventual decline at late times. A review and comparison of several nonlinear theory expansions was presented by Holmes *et al.* [29]. This review found good agreement between the competing non-linear theories but highlighted their limitation at high Mach numbers.

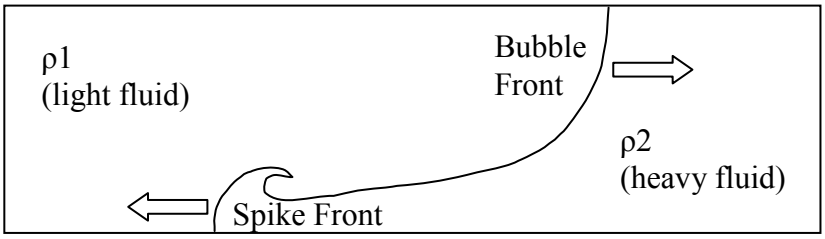

Figure 1.4: Schematic of the bubble and spike formation in an RMI.

The linear and non-linear theories presented so far have been for a single mode perturbation, but as discussed in section 1.1, complex perturbation in an interface can be broken down into the sum of many individual modes. The growth rate of these modes can be complicated by bubble competition and merger. This type of model is frequently employed in the RTI community. Bubble completion was examined for a two mode case in both the RTI and RMI by Hecht *et al.* [30], Alon *et al.* [31] and Sadot *et al.* [32]. A late time mixing width growth model of the form in equation 1.26 has been proposed [26]. The determination of θ has been a great source of debate in the RMI community. Alon *et al.* [31] found θ to be 0.4 at low Atwood numbers up to and including 1. Thornber et al. [33] reports values of 0.26 to 0.30 for single shocked multimode RMI

simulations and more recently lower values of 0.26 to 0.28 [34] for simulations including reshock.

$$h \sim t^{\theta} \tag{1.26}$$

1.3.2 Experimental work and simulations

Having reviewed the theoretical work on the RMI the validation of these theories can now be examined through experiments and simulations. These two methods of examining the RMI are deeply intertwined with experiments being used to test simulation codes, and simulations being used to examine details of experimental work and expand on them by providing faster results over a wide range of conditions.

The experiments on the RMI can be divided into two coordinate systems; rectangular 2D and 3D experiments, and spherical converging 3D experiments, the later of these being employed in high energy laser experiments like the OMEGA laser system [35], [36], the National Ignition Facility experiments [37], [38] and others [39]. These experiments often involve complex combinations of the RTI, RMI, and KHI, and focus on the compression efficiency of targets for inertial confinement fusion (ICF), or super novae evolution discussed in section 1.4. In these experiments, multiple lasers are aimed at a target from various angles in a spherical or hemispherical orientation. These lasers will impact an ablator which will drive a 3-dimensional shock wave, which then propagates through a spherical interface and thus generates the RMI. Simulations of this geometry have been performed using various codes [38], [40], [41], [42]. While many applications of the RMI involve a 3D spherical geometry, the problem can be studied

using rectangular geometry experiments with little error [43]. This type of geometry is the one employed in the work presented in this dissertation.

Using the rectangular geometry the problem of generating the RMI in experiments can broken down by two major choices which categorize the previous experimental works. The two choices are, 'what method will be used to generate the impulsive acceleration,' and 'what method will be used to generate the perturbation between the density gradient and the pressure gradient?' The problem of generating the impulsive acceleration will be examined first. Three primary methods have been identified for discussion; laser ablation, mechanical acceleration, and shock wave acceleration. The method of laser ablation was discussed in relation to 3D spherical experiments previously, and requires high energy lasers and an ablator material. The impact of a high energy laser on an ablative material like polystyrene, polycarbonate or beryllium [44] can be used to drive a high energy shock though an adjacent material. This method creates very strong shocks with high pressures on the order of 10Mbar. These laser driven experiments and simulations of these experiments have been used to study single mode RMI [45], blast wave driven RTI [46], [47] and even high energy KHI [48].

Another method to generate the impulsive acceleration is to accelerate the experimental apparatus. This method has been employed by the University of Arizona group. The experiment is set up in a tank with the fluids in a stable stratification. The tank is attached to a sled which is dropped and accelerated by a spring at the bottom of the drop [49], [50]. The sled method has also been used to perform RTI experiments by

creating a continuous acceleration opposite to gravity using air pressure [51], rockets [52], and linear electric motors [53], [54]. The final method to be discussed is the mechanical generation of a shock wave to impulsively accelerate the interface. This method employs a shock tube where the shock wave is generated by the sudden release of pressure from a driver section into the driven section. The compression waves from this release of pressure stack up to form a shock front and then intersect the interface which contains the density gradient. This is the method to be used in the work presented later and is discussed in the following paragraphs with its relation to the perturbation methods. The mechanically generated shock wave can also reflect from the end of the shock tube and reintersect the once shocked interface from the other side in a process known as reshock. This reshock will generate additional vorticity and mixing while creating multiple secondary compressible waves which will interact with the mixing layer creating additional mixing. Reshock experiments are of interest for their ability to amplify mixing and accelerate the decay of the organized structures into a state of turbulence as well as to push the capabilities of computational codes due to the large range of scales left in the flow field after their interaction[55], [56].

Having discussed the method for creating the necessary pressure gradient, the methods for creating a misaligned density gradient will now be considered. Before beginning this discussion, it should be noted that the misalignment can be created by a perturbed shock wave (pressure gradient) as discussed in section 2.6 later and published in the authors work [57], although the method of perturbing the density gradient is almost exclusively employed. The earliest method for perturbing the fluid interface was

the one employed by Meshkov [2], which employs a thin membrane to separate the two fluids with a prescribed interface shape. This method has been employed in many shock tube facilities, but has some drawbacks associated with the remnants of the interface which can cause disruptions in the flow field like the development of the late time turbulent mixing zone and cause problems for some optical diagnostics methods [58], [59], [60], [61], [62], [63]. A variation of the membrane experiments is to use a soap film or fluid membrane to shape the interface, such as in a shock bubble interaction [9], [64], [65], [66], [67], [68], [69]. In the shock bubble experiments a bubble of lighter or heavier gas is blown into a soap film using a retractable arm within the shock tube. This arm is then retracted quickly before the shock reaches the bubble which is left to fall or rise within the driven fluid.

Membraneless experiments were developed to avoid the problems associated with the membrane material flow field interactions. One method was to use a plate to separate the gases and prevent diffusion, then retract the plate before the shock interaction [70]. This method seeds the interface with perturbations created as a result of the shear induced by the retracting plate. This method has also been used successfully in RTI experiments [71], [72]. A cylindrical membraneless interface can be created by dropping a column of heavy gas through a light gas as pioneered by Jacobs [73], and employed by others [74], [75]. Two cylinders interacting with on another was considered by Tomkins et al. [76]. This was then extended to several cylinders created together as a gas curtain with a controlled perturbation in a light-heavy-light configuration [77], [78], [79]. This method of interface perturbation creation is limited to the case of a three fluid

interaction where the shock will pass from the driver fluid to the test gas (gas in the cylinder) then back to the driver gas. In this case the upstream fast-slow RMI is inseparable from the downstream slow-fast RMI. Another membraneless method is to rest a light fluid above a heavy fluid in a stable stratification. By creating exit ports at the interface and inlet ports at the top and bottom of the shock tube driven section a continuous flow of the gases can be used to control their diffusion at the interface. Perturbations can then be introduced to the interface by various means such as shaking the interface to develop a single mode wave perturbation [23], [80], [81] like the work presented in section 2.5, vertically oscillating the fluid in the tube [82], [83], or by creating a shear layer and using the resulting KHI as an interface seed [84].

The final method to be discussed is the inclined interface perturbation which was studied in great detail in this work. The inclined interface perturbation relies on a membraneless stratification of gases like those discussed above. The perturbation is created by inclining the shock tube with respect to gravity so that the stratified interface rests at an angle to the shock tube and the incident shock which propagates in the direction of the tube (fig. 1.5). This provides a simple, easily described interface where the initial vorticity deposition is constant as the shock interacts with the interface and can be predicted using the vorticity equation (eq. 10). Some early experiments on the inclined interface RMI were presented by Haas [85] and Sturtevant [86] in conference papers. This type of perturbation was also encountered often in the shock refraction problem , discussed in section 1.2, but the post shock flow field (the RMI) was not studied. Simulations were performed and the theory considered for the inclined interface

where circulation deposition was the primary concern [87], and simulations for an inclined gas curtain were performed [88]. A similar "v" shaped interface was considered in theoretical work with simulations as well [89]. A light-heavy-light chevron type interface [90] which has some similarities to the inclined interface was explored in experiments also.

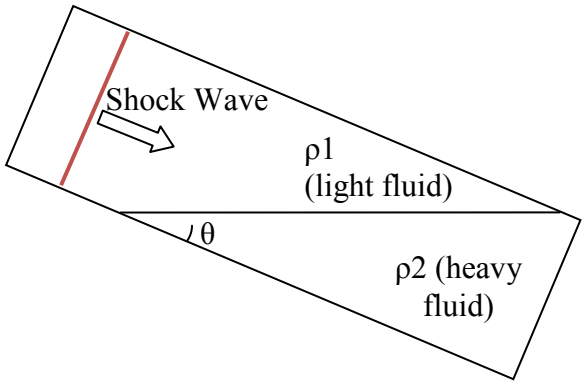

Figure 1.5: Schematic of the initial conditions for the inclined interface RMI

1.4 Applications of the Richtmyer-Meshkov Instability

The RMI occurs in a many natural and man-made systems and has found applications in many areas of science. In stellar phenomena large clouds of gas containing many density inhomogeneities are subject to convection, accretion, stellar winds, and strong shocks created by supernovae [91]. The interaction of these strong shocks on these gaseous has been shown to be a possible mechanism for star formation and solar system organization [92]. These strong shocks can generate significant mixing of the different gasses, temperatures, and densities contained in these clouds [93]. The formation of the RMI along with the RTI in supernova events has been shown to be

necessary to understanding the formation processes of supernova remnants [40]. Experiments and simulations of the interaction of shock waves and stellar density inhomogeneities have been performed and compared with telescope observation using advanced hydrodynamics codes [40], [94], [95] and laser driven shock tube experiments [36], [96], [97].

Another application of the RMI exists in supersonic combustion where the interaction of a shock wave propagating through air into a stream of fuel leads to increased mixing of the fuel and air. This type of interaction has been investigated experimentally and computationally for its use in hydrogen fueled scramjets using shock tubes and steady flow facilities [98], [99], [100]. The interaction of shock waves with density gradients has also found a role in the medical field where shock waves are being used to break up and destroy kidney stones, and gallstones, and even damage tumors [101]. In these shock wave interactions within the body gas bubbles are often created by cavitation. These bubbles will then interact with subsequent shock waves which modifies their effect on the tissue [102].

While the RMI has a wide range of applications in many fields the largest drive of RMI research has been ICF. ICF has the potential to create clean energy free of carbon dioxide production from an abundant fuel source available to all countries. If ICF could be harnessed to create electric power it could provide a relief to international tensions over oil supplies and possibly help us to turn back the environmental damage, global warming, caused by the consumption of carbon fuels.

In ICF a fuel target is compressed by many orders of magnitude to densities and temperatures where the fuel may fuse into larger elements. Various elements may be used as fuel but the ones with the lowest energy barrier for fusion are Deuterium and Tritium [103], heavy forms of hydrogen. During compression the nuclei of these elements are pushed so close together that the nuclear force overcomes the electrostatic force and pulls the nuclei together into a stable helium element. This form of fusion is one of the forms which has the side effect of releasing free neutrons similar to fission reactions. These neutrons contain a substantial amount of energy that can be captured by slowing them down in water or other materials, or by using them to convert fertile material in fission-reactor fuel into fissile material that can be used again in fission reactors. Either method allows ICF to produce substantial amounts of energy from elements that can be obtained readily by refining them from ocean water.

The primary method explored in ICF for compressing the fuel to the required densities has been laser compression via an ablative material as explored by the NOVA laser facility [104], and the more recent National Ignition Facility (NIF) [37]. The NIF facility uses 192 laser beams in a semi-spherical orientation which provide more than 1.8MJ of laser energy or over 500 trillion watts. In the NIF experiments a gold cylinder, the hohlraum, is placed around the fuel target. When the hohlraum is struck by the NIF lasers it will absorb the energy and emit the thermal energy as x-rays back into the fuel target (fig. 1.6). This method is known as indirect drive and was adopted in the NIF experiments for its ability to provide a more uniform heating of the Beryllium ablator material on the fuel target. The laser firing is timed to contain four peaks in power which

control the acceleration of the compressing fuel and the timing of the shock created from the ablator material [38]. These pulses are timed in such a way as to control the formation of the RMI and RTI in the fuel target. The RMI is formed between the ablator material layer and the fuel as well as in layers within the fuel as it compresses. The RMI only develops as a result of perturbations in the fuel target resulting from its manufacturing and from perturbations in the heating generated from the x-rays incident on the ablator material. As the RMI develops and the perturbations are amplified mixing of the high density fuel with lower density material occurs. This mixing reduces the fusion yield of the target. Control of the RMI and RTI are critical to increasing the fusion yield of ICF and making it a viable power source.

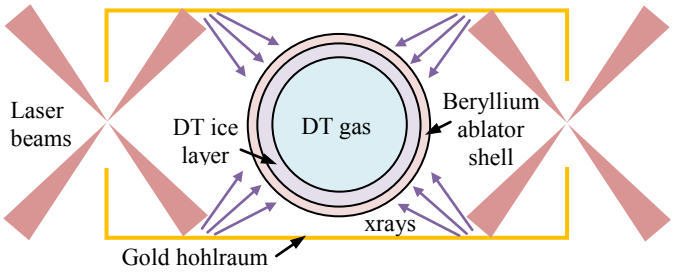

Figure 1.6: Illustration of the hohlraum and fuel target used in the National Ignition Facility (NIF).

1.5 Section Outline

The remainder of this dissertation is divided into two main sections which comprised the work performed for fulfillment of the PhD requirements; computational work and experimental work. The computation work is examined first as it was performed to assist in the design of the experimental work. The computation work

section is organized as follows; (1) A description of the computational code, ARES, used to perform the work is presented, (2) the parametric study of the inclined interface, performed during the design phase of the shock tube facility, is presented, (3) then a multimode inclined interface perturbation study is reviewed, (4) followed by a study of the formation of a non-uniform RMI structure known as the reverse jet, (5) and finally the computational work is concluded by examining the perturbations induced in the transmitted shock wave by the RMI and their decay rate.

The experimental work is presented second but will routinely call upon the material covered in the computational work and use simulations to better analyze the experimental data. The experimental work will cover design, methods, and results. This section will be divided as follows; (1) the design of the experimental apparatus, the Texas A&M university fluid mixing shock tube facility (TAMUFMSTF) , will be covered, (2) the instrumentation and controls system design and capabilities will be presented, (3) the shock tube operating procedures will detailed, (4) initial experimental results and start up efforts will be reviewed, (5) and finally an experimental campaign on the inclined interface RMI will pre presented with results compared to simulations performed using the ARES code.

2 COMPUTATIONAL WORK[*]

The computational work presented in the following major section was undertaken to assist in the design of the TAMUFMSTF (fig. 2.1) and planning of experiments to be performed. As discussed in section 1.3.2 the inclined interface RMI offers many unique advantages for both experiments and simulations. The inclined interface perturbation is simple to set up experimentally and provides easily quantified initial conditions. For simulations the inclined interface perturbation presents a set of conditions which can push the abilities of current hydrodynamics codes by providing highly non-linear initial conditions, strong secondary compressible effects, and sharp corners where the interface meets the computation domain boundaries. The design of a new, unique, large experimental apparatus like the TAMUFMSTF requires a large time and financial investment, and has a high degree of uncertainty. The computational work provided a means of estimating the results of experiments and providing design criteria for the facility. Results from the computational work led to major design revisions in the

[*] Reprinted with permission from "Computational parametric study of a Richtmyer-Meshkov instability for an inclined interface" by J. McFarland, J. Greenough, and D. Ranjan, 2011. *Physical Review E*, 84, 026303, Copyright 2011 by the American Physical Society.

[*] "Springer and Shock Waves, 22, 2012, 511-519, Effect of incident shock wave strength on the decay of Richtmyer–Meshkov instability-introduced perturbations in the refracted shock wave, C. Bailie, J. McFarland, J. Greenough, and D. Ranjan, copyright Springer-Verlag 2012 is given to the publication in which the material was originally published, by adding; with kind permission from Springer Science and Business Media"

[*] Reprinted with permission from "Investigation of the Initial Perturbation Amplitude for the Inclined Interface Richtmyer-Meshkov Instability" by J. McFarland, J. Greenough, and D. Ranjan, 2013. *Physica Scripta*, T155, 014014, Copyright 2013 by the Royal Swedish Academy of Sciences.

[*] Reprinted from "Non-uniform volumetric structures in Richtmyer-Meshkov flows," by M. Stanic , J McFarland , R. Stellingwerf , J. Cassibry , D. Ranjan , R. Bonazza , J. Greenough. In review. *Physics of Fluids*. This paper has been submitted for publication in Physics of Fluids.

TAMUFMSTF, such as an increase in the test section length, redesign of the interface suction slots, and an increase in the strength criteria for the test section windows. These design changes will be examined further in section 3.1.

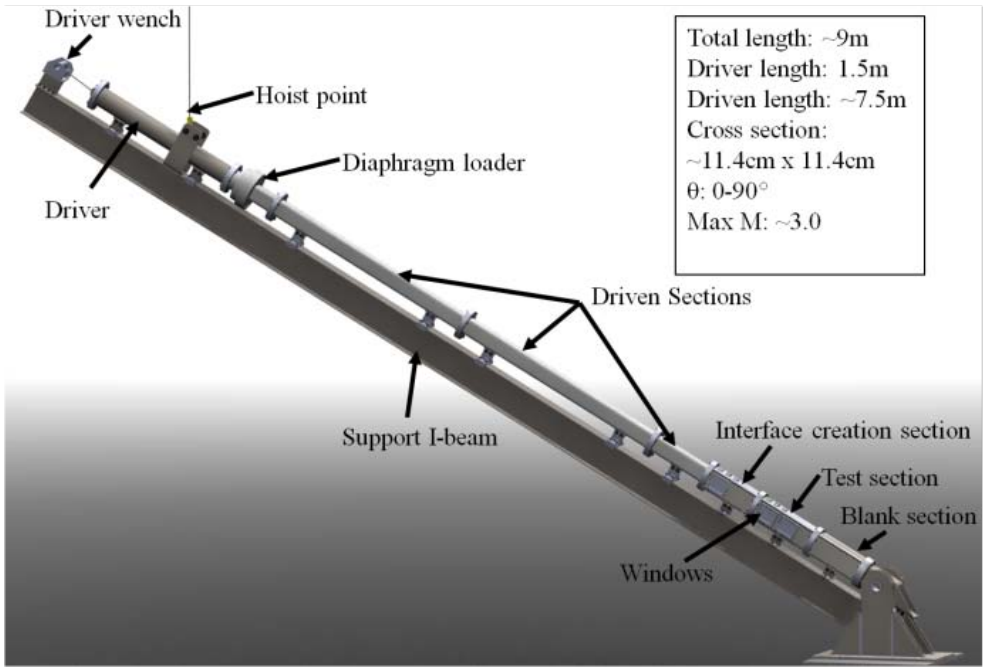

Figure 2.1: Schematic of the Texas A&M University Shock Tube Facility.

Besides providing experimental design criteria the computational work lead to the first major examination of the inclined interface RMI, the creation of a new mixing width growth rate scaling method for a non-linear inclined interface, the discovery of the linear/non-linear initial perturbation threshold, the examination of a RMI structure recently termed the reverse jet, and the first extensive examination of the perturbations introduced into the transmitted shock by the RMI.

2.1 ARES Code Description

The simulations presented in this dissertation were performed using the ARES code developed at Lawrence Livermore National Laboratory (LLNL). ARES is classified as an Arbitrary Lagrange Eulerian (ALE) code, a method that is popular among other hydrodynamics codes like HYDRA [105], ALEGRA [106], and CALE [42]. ALE codes use an Eulerian grid which can be allowed to move during a Lagragian time step. After this time step the resulting node location can then be remapped back to the Eulerian grid. ALE codes may also be run in a purely Eulerian or Lagrangian mode. Lagrangian codes are often used for solid modeling and allow for good interface tracking but require frequent remapping as nodes are allowed to concentrate in areas of high density. Eulerian methods are effective for fluid flows but have trouble tracking interface locations precisely. ALE codes combine the strengths of these methods in hydrodynamics problems to track fluid interfaces precisely and maintain high resolution in the fluid flow [107].

In the ARES code the Lagrange time advancement is second-order predictor-corrector and uses the Gauss Divergence theorem to give the discrete finite difference equations[108]. All numerical differences are fully second order in space. Velocities are defined at mesh nodes and density and internal energy are defined at the zone centers using piecewise constant profiles. Artificial viscosity is used to suppress spurious oscillations[109]. A second-order remap[110] is applied to the solution after the Lagrange step.

ARES employs an adaptive mesh refinement (AMR) capability that allows it to increase the number of nodes in areas of greater interest. This mesh refinement is applied during the remap from the Lagrangian time step to the Eulerian grid. The simulations presented in this dissertation were run with an Eulerian mesh, and used the AMR capabilities to refine the mesh size. This refinement was performed based on the second gradient of density or pressure allowing acoustic effects and density interfaces to be refined, which was ideal for the RMI. More complex mesh criteria were enforced which forced areas upstream of the interface, which were of no interest, to be maintained at the lowest mesh refinement. The use of the AMR capabilities was found to cut the computational time down by a factor of 5-7 compared to a fully refined simulation. In the highest resolution simulations were performed with 5 levels of refinement which spanned from a resolution of 15 nodes across the interface height (7.62mm/node) to 1215 nodes across (94 μm/node). While ARES is capable of employing subgrid turbulence models, these were not employed in these simulations, and so the turbulent energy at subgrid scales was dissipated out of the system. This energy scale cut off makes ARES perform similar to an Implicit Large Eddy Simulation (ILES) in that the subgrid scales are not modeled while the full Navier-Stokes equations are used for the scales above this cut off.

For the simulations in this dissertation new viscosity and diffusion models were developed for ARES to simulate the gas properties at the lower energy densities required for the shock tube simulations. The viscosity model developed follows the Sutherland form shown in equation 2.1, where F_1 and F_2 are density and pressure correction factors

which were not used for these simulations. The remaining coefficients for this equation are given in table 2.1 for the various gasses used. The viscosity model allowed for the development of boundary layers which can significantly affect the growth rate of the interface mixing width, by creating an artificial acceleration of the interface due to mass transport into the boundary layers [111]. While ARES employs an artificial viscosity the addition of a true viscosity to the fluid equations allowed for a more realistic damping of the small RMI features as seen in experiments.

$$\mu = \left[\left(\nu_c + \nu_a \cdot \frac{T^{\nu_n}}{\nu_b + T} \right) F_1 \right] F_2 \tag{2.1}$$

Table 2.1: Gas coefficient used in ARES viscosity model.

Gas	ν_a (g/(cm μs $K^{1/2}$))	ν_b (K)	ν_c (g/(cm μs))	ν_n
Air	1.450E-11	110.4	0	1.5
N_2	1.407E-11	111.0	0	1.5
He	1.513E-11	97.60	0	1.5
CO_2	1.572E-11	240.0	0	1.5
SF_6	1.590E-11	243.8	0	1.5

The gas diffusion model used equation 2.2 to determine the diffusion coefficient, where the coefficients $\boldsymbol{\delta_a}$, $\boldsymbol{\delta_b}$, and $\boldsymbol{\delta_d}$ are 1.0, 0.0, and1.5 respectively. The coefficient $\boldsymbol{\delta_c}$ is given in equation 29, and was chosen to fit the empirical correlation given by Gilliland [112], where $\boldsymbol{\nu_a}$ and $\boldsymbol{\nu_b}$ are species coefficients given by Poling *et al.*[113]. The coefficient values for equation 2.3 for the gasses used are given in table 2.2. To use the diffusion model properly the simulation must be initialized with a diffuse interface. To

do this the interface mass concentrations were set up using an error function given in equations 2.4-2.6, where $\boldsymbol{\varepsilon}$ is the normal distance from the interface and the coefficients are given in table 2.3. The initially diffuse interface serves to better model the actual conditions present in an experiment. In experiments the initially diffuse interface has the effect of decreasing high Atwood number effects on the development of the post shock flow field. After the simulation was begun the diffusion model allowed for continued diffusion of the two species along the interface. As the interface is stretched by the RMI the species diffusion becomes more significant. The application of the species diffusion model further damps out small scale features created by the RMI, and allows for a the rate of mixing to be measured through the amount of diffused mass.

$$D = \frac{\delta_a \left(\delta_b + \delta_c T^{\delta_d} \right)}{P} \tag{2.2}$$

$$d_c = \frac{435.7}{\left(n_{s1}{}^{1/3} + n_{s2}{}^{1/3} \right)^2} \sqrt{\frac{1}{mw_{s1}} + \frac{1}{mw_{s2}}} \tag{2.3}$$

$$mf_1 = 1 - \frac{1}{2}\left(1 + erf\right) \tag{2.4}$$

$$erf = \left[1 - \left(\left(\left(\left(\left(a_5 t_m + a_4 \right) t_m \right) + a_3 \right) * t_m + a_2 \right) * t_m + a1 \right) * t_m * \exp(-\varepsilon * \varepsilon) \right] * \mathrm{sgn}(\varepsilon) \tag{2.5}$$

$$t_m = \frac{1}{1 + p * \varepsilon} \tag{2.6}$$

Table 2.2: Gas coefficients used in ARES diffusion model.

Gas	*n*	*mw* (mol/g)
Air	19.7	28.967
N_2	18.5	28.013
He	2.67	4.003
CO_2	26.9	44.01
SF_6	71.3	146.054

Table 2.3: Coefficients for the initial interface diffusion error function.

Coefficient	Value
a_1	0.254829592
a_2	-0.284496736
a_3	1.421413741
a_4	-1.453152027
a_5	1.061405429
p	0.3275911

The diffusion model also included an enthalpy diffusion term added to the energy equation which accounts for the enthalpy flux created by the diffusing species. As the species diffuse into one another they must carry their enthalpy as well as their mass with them. In multifluid simulations where the fluid molecular weights have a large disparity the error in neglecting enthalpy diffusion can become large. When this term is neglected, as in many hydrodynamics codes, it will result in non-real temperature profiles at the interface and a violation of the 2nd law of thermodynamics. Without the enthalpy flux term areas of high and low temperatures develop at the interface as mass crosses the boundary but does not carries its energy. This leads to an area near the interface which has increased or decreased in density but has not gained or lost energy, meaning the fluid energy must be spread among more or less mass depending on molecular weight of the

fluid diffusing. The addition of the enthalpy flux term also allows the formation of acoustic waves which emanate out from the mixing interface as a result of the change in fluid enthalpy [114].

2.2 One Dimensional Gas Dynamics and X-T Plots

During the parametric study the 1D gas dynamics plots, X-T plots, were developed to explore the timing factors and pressures for the design of the shock tube (fig. 2.2). These plots show the pressure in the shock tube plotted as a function of location along the length of the tube (x direction) and time. They were made by running ARES in a 2D mode with only three nodes across the height of the shock tube domain while running with a node spacing of ~2cm through the length of the shock tube. The plots allowed for the driver, driven and test section lengths to be selected based on timing criteria for the development of the RMI. The timing criteria depended on the interaction of the various major compressible waves. Upon the release of the high pressure driver gas a shock wave is formed travelling towards the test section (fig. 2.2A) while expansion waves are formed travelling towards the driver end wall (fig 2.2D). These expansion waves reflect from the driver end wall and head back towards the test section and interface (fig. 2.2C), as discussed in section 1.2. The expansion waves create a gradual time dependent acceleration of the post shock gases opposite in sign to the acceleration created by the shock (they slow the post shock gas). Since the RMI is based on an impulsive acceleration, and the intersection of the expansion waves with the interface (fig. 2.2D) would create a semi-constant acceleration over time, they cannot be allowed to intersect the interface during the time period it is under investigation.

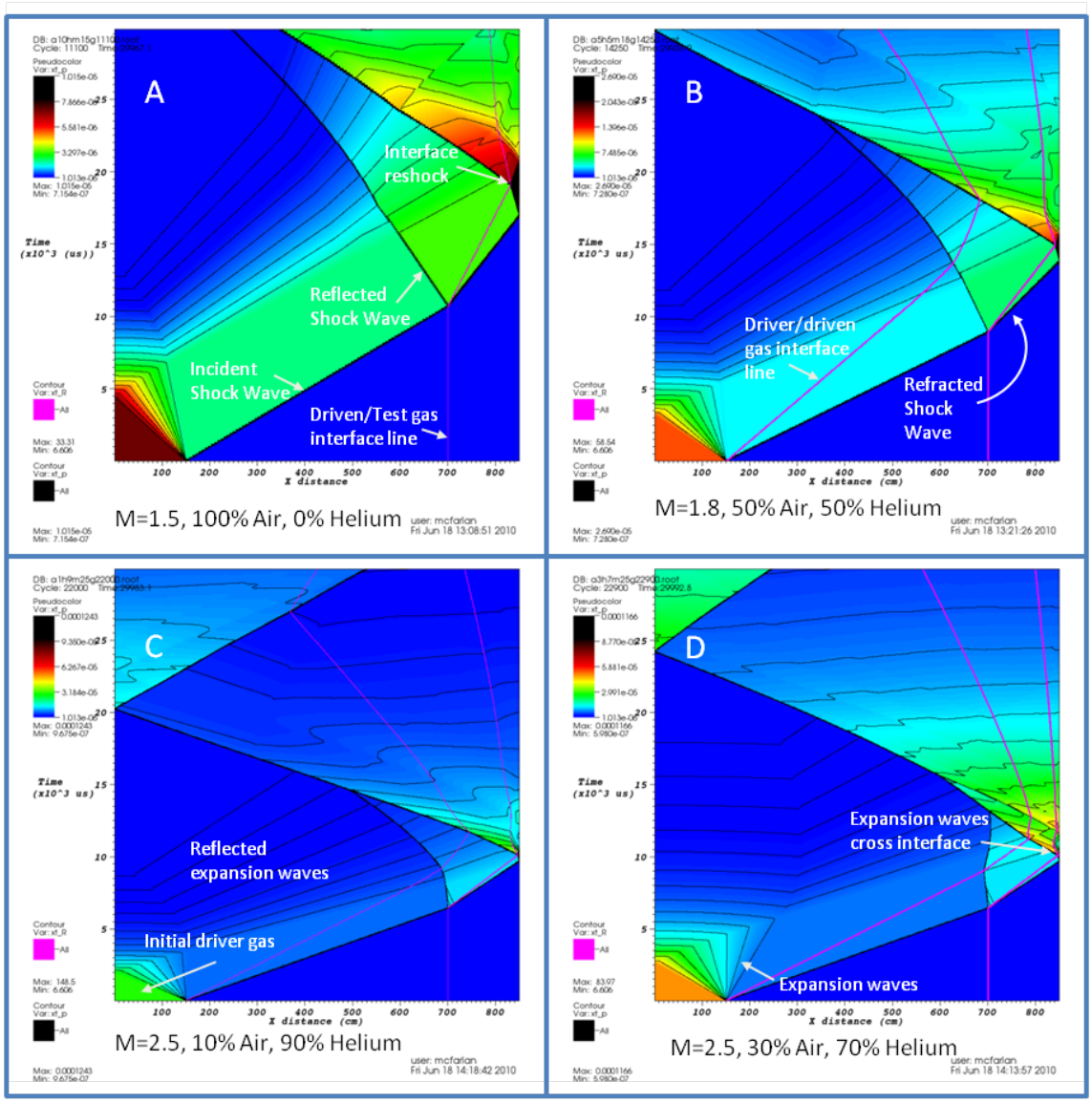

Figure 2.2: X-T plots created with ARES for 4 different cases. The cases are for various Mach numbers and driver gas compositions. The Mach number is given on each subfigure as M=(Mach number). The gas composition percentage by mass follows the Mach number on each subfigure.

The timing of these waves can be controlled by changing the length of the driver section or by changing the composition of the gas in the driver. A slow driver gas, like air, has the effect of slowing down the expansion waves but usually results in the need for a higher driver pressure for a given incident shock strength. A fast gas like helium, requires lower driver pressures but results in faster reflected expansion waves a shorter time before they intersect the interface. This is shown by comparing figure 2.2C and 2.2D, where the incident Mach number is 2.5 for both but case 2.2C uses a faster driver gas (more helium), and 2.2D uses a slower driver gas (more air). Comparing these figures it can be seen that the expansion waves travel faster in case 2.2C, but that it also has a lower driver pressure. Increasing the driver length increases the time required for the expansion waves to intersect the interface, but requires more gas for each experiment. In the case of slower incident Mach numbers the driver gas pressure will be lower and slower gases can be used without pushing the driver pressure to high (figs. 2.2A and 2.2B).

From these plots it can be seen that the highest pressure in the shock tube will occur in the time between when the transmitted shock is reflected from the test section end wall, and when the reflected transmitted shock is reflected again of the interface as an expansion fan (fig. 2.2A). During this time a limited length of the tube will be subjected to pressures as high as 12MPA according to the X-T plots (fig. 2.2D). This prediction provided a strict design requirement that if the process of reshock were to be examined using optical techniques the windows for observing it would have to withstand

this pressure. Figure 2.3 shows a close up of the reshock pressures for case 2.2C which reveals that the reshock pressure is highly dynamic lasting for less than 0.5ms.

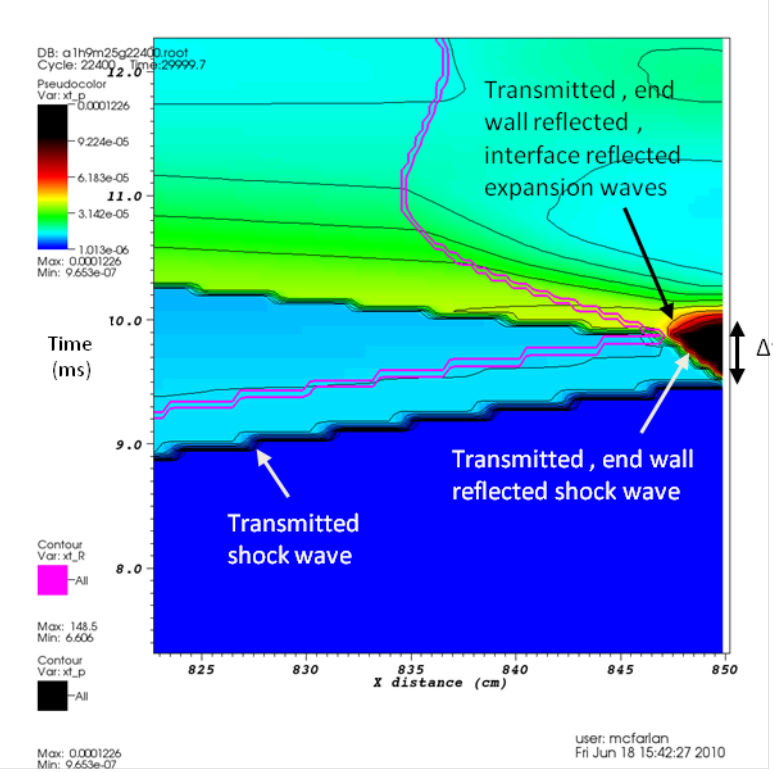

Figure 2.3: Close up of figure 6C showing the reshock pressures and duration.

2.3 Inclined Interface Initial Parametric Study

The inclined interface RMI parametric study was performed initially to aid in the design of the TAMUFMSTF, but was expended to explore many interesting features of the inclined interface RMI through a wide sweep or parameters. From the parametric study a new mixing width scaling method was developed. This section will proceed by first examining the computational set up and parameters to be studied in the simulations,

then the results will be examined through qualitative measures, and finally a quantitative measure of the mixing will developed and presented.

2.3.1Computation set up for initial parametric study

This initial parametric study explored the effects of inclination angle (interface perturbation), incident shock strength (pressure gradient), and Atwood number (density gradient). A set of simulations were performed at three different inclination angles 30°, 45°, and 60°, and two different Atwood numbers, air over SF_6 (A~0.67) and helium over SF_6 (A~0.95). For the air over SF_6 interface three incident shock strengths were simulated, Mach 1.5, 2.0, and 2.5. Due to the different properties of helium the incident shock Mach numbers would need to be lower to provide pressure gradient similar to those in the air over SF_6 cases. For the helium over SF_6 interface two incident Mach numbers were simulated 1.2 and 1.5. Table 2.4 summarizes the conditions for the 15 cases simulated in the initial parametric study.

Table 2.4: Condition for the cases simulated in the initial parametric study.

Case	***M***	**θ**	**Gas Pair**
1	1.5	30	Air-SF_6
2	1.5	45	Air-SF_6
3	1.5	60	Air-SF_6
4	2.0	30	Air-SF_6
5	2.0	45	Air-SF_6
6	2.0	60	Air-SF_6
7	2.5	30	Air-SF_6
8	2.5	45	Air-SF_6
9	2.5	60	Air-SF_6
10	1.2	30	He-SF_6
11	1.2	45	He-SF_6
12	1.2	60	He-SF_6
13	1.5	30	He-SF_6
14	1.5	45	He-SF_6
15	1.5	60	He-SF_6

To reduce the required time to perform the 15 simulations the simulation domain was reduced to a length of 250cm, while the height was set at the full shock tube height of 11.43cm. The ARES AMR capability was also employed to reduce the computation times, and for the initial parametric study the diffusion model was excluded to save time as well. The most refined level for these simulations had a node spacing of 282μm. This resolution was selected based on a qualitative comparison with previous experimental work and computational time. These simulations required roughly 24hours on 128 processors (~2.8 Ghz, 2GB RAM/core) (~3000 cpu hrs.). Later simulations of the initial parametric study cases were rerun with the diffusion model turned on, for comparison. Some of these cases are presented in the later sections.

A section of the computational domain is shown in figure 2.4 for illustration, where the full domain extends to 0 cm upstream and 250 cm downstream. The incident

shock wave was initialized 1cm ahead of the upstream most end of the interface, which varied in position for different inclination angles. The downstream, side, and upstream boundaries were all set to reflecting, no slip boundaries. The location of the downstream boundary was set to be a similar distance from the initial interface location as in the TAMUFMSTF to simulate the conditions after reshock. The upstream boundary also contained a source term located 1cm downstream of the boundary, which supplied mass at the post shock conditions to sustain the incident shock wave. This boundary condition was not ideal, as the shock waves reflected from the interface would travel upstream and reflect from this source term back towards the interface as expansion waves. The intersection of the reflected expansion waves with the shocked interface limited the time over which the simulation could be used to model experiments in the TAMUFMSTF.

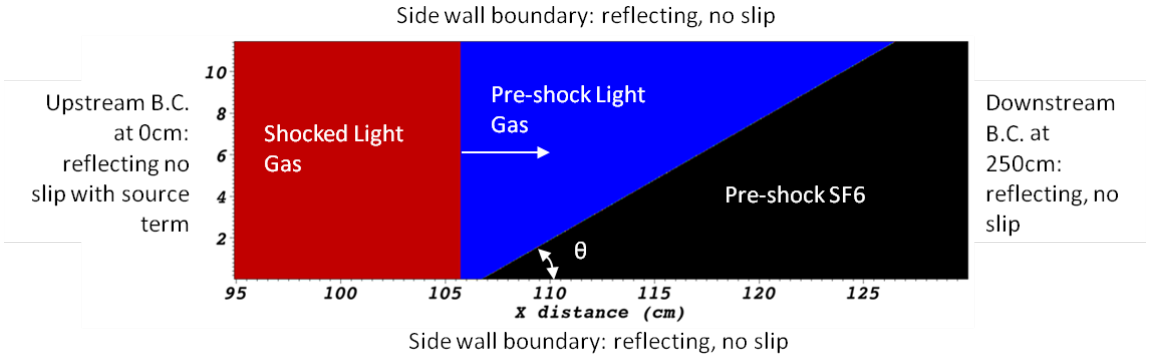

Figure 2.4: Initial conditions for the inclined interface initial parametric study

2.3.2 Qualitative results of the initial parametric study

The results of the initial parametric study will be examined in the following section through a qualitative examination of the density field. The following text was adapted from the authors published work [115] to fit the format of this dissertation.

A time series of density plots, for four different parameter sets, showing the effect of varying each of the 3 parameters discussed in the previous section is presented in Figure 2.5. An exemplar case will be used to aid in comparisons of the results. This case will be case 1 of table 4 (M_i=1.5, θ=30°, A~0.67). The exemplar case (Fig. 2.5 set B) is displayed along with three other cases differing in incident shock Mach number (case 7, Fig. 2.5 set A, M_i=2.5, θ=30°, A~0.67), Atwood number (case 13, Fig. 2.5 set C, M_i=1.5, θ=30°, A~0.95), and interface inclination angle (case 3, Fig. 2.5 set D, M_i=1.5, θ=60°, A~0.67) respectively. Qualitatively, the flows all develop in the following stages:

1. The incident shock wave encounters the inclined interface and generates a reflected shock wave and a transmitted shock wave.
2. The reflected (transmitted) shock wave reflects off of the upper (lower) shocktube wall, interacting with the interface a second time with the reflection from the upper wall being significantly stronger.
3. A more homogeneous region of SF_6 with low mixing evolves behind the transmitted shock front.
4. This region can become disconnected (frame A4 of figure 2.5) from the mixing SF_6 fluid region or remain connected as in Frame D3 of figure 2.5.

5. The transmitted shock wave re-planarizes and the low mixing region of SF_6 becomes rectangular in shape. This is most clearly seen in frame A4 of figure 2.5. In the remainder of the dissertation, we refer to this region of post shock SF_6 as the 'slug' region due to its rectangular shape.

The exemplar case (Fig. 2.5, set B) is characterized by a large mixing region and slug region. In this scenario, a strong lambda shock wave (Fig. 2.5, B1) is formed which travels up the slug until impacting and reflecting off the upper wall. This reflection creates many more secondary compressible effects of high strength that resonate within the slug region (Fig. 2.5, B4). A weak structure similar to a Winkler type vortex [116] or reverse jet is formed within the slug (Fig. 2.5, B3). As the mixing region continues to develop in time, it separates into two large secondary vortical structures of SF_6, (Fig. 2.5, B5) which persist in the flow field to late times.

The effects of incident shock wave Mach number can be examined by comparing the exemplar case (Fig. 2.5, set B) with case 7 (Fig. 2.5, set A). In case 7, the stronger incident shock leads to a higher degree of separation between the mixing region and the slug. In this case the portion of the interface connecting the mixing region to the slug region is flattened by a stronger interface reflected, upper wall reflected shock wave (illustrated in Figs. 14-16). The mixing region is separated by the primary vortex created at the upper wall (Fig. 2.5, A1) which has traveled down the interface. This separation results in the early destruction of the lambda shock allowing the primary transmitted shock to replanarize quickly. The destruction of the lambda shock and the limited width of the slug region suppress the secondary compressible effects within the slug that are

seen in case 1. A strong Winkler type vortex structure is also created within the slug after the lambda shock is destroyed (Fig. 2.5, A2). The Winkler type vortex is joined by other smaller vortical structures at later times (Fig. 2.5, A5)

The effect of the interface Atwood number is shown by comparing case 1 (Fig. 2.5, set B) with case 13 (Fig. 2.5, Set C). It is worth noting that in case 13, the incident shock strength of Mach 1.5 in helium is more similar to the shock strength of case 7 (Mach 2.5) in air, and so it will be compared with this case as well. In case 13, the higher sound speed in helium increases the speed of shock waves reflected from the interface. The change in arrival times of reflected shocks ultimately results in the suppression of the large secondary structures seen in case 7 (Fig. 2.5, A2). In case 13 smaller secondary structures are created by a second refraction of the lambda shock with the interface. The strength of the refracted shock is weaker than that of case 1 and case 7, but its interaction with a relatively flat helium-SF_6 interface makes the secondary structures more visible. Interface inclination effects can be highlighted by comparing the case 1 (Fig. 9, set B) with case 3 (Fig. 2.5, set D). Case 3 is characterized by slower interface growth and a smaller, less mixed, wall-bounded mixing region. The lower inclination angle (less oblique) provides particularly uniform properties in the post shock SF_6, due to the weaker reflected compressible effects (Fig. 2.5, D5). The weakness of reflected compressible effects also results in a simpler interface with fewer secondary spikes and limited mixing. However, a weak Winkler type vortex or reverse spike structure can be seen within the slug (Fig. 2.5, D5) even in this case.

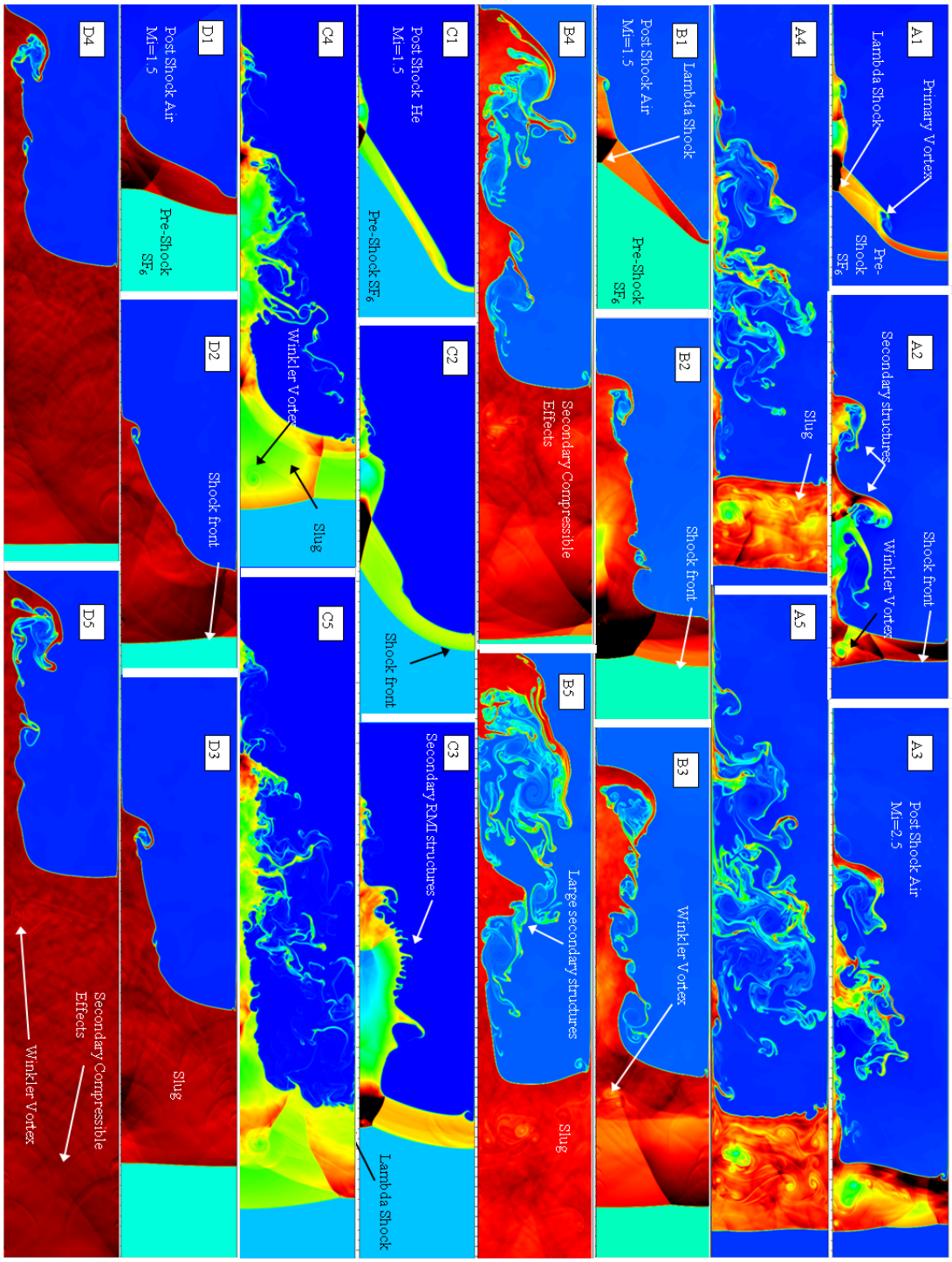

Figure 2.5: Time series plot of density for three different parameter sets. Figures A1-A5, Case 7, at times 0.5, 1.0, 1.5, 2.0, and 2.5 ms respectively. Figures B1-B5, Case 1, at times 0.5, 1.5, 2.5, 4.0, and 5.5 ms. Figures C1-C5, Case 13, at times 0.25, 0.5, 1.0, 1.5, and 2.0 ms. Figures D1-D5, Case 3, at times 0.5, 1.5, 2.5, 4.0, and 5.5 ms.

2.3.3 Quantitative results of the initial parametric study

Having examined the qualitative characteristics of the inclined interface RMI through density plots created from the initial parametric study, the quantitative results will now be examined. For the initial parametric study the measure of most interest was the mixing width growth rate. Predicting the growth rate of an RMI is the first step in controlling it, and so a scaling method for the data was sought which would collapse the growth rates of the RMI over the different parameter sets. This scaling method did not provide a predictive capability directly but instead provided a means to compare the various cases of the inclined interface RMI. The following text, again, follows the words and organization presented in the authors previously published work [115].

Before the mixing width growth rate can be found or scaled the mixing width must be defined. One method for defining the mixing width is to use the width for an equivalent perfectly mixed region. This is the procedure described by Cabot and Cook [117]. Another technique used is to define the mixing width as the distance between the contours of the mole or mass fraction of one of the species. The 1 and 99% or 5 and 95% contours are often selected. This method has the advantage of providing a length that has a physical representation in the experiments and is the one frequently used by experimentalists. It is however sensitive to "noise", as isolated pockets of fluid can accumulate outside of the current mixing width contours and intermittently perturb the mixing width when they accumulate above the designate mass or mole fraction (Fig. 2.6). The equivalent integral method is not subject to this effect. Nevertheless, we adopt

the 5-95% mole fraction method of computing the mixing width, so that it can be compared easily to the experimental results in the following sections.

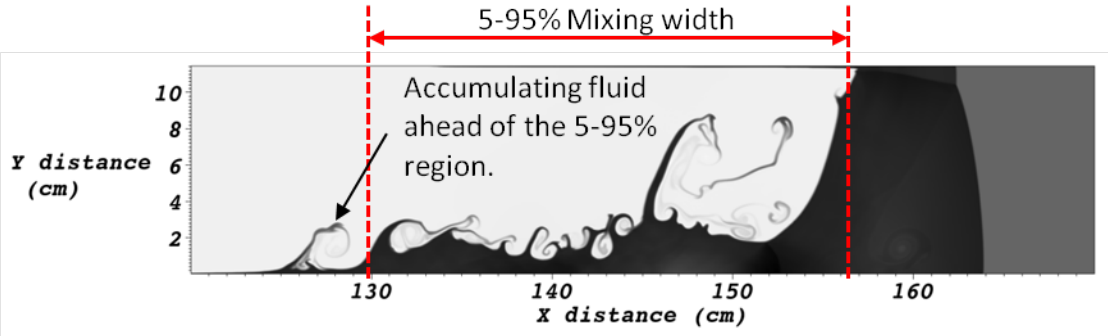

Figure 2.6: Illustration of the flow field showing the 5-95% mole concentration mixing width.

The adapted Richtmyer impulsive model (ARIM) scaling was tested as a first estimate to determine its ability to scale the simulation data and to guide the development of a new scaling method appropriate for the inclined interface. In adapting Richtmyer's impulsive model, we first define the amplitude and wavelength as shown in figure 11. The initial interface amplitude was defined as the length of the interface measured in the direction of travel of the incident shock wave (Figure 2.7). The interface wavelength was defined as twice the length of the interface perpendicular to the direction of travel of the incident shock wave. This is done since we view the interface as symmetric about the lower wall giving a triangular shaped initial condition which somewhat resembles the continuous sine wave for which Richtmyer's model was intended for.

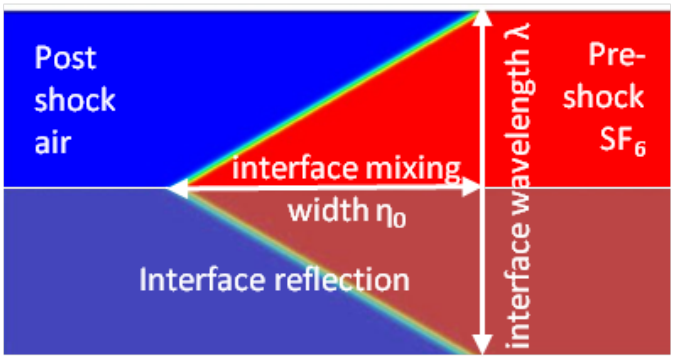

Figure 2.7: Illustration showing the interface initial perturbation amplitude and wavelength as used in the scaling methods.

Equations 33-37 define the ARIM used to analyze the simulations. Equation 2.7 defines a non-dimensional time, τ_{ARIM}, with an offset time, t^*_{ARIM}, that is the time required for the shock wave to traverse the inclined interface amplitude η, and is given explicitly in equation 2.8. This offset time is similar to the cloud-crushing time term, used in shock-bubble interactions literature[67]. A non-dimensional amplitude, $\overline{\eta}_{ARIM}$ (eqn. 2.9), is also offset by the post-shock amplitude, η_0'. Equation 2.10 gives the impulsive growth rate adapted from Richtmyer's model, and is similar to equation 1.22, except here, we use the post-shock amplitude, η_0', at time t^*_{ARIM}, as described in equation 2.8. Equation 2.11 ensures that the initial ARIM amplitude is zero, at $t = t^*_{ARIM}$. The 1D gas dynamic parameters and wave speeds used in these calculations are given in Table 2.5 and 2.6.

$$\tau_{ARIM} = k\dot{\eta}_0\left(t - t^*\right) \tag{2.7}$$

$$t^*_{ARIM} = \lambda/\left(2w_i \tan\theta\right) \tag{2.8}$$

$$\overline{\eta}_{ARIM} = k(\eta - \eta'_0) \tag{2.9}$$

$$\dot{\eta}_0 = k\eta'_0 A'[v] \tag{2.10}$$

$$\eta'_0 = \eta\left(t^*\right) \tag{2.11}$$

Table 2.5: Gas properties for 1D gas dynamics estimations

Initial Parameters	Ratio of specific heats γ	Gas constant R (J/(kg K))	Initial Gas Temperature (K)	Initial Gas Pressure (kPa)
Air	1.4	287	300	101.3
Helium	1.667	2077	300	101.3
SF_6	1.09	56.92	300	101.3

Table 2.6: Wave speeds calculated using 1D gas dynamics equations

Incident Mach Number	Light Gas	Heavy Gas	w_i (m/s)	w_t (m/s)	w_{rrt} (m/s)
1.2	Helium	SF_6	1223.00	192.73	156.34
1.5	Helium	SF_6	1528.76	282.05	177.56
1.5	Air	SF_6	520.75	242.76	156.56
2	Air	SF_6	694.38	353.75	167.23
2.5	Air	SF_6	867.97	465.55	197.17

The non-dimensionalized data from the ARIM scaling for the Air-SF_6 simulations is plotted below in Figure 2.8. For all mixing width plots, the key lists the cases described by the light gas name, the Mach number, excluding the decimal point, preceded by the letter M, and inclination angle preceded by the letter A. In Figure 2.8, the curves with constant angle of inclination and different incident shock strengths appear to collapse well. However the scaling does not account for the angle of inclination in its current form.

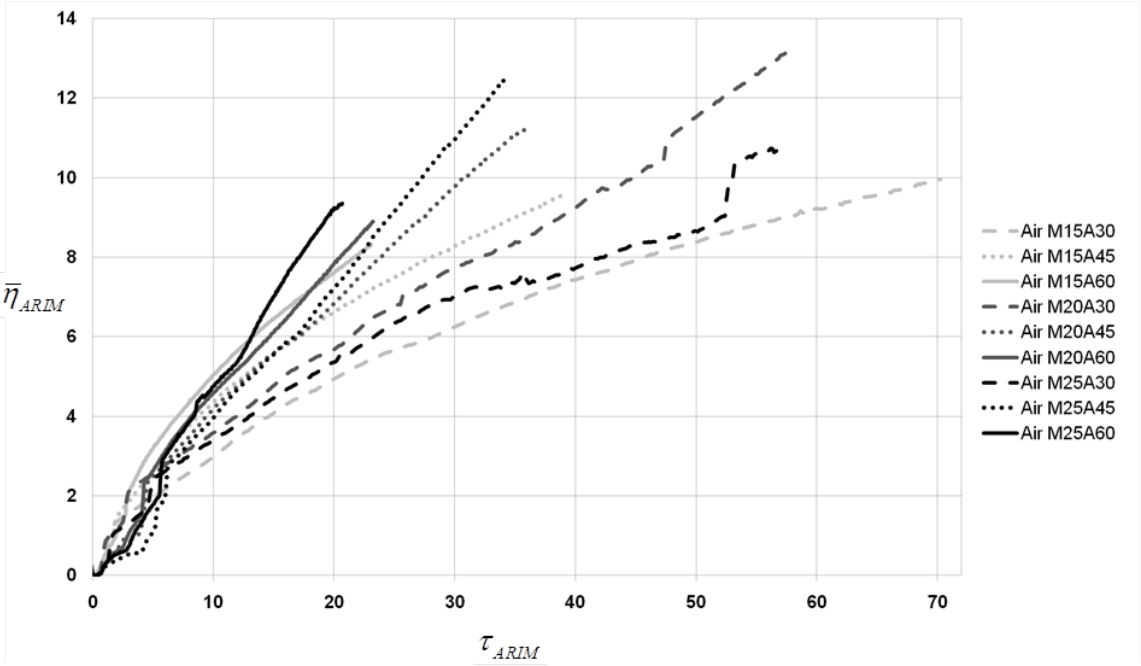

Figure 2.8: Mixing width measurements non-dimensionalized using the Adapted Richmyer Impulsive Model for all Air over SF_6 cases.

For early times, say $\tau < 25$, the collapse is not as good as it is at later τ. This is partially due to the discontinuities in mixing width measurements discussed previously, but also due to the initial non-linear growth that occurs after the incident shock wave

traverses the interface initial amplitude. The data is cropped at the onset of reshock from the downstream boundary. Sudden increases in the mixing width are visible towards the end of some data sets. These sudden increases are due to the mixing width definition errors discussed previously.

Figure 2.9 shows non-dimensionalized helium-SF_6 simulation data compared to a sample of the Air-SF_6 data for comparison. Overall it is seen that the collapse is poor, but that the helium-SF_6 simulations fall in the same range of non-dimensional growth rates as the air-SF_6 simulations. This is suggests that the ARIM scaling made an improvement on the collapse of the data for different Atwood numbers but it will require further Atwood number considerations. It can also be seen again in figure 2.9 that the ARIM scaling is not accounting for the different initial interface inclination angles correctly.

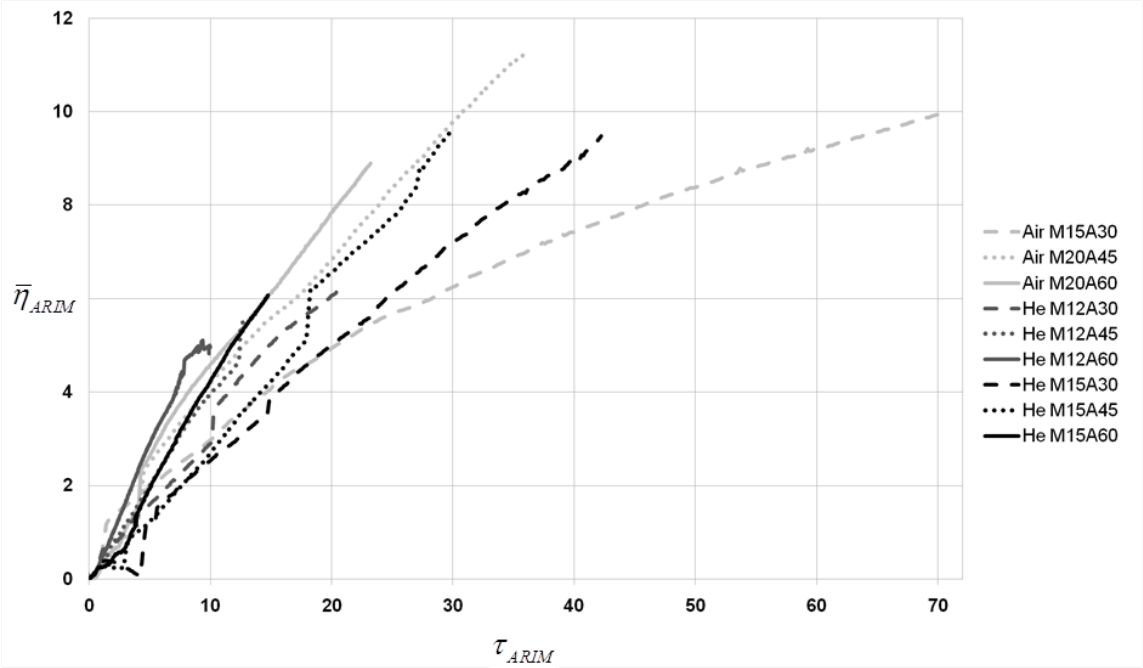

Figure 2.9: Mixing width measurements non-dimensionalized using the Adapted Richmyer Impulsive Model for selected Air over SF_6 cases and helium over SF_6 cases.

It appears that the ARIM scaling must be adjusted to account for the interface geometry and the initial non-linear compression of the interface. The strategy for arriving at a new early time, inclined interface scaling (IIS) was to use the basic pattern of the Richtmyer impulsive model scaling but to select parameters appropriate to an inclined interface. The Richtmyer impulsive model scaling consists of an offset time multiplied by a gas pair ratio and divided by characteristic time (equation 2.12). The scaling methods ability to scale data sets with different density gradients was not modified and the Atwood number was used again to account for changes in the density gradients.

$$\tau = \frac{A\left(t - t^*\right)}{t_{char}} \tag{2.12}$$

The characteristic time in the Richtmyer impulsive model scaling was found from a characteristic velocity, the interface jump velocity, and a characteristic length, the wave number squared divided by the post shock interface amplitude. For the IIS it was found that the transmitted shock wave speed (w_t) was a more accurate characteristic velocity. This is because the important secondary compressible effects (interface reflected, wall reflected, interface transmitted ($I_R W_R I_T$) shock wave, and subsequent reflections) travel at speeds that scale more closely with the transmitted wave speed. The importance of these secondary compressible effects is explained further with respect to the selection of an offset time later.

The characteristic length was selected by examining the effects of the length of the interface parallel (height) and perpendicular (width) to the incident shock wave velocity. The result was a characteristic length term called, the effective λ given by equation 2.13. This term can be described as the interface width that would be required for each inclination angle if the interface height were held constant across all inclination angles, θ. The resulting characteristic length is defined as $\lambda^2 / \left(2\eta_0\right)$. This is similar to the characteristic length for the ARIM scaling ($\lambda^2 / 4\pi^2\eta_0'$). The difference between the two scaling methods is that the ARIM scaling uses the post shock compressed amplitude, whereas the IIS uses the initial interface height.

$$\lambda_E = \lambda \cdot \tan(\theta) \tag{2.13}$$

Another difference in the IIS method was to use a more accurate offset time to better predict the initial non-linear compression time. The ARIM scaling was offset by the time it took for the incident shock wave to traverse the height of the interface. This accounts for the initial compression of the interface by the incident shock wave but misses the compression effects of the secondary compressible waves. After the incident shock wave is transmitted, secondary compression and expansion waves continue to traverse the width of the interface. These waves increase in strength as the interface inclination angle becomes more oblique (smaller θ). The strength of these waves diminishes with every subsequent interaction with an interface or boundary that occurs.

The first of these secondary effects is shown in Figure 2.10. This wave is denoted as the interface reflected, wall reflected (I_RW_R) shock wave. The strength of this shock wave is sufficient to cause a compression of the interface along its width, and to extend the initial non-linear compression time of the interface. Subsequent waves will continue to alter the growth rate at a diminishing rate. The time at which this wave has compressed the interface will approximate the end of the initial non-linear compression time.

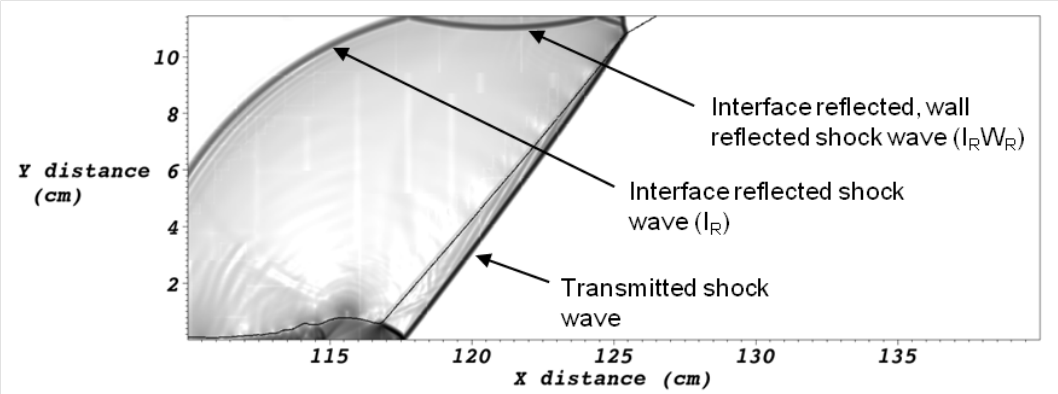

Figure 2.10: Gradient of Pressure plot at an early time (t~0.226ms) after shock interaction for case 7.

To predict the time at which the I_RW_R shock wave has compressed the interface, 1D gas dynamic equations were used. The initial compression time from the incident shock wave was again calculated using the 1D incident shock speed and the interface height. At the end of this time it was assumed that part of I_RW_R shock transmits through the interface. The transmitted leg of this wave ($I_RW_RI_T$) was used to determine the end of the initial nonlinear compression time since it had the lower speed. While the 1D calculated speed of the un-transmitted leg of the wave is higher, the wave is limited by the transmitted leg (Figure 2.11). Using the 1D approximated speed of the transmitted leg more accurately predicted the time at which the transmitted leg has reached the wall (Figure 2.12) and the compression of the interface from this wave is complete. The width compression time is then determined from the 1D velocity of the $I_RW_RI_T$ shock wave (w_{rrt}), and the width of the interface. This time is added to the initial compression time to yield the new offset time discussed below.

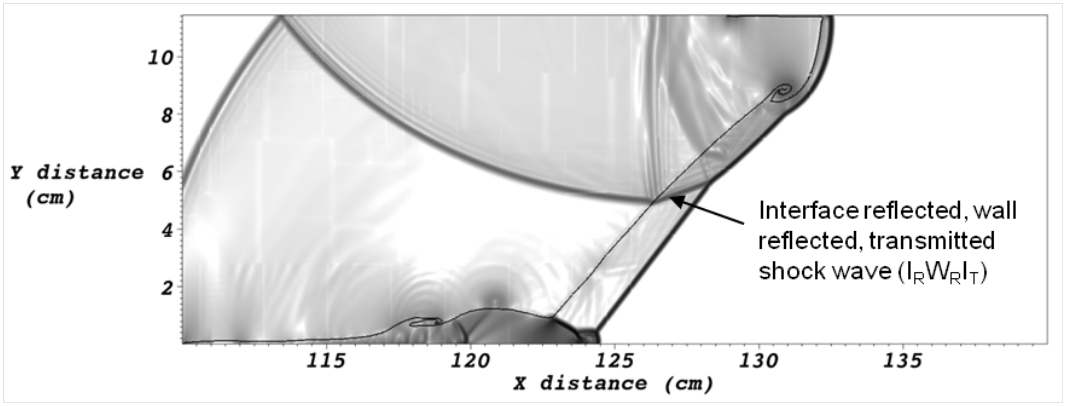

Figure 2.11: Gradient of Pressure plot at time t~0.302ms after shock interaction for case 7.

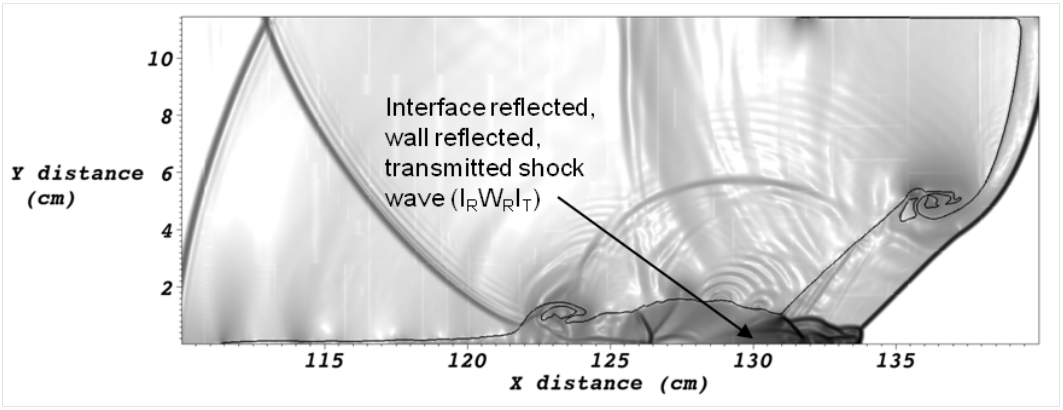

Figure 2.12: Gradient of Pressure plot at time t~0.524ms after shock interaction for case 7.

Equations for the IIS method are summarized in equations 2.14-2.17. The calculated 1D transmitted wave speeds used in equations 40 and 41 can be found in Table 5 of the previous section. The results of the IIS are presented in figures 2.13 and

2.14. It can be seen in figure 2.13, that there is less scatter in the data, as compared to figure 2.8. Furthermore the shape of the scaled curves is much more linear. The IIS method appears to account better for the nonlinearity of the problem as well as for the angle of inclination. However, it would appear from figure 2.14, that the agreement between helium-SF_6 cases is not as good. The errors associate with the mixing width algorithm, creates artificial jumps in the mixing width data that then offset the non-dimensional mixing width. If the slopes after these jumps are compared to each other, it can be seen that the growth rates are similar for all cases. Also in Figure 2.14 (air-SF_6) these jumps in the mixing width can be seen to cause an artificial divergence in the data at very early times (near τ=0).

$$t^* = \frac{\lambda}{2w_i \tan\theta} + \frac{\lambda}{2w_{rrt}} \tag{2.14}$$

$$\tau = \frac{w_t A'}{\lambda_E}\left(t - t^*\right) \tag{2.15}$$

$$\overline{\eta} = \frac{\left(\eta - \eta^*\right)}{\lambda_E} \tag{2.16}$$

$$\eta^* = \eta(t^*) \tag{2.17}$$

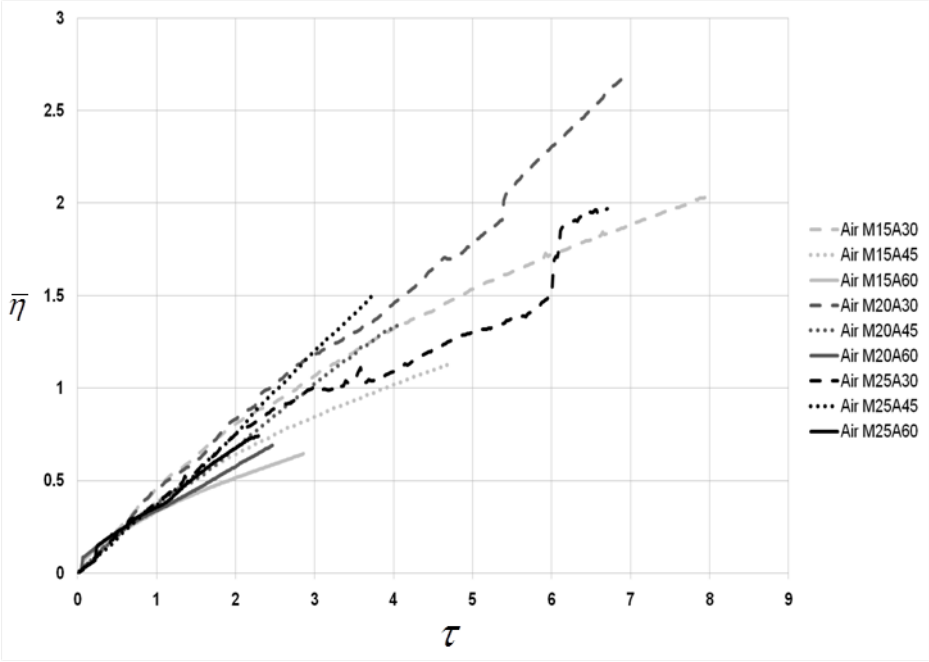

Figure 2.13: Mixing width measurements non-dimensionalized using the Inclined Interface Scaling method for all Air over SF_6 cases.

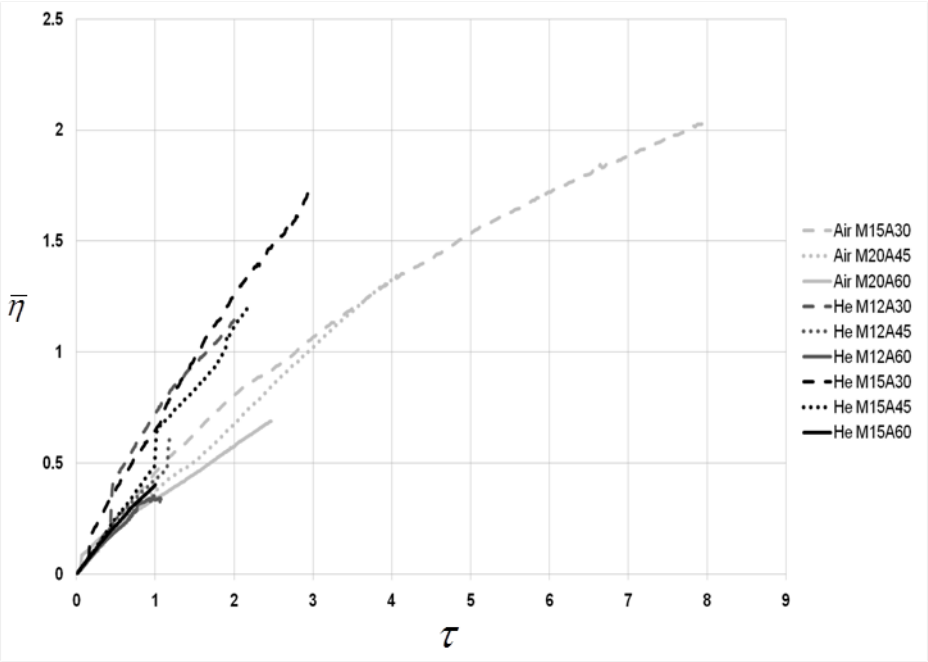

Figure 2.14: Mixing width measurements non-dimensionalized using the Inclined Interface Scaling method for selected Air over SF_6 cases and helium over SF_6 cases.

To compare the performance of the two scaling methods the coefficient of variance (standard deviation / mean) was plotted for the air-SF6 cases in figure 2.15. The coefficient of variation shows how well data from different cases are collapsing to a single line (the mean), where a lower value indicates the data is closer to a common line. Comparing the coefficient of variance for the two different scaling methods is complicated because the two scaling methods do not have a common τ, nor can the two non-dimensional times be scaled to each other. To attempt a fair comparison of the two scaling methods the non-dimensional mixing width was compared between two common events, the start of the shock-interaction with the interface (τ,τ_{ARIM}=0) and the first reshock that occurs. This reshock occurs in the M=2.5, θ=60° case for both scaling methods. Figure 2.15 shows the coefficient of variance is lower for the IIS method. The IIS method shows a large improvement at early times with the exception of the spike at τ of approximately 0.1. This spike is an error again due to an artificial rise in the mixing width created by the mixing width definition. If the error which produced the spike was resolved the new scaling method should result in less than a 10% deviation from the mean non-dimensional mixing width up to τ of 0.85. The deviation only increases to approximately 15% at τ of 2 where the first reshock occurs. The helium-SF_6 data showed similar improvement when plotted alone as well as when incorporated with the air-SF6 data but neither scaling method performed well at higher Atwood numbers.

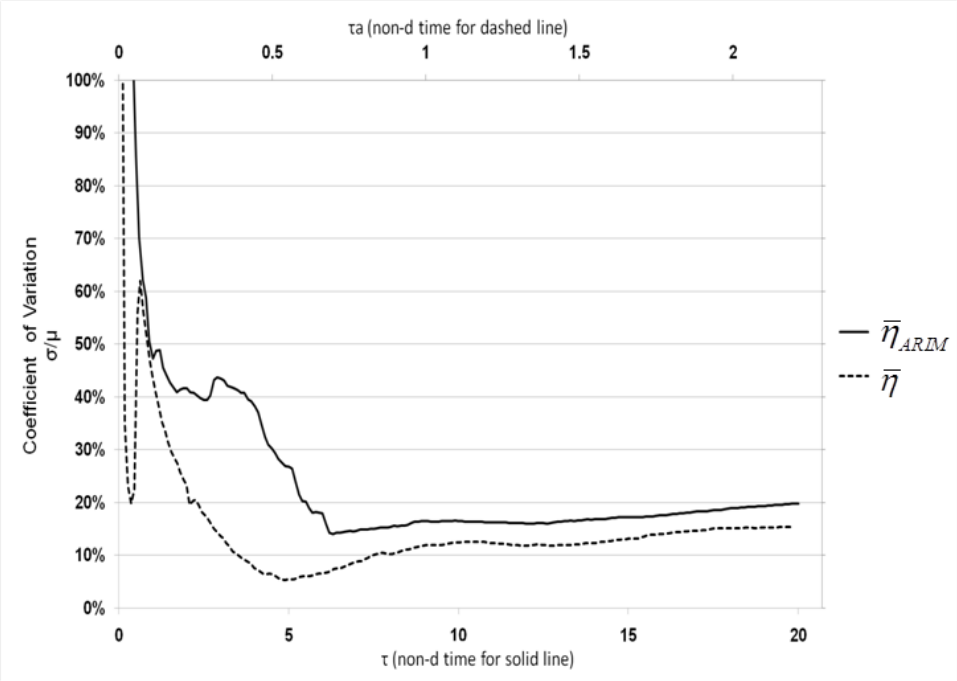

Figure 2.15: Coefficient of variation for the non-dimensional mixing width plotted for air SF6. $\overline{\eta}_{ARIM}$ is the non-dimensional mixing width for the adapted Richtmyer impulsive model scaling and $\overline{\eta}$ is the non-dimensional mixing width for the new scaling method.

2.3.4 Conclusion from the initial parametric study

From flow-field visualization of the inclined interface problem, within the parameter space studies here, it can be clearly seen the shock refraction pattern has a significant effect on the developing morphology of the interface. These density plots show the evolution of two main regions in the flow field: a mixing region containing both species, dominated by large vortical structure, and a more homogenous region of unmixed fluid which can separate away from the mixing region in some cases. The early time growth rate of the mixing width is predicted poorly using the Richtmyer impulsive model scaling as adapted in this dissertation for the inclined interface. The adapted

Richtmyer impulsive model scaling struggles to collapse the data from different inclination angles. A new scaling method, the inclined interface scaling (IIS) method, was proposed that collapses the data for different incident shock wave Mach numbers, and interface inclination angles well at early times. The IIS method improved agreement for different Atwood numbers but still requires some improvement. This method uses the 1D gas dynamics wave speeds for the incident shock wave and the interface reflected, wall reflected, transmitted shock wave to predict the end of the initial nonlinear compression of the interface. The characteristic velocity for the IIS method was the 1D transmitted wave speed instead of the interface jump velocity used in the Richtmyer impulsive model.

2.4 Linear Versus Non-linear Initial Perturbations

As discussed in section 1.3.1 the initial interface perturbation can be categorized by the ratio of its amplitude to wavelength, η/λ as linear or non-linear. The traditional definition for initial perturbation linearity is when the amplitude to wavelength ratio is less than 0.1, ($\eta/\lambda<0.1$) [26]. In the parametric study the interface inclination angle controlled this ratio (eq. 33). The initial angles studied were 30°, 45°, and 60° which corresponded to amplitude to wavelength ratios of ~0.87, 0.5, and ~0.29 respectively. All of these angles corresponded to initial perturbations that were highly non-linear. To study the linear initial perturbation regime the initial parametric study was extended to include some linear cases. This section will be organized as follows; modifications to the computational set up and the parameters sets studied will be presented, then qualitative results will be presented by examining density, pressure, and vorticity plots, finally

qualitative measures of the interface characteristics will be presented using statistical measures of the interface, and measures of the interface mixing.

2.4.1 Computational set up and additional parametric sets

For the interface perturbation linearity study 3 additional inclination angles were simulated, 75°, 80°, and 85°. These inclination angles spanned from weakly non-linear to linear initial perturbations. These inclination angles were run only for the air over SF_6 interface with an incident mach number of 2.5, except for the 80° case which was run for Mach 1.5, 2.0, and 2.5. Table 2.7 summarizes the parametric cases studied for the linear versus non-linear initial perturbation study and gives their amplitude to wavelength ratio (η/λ), where cases with $\eta/\lambda < 0.1$ are considered the linear cases. The helium over SF_6 interface was not simulated in the linear regime.

Table 2.7: Interface linearity study cases.

Case	***M***	**θ**	**η/λ**
1	1.5	30	0.866
2	1.5	45	0.500
3	1.5	60	0.289
4	1.5	80	0.088
5	2.0	30	0.866
6	2.0	45	0.500
7	2.0	60	0.289
8	2.0	80	0.088
9	2.5	30	0.866
10	2.5	45	0.500
11	2.5	60	0.289
12	2.5	75	0.134
13	2.5	80	0.088
14	2.5	85	0.044

The computational set up for the linear interface perturbation study is similar to that of the initial parametric study. Like the initial parametric study all of the boundary conditions were reflecting no slip boundaries with the upstream boundary containing a source term to sustain the shock. The shock was initialized 1 cm upstream of the upstream most point of the interface. Figure 2.16 shows the initial conditions for the interface linearity study. The highest level of refinement for the AMR was 282μm for the bulk of the simulations, but resolution study was run and for two example cases the max resolution was increased to 94μm for the highest level of refinement. For this study the ARES diffusion model was turned on, and the interface was initialized with an initial diffusion thickness of 1cm using the stratification model presented in section 2.1. The air over SF_6 cases presented in section 2.3 and used again for the interface linearity study were rerun using the diffusion model to provide accurate comparisons with the new linear cases.

The effect of the diffusion model was examined by comparing the air over SF_6, Mach 2.5, 30° inclination case with and without diffusion at a resolution of 282μm. The effects were examined by comparing the mixing width, defined by the 5 and 95% contours as before, and the total circulation, discussed later in section 2.4.4. Figure 2.17 shows the mixing width measurements plotted over time for the cases with and without diffusion. From this figure it can be seen that the application of the diffusion model damps out the sudden jumps in mixing width discussed previously in section 2.3.3. It can also be seen that the initially diffuse interface has little impact on the mixing width at early times. At late times, before reshock the diffuse interface reaches a higher mixing

width. It reality, both cases probably reach the same mixing width, but the diffuse case is tracked easier by the mixing width algorithm. The circulation is plotted in figure 2.18 and shows that the trends are similar for both cases. The diffuse case is almost identical to the non-diffuse case at early times but at late times it has more negative circulation before reshock and reaches a higher circulation after reshock.

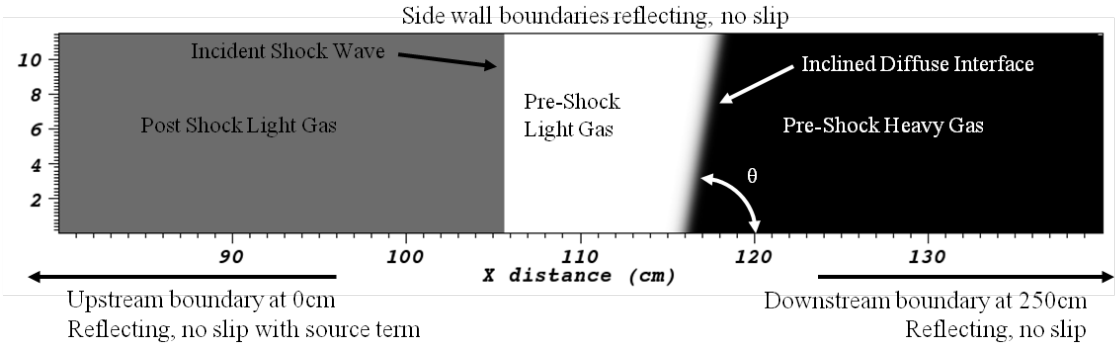

Figure 2.16: Initial conditions for the interface linearity study.

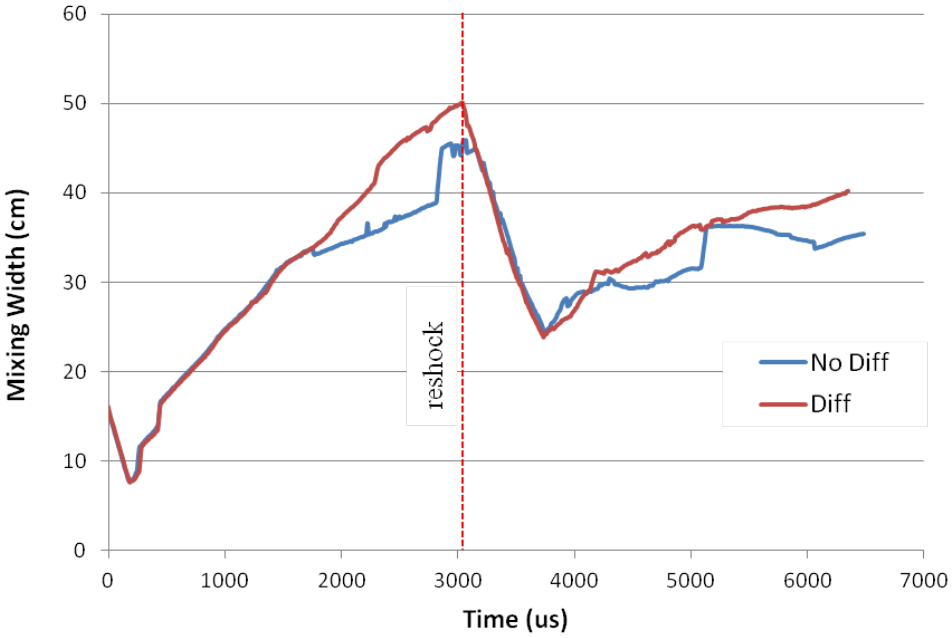

Figure 2.17: Mixing width plots for case 9 with and without diffusion.

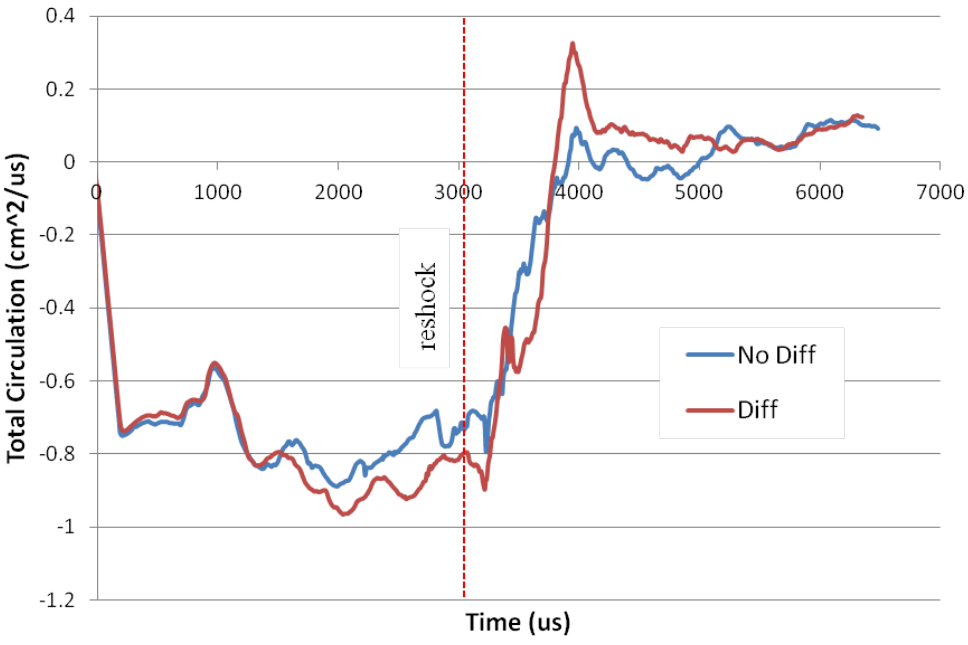

Figure 2.18: Total circulation plot for case 9 with and without diffusion.

2.4.2 Resolution study

The problem of selecting the proper resolution for the simulations was neglected in the initial parametric study. In this stud the resolution was selected by a heuristic approach that sought only to determine what resolution provided results which looked most like the conditions observed in previous experiments. More computer resources were available when the interface linearity study was started and so higher resolutions were attainable with more cpu time available. During the resolution study the AMR criteria were adapted and optimized to speed up the computations. Four resolutions were investigated for the air over SF_6, Mach 2.5, 30° inclination case. These resolutions are summarized in table 2.8. To determine the appropriate resolution for the simulations convergence was sought for flow field parameters. The mixing width, mix mass, and circulation were plotted over time for the four resolutions. The results would be considered to be converged when two resolutions provided results that were nearly identical (within a few percent) over time.

Table 2.8: Cases for the resolution study

Case	Base resolution (mm)	Refinement levels	Max resolution (μm)
Res 282	7.62	4	282
Res 169	4.57	4	169
Res 94	7.62	5	94
Res 56	4.57	5	56

Figure 2.19 shows the mixing width over time for the four resolutions. From this plot it can be seen that the mixing widths are nearly identical for all resolutions with the only difference being the time at which the mixing width jumps at early times from the

mixing width algorithm error discussed before. However when the mix mass for the four resolutions is examined the agreement is not as good. Figure 2.20 shows the mix mass steadily rising as the resolution increases with no convergence being achieved. The reason for this is that smaller scale vorticies are produced with higher resolution, creating more vorticity overall and increasing the mixing. This is visible in figure 2.21, where the positive and negative components of circulation (area integral of vorticity) are plotted over time for the four cases. This plots shows the vorticity steadily increasing with resolution and no convergence being achieved. The reason that convergence is not achieved is that the turbulence length scales for this flow field are quite small. The necessary resolution for convergence of vorticity dependent parameters is on the order of viscous length scale, defined in equation 2.18. The viscous length scale is plotted for the high resolution case 9 data at 3 different times in Figure 2.22. This figure shows that viscous length scale is as small as 2e-3μm, while the best resolution achievable with the available computational resources was 94μm. These numbers are off by a factor of many orders of magnitude meaning that convergence will be impossible without the addition of a subgrid model. While convergence could not be achieved it will seen in later sections that the results still accurately model the main features of the inclined interface RMI.

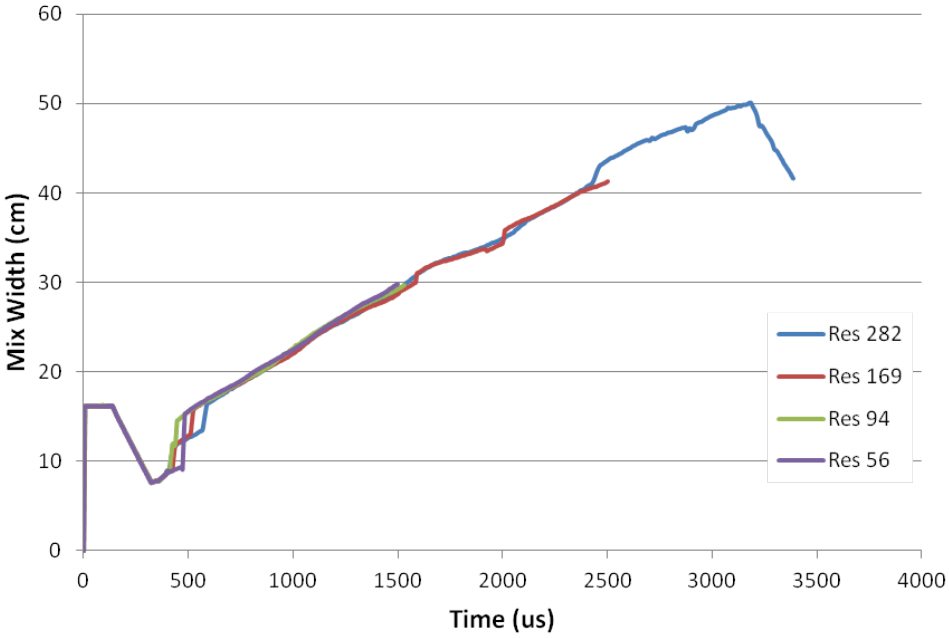

Figure 2.19: Mixing width over time for four resolutions.

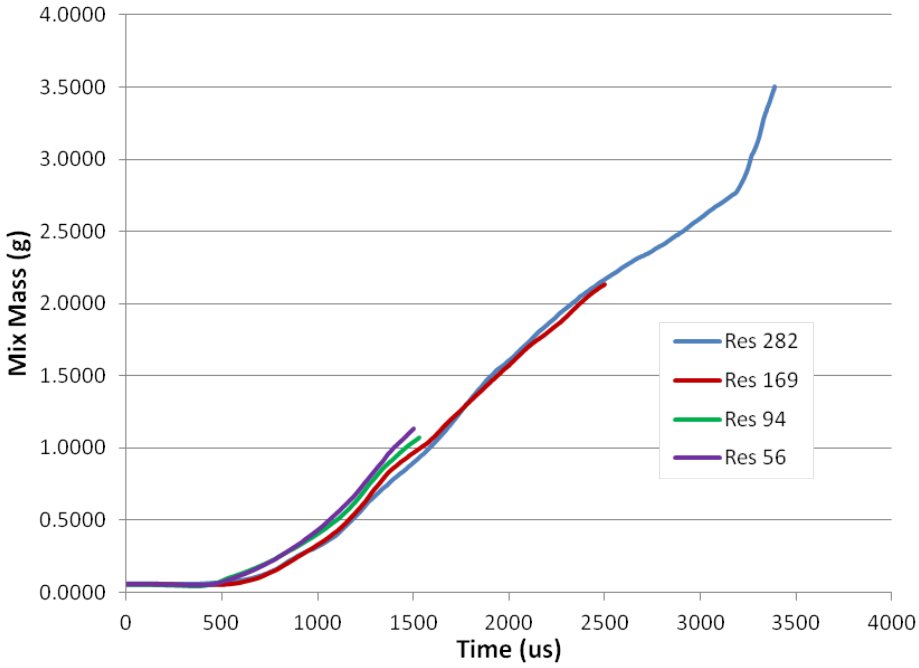

Figure 2.20: Mix mass over time for four resolutions.

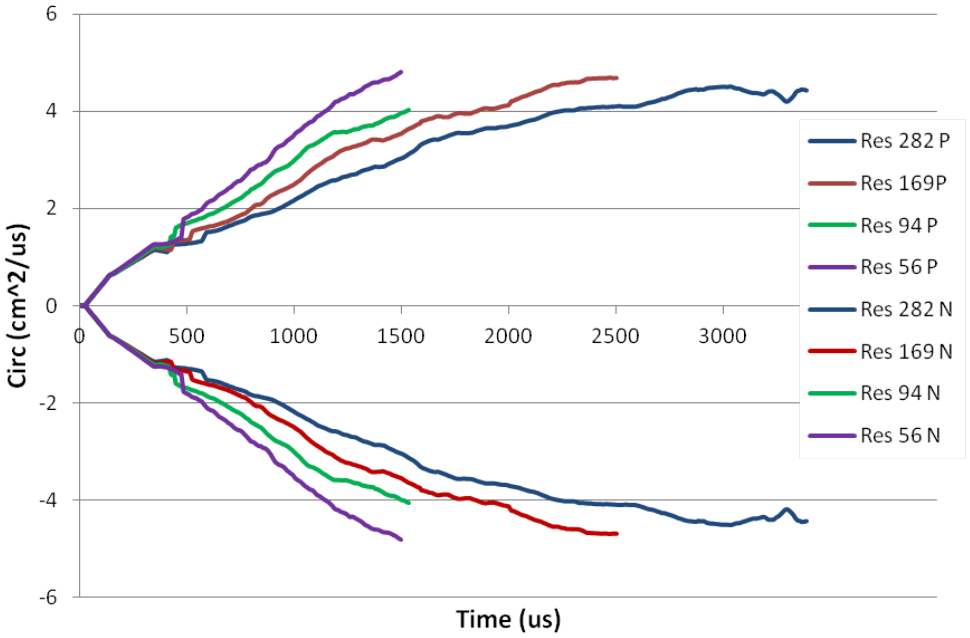

Figure 2.21: Positive and negative circulation over time for four resolutions.

$$VL = \frac{\mu}{\rho V} \tag{2.18}$$

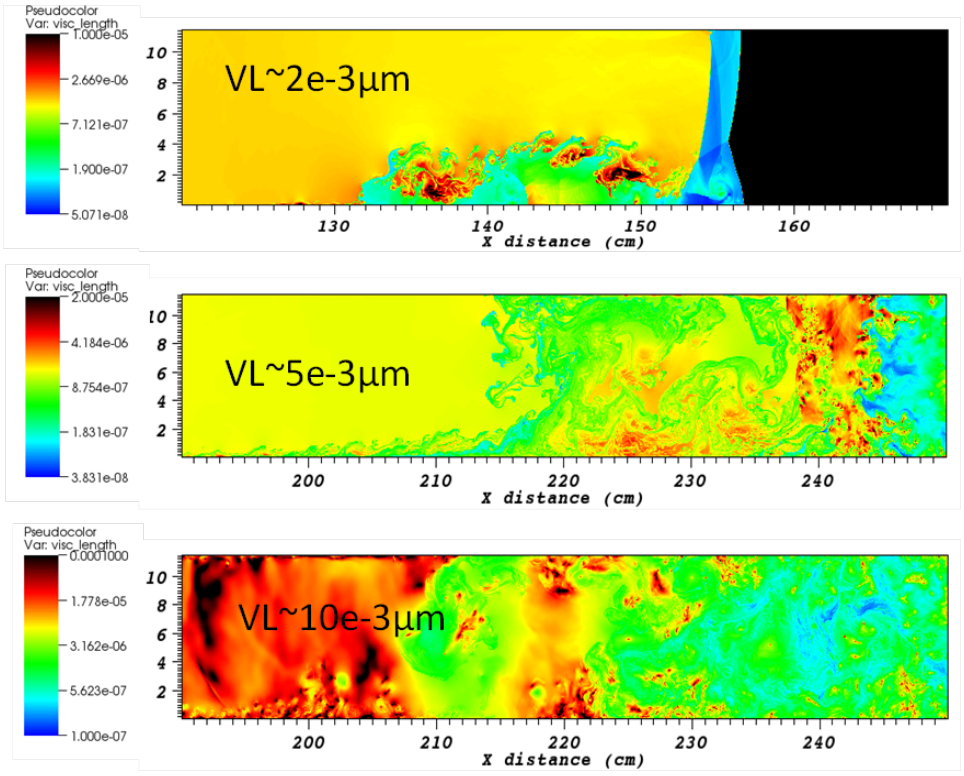

Figure 2.22: Viscous length scales for case 9 at three times; top t=1ms, middle t=3.5ms, and bottom t=6.5ms.

2.4.3Qualitative comparison of linear and non-linear cases

Having examined the computational set up and justified the resolution selection and limitations for the simulations presented, a qualitative comparison of the RMI with linear and non-linear initial perturbations will now be presented. The following text will closely follow the text of the Authors previously published work on the subject [118]. Two cases will be used as characteristic examples of the linear and non-linear interfaces, case 13 (θ=80, M=2.5), the linear exemplar, and case 9, (θ=30, M=2.5) the non-linear exemplar. The density, pressure, and vorticity fields are shown in figure 2.23 for the evolution of the two example cases at the lower resolution of 282μm. For the linear case, it can be seen that the flow field evolution is markedly less complex. The secondary compressible effects are much weaker and do not significantly increase the vorticity, the mixing region remains much more connected to the slug region, and the Winkler type or reverse spike structure does not evolve.

The primary difference between the nonlinear and the linear case is the existence of the secondary compressible effects in the non-linear case. For the linear case, the interface is mostly parallel to the incident shock wave meaning the reflected shock will travel mostly upstream leaving only a weak leg to intersect the upper wall as seen in figure 2.23 E1. With no large pressure gradients present at later times the weak waves created by the small, upper wall reflected portion of the interface reflected shock wave become visible as they reverberate though the slug region (figure 2.23 D3). These waves are not visible in the nonlinear case because the strength of the initial upper wall reflected shock was such that it created a more complex flow field in the slug region.

The vorticity for the linear perturbation case is limited to the interface line with some small amounts of vorticity being created by the weak reverberating waves within the slug region (figure 2.23 E3). Only one well organized vortex is visible at the tip of the spike formation (figure 2.23 E6). For the nonlinear perturbation the vorticity is increased continually as the stronger secondary compressible effects continue to intersect the interface in the mixing region (figure 2.23 C2-4). The density fields for the linear case show that the mixing region remains well connected to the slug region even at late times (figure 2.23 D6). The mixing region for the nonlinear case, on the other hand, nearly separates at early times (figure 2.23 A2) and is only connected by the boundary layer at late times (figure 2.23 A5).

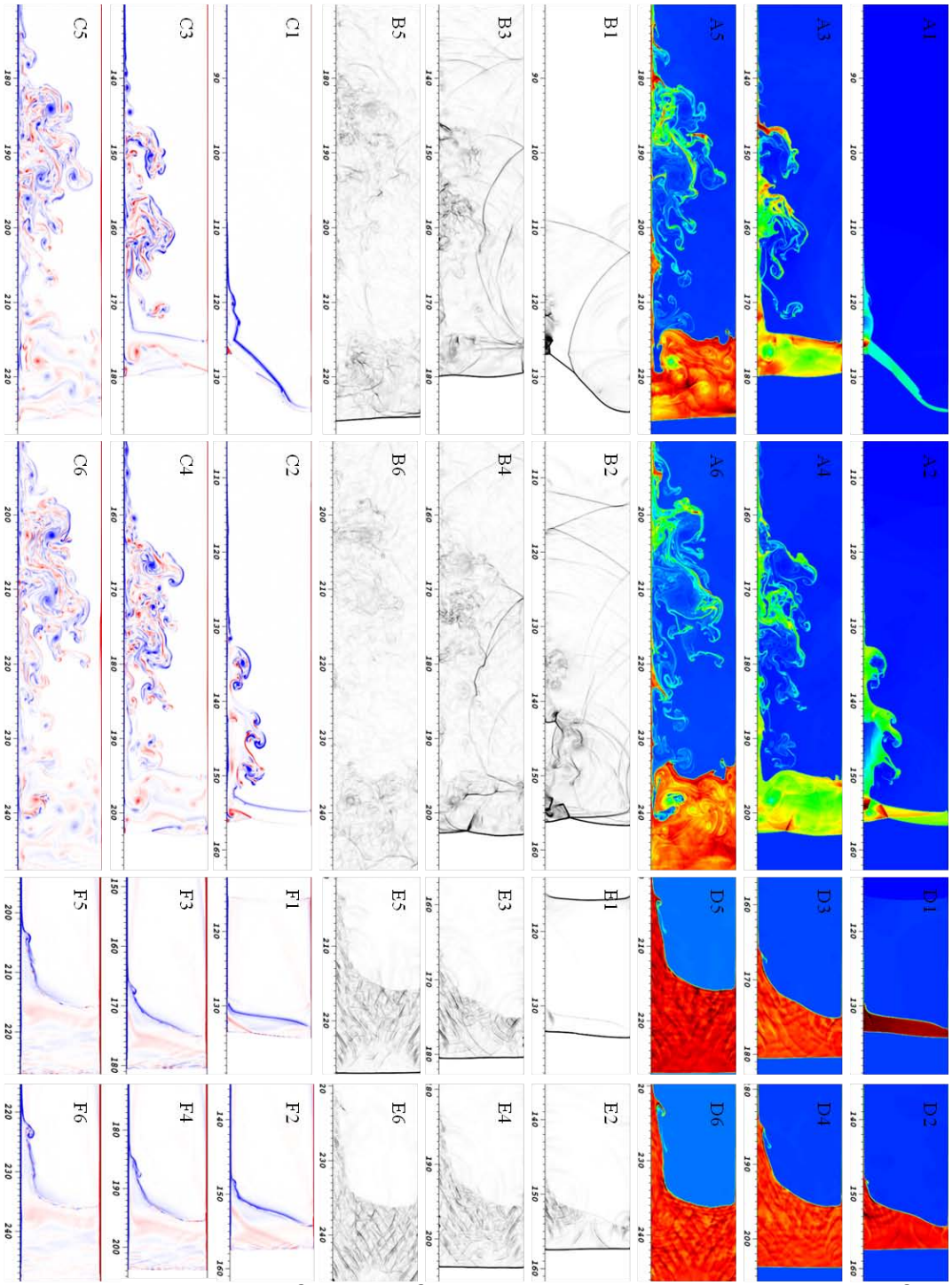

Figure 2.23: Time series of density (figure sets A and D), pressure gradient (figure sets B and E), and vorticity (figure sets C and F) plots. These are for initially non-linear (case 9, figure sets A-C) and linear cases (case 13 figure sets D-F) at times 0.5, 1.0, 1.5, 2.0, 2.5, and 3.0ms (numbers 1-6 respectively).

At late times the interface will undergo the process of reshock where it will be re-accelerated by the transmitted shock which has reflected from the end wall of the test section. This process will further amplify the mixing of the two flow fields and provide additional data to compare the two example cases. The following text describing the flow fields near and after reshock was adapted from the Authors work to be submitted for publication. Figures 2.24 through 2.29 show density vorticity, and chi plots plots for the linear 30° and the non-linear 80° flow fields before and after reshock. The chi plots show the scalar dissipation rate and the chi term is defined in equation 2.19 where D is the mass diffusion coefficient, and y_1 and y_2 are the species mass fractions. This term has been used in other works [119] to show the level of mixing occurring at small scales. In Figure 27A it can be seen that for the non-linear case before reshock the flow field exhibits the 2 main regions described earlier, the mixing region, and the slug region. Before reshock, the mixing region is characterized by disordered vorticies and is the primary region of vorticity and species mixing (Fig. 2.25A). After reshock, the slug region loses organization and becomes the primary mixing region (Fig. 2.24B). The onset of reshock causes the formation of many smaller vorticies in the remnants of the slug region (Fig. 2.25B). At late times, vorticity begins to decrease and the small vorticies merge into larger ones (Fig. 2.25C). As these vorticies coalesce they produce more well organized mass projectiles of SF_6 (Fig. 2.24C). The molecular mixing at these late times has become less intense but has increased in area greatly (Fig. 2.26C).

$$\chi = D * \frac{d}{dx} y_1 * \frac{d}{dx} y_2 \tag{2.19}$$

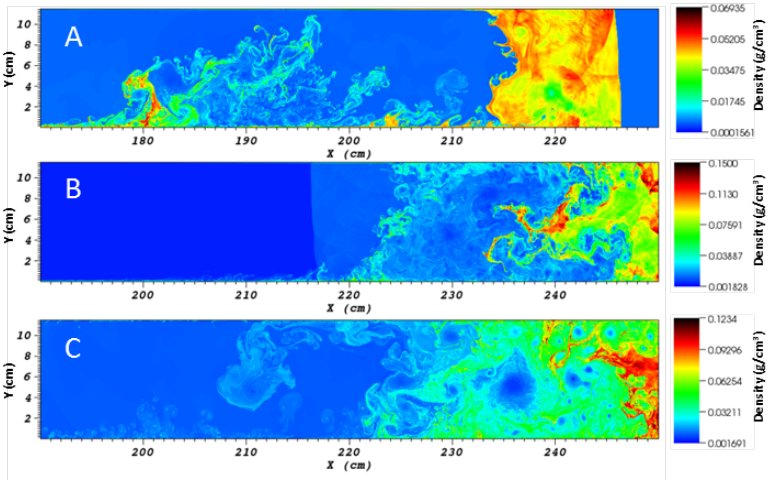

Figure 2.24: Density contour plots for the non-linear example case at three times; a) late time prior to reshock (2.5ms), b) early time after onset of reshock (4ms), c) late time after onset of reshock (6.5ms). The scale is unique for each time. Here the maximum resolution is 94 µm.

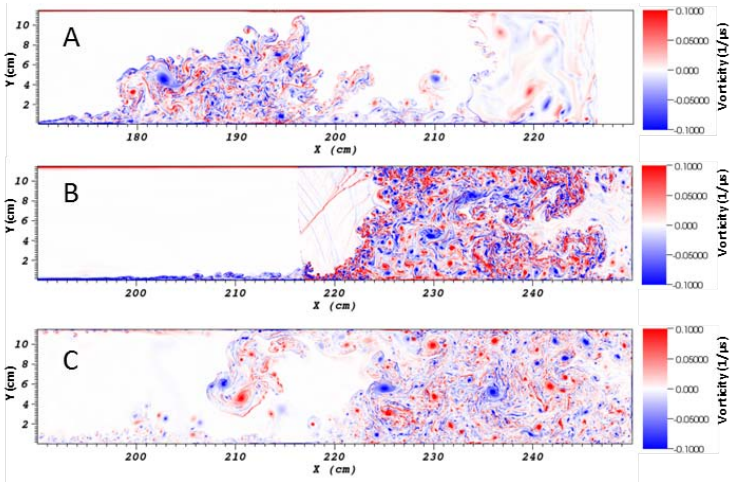

Figure 2.25: Vorticity contour plots for the non-linear example case at three times; a) late time prior to reshock (2.5ms), b) early time after onset of reshock (4ms), c) late time after onset of reshock (6.5ms). Here red represents positive vorticity and blue represents negative vorticity. The scale is uniform for all times. The maximum resolution is 94 µm in this plot.

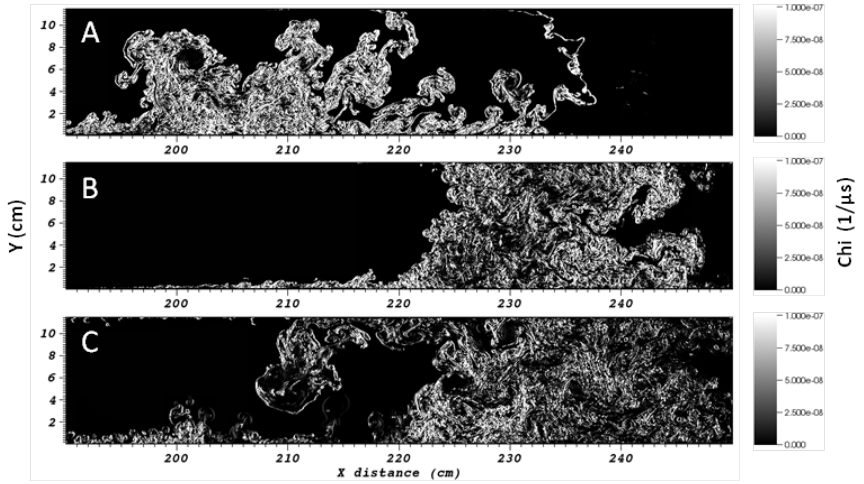

Figure 2.26: Chi contour plots for non-linear example case at three times; a) late time prior to reshock (3ms), b) early time after onset of reshock (4ms), c) late time after onset of reshock (6.5ms). Here white shows areas of high molecular mixing. The scale is uniform for all times.

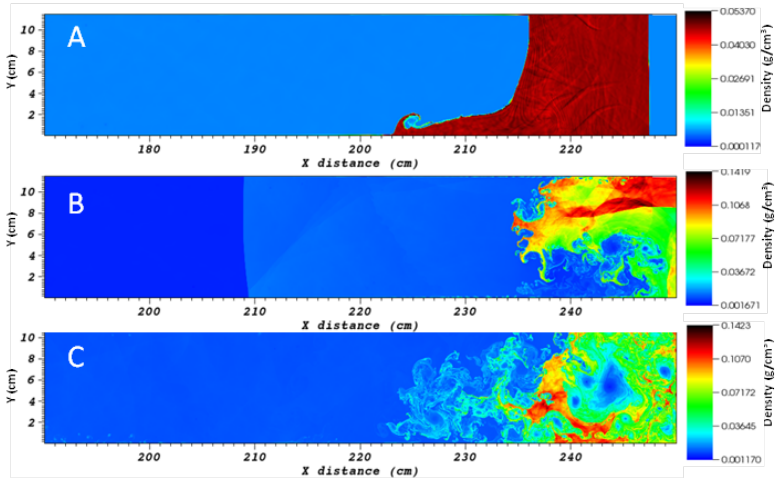

Figure 2.27: Density contour plots for the linear example case at three times; a) late time prior to reshock (2.5ms), b) early time after onset of reshock (4ms), c) late time after onset of reshock (6.5ms). The scale is unique for each time. The maximum resolution is 94 µm in this plot.

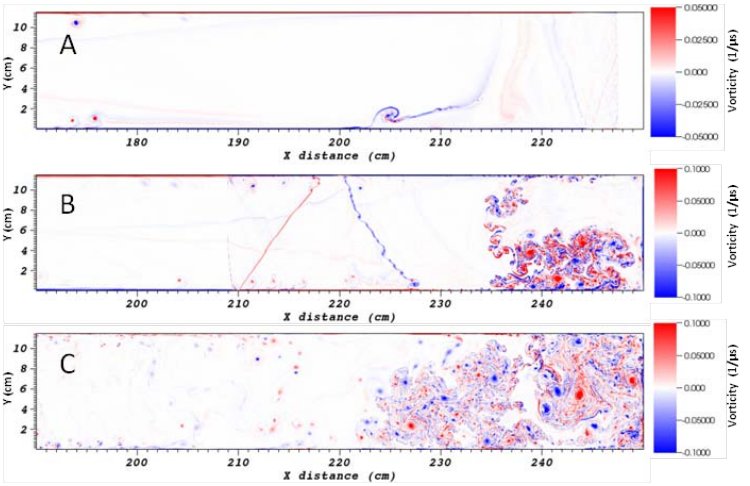

Figure 2.28: Vorticity contour plots for the linear example case at three times; a) late time prior to reshock (2.5ms), b) early time after onset of reshock (4ms), c) late time after onset of reshock (6.5ms). Here red represents positive vorticity and blue represents negative vorticity. The scale is uniform for all times. The maximum resolution is 94 µm in this plot.

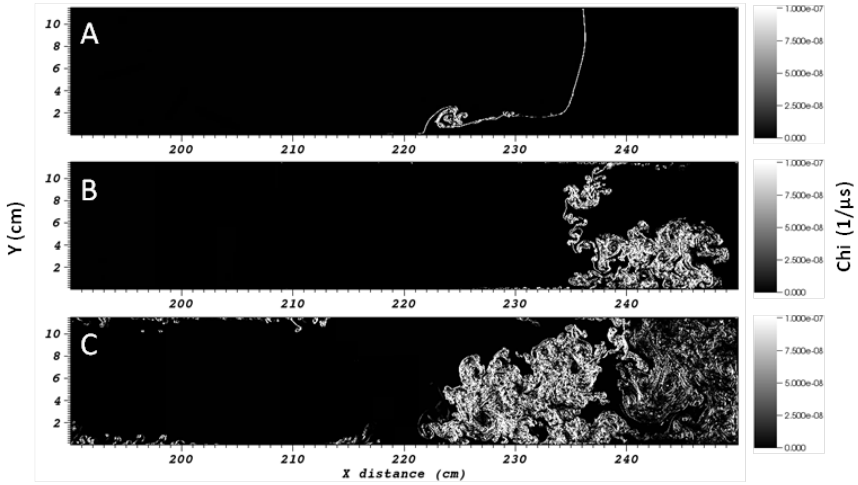

Figure 2.29: Chi contour plots for the linear example case at three times; a) late time prior to reshock (3ms), b) early time after onset of reshock (4ms), c) late time after onset of reshock (6.5ms). Here white shows areas of high molecular mixing. The scale is uniform for all times.

Figures 2.26A shows that linear case remains well organized and exhibits low mixing before reshock unlike the non-linear case. In the linear case an organized spike structure is formed. This spike is unable to break away from the post shock SF_6 and separate into a mixing region, but the low mixing homogeneous post shock SF_6 slug region is still formed. For this case there is only one well formed vortex at the spike front before reshock (Fig. 2.28A) as opposed to the linear case where there are many strong vorticies present at this time. The onset of reshock generates an impulsive acceleration opposite to the incident shock, and inverts the spike drawing the slug region out to mix with the reshocked air (Fig. 2.27B). The strongest vorticity is generated in the region where the spike was inverted into the slug region (Fig 2.28B). The vorticity at early times after reshock is more localized in the linear case than the non-linear case. At late times after reshock small structures have evolved (Fig. 2.27C) from the amplified vorticity (Fig. 2.28C) which has begun to decay as energy is dissipated to smaller scales. The molecular mixing is greatly increased and is divided into a region of moderat mixing near the end wall, and a region of higher intensity mixing at the upstream, air side (Fig. 2.29C). At these times the density fields for the two cases bear some resemblance while the vorticity fields show that the linear case has far fewer and smaller vorticies than the non-linear case, and that the non-linear case processes some well organized vortex projectile pairs.

2.4.4 Quantitative comparison of linear and non-linear cases

The quantitative comparison of the linear (case 13 θ=80, M=2.5) and non-linear (case 9 θ=30, M=2.5) example cases will be conducted by first looking a statistical

measures of the interface density and the turbulent Mach number, then by examining the mixing width growth rates and mix mass, and finally by examining quantitative measures of the flow field vorticity. The following text on the statistical measure of density and the turbulent Mach number is adapted from the Authors previously published works [115], [118].

To quantitatively highlight the differences in development of the mixing and slug regions between the two cases plots of the density averaged in the direction parallel to the incident shock wave (eqn. 2.20) versus the distance perpendicular to the shock were generated. The standard deviation (eqn. 2.21) was also plotted in the same manner to highlight the variance in the density data at any location. The standard deviation can serve as an approximation of the mixing of the two species at a location as long as the density perturbations due to the presence of local shock waves are negligible. A high standard deviation represents an area where the gases are mixing, and low area represents an area of uniform gas species. Figure 2.30 shows the average and standard deviation of density for the two cases at three different times. At all 3 times the nonlinear (30 degree case) has a wider region of high standard deviation indicating the larger mixing region. In figure 2.30 B the slug region is visible for both cases as the area where the average density is high and the standard deviation is low. At late times the standard deviation in the slug region of nonlinear case has an increased standard deviation due to the development of the Winkler type structure.

$$\rho_{avg} = \frac{\sum_{i=1}^{N} \rho_i \cdot \Delta y_i}{\sum_{i=1}^{N} \Delta y_i} \tag{2.20}$$

$$\rho_{stdev} = \sqrt{\frac{1}{N} \sum_{i=1}^{N} \left(\rho_i - \rho_{avg} \right)^2} \tag{2.21}$$

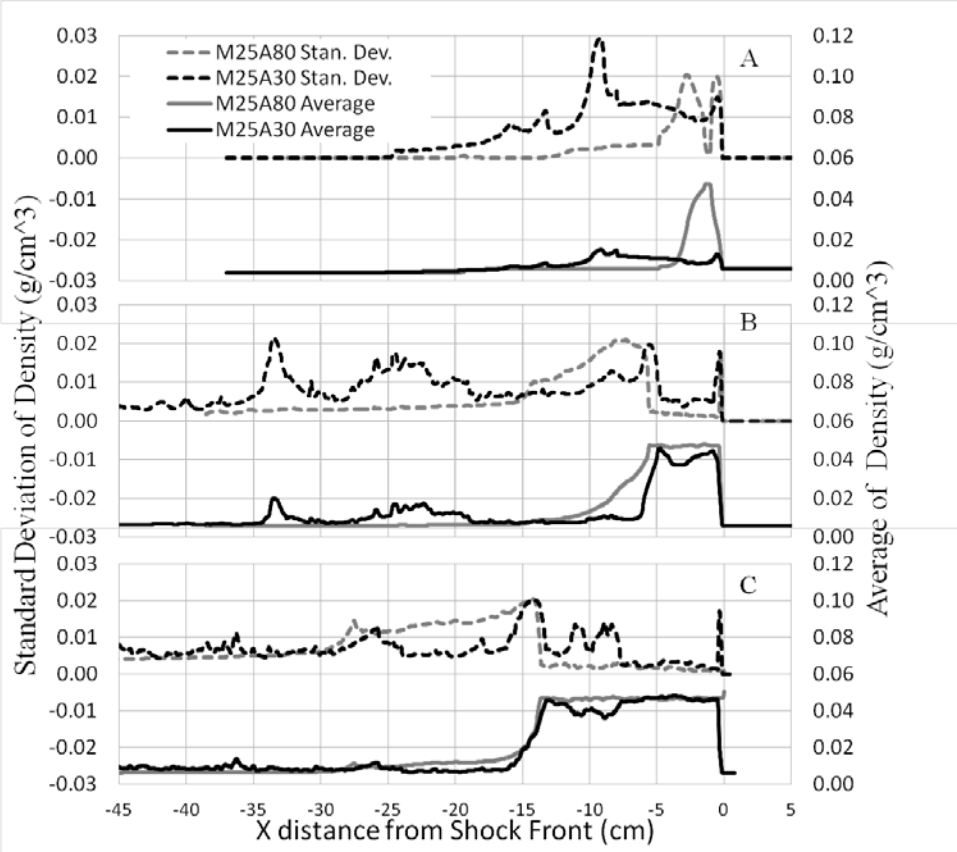

Figure 2.30: Average and standard deviation of density for the nonlinear and linear cases at three different times; 0.5, 1.5 and 3.0ms (A, B, and C respectively). In these plots, solid and dotted line represents average and standard deviation of density respectively.

The turbulent Mach number, as defined by equation 2.22 where $\langle\ \rangle$ indicates the average is taken, can be plotted in the same manner as the average and standard deviation of density. The turbulent Mach number gives an indication of the relative importance of compressible effects for the velocity perturbations. High turbulent Mach numbers indicate that the perturbations in the velocity field are approaching sonic speeds. The turbulent Mach number is sensitive to the standard deviation of the flow field. As mentioned above the standard deviation of the density for the nonlinear case is high in comparison to the average for a large area of the flow field. This means that turbulent Mach number will have a large variation as well since the average sound speed will have a high variation similar to that of the density.

$$T_m = \frac{\langle u' \rangle}{\langle a \rangle} \tag{2.22}$$

In figure 2.31 is the turbulent Mach number is plotted for the two cases at three different times. At all three times it can be seen that the turbulent Mach number spikes just behind the shock front for both the nonlinear and linear cases. This spike is due to the presence of reverberating waves close to the shock front. At early times the turbulent Mach number remains high (>0.8) behind the shock front for the non linear case. One can also observe higher values of the turbulent Mach number for non-linear case in the region between 2 to 7 cm behind the shock front. This region corresponds to the "slug" region discussed above. The presence of Winkler-type structure in this region is responsible for these fluctuations. At all times, the nonlinear case's turbulent Mach number remains higher at most locations after the "slug" region and contains more

fluctuations than the linear case. This notably higher turbulent Mach number at all locations for the nonlinear case is another important distinction between the two cases.

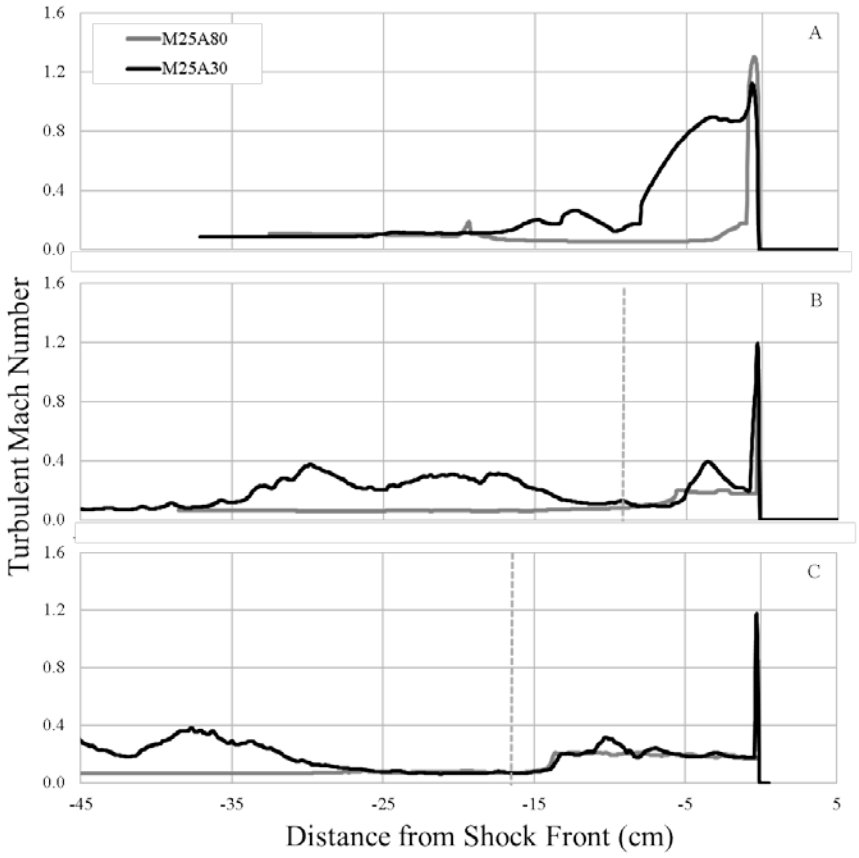

Figure 2.31: Turbulent Mach number for the nonlinear and linear cases at 3 different times 0.5, 1.5 and 3.0ms (A, B, and C respectively). The vertical dashed line approximates the end of the "slug" region.

Another method to compare the linear and non-linear cases is to examine the mixing measurement of the interface. To do this the inclined interface scaling method (IIS) discussed first in section 2.3.3. Figure 2.32 shows the scaled data using the IIS

method for the cases listed in table 7. It can be seen that none of the linear perturbation cases (M15A80, M20A80, M25A80, M25A85) collapse with the nonlinear cases. Case 12 (M25A75) can be considered to be a quasi linear case since its initial η/λ is near the linear regime cut off. In figure 2.33 it can be seen that case 12 collapses well with the non-linear cases at early times before diverging at later times. This divergence from the collapse line at late times occurs for the nonlinear cases as well. This trend suggests that between the inclination angles of 75 and 80° the growth regime changes. As discussed in the previous section this is likely due the secondary compressible effects becoming much weaker as the inclination angle increases. The 80° inclination angle cases display a jump in the non-dimensional mixing width that is due to the errors associated with the definition of the mixing width discussed above. After these jumps the non-dimensional mixing width growth rate for these three cases seems to collapse well. This suggests that here the IIS method is working well for variations in incident shock Mach number. However when inclination angles are compared for a constant incident Mach number in the linear regime the collapse is poor as for cases 12-14 (M25A75, M25A80, M25A85).

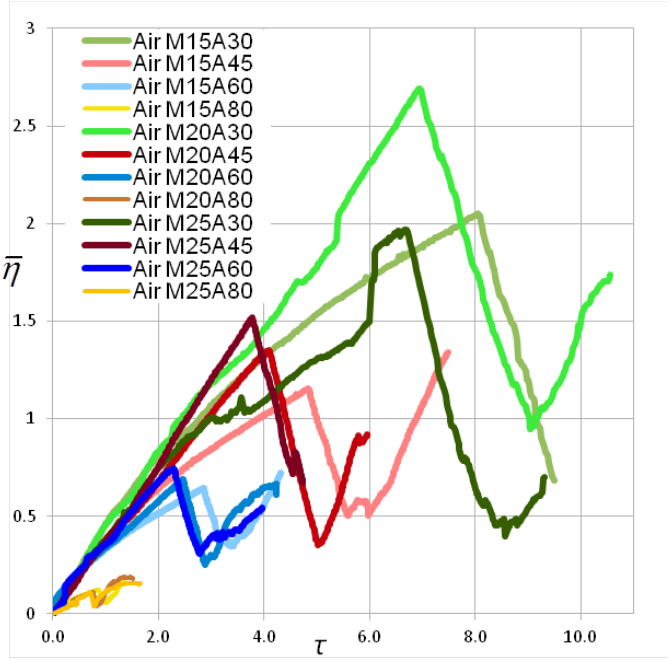

Figure 2.32: Non-dimensional mixing width versus time for all cases.

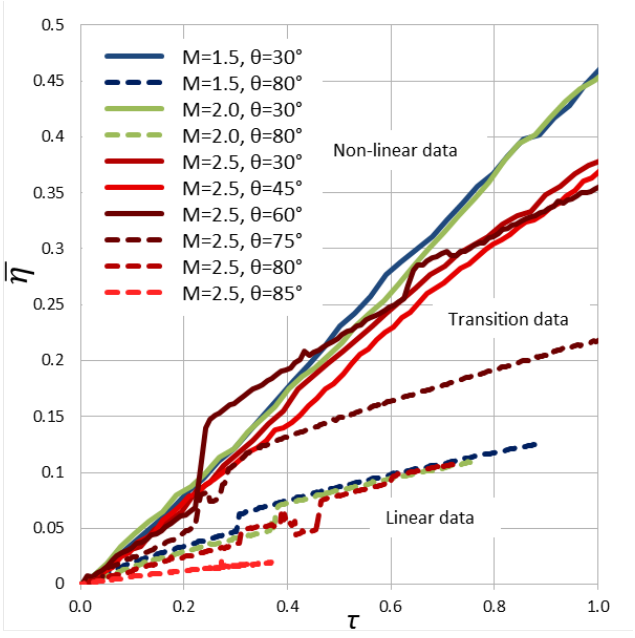

Figure 2.33: Close up of non-dimensional mixing width versus time for all cases.

In Figure 2.32 the effect of reshock is visible as the scaled mixing widths undergo a compression at late times and then begin to grow again. The IIS method was applied to the post shock mixing width data independently, with a modification to the offset time. This time was modified to be the time at which the mixing width had reached its minimum value after reshock. The non-dimensional mixing width was offset by the non-dimensional mixing width at the offset time. While the IIS method was developed for the conditions before reshock it can be applied to post reshock times with some success since reshock characteristic scales will scale with their pre-reshock counterparts. The scaled reshock mixing width data is shown in Figure 2.34. From this figure it can be seen that the initial growth rates after reshock are similar for both the linear and non-linear cases. While the non-dimensionalized growth rates diverge greatly at later times, the growth rates of the linear cases lie within the bounds of the growth rates of the non-linear cases.

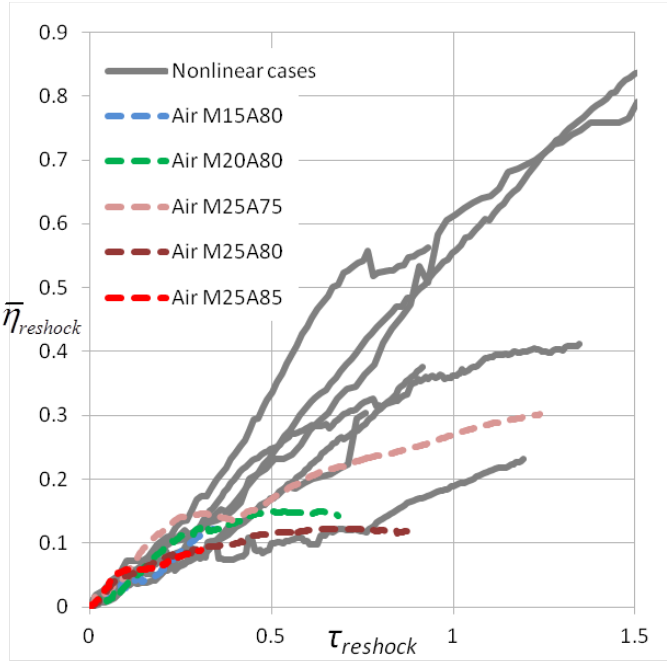

Figure 2.34: Scaled reshock mixing width versus scaled time for selected linear and non-linear initial perturbation cases. Data sets are described in the key as follows; the number following the m is the mach number multiplied by 10, the number following the a in the interface inclination angle in degrees. Linear cases are represented by grey lines. No trend or difference in the linear and nonlinear cases is visible suggesting the initial condition have had little effect on the post reshock growth rates.

The total mix mass of the flow field can be found by summing the mix mass over the mixing area. Figure 2.35 shows the total mix mass of flow fields before and after reshock. For the non-linear case the mix mass begins increasing as a result of the incident shock generating the first RMI. For the linear case very little mass mixes until the onset of reshock. Both cases exhibit a similar rate of increase in their mix mass after reshock. While the mix mass production rate is similar (~2.5g/ms) for both cases at early times after reshock, the linear case mix mass production rate remains high while the non-

linear case begins to asymptote at late times. The difference in mix mass between the two cases decreases from 2.8g at reshock to 2.0g at late times. The majority of the mix mass for both cases can be seen to be produced after reshock, where the increased vorticity continues to increase the surface area for diffusion between the air and SF_6.

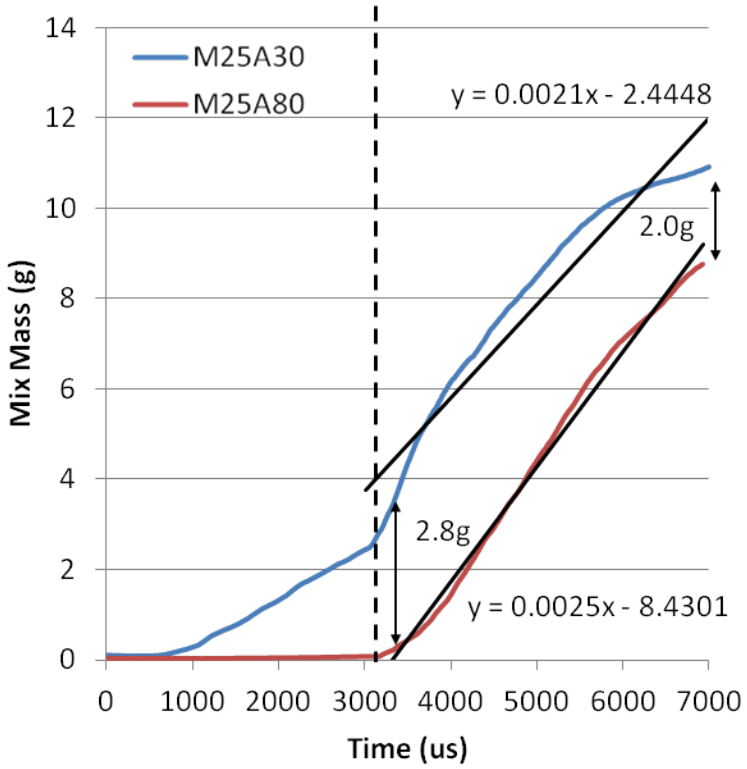

Figure 2.35: Mix mass plotted over time. The blue line represents the non-linear case, and the red line represents the linear case. The dashed line approximates the time at which reshock occurs.

Having compared the linear and non-linear cases through measures of mixing they will now be examined using circulation plots. The circulation, defined by Equation 2.23,

can be used to show the total vorticity in a flow field. Since the simulation used contained boundary layers, the circulation was summed over the core of the flow field which excluded the boundary layer vorticity. Summing the positive and negative vorticity masks the total amount of vorticity produced which can be shown by separating the positive and negative components, as seen in Figure 2.36 for the linear and non-linear interface cases. From this figure it can be seen that the initial intersection of the incident shock and the interface results in the production of negative vorticity for both cases. For the linear case very little vorticity is produced initially, while for the non-linear case a greater amount is produced. Positive vorticity then begins to be produced at a lower rate with negative vorticity still dominating the flow until the onset of reshock for both cases.

$$\Gamma = \int_A n_i \omega_i \partial S \tag{2.23}$$

After reshock positive vorticity is produced in greater amounts for both cases. For the linear cases the positive vorticity quickly dominates the weak amount of negative vorticity produced by the initial incident shock wave. The non-linear case has a relaxation time of approximately 1ms where the initial effects of the reshock are strongest on the circulation before it begins to decay. During this time the positive vorticity produced by reshock overcomes the previously produced negative vorticity leaving the flow with a near zero net vorticity. The rate of increase in positive and negative vorticity is greater for the nonlinear case at early post reshock times with a peak being reached at approximately 3.8ms. The difference in circulation for the two cases

shrinks from ~2cm^2/us at reshock to ~1cm^2/us at late times after reshock. At late times the vorticity decays for both cases leaving the linear case with a slightly negative circulation and the non-linear case with slightly positive circulation. The nonlinear case shows a weak power law decay (an exponent of ~-0.6) after the post reshock circulation peak while the linear case exhibits a linear decay. This is due to the more homogeneous distribution of scales produced in the post shock flow by the nonlinear case which begin to cascade to smaller scales quickly.

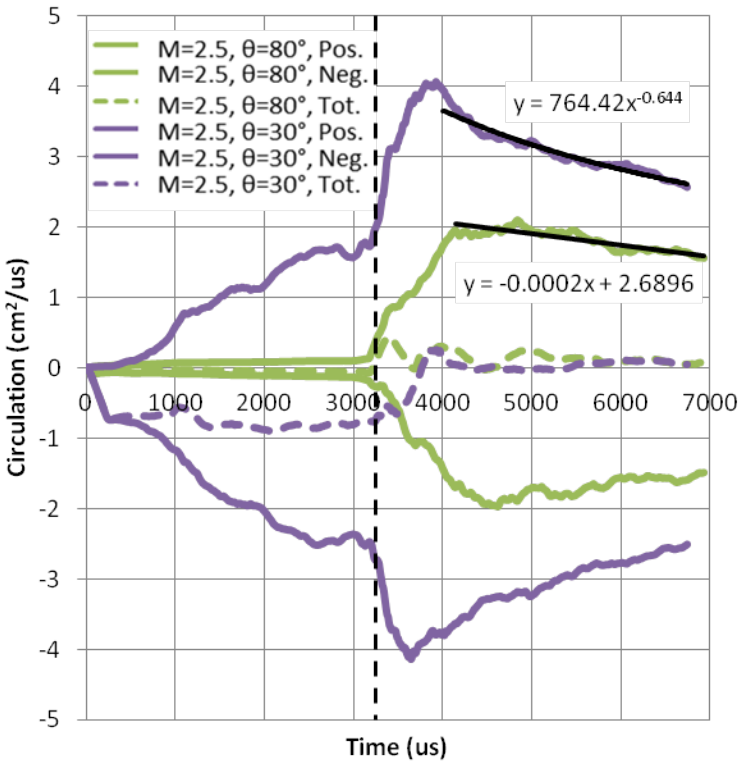

Figure 2.36: Plot of circulation over time. The green and purple lines represent the linear and non-linear interface cases, respectively. The solid lines show the positive and negative circulation components, and the dotted lines show the sum of these, the total circulation. The dashed black line approximates the time at which reshock occurs.

Another measure of the vorticity in the post shock and post reshock flow fields is the enstrophy, which is the square of the vorticity. Figure 2.37 shows the area integral of the enstrophy for the two flows over time. The linear case shows a more gradual rise in enstrophy than the non-linear case because the reshock travels through a much more organized flow field where the vorticity is increased gradually as it passes from the slug region to the spike. For the non-linear case the reshock produces modest gains in vorticity until it leaves the well organized slug region and enters the mixing where a strong amount of vorticity is already present. When the circulation is examined using enstrophy the difference in vorticity decay trends is magnified. In figure 2.37 the nonlinear case exhibits a strong power law trend (exponent of ~-2.0) while the linear cases exhibits a linear decay trend again.

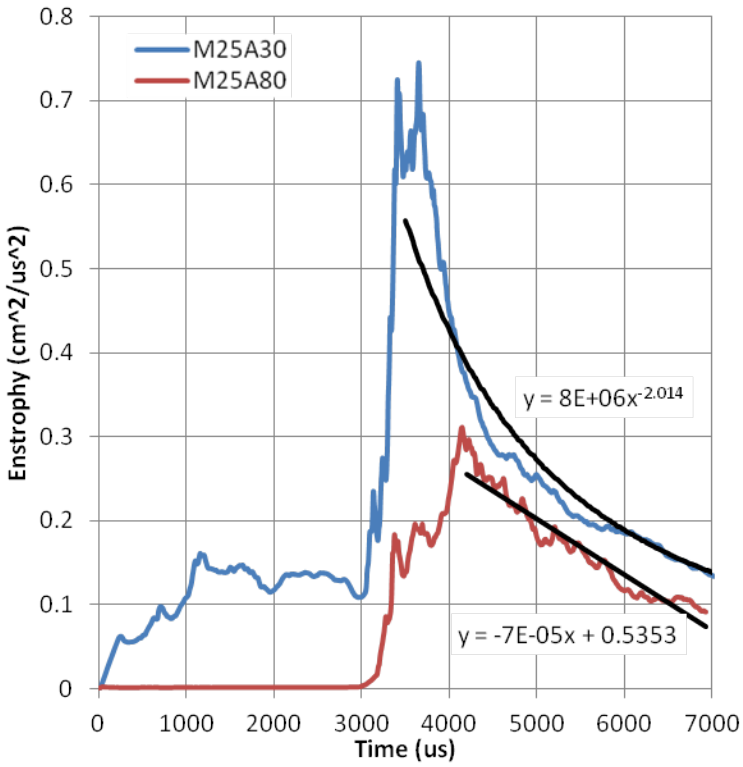

FIGURE 2.37: Enstrophy plot over time. The blue line represents the non-linear case, and the red line represents the linear case. The dashed line approximates the time at which reshock occurs.

The sources of circulation production can be examined by using the compressible vorticity equation shown in Equation 2.24. The equation can be broken down into the four terms annotated below. For simulations reported in this dissertation the vortex stretching and tilting term can be neglected since it is always zero for a 2D flow. These terms can be integrated over the area of the flow field to provide circulation production terms.

$$D_t\omega = \frac{1}{\rho^2}\varepsilon_{ijk}\partial_j(\rho)\partial_k(P) + \nu\partial_j\partial_j\omega_i + \omega_j\partial_j V_i - \omega_i\partial_j V_j \tag{2.24}$$

Baroclinic term — Diffusion term — Vortex stretching/ tilting term — Compressible stretching term

The positive and negative circulation production terms are plotted in Figures 40 and 41 for the non-linear and linear cases respectively, where the diffusion term is plotted on a greatly magnified axis. Figure 2.38 shows that baroclinic production mechanism is the dominant process for vorticity production both before and after reshock. The compressible stretching term contributes significantly as well, while the diffusion term, has little to no effect but follows a similar trend as the other terms. A small spike in the positive baroclinic term is visible in the plot before reshock. This spike is the effect of vortex projectile which, while not created by the boundary layers, grew from the boundary layer and entrained some of the boundary layer vorticity temporarily. In Figure 2.39 it can be seen that after the initial interaction of the incident shock and the interface, there is little production from the baroclinic or compressible stretching terms. Small spikes are present at the time of initial shock interaction when the vorticity production mechanism are the most organized. The overall lack of vorticity production in the post incident shock flow field is due to the lack of strong secondary shock waves which reverberate through the flow field in the non-linear case.

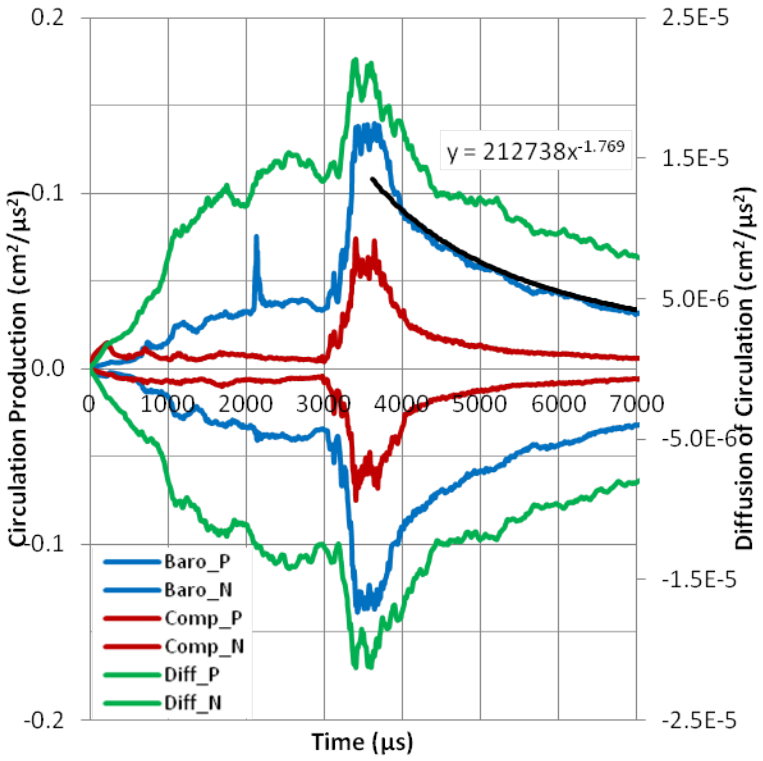

Figure 2.38: Plot of positive and negative circulation production terms over time for the non-linear case. The green lines are the circulation diffusion plotted on the right axis. The blue and red lines are the baroclinic and compressible stretching production terms plotted on the left axis. The dashed line approximates the time at which reshock occurs.

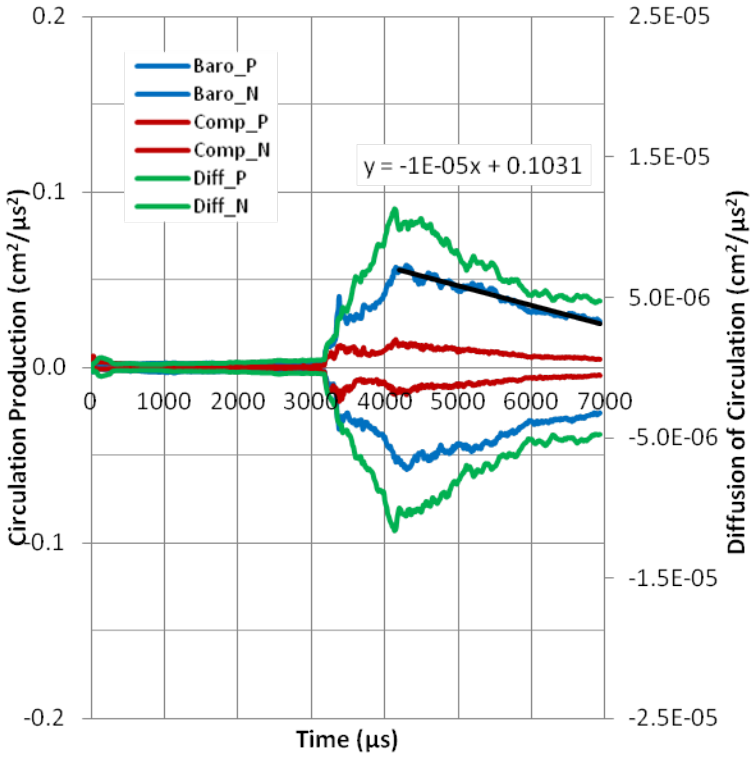

Figure 2.39: Plot of positive and negative circulation production terms over time for the linear case. The green lines are the circulation diffusion plotted on the right axis. The blue and red lines are the baroclinic and compressible stretching production terms plotted on the left axis. The dashed line approximates the time at which reshock occurs.

After reshock the all production terms increase significantly for the linear case with the baroclinic term dominating but decaying faster than the compressible stretching term at late times. Figure 2.38 shows that the nonlinear case exhibits a strong increase in vorticity production terms with relaxation times as seen in the circulation and enstrophy plots. After this relaxation time the production terms exhibit a power law decay trend with an exponent of approximately -1.75 for the baroclinic term. The linear case shows a

linear increase in the production terms following the reshock then a linear decay trend in all the production terms. This is because the better organized post reshock density field of the linear case allows the vorticies more time to develop before interacting, merging and decaying. Also, the number of small vorticies in the non-linear case allow for energy to begin quickly dissipating after the initial amplification of the reshock.

2.4.4 Conclusions from the interface linearity study

The inclined interface Richtmyer-Meshkov instability produces distinct differences in flow fields based on the linearity of the initial interface perturbation. Through examination of flow field visualizations for density, pressure gradient, and vorticity for a linear (80° inclination angle) and a non-linear (30° inclination angle) initial perturbation case the differences between the linear and non-linear regimes were shown at times before reshock. The most significant difference between these two cases was the presence or absence of the strong secondary compressible effects that are highlighted in pressure gradient plots. For the non-linear cases the strong secondary compressible effects caused the flow field to divide into a mixing region and a 'slug' region with little mixing. For the linear case no such division occurred. The vorticity remained relatively low and isolated at the interface for the linear case. After reshock, these regions loose organization and the unmixed SF_6 regions become the primary regions for vorticity production and mixing.

The inclined interface scaling method, was tested for the linear perturbation cases. This method was shown to collapse the mixing width growth rate for non-linear cases to a single non-dimensional growth rate in section 2.3. Scaling of the data for the

linear cases using this method showed that a growth regime change occurred near an inclination angle of 80°. This angle was the first to have an η/λ (initial perturbation amplitude over initial perturbation wavelength) value under the proposed linear threshold of 0.1. The reshock mixing width data was scaled using the same method with a different time offset to bring the various cases to a common origin after reshock. This scaled data showed there was some agreement between both linear and nonlinear cases at early non-dimensional times, but that at late times the growth rates of all cases diverged and there was no distinction between the growth rates of the two cases. Mix mass plots showed that the increased vorticity from reshock greatly increased the mix mass and that the rate of increase in mix mass for both cases is similar after reshock.

Due to the asymmetric nature of the inclined interface Richtmyer-Meshkov instability it was seen through graphs of the circulation that the vorticity deposited by the incident shock is initially negative, while the vorticity deposited by the reshock reversed the direction of circulation to be positive. The onset of reshock greatly increased the number of vorticies in the flow field initially. At late times these vorticies combined and were reduced in strength, as seen from the decay of the circulation for both cases. By examining the circulation production terms it was seen that the vorticity was produced primarily by the baroclinic and compressible stretching terms. For the linear case the production terms remained stronger at late times after reshock than they did for the non-linear case due to the more well organized flow field reducing the vorticity interaction and merging.

2.5 Simulations of Multimode Perturbations

The simulations of the inclined interface RMI were performed with a perfect interface containing no additional noise in the interface. In actual experiments some noise, random small wavelength perturbations, will be present. This noise can be amplified and larger wavelength higher amplitude perturbations can be forced on the interface by oscillating or shaking the shock tube. This method has been used by other as discussed in section 1.3.2. The addition of these modes creates a more complicated RMI with the possibility of damping the growth rate by means of selecting the right perturbation modes. To explore this potential for mode interactions with an inclined interface a simulation campaign was undertaken.

2.5.1 Fourier mode decomposition

The inclination of the interface acts mostly as a single large mode, but when attempting to use the multimode models discussed in section 1.3.1 it must be decomposed into its Fourier modes. Figure 2.40 shows the Fourier mode strengths for an inclined interface at an 60° inclination. This figure shows that the inclined interface is dominated by low wave number modes, with a small uptick in the mode strength for very high wave numbers, small wave lengths.

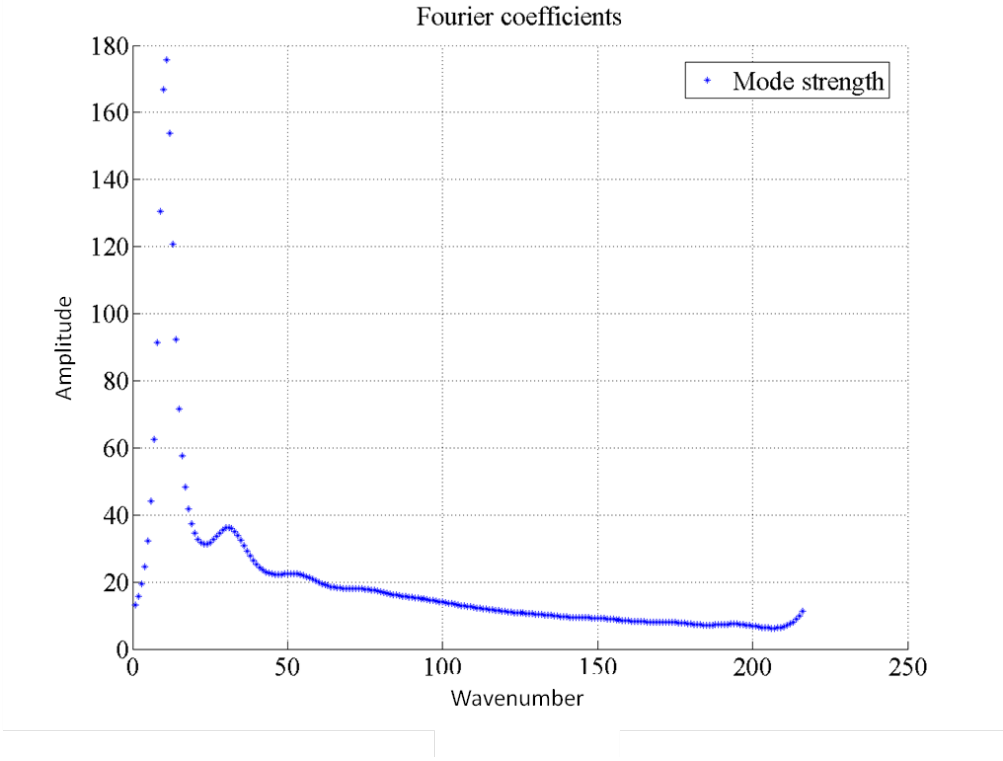

Figure 2.40: Wave number strengths for an 80 °inclined interface.

2.5.2 Qualitative comparison of various multimode configurations

To illustrate the impact of adding wave perturbations on an inclined interface and aid in the design of multimode experiments for the TAMUFMSTF 4 simulations were run with varying modes added to a 60° interface with an incident shock strength of Mach 1.6. The mode information for these cases is given in table 2.9. The preliminary results of the simulations are shown in figure 2.41, which shows species and vorticity plots for the four cases at a time of 4ms after shock interaction with the interface. From these plots it can be seen that the addition of wave perturbations to the inclined interface can increase the overall flow field vorticity a lead to the development of strong well

organized vortices along the interface. The addition of smaller modes in case 3 allows additional small vortices to form on the interface when compared with case 2 which has fewer modes. Case 4, is for a high Atwood number and shows that the addition of multimode wave perturbations has less of an effect on strongly shocked high Atwood number interfaces. This case can compared with case 13 of section 2.3. This case was run to show that high Atwood numbers with multimode perturbations could be used to drive the flow field to a turbulent state quickly.

To complete this study the author will seek to provide a more comprehensive suite of simulations spanning many mode combinations, and to attempt to form a multimode interface in the TAMUFMSTF. The multimode work will also be used to generate low amplitude noise in the interface which should aid in matching the ARES simulations to experimental results. Preliminary experiments, discussed in section 3.4 have shown the better agreement with case 2 of the multimode simulations.

Table 2.9: Multimode study cases

Case	Upper gas	Lower gas	Atwood Number	Mode #	K1 (1/cm)	A1 (cm)	Φ1 (rad)	K2 (1/cm)	A2 (cm)	Φ2 (rad)	K3 (1/cm)	A3 (cm)	Φ3 (rad)	K4 (1/cm)	A4 (cm)	Φ4 (rad)
1	N2	CO2	0.23	0	na	na	na	na	na	na	na	na	na	na	na	na
2	N2	CO2	0.23	3	0.551	0.1	0	1.102	0.05	3.14	1.653	0.05	0.79	na	na	na
3	N2	CO2	0.23	4	0.055	0.2	0	1.649	0.1	1.04	2.748	0.05	0.52	7.153	0.02	0.44
4	He	SF6	0.97	3	0.551	0.1	0	1.102	0.05	3.14	1.653	0.05	0.79	na	na	na

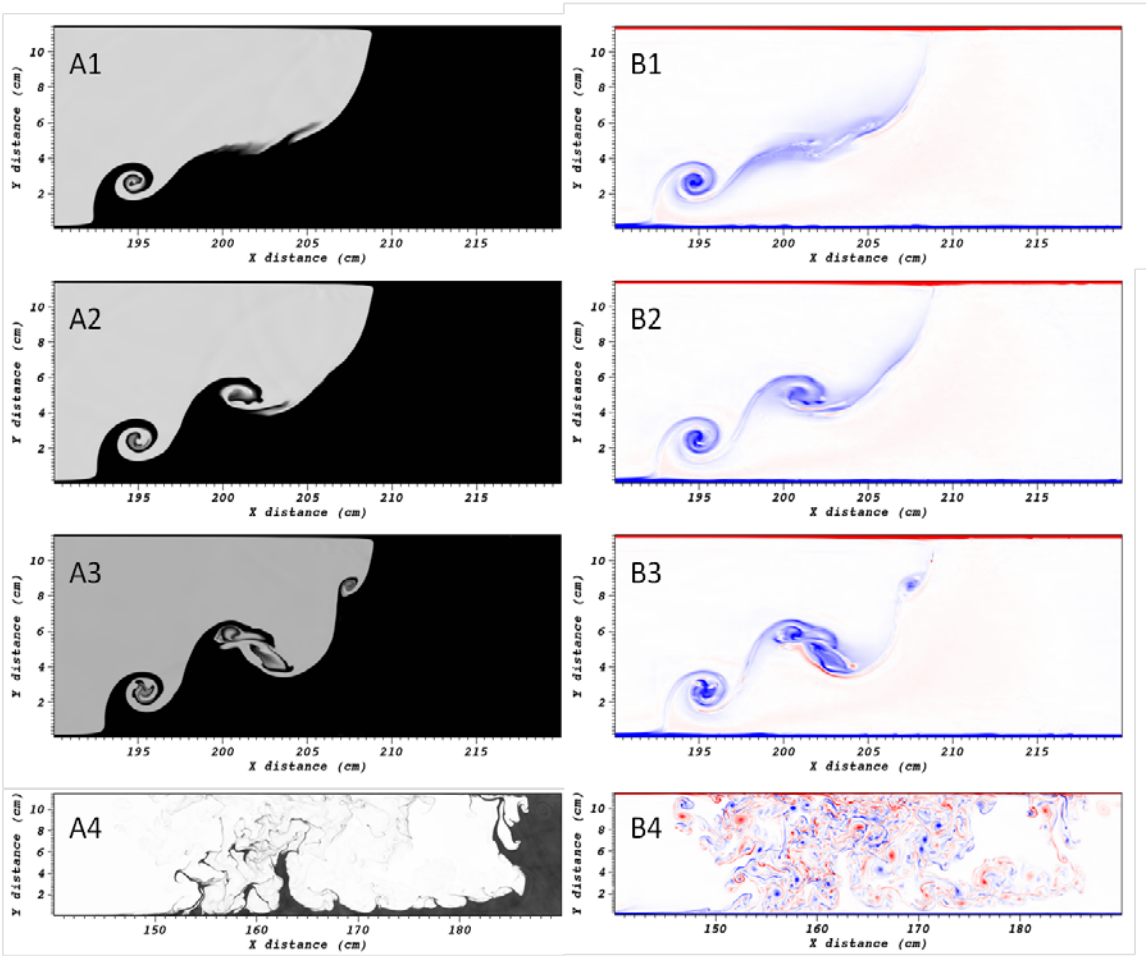

Figure 2.41: Initial results of the multimode simulations. Numbers 1, 2, 3, and 4 correspond to the cases listed in table 2.9. Figures labelled A are species plots where the dark fluid is the heavy species. Figures labelled B are vorticity plots where red indicates positive vorticity strength and blue indicates negative vorticity strength. The plots are made at a time of 4ms after shock interaction with the interface.

2.6 Reverse Jet Study

The reverse spike study was initiated to study the formation of the reverse jet formed in the parametric study simulations and in other experiments [23]. This structure is clearly visible for case 7 in section 2.3, also case 9 in section 2.4. The work on the reverse jet structure is under review for publication at the time of this dissertations submission. What follows is an outline of the work to be completed and the preliminary results of the study.

Two ARES simulations were run to simulate the experimental data given by Motl *et al.* [23]. The two cases run were case 5 and 8. The conditions for these experimental cases are given in table 2.10. These simulations were initialized using the conditions shown in figure 2.42. The shock was initialized by creating a discontinuity in the driver gas between driven gas at post shock conditions and driven gas at unshocked conditions. The interface was prescribed using a single mode wave perturbation with one wavelength across the height of the computational domain. The height and therefore the wavelength were set to 17.36cm for case 5 and 16.7cm for case 8. The length of the domain was set to 200cm. This allowed time for the interface to develop before the shock waves reflected from the interface could reflect from the upstream boundary and re-intersect the interface a second time. The boundaries of the domain are all shock reflection, with a no slip condition. The upstream boundary also contains a source term to sustain the shock wave. All simulations were started at standard conditions (101.3KPa and 300K). Both viscosity and diffusion models were applied in these

simulations. These models were developed for previous works and are described with the necessary constants in the previous section 2.1.

Table 2.10: Conditions for the experiments simulated

Parameter	Case 5	Case 8
Driven Gas	N_2	He
Test Gas	SF_6	SF_6
Atwood Number	0.68	0.95
Shock Mach Number	2.86	1.95
Initial Amplitude η_0 (cm)	1.04	1.36
Initial Wavelength λ (cm)	17.36	16.7
Amplitude to Wavelength Ratio η_0/λ	0.06	0.08

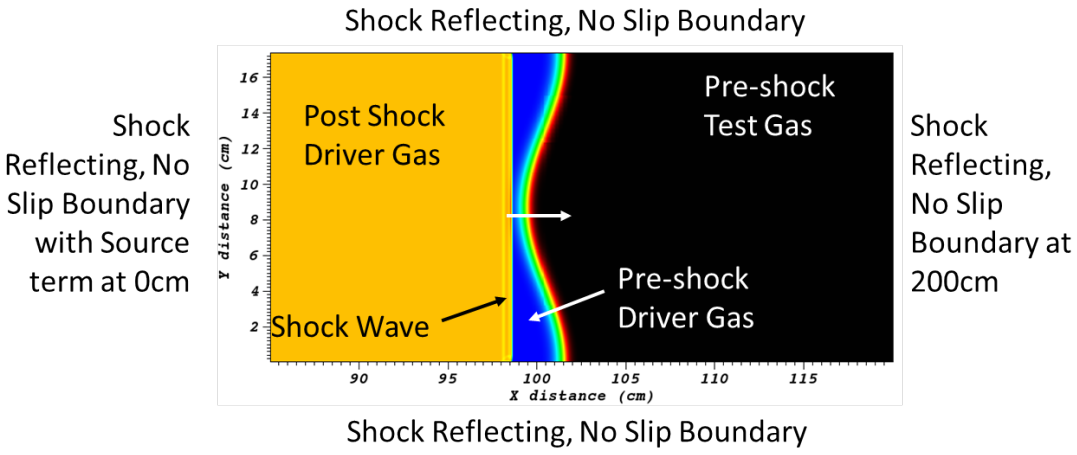

Figure 2.42: Schematic of interface initial conditions.

Case 5 and 8 vary in Atwood number, incident shock strength, and amplitude to wavelength ratio. Case 8 uses a lower incident shock Mach number than case 5 but since this number is obtained in helium the impulsive acceleration for case 8 is actually

higher than for case 5. So, in all parameters case 8 is set up to have a stronger faster developing instability than case 5.

Figures 2.43 through 2.46 show comparisons of cases 5 and 8 using density, temperature, and vorticity plots. The formation of the reverse jet can be seen in the density plots for both cases. The development of the reverse jet occurs earlier for case 8. Strong secondary shock waves can be seen traversing the post shock SF6 to late times. The secondary shocks are split across a shear layer which is evident in the vorticity plots (fig. 46). The development of the reverse jet is evident at earlier times in the vorticity plots as an area where the positive and negative vorticity meet. The vorticity plots also highlight the formation of additional shear layers at later times. Temperature plots (fig. 47) show the reverse jet as an area of low temperature fluid being entrain in a hot spot formed behind the transmitted shockwave.

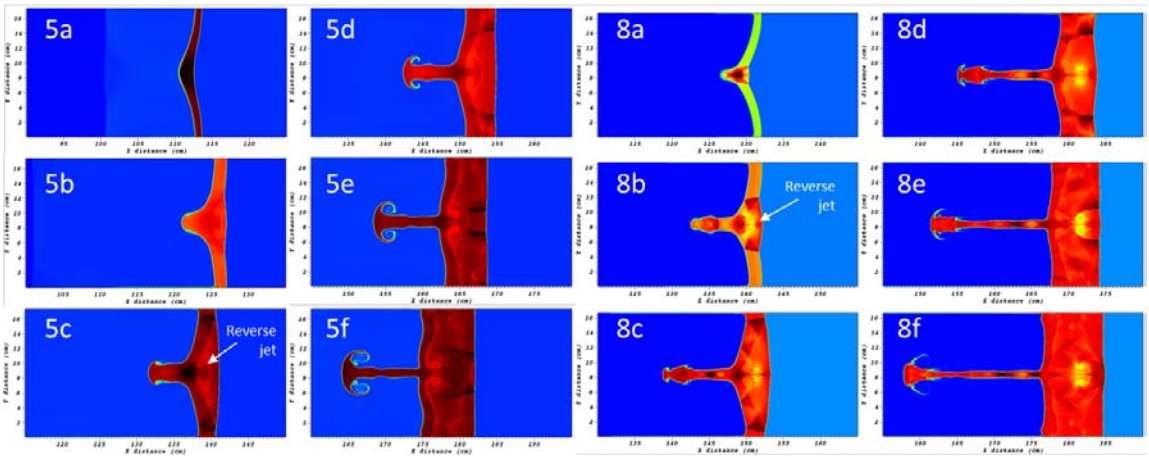

Figure 2.43: Density plots for case 5 and 8. Plots labelled 5 and 8 are for case 5 and 8 respectively. Labels a through f designate the time after the incident shock first intersects the diffuse interface. Plot a is at 250us, b is at 500us, c is at 750us, d is at 1.0ms, e is at 1.25ms, and f is at 1.50ms.

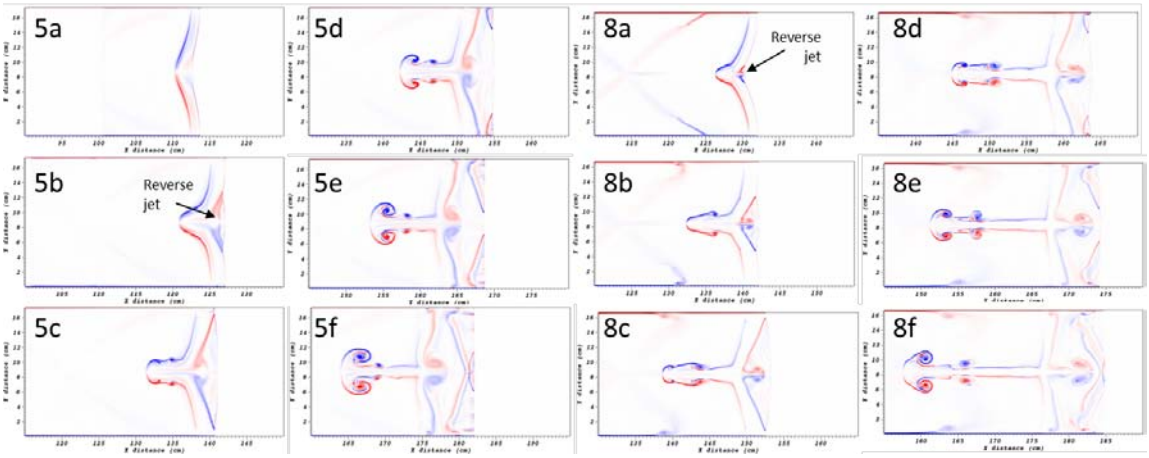

Figure 2.44: Vorticity plots for case 5 and 8. Red and blue areas represent positive and negative vorticity respectively. Plots labelled 5 and 8 are for case 5 and 8 respectively. Labels a through f designate the time after the incident shock first intersects the diffuse interface. Plot a is at 250us, b is at 500us, c is at 750us, d is at 1.0ms, e is at 1.25ms, and f is at 1.50ms.

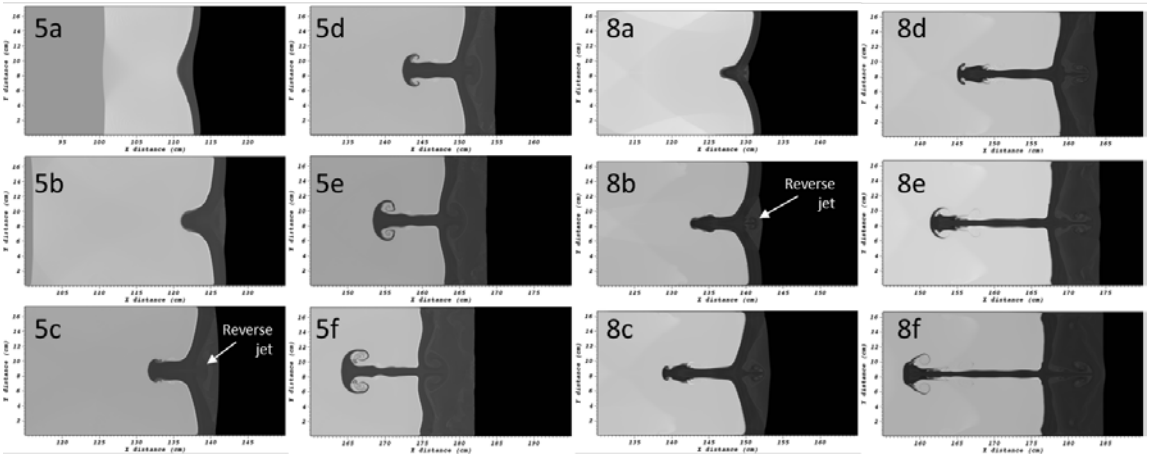

Figure 2.45: Temperature plots for case 5 and 8. Black areas represents 300K fluid and the lightest areas represent approximately 1200K fluid for case 5 and 1000K for case 8 plots. Plots labelled 5 and 8 are for case 5 and 8 respectively. Labels a through f designate the time after the incident shock first intersects the diffuse interface. Plot a is at 250us, b is at 500us, c is at 750us, d is at 1.0ms, e is at 1.25ms, and f is at 1.50ms.

2.7 Shock Refraction Perturbation Study

Mentioned previously the RMI can develop as a result of a perturbed fluid interface or a perturbed pressure gradient. A perturbed pressure gradient is supplied by a perturbed shock front. This interaction of a perturbed shock with an interface occurs often as a side effect of the initial RMI interface shock interaction as was seen in section 2.3 where it was shown that the inclined interface RMI can generate strong secondary shockwaves which reverberate through the interface induce addition hydrodynamic instabilities. This type of interaction is also likely to occur anywhere a RMI is formed. It also opens up the possibility for an experimentalist to use a perturbed shock front to generate the RMI in a shock tube facility. When studying the reshock interaction of the RMI the initial perturbations induced on the transmitted shock front may survive long enough to be reflected from the end wall of the shock tube and play a role in the reshock RMI. To study the behaviour of the perturbations in the refracted shock front a computational study was initiated to determine the decay rate of perturbations introduced by a single mode interface. The following text will closely follow the work previously published by the Author and his co-researcher [57].

2.7.1 Introduction to the shock refraction perturbation problem

The behavior and decay of perturbations on the refracted shock wave pose many interesting question to be studied, but these perturbations have received limited attention in published works so far. One study that did examine the perturbations introduced on the refracted shock wave was that of Aleshin, *et al.* [63] in 1991. Extended details of this work were presented by Aleshin *et al.* [120] in a technical report. Aleshin performed

experiments in which a shock wave interacted with a single mode sine wave perturbation created on an interface using a thin film. The experiments sought to explore how the transmitted shock would be perturbed by this interface perturbation and how the transmitted shock wave perturbation would evolve over time and space. In these experiments the Atwood number and the amplitude to wavelength ratio effects were explored. Schlieren images were used to make measurements of the transmitted shock wave location. While this was the best experimental technique available at the time the resolution of the measurements was severely limited and the measurements were subject to some human interpretation.

The evolution of the transmitted shock wave perturbation was found to be of the form shown in equation 2.25, where a is the amplitude (amplitude will be defined as half the peak to peak amplitude in this dissertation) of the perturbation, C is a constant, S is the distance travelled by the refracted shockwave, λ is the interface perturbation wave length, and n is the decay constant. Equation 2.26 gives the predicted initial amplitude of the refracted shock wave perturbation a^*, where a_0 is the initial interface sine wave perturbation amplitude, and w_i and w_t are incident and refracted shock wave speeds. Figure 2.46 shows the experimental data with the regression fitting the local oscillation peaks. In this study the Atwood number of the interface was varied to find a relationship for n.

$$a/a^* = C(S/\lambda)^n \tag{2.25}$$

$$a^* = a_0(1 - w_i/w_t) \tag{2.26}$$

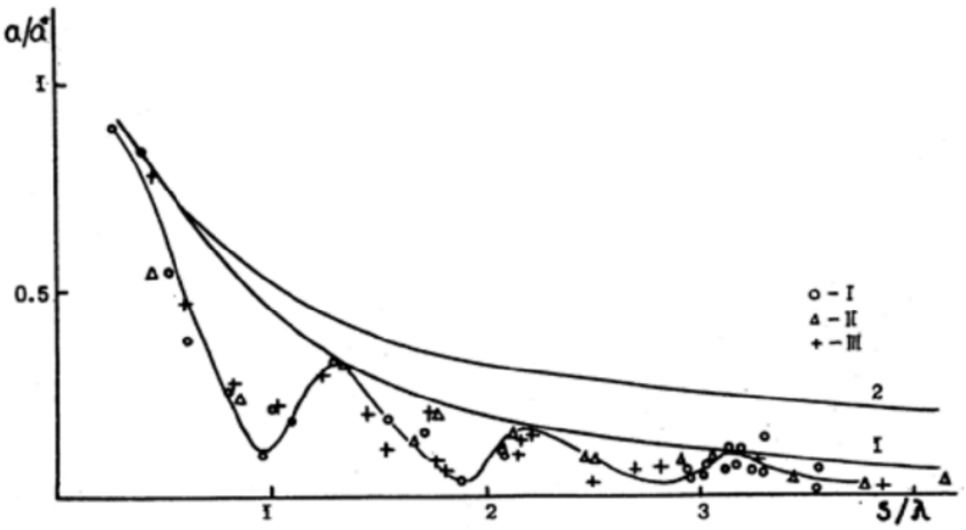

Figure 2.46: Damping of perturbations on the shock front: Reproduced from Aleshin *et al*. [63]. The transmitted shock Mach number in experiments is 4, line 1 is the power law fit for a helium over Xenon interface where symbols I, II, and III in the legend correspond to experimental data for wavelengths of 7.2, 3.6, and 2.4 cm respectively, line 2 is the power law fit for Argon over Xenon.

The work in this section seeks to extend the previous work on refracted shock wave perturbations by exploring the effect of incident shock wave Mach number. The evolution of perturbations introduced to the transmitted shock has been seldom reported on in literature. The decay rate of these perturbations is important for multilayer fluid systems, such as those found in many ICF fuel capsule designs, in which the perturbed shock will interact with additional density gradients. In systems such as these, density gradient perturbations in one layer will cause pressure gradient perturbations which will complicate the RMI generated in subsequent density gradients. The effect of incident shock wave strength on the decay of interface introduced perturbations in the refracted shock wave was studied in this work for the first time using simulations. Simulations

were performed using the ARES hydrodynamics code, described in section 2.7.2. Twenty incident Mach numbers ranging from 1.1 to 3.5 were studied in simulations which required approximately 20,000 cpu hours each. In the previous experimental work the incident shock wave Mach number was not independently varied and its effect was not explored. The detail provided by these simulations allows features of the flow field not visible in the previous experimental work to be examined. Results for the refracted shock wave perturbation amplitude as a function of distance and initial Mach number are reported below. The emphasis of this section rests in developing a model to describe the decay of these perturbations and determine what relation if any exists between incident Mach number and the decay rate of these perturbations.

2.7.2 Computational method

For the ARES simulations presented in this section all interfaces were treated as miscible numerically, but the diffusion model was not applied. This allowed the initial interface to be diffuse but did not allow for additional diffusion to take place as the interface evolved which would have little effect on the transmitted shock front. Artificial viscosity was applied but boundary layers were not included in the simulation. The boundary conditions of the simulation domain were constructed such that the right wall (downstream) was a reflective boundary in the streamwise direction, and the top and bottom walls were reflecting slip walls with no viscous boundary layer (Fig. 2.47). The left wall (upstream) contained an inflow source in the streamwise direction at post shock conditions which sustained the incident shock wave. When the interface reflected shock wave intersected the upstream boundary it would reflect as a non-physical expansion

wave which would reintersect the refracted shock wave at a later time. This time was well beyond the simulation time over which data was taken and so this non-physical expansion wave had no effect on the results.

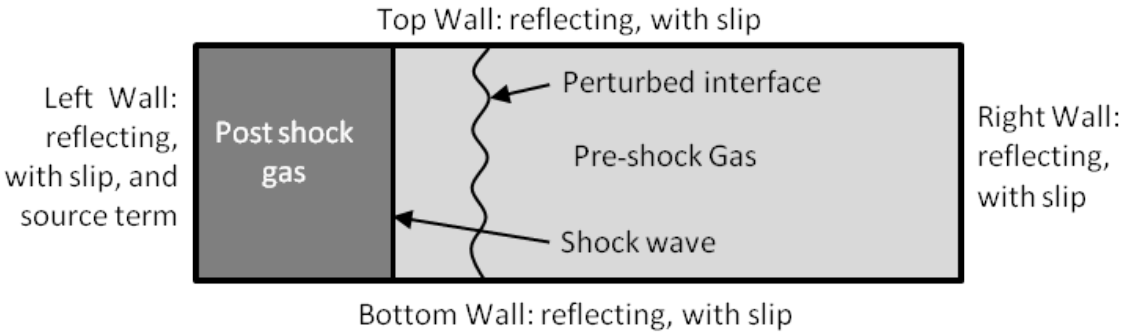

Figure 2.47: Schematic of simulation boundary conditions

The test domain was chosen to measure 250 cm long with a height that varied for each simulation set. The initial location of the shock wave, and interface as well as the initial interface diffusion thickness and perturbation were set uniquely for the different simulations described below. The resolution for the different simulation sets was chosen so that the number of nodes was constant for the different computational domain sizes used. This resolution was selected on the the methods described in sect 2.4 which incorporated a detailed resolution study. For all simulations the initial temperature and pressure were chosen as 298K and 0.5 atm respectively to match the experimental conditions of Aleshin *et al*. [63]. A simulation of an experiment performed by Aleshin *et al.* is presented below for comparison and validation.

2.7.3 Simulations of previous experimental work

To begin the computational work, experimental results from Aleshin *et al.* [120] for helium over xenon interface with an incident shock wave with Mach number of 2.89 were compared to a two-dimensional ARES simulation under the same initial conditions. The simulation domain had a height of 7.2 cm which corresponded to the shock tube cross section used in the experiments. The interface perturbation was a single mode sine wave with wave number of approximately 1.75 cm^{-1} and amplitude of 2 cm, where the wave number, k, is defined in equation 2.27. The initial conditions of the experiment 633B are summarized in Table 2.11. The resolution for this simulation was set to 72 μm. The interface and shock wave were initialized at 20 cm and 10 cm from the left wall respectively, and the initial interface diffusion thickness was set to 0.2 mm. The experiments used a thin film to separate the gases and this diffusion thickness was chosen to attempt to approximate the diffusion that would take place through the thin film.

$$k = 2\pi/\lambda \tag{2.27}$$

Table 2.11: Initial conditions of Aleshin experiment 633B

Initial Mach Number	2.89
Gas Pair	He-Xe
Atwood Number (A)	~0.94
Interface Wavelength (λ)	3.6 cm
Interface Amplitude (a)	2cm
Channel Height	7.2 cm

Aleshin *et al.* measured the velocity of 4 characteristic points in the system as shown in Figure 2.48. C is the tip of a bubble, D is the end of a spike, B is the point on the shock wave at the same vertical location as the tip of a spike, and A is the point on the shockwave at the same vertical location as the tip of the bubble. The simulations showed a flow field not just dominated by a single characteristic spike structure, however, highlighted a spike which had 2 point forked tip. D* was measured as a second possible location of the end of the spike. It is difficult to determine if this forked tip was produced in the experiments, due to the low resolution imagining techniques available at the time. It appears that in some experiments that the forked tip developed while in others it did not. The simulation was carried out to 186μs where the interface had sufficiently evolved to compare it to the experimental results.

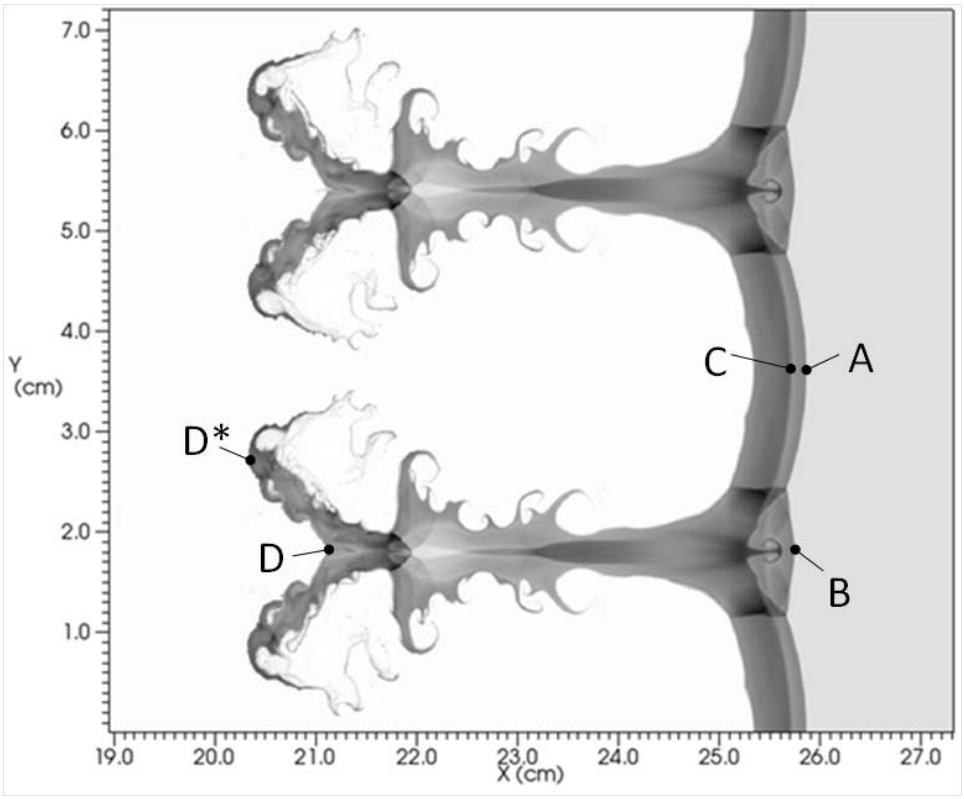

Figure 2.48: Density plot showing the location of characteristic points defined by Aleshin et al. in the experimental work.

The results of the simulation can be seen in Table 2.12. The uncertainty in measurement of experiment 633B is ±5%. Characteristic points A and C fall within the experimental uncertainty while points B and D do not. Point D was affected by the diverging spike tip, which caused it to slow. The placement of point D by ARES did not agree with the experiments; and the comparison of the velocities of points D and D* in ARES to the velocity of experimental data point D shows a higher error.

Table 2.12: Table of velocity measurements taken from Aleshin et al. experiment 633B [120] and derived from ARES simulation of experiment 633B. Units are cm/μs.

Aleshin *et al.*		**ARES**		**Relative Error (%)**
V_A	0.865	V_A	0.85	**1.73**
V_B	0.945	V_B	0.891	**5.71**
V_C	0.65	V_C	0.634	**2.46**
V_D	0.406	V_D	0.452	**11.33**
		V_{D^*}	0.367	**9.61**

Because the behavior of point D is inconsequential to the study of the perturbations on the refracted shock wave, and it is unclear if it was produced in experiments, the ARES simulations were used to predict the behavior of additional experimental parameter sets not explored in the experiments of Aleshin *et al.* One possible explanation for the difference in the ARES simulations and the experiments is that the simulations were performed in 2D. As the interface evolves beyond the linear regime, traditionally defined as $a/\lambda \ll 1$, three dimensional effects become increasing important to accurate modeling of the flow.

2.7.4 Incident shock strength study

The effect of incident shock wave strength on the decay of interface introduced perturbations in the refracted shock wave was studied by performing multiple simulations with varying incident shock wave Mach numbers. The interfacial perturbation was sinusoidal in shape with wave number ~0.94 cm^{-1} centered vertically in the channel 30 cm from the left boundary (Fig. 2.49). The amplitude of the wave was 2.5 cm. The initial diffusion thickness in the mixing layer was set to 1mm to simulate a

membrane-less experiment. The shock wave was initialized a 10 cm from the left boundary. For this Mach number study, the gas pair was chosen to be Air-SF_6, as many of the RMI studies in past have been carried out for this specific gas pair. In these simulations the molecular weight of air and SF_6 is taken to be 30 g/mol and 146 g/mol respectively. The specific heat ratio (gamma) for air and SF_6 is set to 1.4 and 1.09 respectively. The spatial resolution in the simulation was 100 μm, using a mesh with unity aspect ratio. This gives 1000 zones across the 10 cm channel. The initial Mach number in the study was varied between 1.1 and 3. 5. The simulation conditions are summarized in table 2.13.

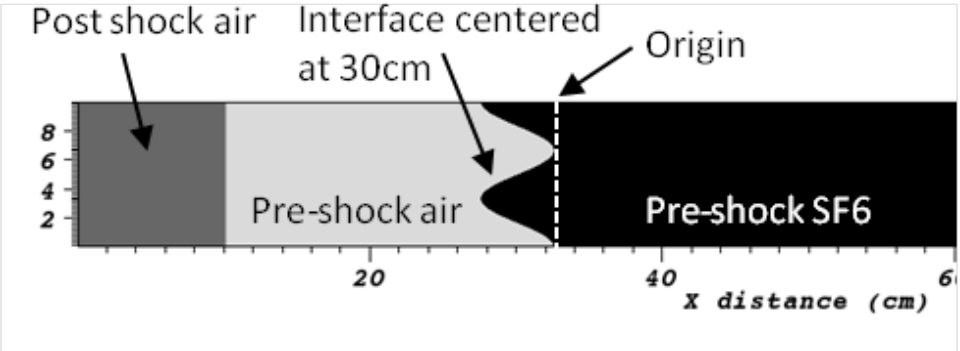

Figure 2.49: Density plot of initial conditions for all Mach numbers.

Table 2.13: Initial conditions of shock strength study

Gas Pair	Air-SF6
Atwood Number (A)	~0.67
Interface Wavelength (λ)	~6.67 cm
Interface Amplitude (a)	2.5 cm
Channel Height	10 cm

In order to evaluate the decay of perturbations in the refracted shock wave, the position of the shock wave, and amplitude of the perturbations in it need to be tracked throughout the simulation. For each case, the leading edge of the shockwave was isolated at every time step as a series of discrete spatial points using the data visualization and analysis software package, VisIt. The average of the horizontal coordinates of the points was taken to be the mean location of the refracted shockwave at a given time step. The amplitude of the perturbation can be expressed as the sum of the absolute values of the deviation at every point of the shock wave location, as seen in equation 2.28, where n is the number of points on the leading edge of the shock wave, X_i is the horizontal coordinate of the n^{th} point, and $\bar{X}$ is the mean location of the shockwave.

$$\frac{1}{n}\sum_{1}^{n}|\bar{x} - x_i|, \tag{2.28}$$

The location of the shock wave was then plotted as the distance it had traveled from its origin, the mean location of the initial interface (30 cm). Graphs of the perturbation amplitude as a function of the mean shockwave location were constructed, as seen in Figure 2.50. The fluctuating nature of the perturbation amplitude is due to the reverberating shock waves which traverse the flow field and are normal to the refracted shock wave (Fig. 2.51). These fluctuations form local maxima points shown in figure 51.

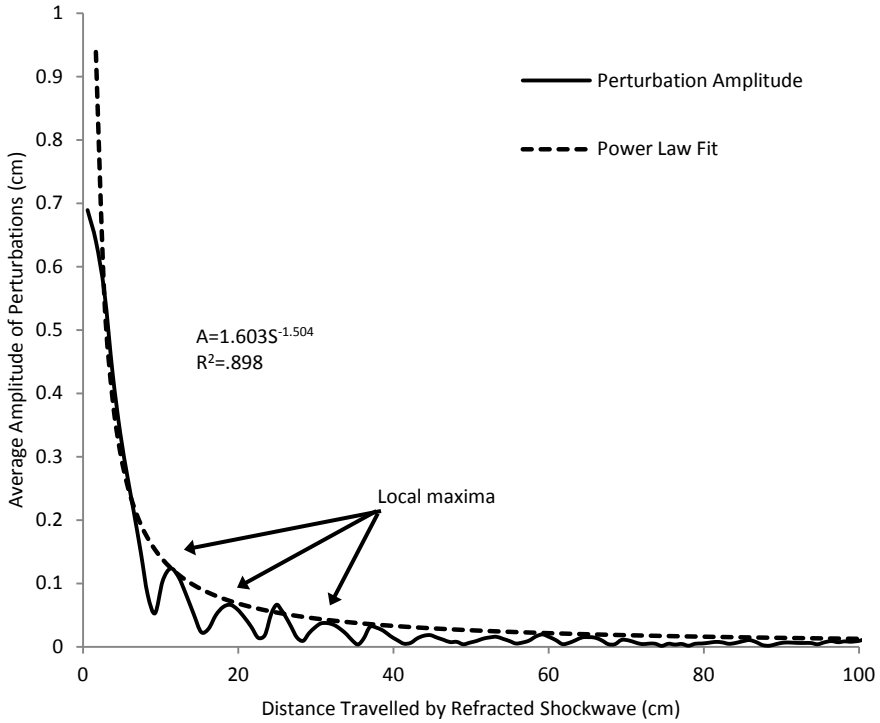

Figure 2.50: Average amplitude of perturbations vs. distance travelled by refracted shockwave for Mach 1.5 with power law regression shown as dashed line.

Figure 2.51 shows a time series of density and pressure gradient plots taken for various distances traveled by the refracted shock front. These plots illustrate the flow field structures which affect the perturbation amplitude. The traversing shock waves are clear in figure 2.51, B4. In figure 2.51, B6 it can be seen that the refracted shock front has nearly replanarized at a traveled distance of 28.75 cm.The density plots show similar flow features discussed in the previous section for reproduction of Aleshin *et al.* experiments. It should be noted that the forking in the spike tip is clearly visible in this case also. This has been highlighted in figure 2.51-A3.

Extensive non-linear regression analysis was performed on the entire data set. The analysis showed that the amplitude decay can be represented as a power law model shown in the equation 2.29, where A is the average amplitude of perturbations (cm), B is the base constant ($cm^{-(E-1)}$), S is the distance travelled by the refracted shockwave (cm), and E is the power constant. It should be noted that while this is the same form as that proposed by Aleshin *et al.*[63], [120] and reported on in section 1, a dimensional form of the equation was used here instead since Atwood number and amplitude to wavelength ratios were not explored, and the curve fit was applied to the entire data set instead of just the peak locations. These modifications to the methods of the previous work resulted in a better defined curve fit with less human interpretation required. The choice of the power law decay model was purely empirical in that it provided the best fit to data. Data points were taken starting at the moment the incident shock had fully refracted into the SF_6. The average horizontal location of the shock front at this moment varied for different incident Mach numbers. This location was estimated as 31.25 cm with an error of below 1% for all incident shock Mach numbers. It should be noted that the data start location can have a large effect on the power law coefficients for low Mach numbers. The coefficients for the power law regression of the Mach 1.5 data set is shown in figure 5 with its associated coefficient of determination (R^2) value. The R^2 value and its interpretation will be discussed in the next section.

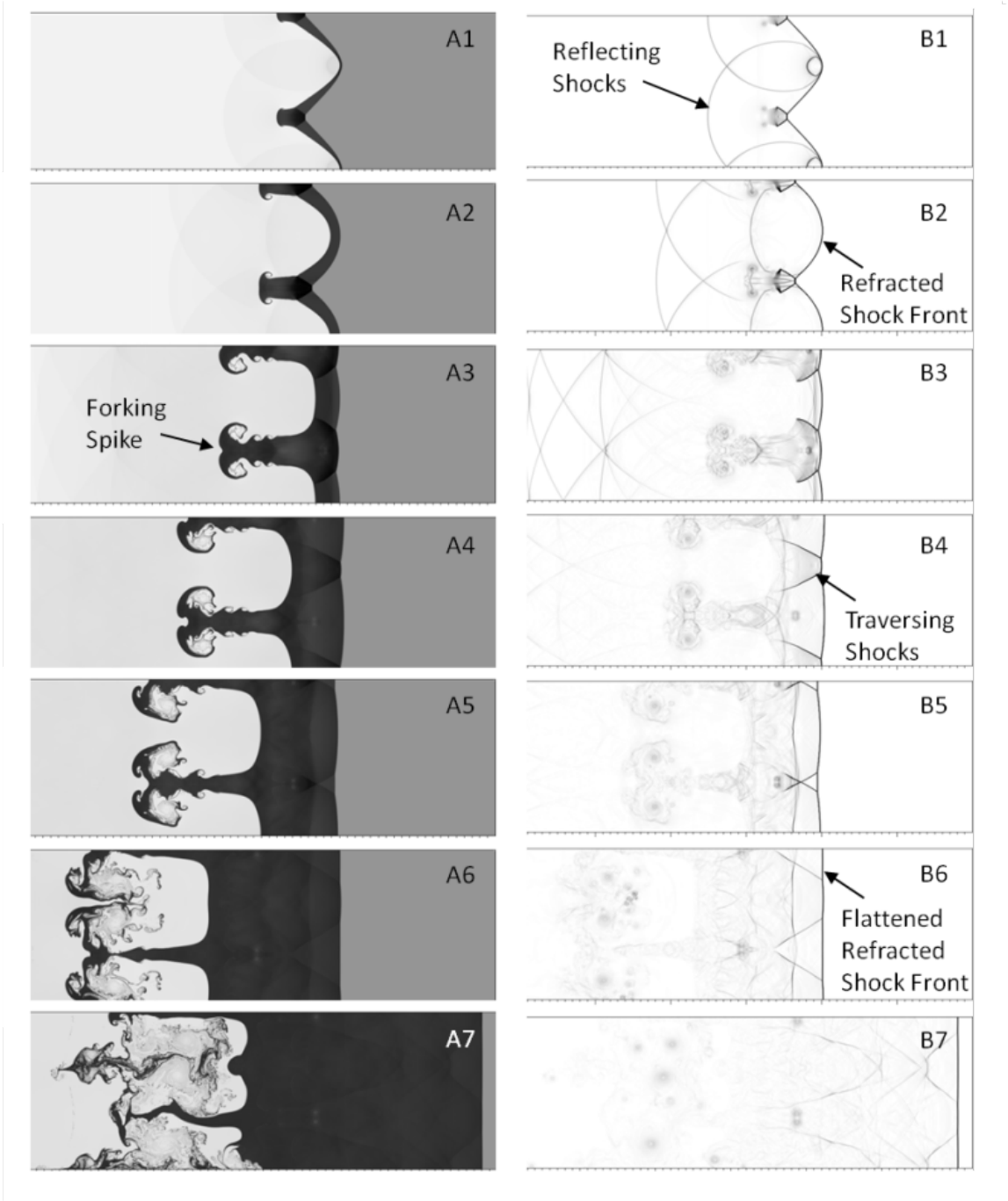

Figure 2.51: Times series of plots for incident shock wave Mach number of 1.5. Series A shows density plots. Series B shows Pressure gradient plots. Images 1-7 are for refracted shock front traveled distances of 1.75, 3.75, 8.75, 13.75, 18.75, 28.75, 48.75 cm respectively.

$$A = B * S^E \tag{2.29}$$

Simulations were carried out for 20 different incident shockwave Mach numbers from 1.1 to 3.5. The data was processed to find the coefficients for a power law regression of the perturbation amplitudes as discussed above in section 4.2. Table 2.14 lists the power law constants for each case according to equation 2.30 and the R^2 values.

Table 2.14: List of power law constants derived by power law regression for each Mach number case

Mach	B	E	R^2
1.100	1.631	-1.094	0.900
1.250	1.635	-1.099	0.900
1.500	1.603	-1.054	0.898
1.550	1.504	-1.015	0.883
1.650	1.312	-0.953	0.860
1.750	1.502	-1.003	0.864
1.800	2.095	-1.135	0.908
1.850	1.948	-1.098	0.897
1.900	1.764	-1.033	0.892
1.950	1.602	-0.968	0.883
2.000	1.419	-0.881	0.874
2.050	1.362	-0.840	0.863
2.100	1.246	-0.776	0.849
2.150	1.179	-0.738	0.838
2.250	1.210	-0.721	0.810
2.500	1.279	-0.653	0.717
2.750	1.183	-0.602	0.647
3.000	1.056	-0.533	0.637
3.250	1.080	-0.517	0.621
3.500	0.954	-0.448	0.522

Figure 2.52 shows the R^2 values of the power regression over the range of Mach numbers, where R^2 is one minus the ratio of the variance of the of the model error to the variance of the data, and shows how well the regression predicts the behavior of the data. Equation 56 defines R^2, where Y_i is the data point, $\bar{Y}$ is the average of the data, and f_i is the value predicted by the regression equation. The primary contribution to the degradation of the R^2 value comes from the oscillatory nature of the data sets which produces an increased variance of the model error. For high Mach numbers at late times the oscillations become large, with larger periods (Fig. 2.53). As shown in table 2.14, these high Mach number sets produce lower R^2 values (0.52 at Mach 3.5). Considering the large variance in the high Mach number data sets where the R^2 value drops, and the oscillatory nature of the data, it is believed the power law regression is adequate for describing the behavior of the decay.

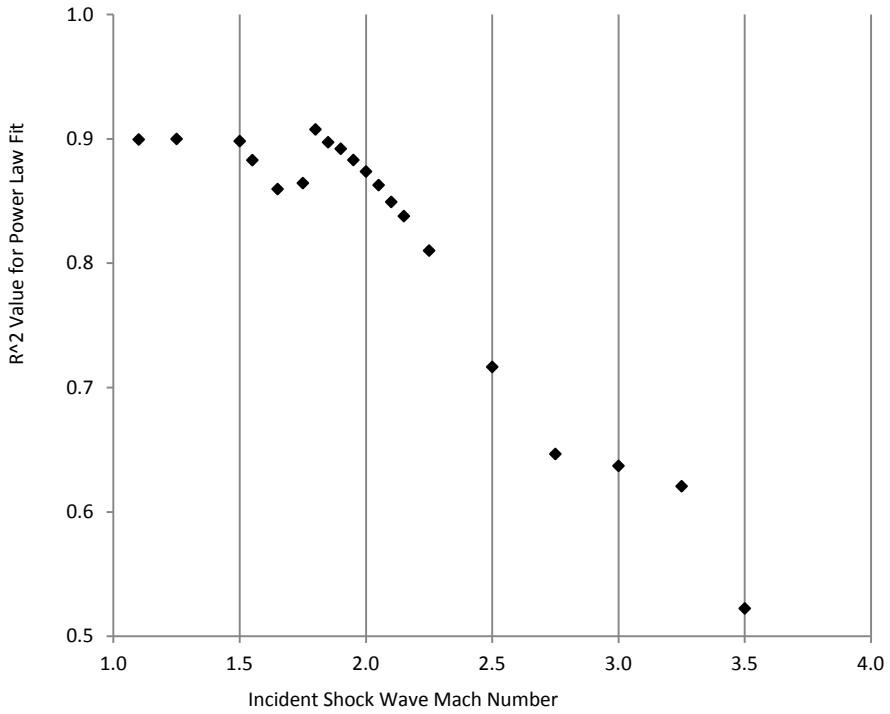

Figure 2.52: R^2 values of power regression for each Mach number case.

$$R^2 = 1 - \sum (Y_i - f_i)^2 / \sum (Y_i - \bar{Y})^2 \tag{2.30}$$

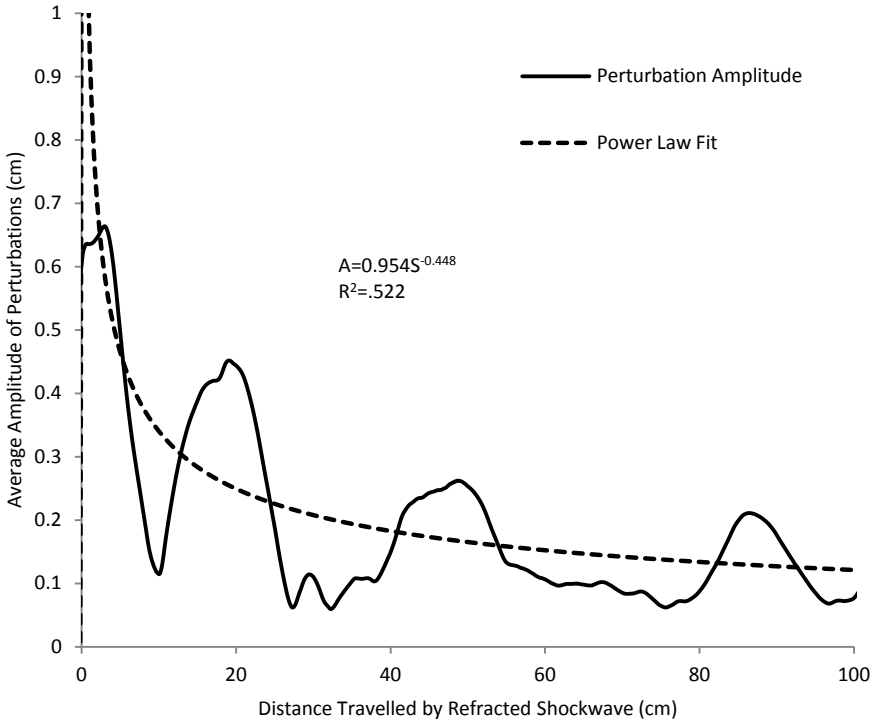

Figure 2.53: Average amplitude of perturbations vs. distance travelled by refracted shockwave for Mach 3.5 with power law regression shown as dashed line.

When the base and power constants are plotted against Mach number (Fig. 2.54), a clear transition region can be seen between approximately Mach 1.75 and 2. This transition region seems to divide the data into two regions with separate correlations, one for high incident Mach number, and another for low incident Mach number. This transition region is caused by a resonance in the secondary shock waves that traverse the primary shock front. This resonance seems to peak at an incident mach number of 1.85. As seen in Figure 2.54a, the base constant trends downward before turning less steeply downward after the transition region. In Figure 2.53b, the power constant trends upward

before the transition region and then resumes its upward trend at a slightly increased slope after the transition region.

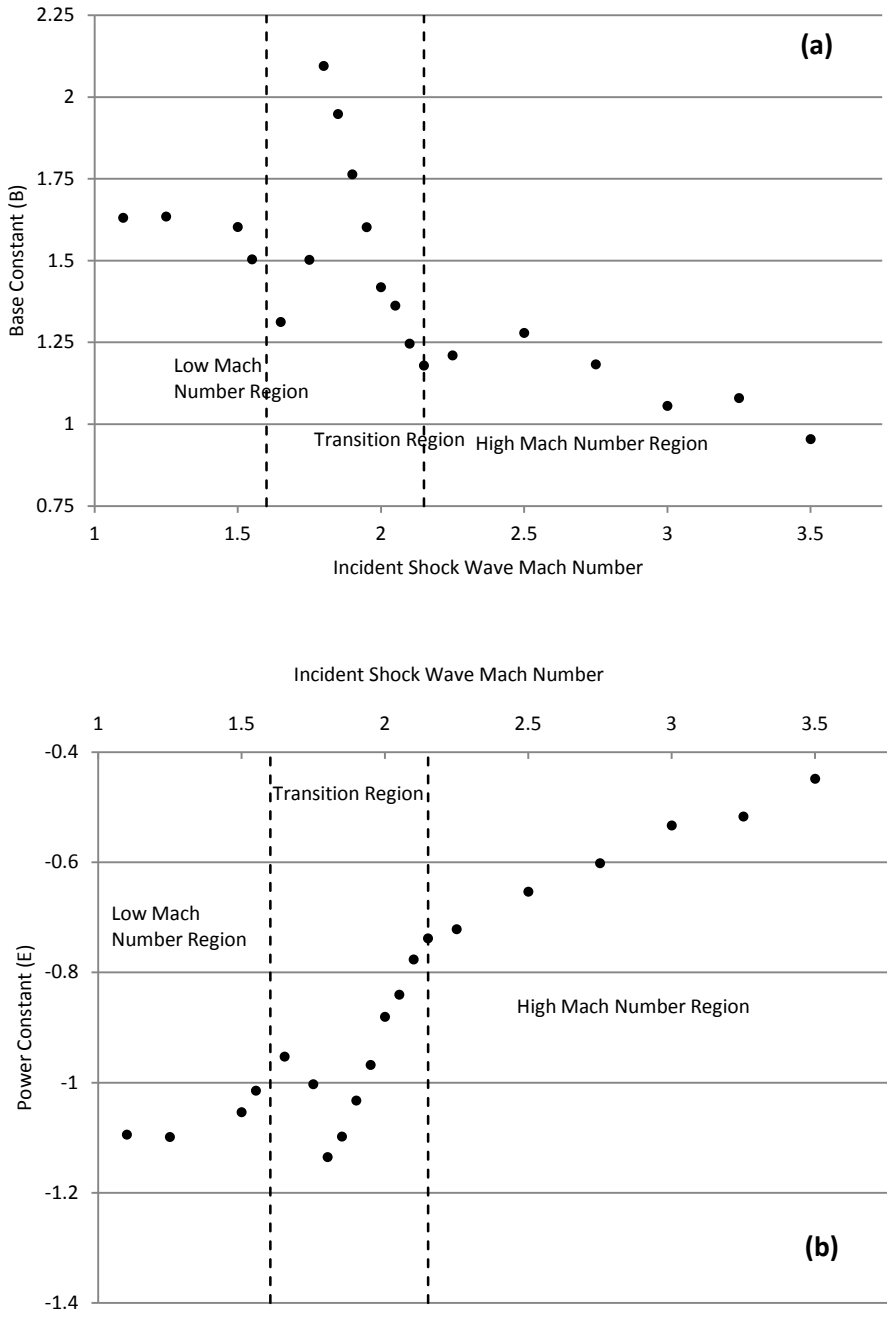

Figure 2.54: (a) Base constant of power regression vs. Mach number. (b) Power constant of power regression vs. Mach number.

Figure 2.55a shows the trends of the base constant in the two Mach regions. The linear trend is nearly continuous through the transition region if the transition data points are neglected. The base constant is related to the post shock interface amplitude since the peaks of the oscillating perturbation amplitude are scaled by the base constant. As the incident shock strength increases the post shock interface amplitude decreases as does the base constant. Theoretically this means the base constant should be a simple function of the post shock amplitude but in practice it is complicated at late times by interactions with the decay rate of the perturbations.

In figure 2.55b, the trend of the power constant at low and high Mach numbers can be seen to be linear like the base constant. If the transition region data is ignored again the power constant data can be seen to also have a nearly continuous linear trend. The power constant is driven by decay of the perturbation waves as they interact with each other. The high Mach number perturbation waves possess more energy and are able to persist through more wave interactions allowing them to remain stronger at greater distance downstream from the initial interface location. This is why the power constant increases with incident shock strength.

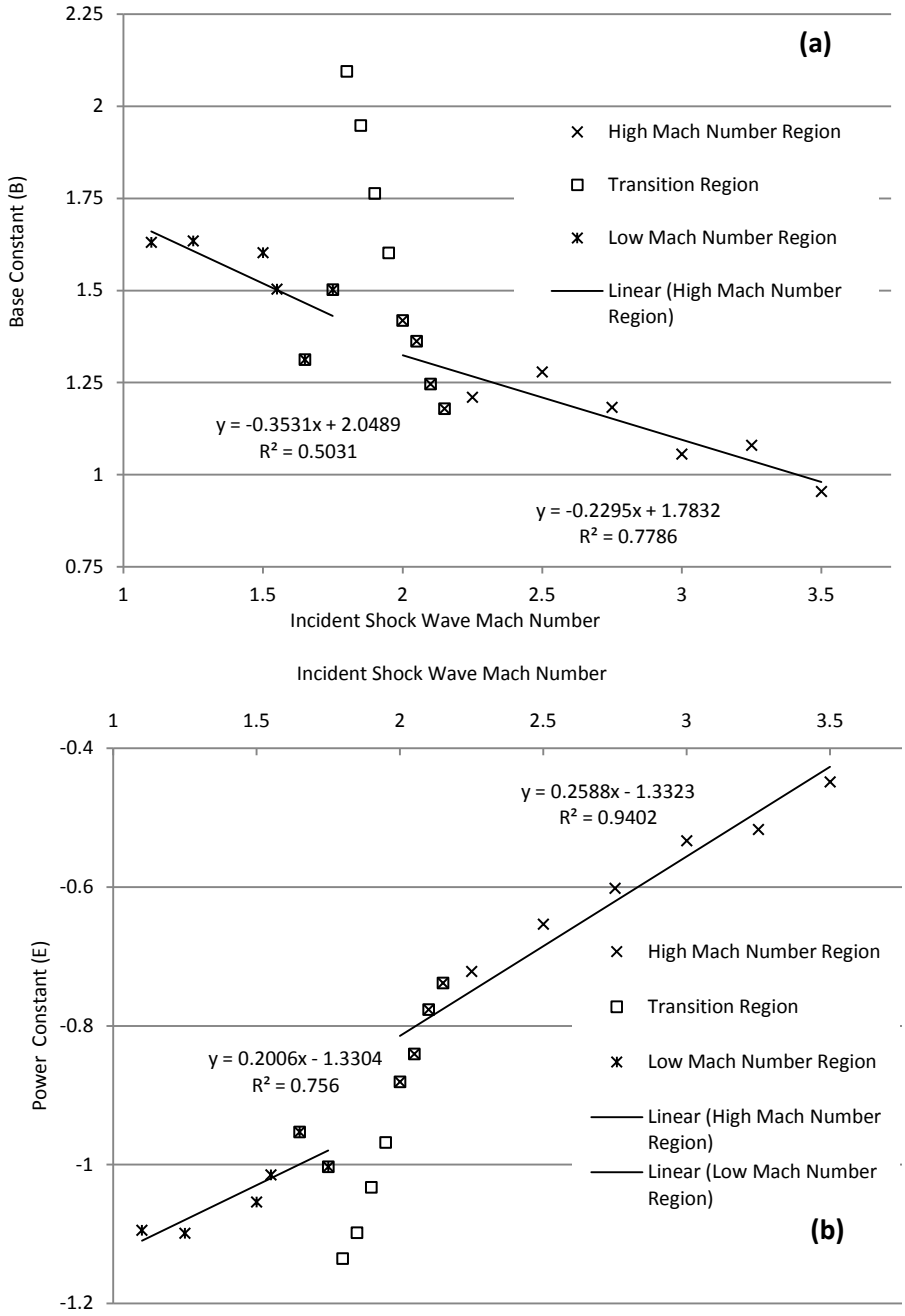

Figure 2.55: (a) Base constant vs. Mach number. (b) Power constant vs. Mach number. Low Mach numbers follow a linear trend between Mach 1.1 and 1.75. High Mach numbers follow a linear trend between Mach 2 and 3.5.

The existence of the transition region may be due to the complexities of the transition to a supersonic post-shock flow and the increasingly coupled flow caused by it. These secondary shock waves may complement or interfere with the refracted shock wave amplitude depending on the phase of the perturbations on the refracted shock wave. This kind of interaction can cause the resonance observed in the Mach 1.85 shock wave flow field. Figure 2.56 shows the complexity and strength of these secondary waves is much higher for the Mach 1.85 case where resonance occurs. According to 1D gas dynamics this transition should occur near an incident Mach number of 1.5, but for a 2D flow this transition Mach number is less definite and can occur at higher Mach numbers.

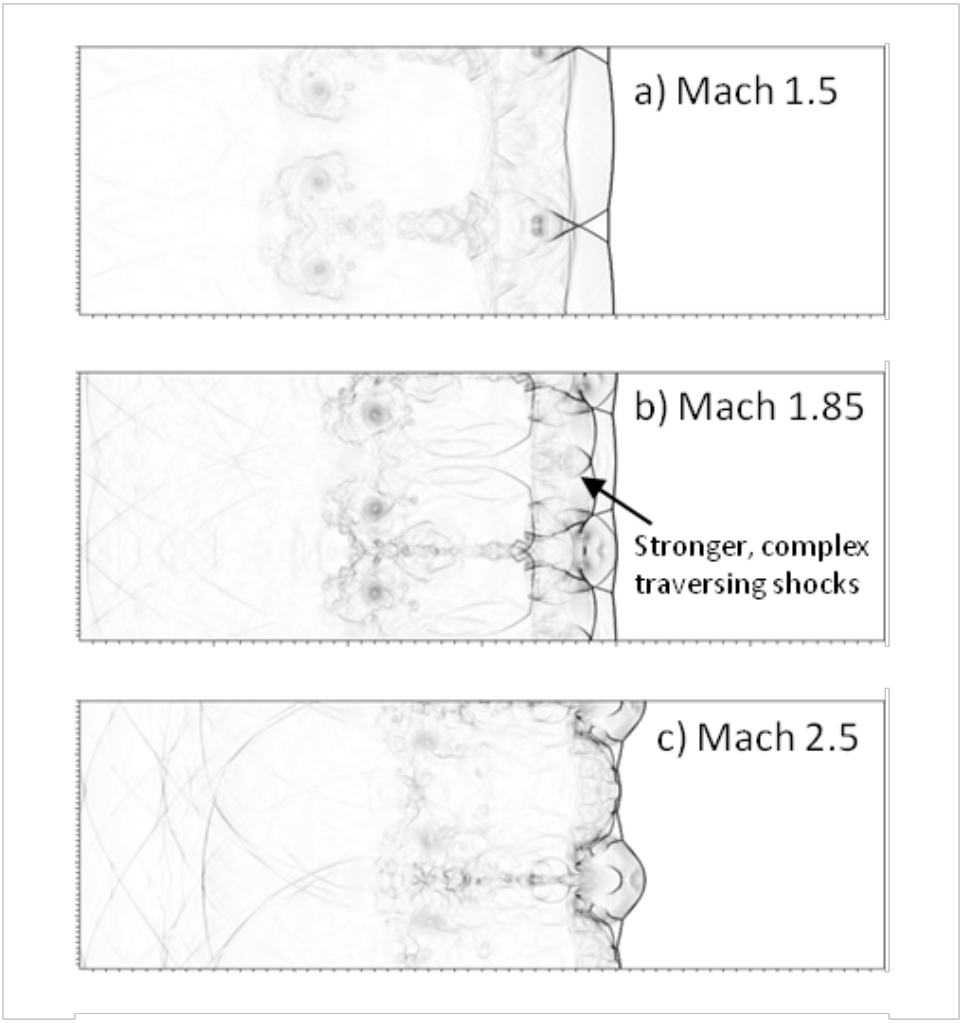

Figure 2.56: Gradient of pressure plots for 3 Mach numbers; a) Mach 1.5, b) Mach 1.85, c) Mach 2.5, at a refracted shock traveled distance of 28.75 cm.

At low Mach numbers the constants act to create a fast decay in the perturbation of the refracted shock with small amplitude perturbation remaining to late times (Fig. 2.54). The low Mach number cases correspond to large (more negative) power constants and larger base constants. The large power constants cause a faster decay and the large base constants result in small amplitudes lingering at late times.

In the high Mach number regime, the decay is characterized by small power constants and smaller base constants. Small power constants cause slow decay (Fig. 2.55). By this token, the effect of perturbing the shock wave by the density interface is more significant at late times for high Mach number cases. For example, in the simulation for incident Mach number of 1.5 (Fig. 2.50), the average amplitude of perturbations at approximately 1.0m from the initial location of the refracted shockwave was ~.01 cm whereas for Mach 2.5 (Fig. 2.57) the amplitude was ~0.07 cm. This amplitude is ~10% of the initial refracted shock wave amplitude, and is ~ 3% of the initial interface perturbation, which may be large enough to create noticeable effects in the baroclinic vorticity production if it intersects a second interface or returns as a reshock.

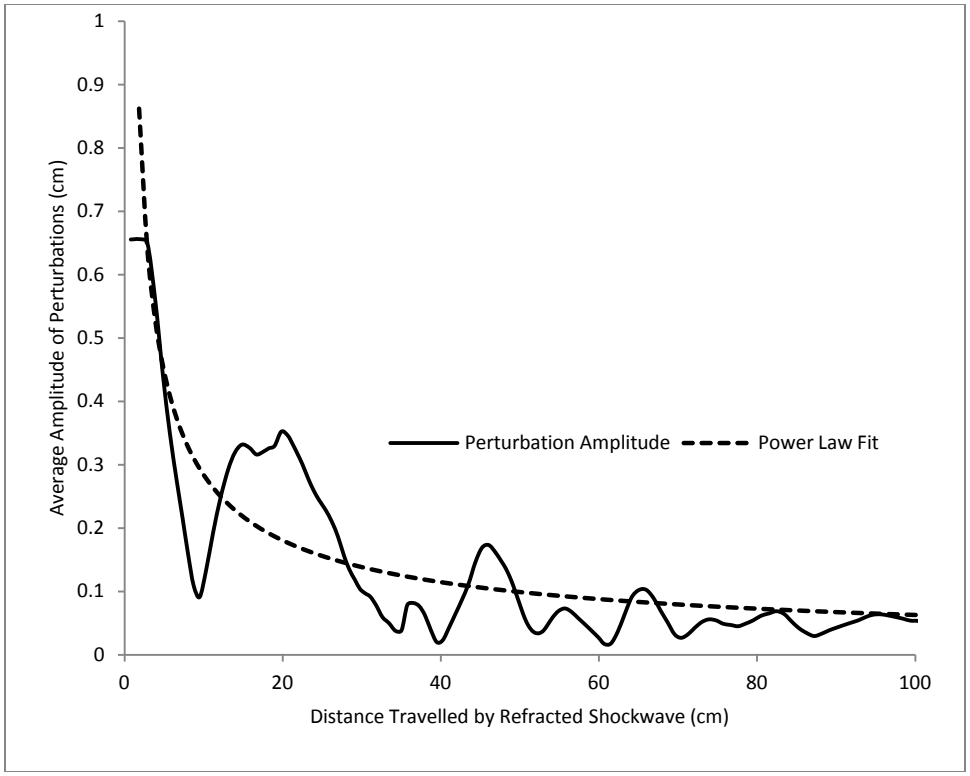

Figure 2.57: Average amplitude of perturbations vs. distance travelled by refracted shockwave. Local maxima are shown as dots and a power law regression of local maxima as dashed line for an incident shock Mach number of 2.5.

2.7.5 Conclusions from the shock refraction study

The results presented here show that the power law decay method, similar to the one proposed by Aleshin *et al.* [63], can be used to describe the decay of the perturbations present on the shock wave created when it encounters a perturbed variable density interface. The proposed model fits the data for low incident Mach numbers well while at higher mach numbers the presence of large and irregular late time oscillation of the perturbation amplitude make it hard for the power law to fit as effectively. When the coefficients from the power law decay model are plotted versus Mach number, a distinct transition region can be seen. This region is likely to result from the transition of the

post-shock SF_6 velocity from subsonic to supersonic range in the lab frame. This region separates the data into a high and low Mach number region. These regions each have their own correlation between the coefficients of the power law decay and the incident shock Mach number. At high Mach numbers, perturbations induced on the refracted shock wave will persist even at late times, and may act as a secondary source of baroclinic vorticity production in shock tube experiments after reshock. Therefore, one needs to very careful while pursuing reshock studies for RMI at high Mach number. The end-wall should be far enough from the initial interface, which guarantees the planarity of the refracted shock wave before reaching the wall.

3 SHOCK TUBE DESIGN

While the design and construction of an experimental facility like the shock tube is not publishable scientific work it did comprise the largest portion of the author's PhD work. The design, instrumentation, and operation of the facility is presented in the following sections in detail as a guide to future operators of the facility and as a record of the thousands of hours of work that were undertaken by the author and others to create this new experimental facility.

3.1 Early Shock Tube Design

The requirements for the new shock tube facility were identified in the fall of 2009. These basic requirements were that the shock tube be capable of inclinations from 0 to 90°, be of sufficient length to support a planar shock wave, be capable of incident shock wave Mach numbers of 2.5 in atmospheric pressure air, and have sufficient cross sectional area to perform experiments with minimal boundary effects. Of these basic requirements the ability to incline the shock tube presented the most difficult challenge. As part of his undergraduate thesis work [121], Peter Koppenberger, working with the author, performed an initial design study to estimate the cost of producing an inclined shock tube (Fig. 3.1). This study identified that the tube length would need to be approximately 8m (based on wave speeds and experimental durations) and that the test section would need to withstand reshock pressures of up to 2.5MPa (these requirements are discussed in detail later in this section). The estimated weight of such a facility would likely require a heavy duty wench or overhead crane to lift it into position and a support system to hold it in place after releasing it from the wench or crane. Many

aspects of this early design were not included in the final shock tube design such as its 6 inch cross section, its double driver for running multiple incident shockwaves, or its pivot and support system. Some aspects were incorporated by the author into the final design including the modular design, and the beam mounting system.

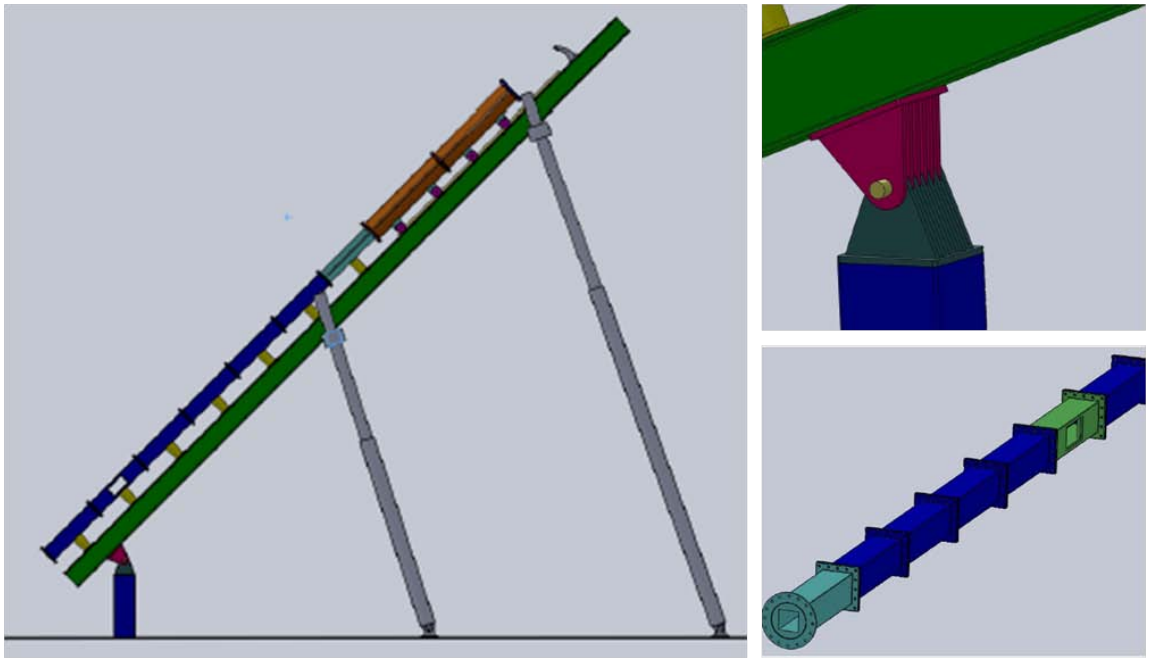

Figure 3.1: Solid works model of the initial shock tube design created by Peter Koppenberger. Left: The shock tube at a 45° angle with telescoping supports to hold its position. Right Top: The hinge mechanism. Right Bottom: The tube sections highlighting its modular construction method.

3.2 Cal Tech Shock Tube Pieces

The shock tube design underwent a major revision in the spring of 2010, when pieces from a former shock tube were donated to the Texas A&M fluids mixing lab by the Wisconsin Shock Tube Laboratory in Madison. These pieces were from a shock tube

facility that was constructed by and last operated with the Sturtevant group at Cal Tech in the 1980's. The primary pieces of interest from the donated lot were three pieces of 4.5 inch square cross section steel tubing that had a combined length of 16ft and hydraulic diaphragm loading section. The square tubing had a nearly square cross section with a 3/8" radius fillet in the corners which was a side effect of the extrusion process. The walls of these sections were ¾" thick. Construction drawings from the Cal Tech shock tube showed their composition to be 4140 carbon steel, but the fact that it has far weaker magnetic properties and its color suggests that it is stainless. While the exact steel alloy composition could not be determined, conservative FEA calculations showed the sections could withstand incident shock strengths far in excess of Mach 3.0 (Fig. 3.2).

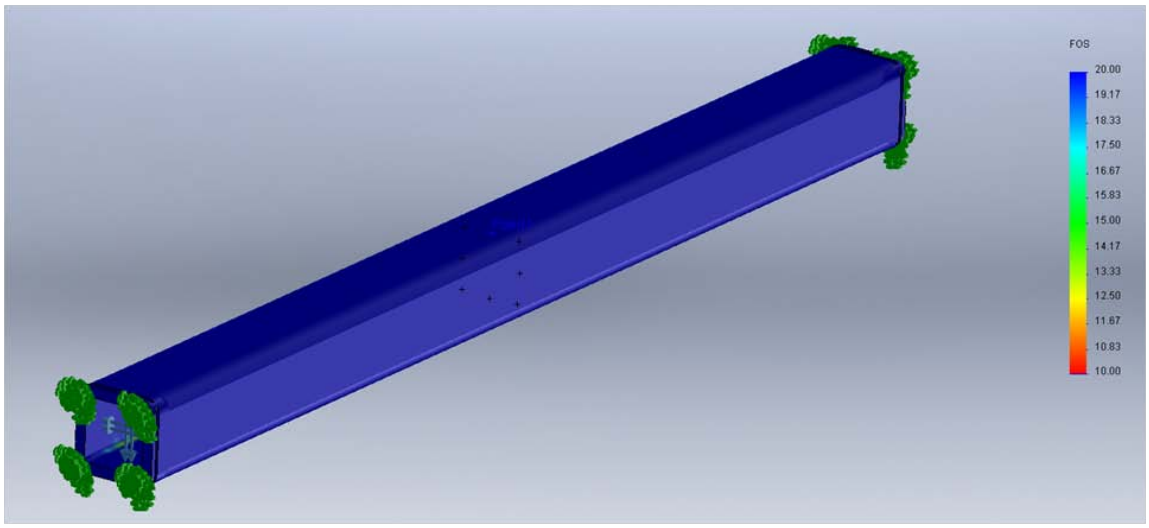

Figure 3.2: Solid works FEA calculation showing the factor of safety for the square cross section extruded tube section. Since the material was unknown a conservative estimate was made using an annealed 201 stainless alloy with a yield strength of 42ksi.

The hydraulic diaphragm loader (fig. 3.3) that was donated was of great value since it was designed to allow diaphragms to be loaded into the shock tube without the need to loosen and retorque any bolted connections. Many shock tubes rely on the use of a bolted connection between the driver and driven section where the diaphragm is held. This connection, while strong, is time consuming to remove and reconnect. The hydraulic diaphragm loader uses an easy-to-remove collar and a hydraulic ram to clamp a diaphragm in place with sufficient pressure to prevent leakage. The hydraulic pump used for this system was repaired and put into service in the shock tube facility. With this pump the hydraulic diaphragm loader is capable of applying over 200,000 lbf to the diaphragm. This force allows the hydraulic diaphragm loader to deform and clamp steel diaphragms up to 1/8” thick.

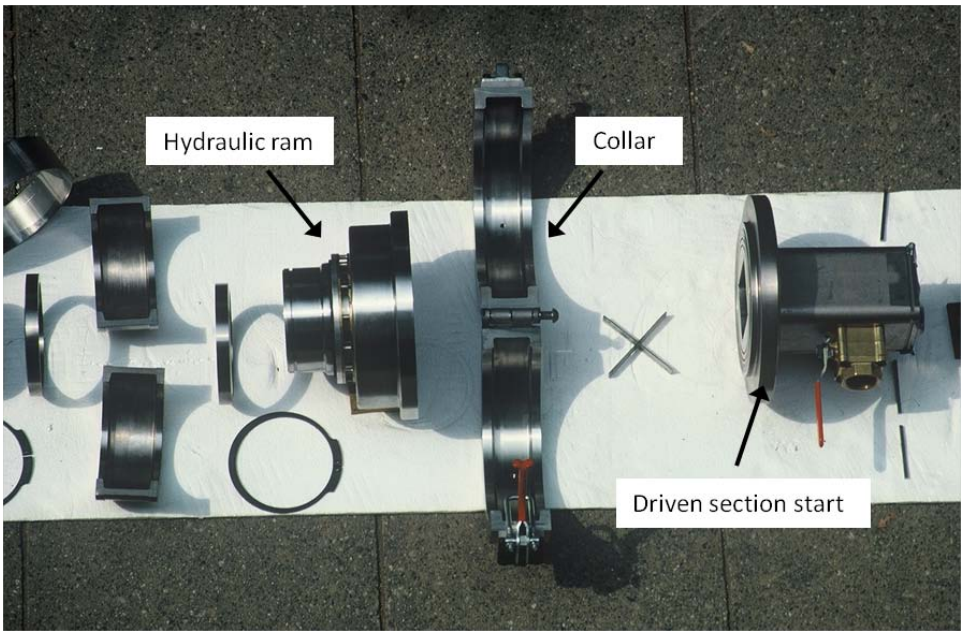

Figure 3.3: Image of the hydraulic ram near its time of original construction (1980s).

3.3 Test Section Design

With these pieces having been acquired the design of the shock tube facility was designed to incorporate them with the most notable modification being a reduction in the shock tube cross section to 4.5” by 4.5”. The next major feature to be designed was the test section which would bear the brunt of the reshock forces, require optically transparent windows, and have sharp interior corners to maintain the best possible 2D flow. The test section was constructed of three subsections which could be reordered for different experimental conditions. These sections were named the interface creation section, the reshock section, and the primary test section. The following discussion of the test section will refer to them collectively as the test section since the design challenges faced in each of these sections were the same.

It was decided early on in the test section design phase that the windows would have to be bolted into place, requiring tapped threads to be incorporated into the test section. The need for these tapped holes outlining the window openings drove the size constraints for the test section pieces requiring the test section outside cross section to exceed the internal cross section by 2 inches to each side. This translated to the shock tube walls being 2 inches thick. Fabrication options were explored for creating a tube like assembly for the test section. Wire Electrical Discharge Machining (EDM) was explored but prohibited by cost and depth of the cut. Using extruded tube similar to the inherited driven section was also considered but could not be found in the required size nor could it be produced with sharp corners in the interior cross section. A welded

construction was explored was ruled out due to the depth of welds required and the difficulty in maintaining tolerances.

Finally, a bolted construction was decided on not only because it met the design requirements but because it also had the advantage of allowing the test sections to be disassembled and reconfigured for different optical techniques. The test section design was then driven by the bolt design required to support the forces created by the reshock pressure, found from ARES simulations. Bolt design is not a simple matter when designing for high forces. Long established empirical rules were used to select the ideal bolt design, based on the number of bolts, the bolt size, and the bolt material grade. An effort was made to ensure that the bolt design selected for the shock tube test section would be equally strong to shear and tensile forces exerted on the test section. It is worth noting that this does not imply the bolts were designed to hold shear. In a proper bolted connection design shear forces are held by the friction between the two pieces being bolted, not the bolt itself.

For an ideal bolt design it is desirable that the bolt fail in tension, not from thread shear, and that the female thread remain intact. This is because a bolt which fails in shear will rise out of its hole or fall out all together making it easy to spot. Also, in the case of the test section construction the female threads would be machined into expensive fabricated parts, making them far more costly to repair or replace than a broken bolt. In the final design the cost of a bolt was around $0.14, while the test section pieces were on the order of $1000 each. The material properties of the test section pieces were driven by the strength required for the female threads to with stand the pressure forces. The

material selected was 4140 steal heat treaded to a hardness of RC 32. This material has an ultimate tensile strength of greater than 100ksi. To ensure the bolts would fail before the threads in the test section components metric graded 8.8 bolts were selected. The number and diameter of the bolts was selected to minimize the size of the test section components while allowing them to hold the required forces with a factor of safety of 2 to all bolt failure modes.

An important consideration in a bolted joint design is the preload placed on the bolt. The axial preload works against the fluctuating tensile loads which reduces the magnitude of the cyclic loading amplitude and prevent joint separation. Axial preload is also used to resist shear forces by increasing the normal force applied to the two bolted pieces and thereby increasing the friction force between them. As a tensile load is applied to a preloaded bolt up to 90% of the additional force goes into relaxing the compressed bolted members, meaning the net tensile load on the bolt increases by a small amount.

Axial preload is often applied by setting the bolt torque. This is a vague way of attempting to measure the applied axial force, since it depends heavily on the friction coefficient between the bolt and female threads. The friction coefficient between uncoated bolts has large variations and can be up to double the mean value. To control this effect the shock tube bolted joints employ an anti-seize compound which reduced this variation to ±15%. The next uncertainty in gauging the axial preload is the accuracy of torque measuring wrenches. Standard “clicker bar” torque wrenches have estimated uncertainties of ±25%. Special wrenches were purchased in multiple torque ranges for

the shock tube bolted connections which have accuracies of ±0.03% to reduce the axial preload uncertainty. When reassembling these bolted connections care must be taken to ensure they are properly coated in clean anti-seize and torque to the proper values. The torque values currently used in the tube are given in table 3.1 with the bolt sizes and grades.

Table 3.1: Bolt torque specifications

Bolt location	Size	Grade	Torque spec . (N-m)
Test section (TS) assembly	M10x1.5	8.8	22.6
TS flange to TS	M8x1.25	8.8	13.7
Flange to flange	M14x2.0	8.8	88
Fused silica window	M8x1.25	8.8	9.2
Riser clamp to beam	M20x2.5	8.8	150
Riser to shock tube (ST) tabs	M20x2.5	8.8	150
ST pivot base to floor	M20x2.5	8.8	190
Riser plate bolt down configuration	M14x2.0	9.8	122
Beam plate connections	M14x2.0	8.8	88
Window flange top to bottom	M6x1.0	8.8	6.6

To create the fluid interface the gas co-flow method pioneered in other shock tubes for RMI experiments was used. This method creates a stable stratified interface that minimizes diffusion by allowing a light gas to sit on top of a heavy gas and to continuously exhaust the diffusing gases at the interface and replace them with fresh

pure gases. This is achieved by flowing the light and heavy gases from the top and bottom of the tube respectively. Then, at the interface location, the gases are allowed to exit through slots in the test section wall out to atmosphere as they diffuse. Valves were required at the inlets and exits of the gases to shut the flow down before the shock wave passes and prevent high pressure post shock gas from escaping the tube. These valves created a necessary small pressure differential between the gas inside the tube and the atmosphere.

The interface plane contains four edges incident with the shock tube walls that could be used as locations for the suction slots. Using the longest of these would minimize the interface diffusion variation from the slot to the center of the interface, but this edge was the edge which was incident on the window that would be required for imaging the interface at early times. No solution could be found which would allow the camera to image the interface through a slotted wall so the two edged perpendicular to the imaging plane were chosen (fig. 3.4). The slots would have to penetrate through the entire 2 inch thick walls. The required slot thickness was estimated to be 0.250", although this was found to be excessive after the tube began operation. Machining narrow slots through 2 inch thick steel is time consuming and expensive so a multi-component construction was selected for the tube top and bottom walls which would contain the slots (fig. 3.5). This construction allowed trapezoidal slots to be machine into the sides of the pieces then joined together during test section construction and sealed with rubber chord (o-ring stock). The slot location had to be specific to interface inclination angles, so multiple slot locations were created which would accommodate

inclination angles of 30°, 45°, and 60°, but when combined in other permutations could yield additional angles.

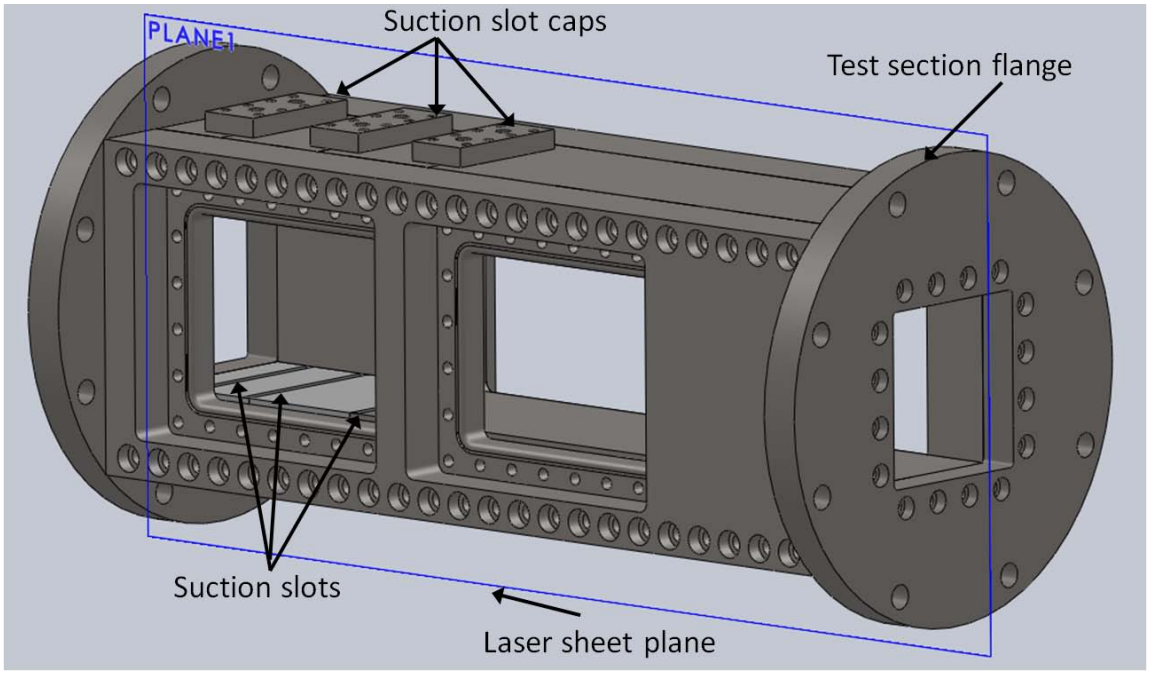

Figure 3.4: Solidworks model of the primary test section showing the slot location, and the laser sheet location marked by the blue outlined plane.

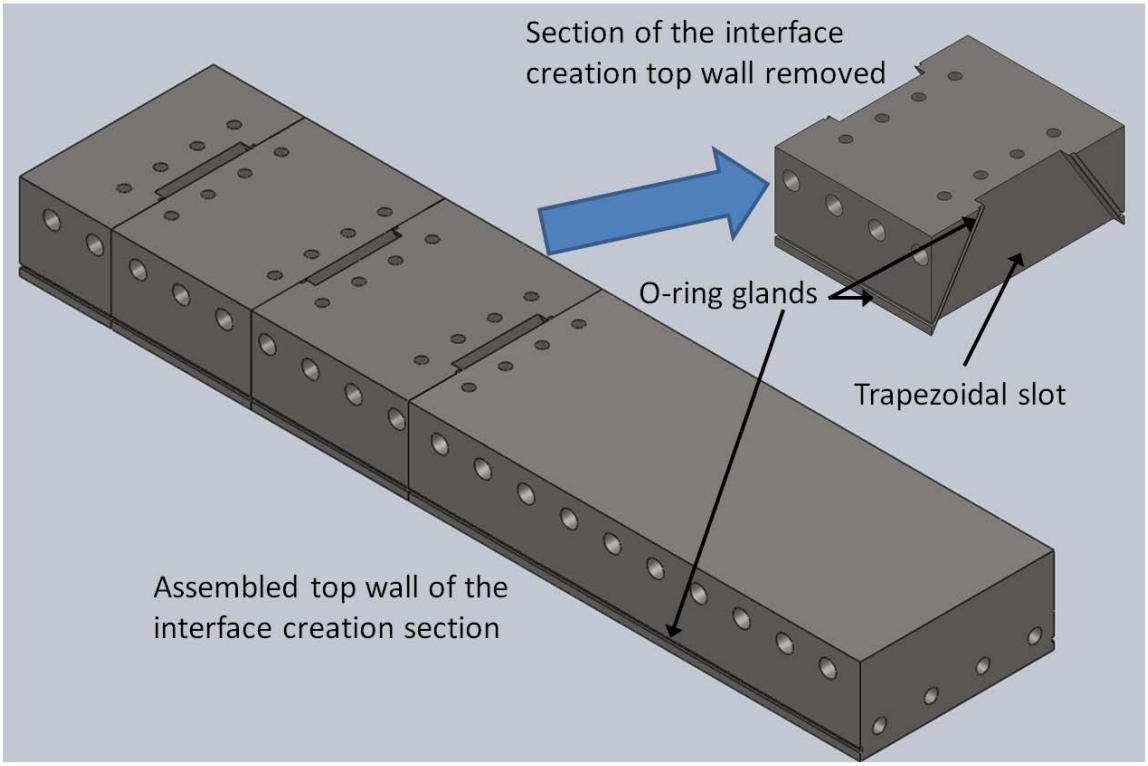

Figure 3.5: Solidworks model of the interface creation section top wall showing the slot location, and the method in which the slots were designed.

The test section was designed in three separate subsections (fig. 3.6) which could be rearranged for various experimental conditions. Each of these subsections was designed for a particular purpose. The first of these subsections was the interface creation section which, as the name implies, was responsible for creating the fluid interface. This section contained suction slots and two windows holes. The primary test section was designed to be used for visualization of the developing interface, but also contained suction slots so that it could be used for visualizing the interface at very early times. The last section was the reshock section which was initially designed with no

windows and no slots so that it could withstand the maximum reshock pressures possible. Later two window holes were added to this section to allow the interface to be visualized at late times. These sections were joined to one another using a flange design which was then incorporated into the steel tube pieces of the driven section that were formally part of the Cal Tech shock tube. Using this common flange pattern throughout the shock tube allows pieces to be interchanged into any location. Since the test section pieces were constructed using a bolted design rubber o-ring chord was required to seal the sections and o-ring grooves can be found cut into the sides of many of the pieces when the section are disassembled.

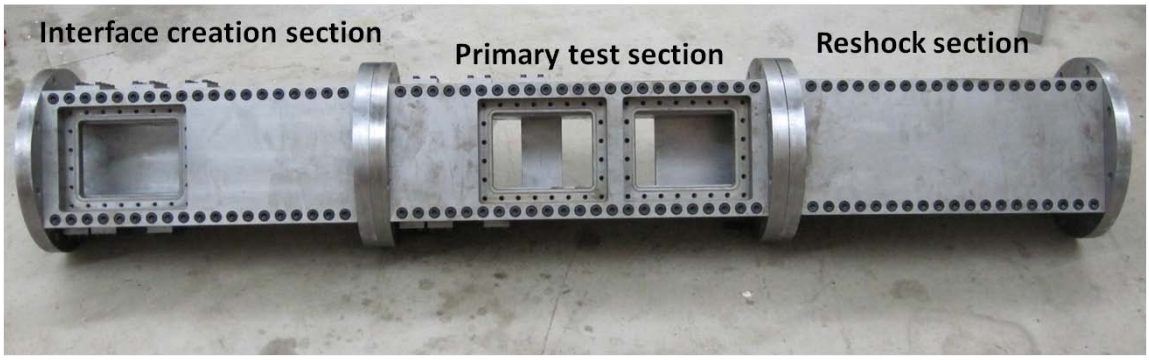

Figure 3.6: Image of the test section with its subsection labeled before it was connected to the assembled shock tube.

3.4 Window Design

The window design and the test section design were carried out in parallel since their design requirements were interdependent. It was required of the windows that they be removable since they are the most expensive piece of the shock tube construction, and minimizing their numbers was critical. Again, a bolted connection was used. The

windows would be required to withstand the full force of the reshock pressure, but would also have to be optically transparent to the visible spectrum, and the far UV spectrum (required by acetone fluorescence in the PLIF diagnostic technique). The standard material used in these conditions was fused silica, or fused quartz. These materials are essentially the same as far as properties are concerned and no effort will be made to distinguish between them from here on. This material is expensive, brittle, and difficult to machine making it essential to simplify the design to reduce material and machining requirements.

The window design was driven by the need to spread the load from the interior surface exposed to the reshock pressure to the largest possible area on the exterior of the window while maintaining a large field of view. The field of view to be imaged would be in the center of the tube, a distance of 2.25" in from the exterior wall or window. In order to minimize optical distortions and fringe effects the cameras used for capturing images would need to use lenses with moderate focal lengths. This meant the window would need to be nearly as large as the field of view in the center of the tube. With this in mind it was decided that the window would maintain the full height of the tube interior, 4.5 inches. The width of the window was determined by the need to have a continuous visible length of the tube of approximately 0.5m. This might seem to require one very long window to maintain continuous visibility, but instead the windows were alternated between the two walls parallel to the imaging plane in the center of the tube (fig.3.7). The width of the windows was then driven by the need to maintain overlapping

visible areas while minimizing the excess width beyond the square area which was optimal for carrying the pressure stresses. This width was found to be 6 inches.

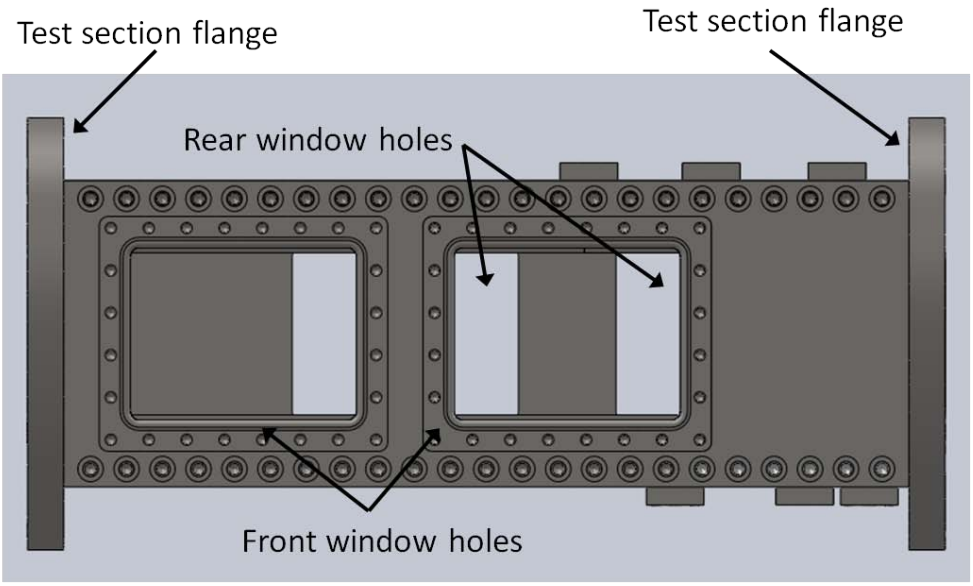

Figure 3.7: Solidworks model of the primary test section illustrating how the windows were staggered from front to back with overlapping fields of view.

The thickness and shape of the convergence from the interior to exterior surfaces was then found using FEA analysis performed in Solidworks (fig. 3.8). While the optimal convergence cross section was to be a converging trapezoid (fig. 3.9) this approach was limited due to the fact that it would require a four axis CNC machining process capable of working on fused silica. This consideration of the fabrication process in the design optimization was a common theme throughout the shock tube design which must be considered in any design. A stair step design which could be machined on a 3 axis machine using a ball mill to fillet the inside corner and the stress concentration there was selected instead (fig.3.8). With the cross section of the window selected the

thickness could then be optimized. Using available stock thickness of fused silica material a two inch thickness was selected.

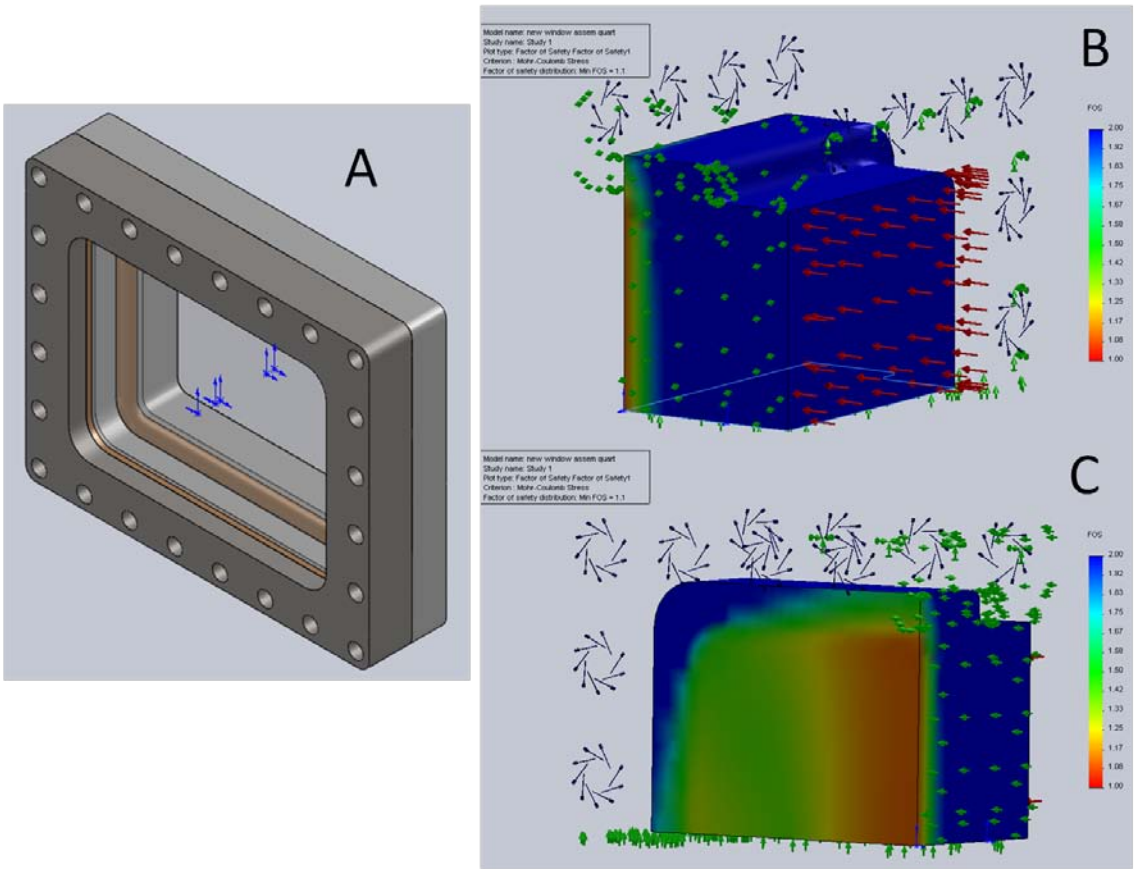

Figure 3.8: Solidworks model of the window assembly. A) The whole window assembly including the two steel flanges, the nylon gaskets, and the fused silica window. B and C) A FOS plots based on Mohr-Coulomb stresses from a Solidworks FEA. The minimum FOS is 1.1, using a pressure of 12MPa, with bolt preloads optimized and a conservative estimation of the brittle mode failure stress for the fused silica.

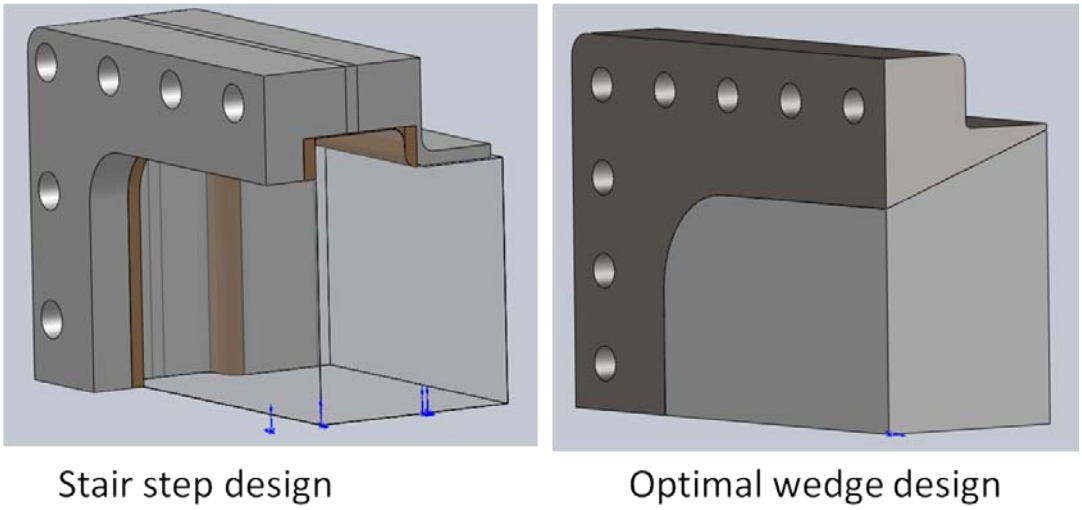

Figure 3.9: Solidworks models of two window profiles developed.

To enable the window to be bolted into the test section it was designed to be encased in a steel flange which contained the holes for bolting the window in place. It was necessary to place the holes in the steel flange rather than the fused silica window due to the manufacturing cost and the material properties of fused silica which made it risky to cyclically load by tightening and releasing bolt loads repeatedly. Another consideration in mounting the window in a steel flange was how to absorb movement between the pieces when loaded by the reshock pressure. That is, the window will react in a slightly different way than the steel flange. With this movement in mind a more elastic material, nylon 6, was selected to take up any differences in displacement between the two pieces. Nylon gaskets were made for both the top and bottom interfaces between the fused silica and the steel flange (fig. 3.8).

It should be noted that the FEA (fig. 3.8) was performed using a pressure which is double the maximum reshock pressure. This is to attempt to account for the dynamic nature of the force. No, rules exist for estimating the effect of dynamic pressure load applied over an increasing area with time. Instead a the load was estimated as if it was applied to the entire surface at once which leads to the empirical estimation rule that the dynamic load is twice the static equivalent. Using this rule it was then difficult to assess the properties of fused silica and determine the failure criteria since it is a brittle material. Several estimates of the factor of safety were made which ranged from just under one to 1.5. This was not the intent of the Author's design to have this low factor of safety, but the design was initially conducted using incorrect properties for the fused silica material which lead to an initial over estimate of its factor of safety. It is the Authors opinion that these windows should be used very cautiously for Mach number over 2.0.

At this point it should be acknowledged that the final design was not reached without a trial and initial failure. The initial window and flange design incorporated thinner gaskets and a flange design which allowed the window to sit flush with the interior wall of the tube (the current deign is recessed by .010"). This initial design failed to account for a critical consideration in engineering design, tolerances, and was designed without consideration for variations in fabrication. Of the four pieces which were initially machined with window mounting holes, one was machined with 0.020" tolerance error. This was outside the original specified design tolerance of 0.005". This tolerance error allowed an edge of the fused silica portion of the window assembly to

come into contact with the bottom edge of the window mounting hole (fig. 3.10), and placed a bending load on the window which it could not bear (fig. 3.11). This design flaw was fixed by having the tolerance error in the window mounting piece corrected, and to increase the clearance at the bottom of the window when it was mounted in place to 0.010".

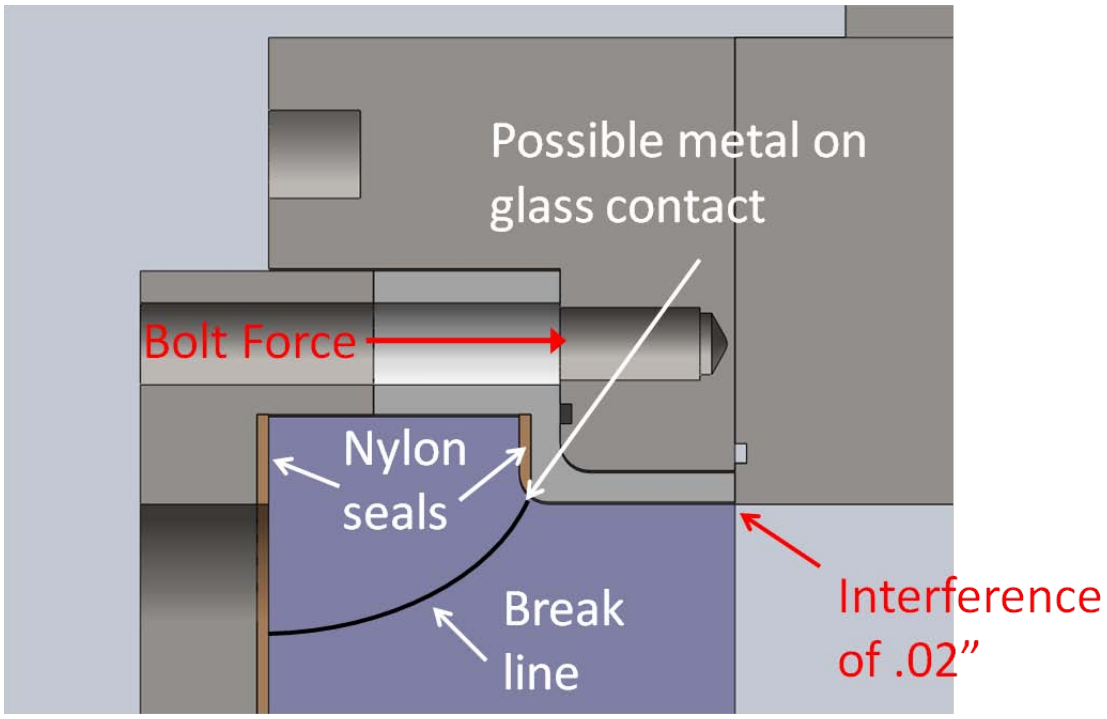

Figure 3.10: Solidworks model showing the cause for the window failure.

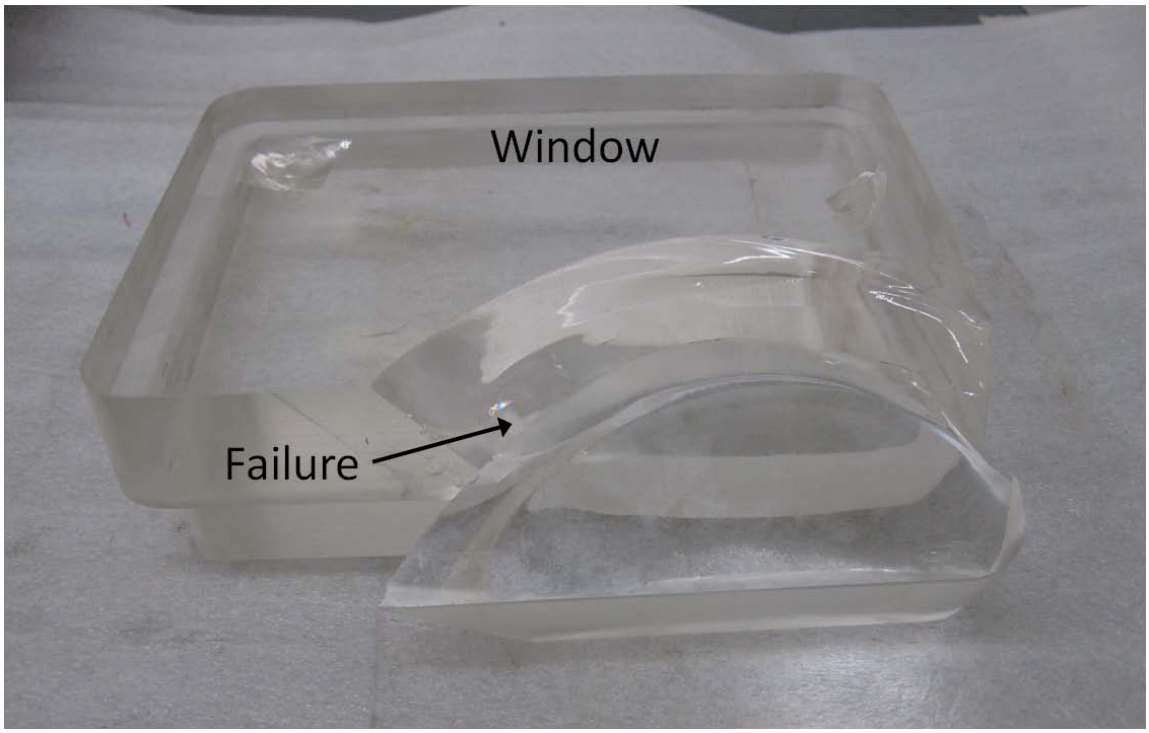

Figure 3.11: Image of the broken window.

In an attempt to improve the window strength and reduce the accidental failures due to the brittle nature of fused silica a new set of windows was constructed from acrylic (fig. 3.12). Acrylic has similar strength properties to fused silica but will fail only after some elastic deformation making it easier to predict failure and detect wear on the material. Acrylic however does not transmit light below 350nm. The fluorescence spectrum from acetone PLIF starts just below 350nm and peaks at just above 400nm. Using acrylic windows cuts of less than 10% of the available light in the PLIF signal for acetone, which is an acceptable loss. Another major drawback to acrylic is that it is susceptible to acetone erosion. Informal tests were run where samples of acrylic were

subjected to acetone liquid and vapor. The sample in the liquid acetone lost the ability to hold its form in less than two hours. The sample in the vapor was exposed for 24 hours and showed no ill effects initially. After a month had passed outside of the acetone vapor it was noticed that the sample had a cloudy appearance, which was likely a delayed effect of its exposure to the acetone vapor. To protect the acrylic, coatings can be applied like a thin layer of LDPE which is not susceptible to acetone. Acrylic has one very important advantage that in the author's eyes overcomes it weaknesses, it is very cheap compared to fused silica.

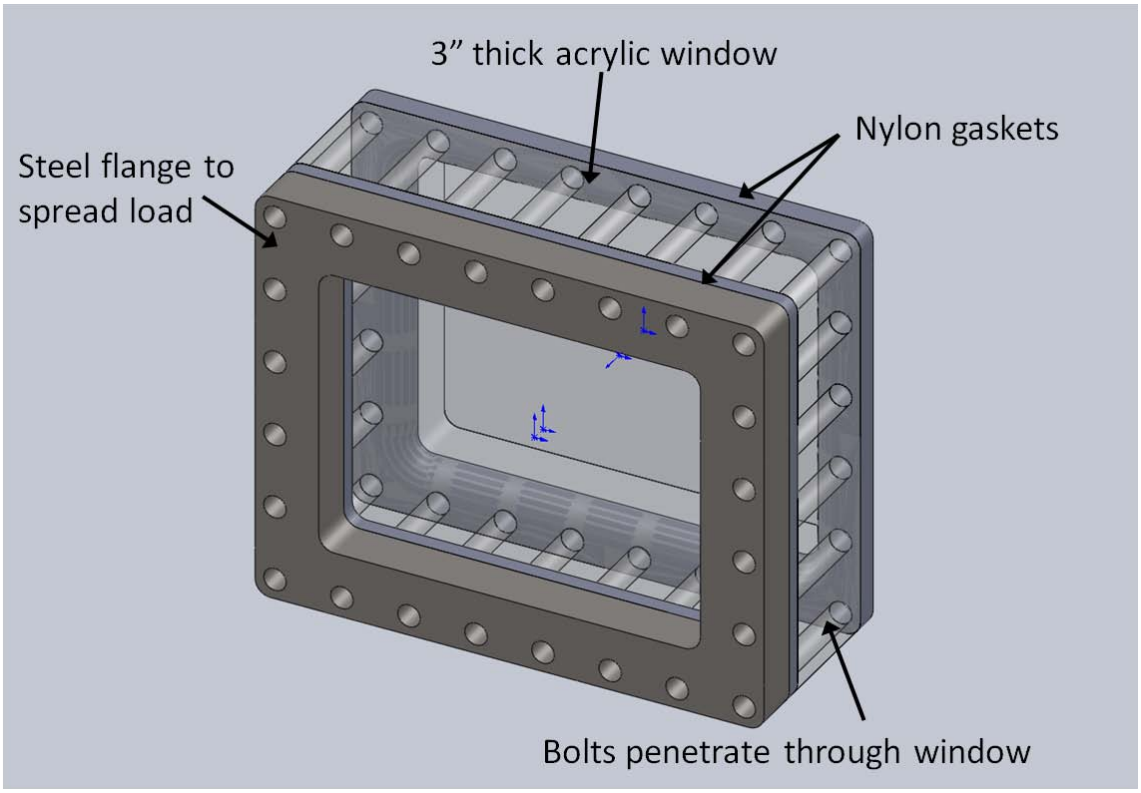

Figure 3.12: Solidworks model of the new acrylic window design.

Two new acrylic windows were constructed with an improved design that has an estimated factor of safety of 3.0 at the same reshock conditions the fused silica design was tested. These windows do not use the steel flange design and were fabricated for nearly a tenth of the cost of the fused silica versions. These windows were coated in a thin protective coating which should increase their resistance to acetone corrosion. At the time of this dissertations construction the windows have just entered service in the shock tube and remain to be tested under a wider range of experimental conditions. To increase the effectiveness of the acrylic window design a different PLIF system was devised by the author. This system would use biacetyl gas and a modified laser wavelength of near 400nm. This would allow all windows including the laser window (discussed later) to be constructed of acrylic and to be safe from acetone corrosion. The complete development of the PLIF system is left to future shock tube researchers.

To complete the optical instrumentation access abilities of the test section one final window was needed to allow the laser sheet into the shock tube. The laser window was placed in the bottom of the tube and was constructed with a similar steel flange and fused silica window design. This window has the greatest pressure placed on it by the reshock wave. It also has the greatest affect on the optical instrumentations signal strength because all laser light entering the tube must transmit through it. To minimize the laser light lost in the window the window thickness must be minimized, but to with stand the reshock pressure the window must be made thicker. These two requirements had to be balanced. For acetone PLIF diagnostics the window would have to pass 266nm light efficiently. Fused silica is one of the very few material available that can transmit

266nm light with low losses. Since the laser would be entering the tube as a sheet of light a rectangular slit shape was selected. The longer the windows viewable area the easier it would be to diverge the laser sheet for pictures in the lowest section of the test section. However, the longer the window was the greater the stresses it would be subjected to by reshock. A compromise for all these conflicting requirements was found and the window was designed to be 1" thick with a 0.375" visible area width, and a 2" visible area height (fig. 3.13). FEA showed this design to be more than capable of withstanding the reshock pressures in part due to its small visible area. Initial testing of the windows laser transmittance abilities found it to be capable of transmitting nearly 90% of incident 266nm laser light.

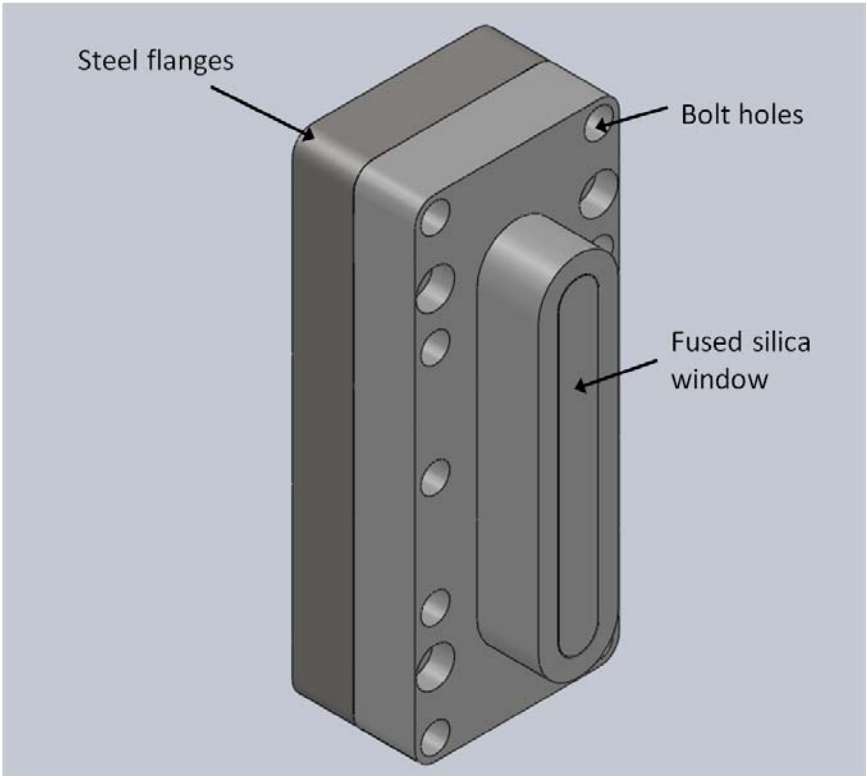

Figure 3.13: Solidworks model of the laser window assembly.

3.5 Driver Design

With the driven section acquired and the test section designed the next piece of equipment that would be required for the operation of the shock tube is the driver which stores the compressed driver gas behind the diaphragm. After the diaphragm ruptures the driver gas is released into the driver section creating the shock front. As the gas is released it is consumed by expansion waves which travel up the driver section. The driver section size is defined by its ability to supply the needed gas to support the shock front. The driver gas pressure can be calculated using simple algebraic 1D gas dynamics

equations. These calculations showed that a driver pressure of up to 2000psi would be required if pure air was used as the driver gas. This pressure can be reduced by using different gases for the driver gas. Helium in particular reduces the driver gas pressure greatly, but also has a much greater sound speed. This higher sound speed is detrimental because it reduces the time during which the shock front can travel down the tube without being affected by the limited driver size. The information about the limited driver size is carried to the shock front by expansion waves as discussed in the following paragraph. To achieve the minimum driver pressure required for each experiment the driver gas can be tuned by changing the ratio of Air to helium or other gasses. Using a mixed driver gas it was found that the maximum driver pressure required would be approximately 800psi for shock wave Mach numbers of 2.5 in air.

The driver's ability to support the shock front can viewed in two ways. In a 1D gas dynamics approximation where the cross section is uniform throughout the tube it is the length of the driver which determines how long it can sustain a given shock strength. The expansion waves which travel up the driver consuming the gas will reflect from the driver end wall and begin traveling down the tube to catch up with the shock front. These waves travel at the speed of sound behind the shock front which has not only raised the speed of sound in the post shock fluid behind it but has also induced a velocity which is traveling towards the shock front. It is because of this induced velocity and increased sound speed that expansion waves will always catch up to shock front when they are traveling in the same direction behind it. When these waves catch up to the shock front they will begin steadily weakening it. The longer the driver section the

longer the reflection of the expansion waves will be delayed. This is one way to choose the driver length.

The other method for predicting the driver volume uses a 2D approach where the driver may have a different cross section. In this approach the driver can be thought of as a supply of post shock mass. While the shock wave is compressing the driven gas to higher densities the driver gas is expanding to the post shock pressure. A simple calculation can be used to estimate the volume of compressed driver gas required to expand to the volume that will be required behind the shock front when it has completed its interaction with the interface. Using these methods a conservative estimate was made of the driver volume required for the strongest expected shock waves required in experiments, Mach 2.5 into air.

The result of the above considerations was to use a round driver with a 6.25" internal diameter, which could carry a greater volume and would be stronger due to its shape. Many material options were available including tubing or pipe. 1020 DOM tubing was selected due to its much higher strength from the cold working process involved in its construction. However, DOM tubing is not normally used for pressure applications where as pipe is rated by ASME standards for pressure. If the driver was to be constructed again it is the Author's judgment that pipe should be used instead since it is intended for pressure vessels and is rated by ASME standards. The DOM tubing was welded to 1045 cold rolled steel flanges to mate it to the hydraulic diaphragm loader. A 0.5" wall thickness was decided upon based on a simplified FEA using Solidworks (fig. 3.14) which showed an estimated FOS of 9.5 with a 1000psi driver pressure.

Considering the cyclic nature of the pressure loading the driver will undergo in its life this factor of safety was considered to be safe.

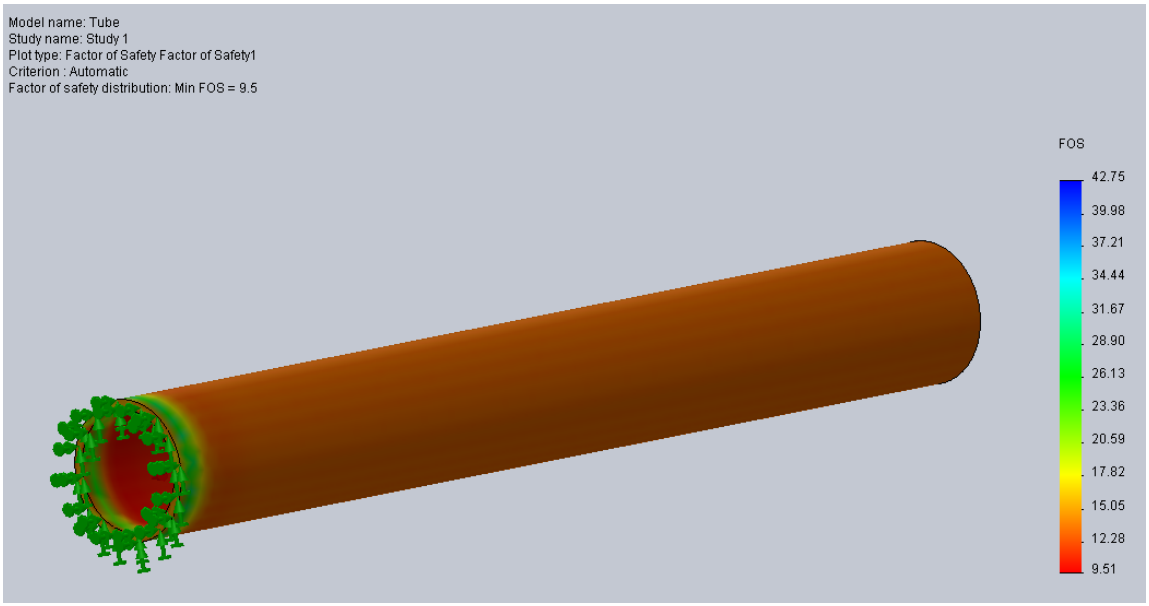

Figure 3.14: Simplified Solidworks FEA of driver FOS under 1000psi internal pressure.

3.5.1 Shock tube support design

A support system was designed for the shock tube to enable it to pivot and to add additional mass and rigidity to the system to resist vibrations during experiments. The shock tube support consisted of three major components: the I-beam, the pivot mount, and the stand. The purpose of the I-beam was to provide a continuous surface with which to mount the shock tube components, and to provide rigidity and mass to the pivoting tube. Having a continuous beam in place under the tube sections also allows for sections to be removed without the tube needing to be completely disassembled. Each of

the shock tube sections, the three test section pieces, the three driven sections, and the driver, was equipped with a mounting point to connect to the beam. The only piece which is not mounted with its own connection to the beam is the hydraulic diaphragm loader since its operation requires that it be free to move and be disassembled. The remainder of the shock tube pieces are connected using risers (fig. 3.15) which bolt to the pieces and clamp or bolt to the beam. The driver and driven risers use a clamping mechanism to interface with the beam which allows for expansion or contraction of these pieces under stress. The test section risers were bolted to the beam in an effort to share some of the reshock stresses with the I-beam. The driver clamps are usually not engaged so that the driver may slide freely as is required when the diaphragm is replaced.

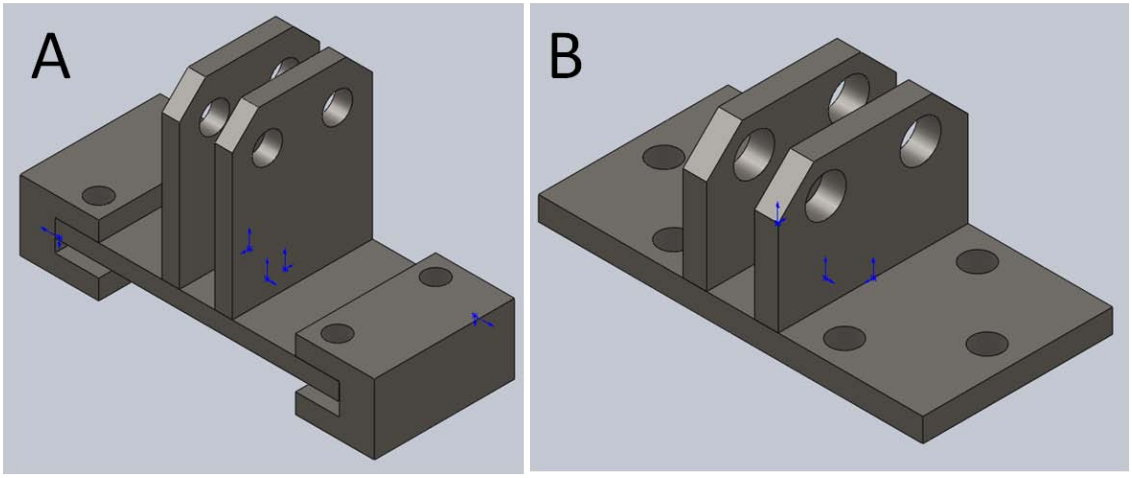

Figure 3.15: Solidworks model of the shock tube support risers which connect the tube pieces to the support beam. A) a riser which clamps to the beam. B) a riser which bolts to the beam.

The I-beam was cut into a 23’ piece, a 7’ piece and a 2’ piece. These pieces are bolted together using splicing plates which carry the beam loads through the connections. The purpose of cutting the beam and adding bolted connection was to allow for the shortening of the tube. The lengths were chosen to match lengths of the driven section which might be removed, 7’ and 2’ are the length of these pieces. The reason the tube may need to be shortened is because the tube was designed to go to a 90° (vertical) angle in a building with 30’ ceilings. The tube is approximately 32’ long with a pivot point that sits approximately 2.5’ above the floor. This means the tube will need to be shortened to reach 90° in its current location. The beam was chosen to be a 40lb/foot w12 (wide flange) since the width of the beam flanges was near the test section width, and its load carrying capacity gave it the ability to easily carry the distributed mass of the shock tube. Even though the shock tube is capable of supporting its own load in the event that a piece is removed it will lose its load carrying capacity and the beam will be required to support it.

To allow the entire tube assembly to be inclined at various angles a pivot point was required which would fix the tube to the ground but allow it to incline. This pivot point would be required to transmit the full load of the shock wave pressures to the ground at all inclination angles from 0° to 90°. These loads were predicted using the pressures predicted by quasi 1D Ares simulations and the internal area subject to pressure in the tube. The initial loading from the diaphragm rupture and the first shock reflection from the lower wall provide the greatest loads on the pivot point. Subsequent shock reflections diminish in strength as the pressure in the tube is equalized through

multiple shock and expansion wave reflections and interactions. The estimated loading on the tube over time was plotted in figure 3.16. These forces would have to be carried at two extremes, the 0° and 90° cases. The 0° (horizontal) case presented the greatest challenge since the pivot point would have to be above the floor by some minimum distance which creates a moment arm at this angle.

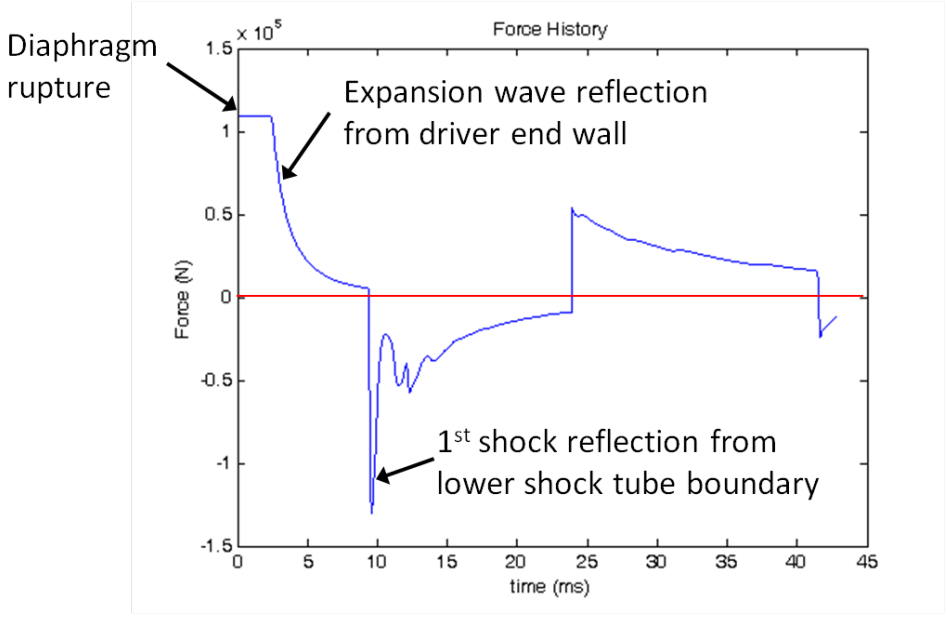

Figure 3.16: An estimated force history for the shock tube pivot based on 1D ARES simulations and internal pressure areas for the first two shock reflections from the lower wall.

Using ASTM A513 high strength rectangular structural steel tubing a design was created (fig. 3.17) which could resist the large bending moments which would be created at the horizontal inclination angle. The tube selected was a 12”x4” rectangular tube with 0.5” thick walls. This tube was reinforced with buttresses made of cut section of the same tube type. Two of these mounts would be used to support a pivot bearing on either

side of the shock tube. These tubes were welded to a 0.5” thick plate which contained holes for bolting the assembly to the floor. More sophisticated bearing designs were considered for the pivot point but considering the relative infrequency with which the tube would be required to change angle a simple journal bear design was selected. This design simply consisted of a well fitted greased tube ridding inside of another.

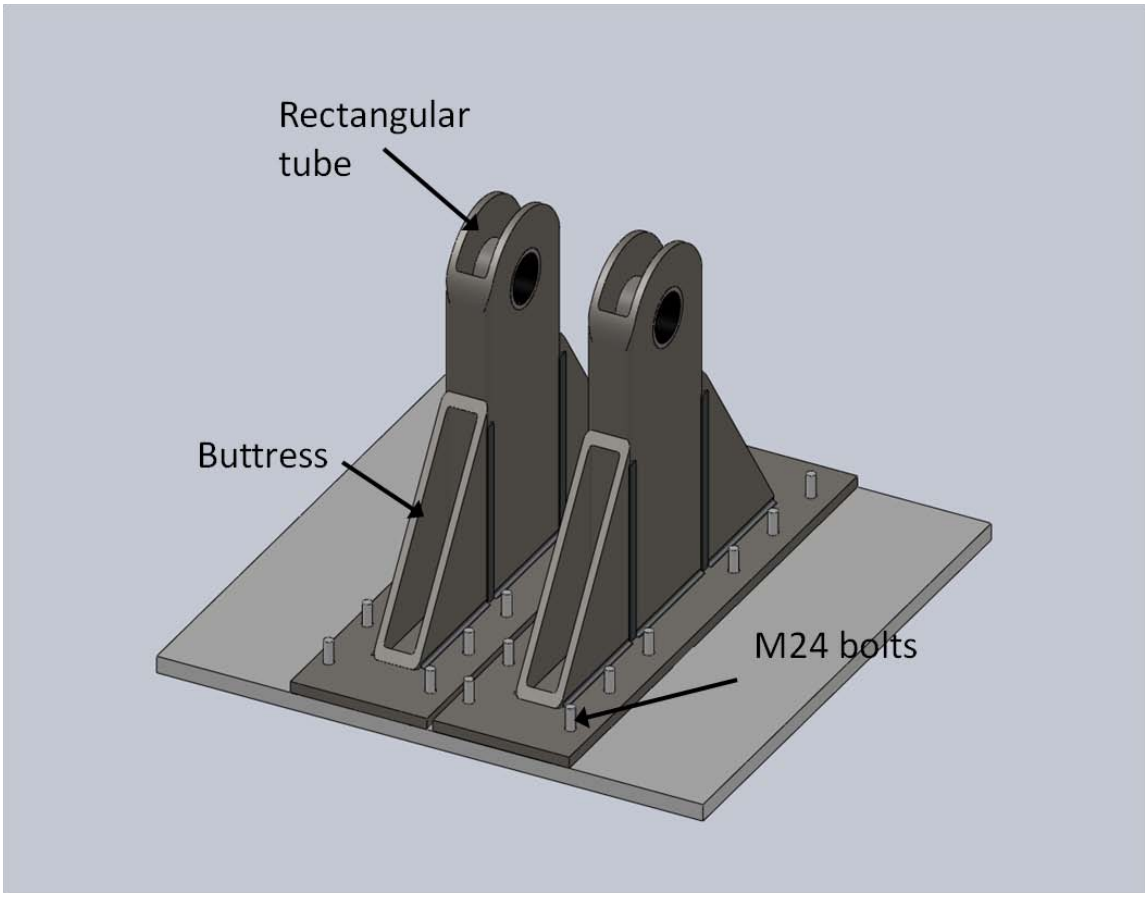

Figure 3.17: Solidworks model of the shock tube pivot point ground mount.

To connect the pivot point to the shock tube many positions were considered but the strongest position was easily determined to be where the shock forces would be directed through the center of the pivot thereby creating no moment. A simple continuous tube could be used as a pivot pin but it would pass through the same area that the laser would need to pass through to enter the tube. For this reason a more complicated design was created which allowed the center of the pivot pin to be removed and the forces to pass through a square tube which bolted to the shock tube (fig. 3.18). FEA showed this to be a capable design with a conservatively estimated minimum FOS of 1.5 at the anticipated maximum shock forces. To ensure the two separate pieces of the pin were aligned the assembly was constructed exactly as its design was imagined. A continuous tube (pin) was inserted into the assembly and welded in place. Then the middle of the pin was cut out.

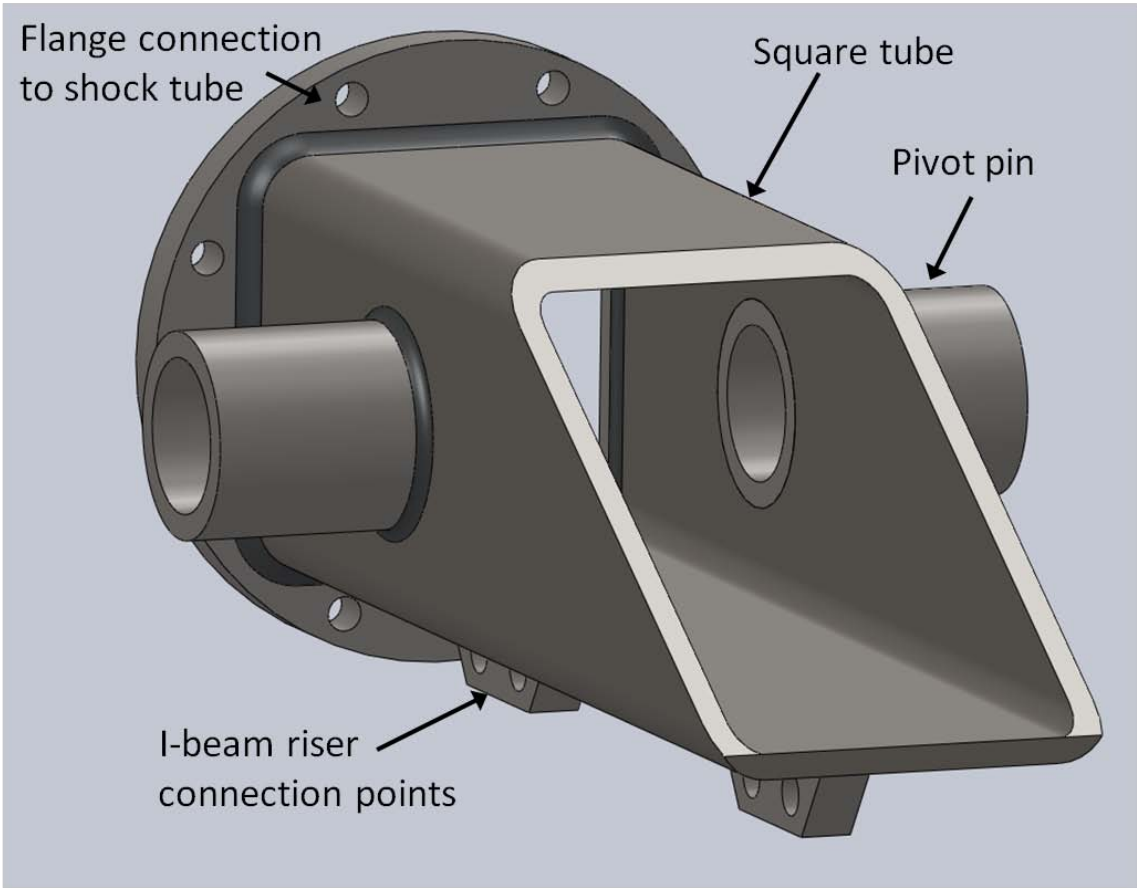

Figure 3.18: Solidworks model of the shock tube to pivot point connection.

The forces transmitted to the ground by the pivot are significant and far beyond the design stresses of typical concrete flooring. To carry these forces the lab space, which was customized for the shock tube and managed by the Author, used a 4’ cube concrete block imbedded 4’ deep in the ground to transmit the loads beyond the foundation and into the earth. This block was vibration isolated from the surrounding flooring using 0.5” concrete vibration damping material. Twenty four M20 bolts were imbedded in this concrete block when it was poured. These bolts travel the entire depth

of the block to provide the greatest strength and resistance to tear out. An additional layer of rubber vibration isolating mat was placed between the shock tube pivot mounts and this concrete block.

The tube is hoisted into place using an overhead crane which has a 2 ton carrying capacity, a 23’11” hook height, and a moveable area of nearly 50’ by 50’. This crane was specified by the Author and incorporated into the lab space with a primary purpose of lifting the shock tube into position. The crane hook interfaces to the shock tube through an attachment point bolted to the I-beam (fig. 3.19). This attachment point was built by cutting a 20”x8”x18” long ASTM A513 rectangular tube with a 0.5” wall thickness into two ”L” shaped pieces which bolted to the tube. A 1-1/4” bolt was then inserted through the two pieces and above the tube to provide a removable hoist pin for lifting the tube. As always FEA calculations were made to estimate the factor of safety for this design, which was greater than 5.

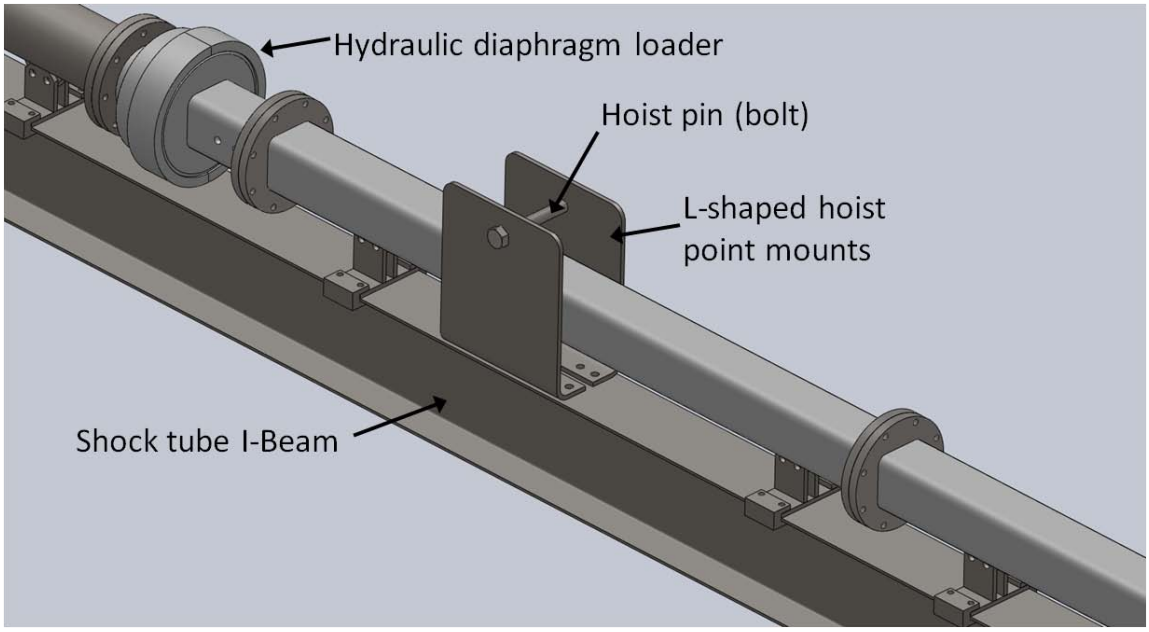

Figure 3.19: Solidworks model of the shock tube crane hoist point mount.

With the tube lifted into position by the crane a stand was needed which could be used to hold the tube in place and allow the crane to be released from the tube. This stand went through two designs. The first design was constructed of thin walled 14gauge steel tube and clamped to the bottom of the I-beam to keep it from sliding out of place when put under load. This stand was only 10' tall and had the advantage of being light enough to be carried by two students when it needed to be moved. It showed some signs of deformation though after approximately 8 months of use. The areas which were deforming were where feet bolted into the stand which transmitted the loads to the floor. This deformation could have been easily prevented with some reinforcement in this area but it was decided that the stand required too much time to remove and that a heavy built design would provide some addition peace of mind to the Author.

The current stand was built of 3/16” thick ASTM A513 square and rectangular tube. The stand is nearly 16’ tall which allows it to carry the shock tube loads at a larger moment arm from the pivot point. The larger size and thick steel construction made it impossible to be moved without heavy duty casters. The stand is wheeled into place using these casters and then lifted from them using high-strength leveling feet. The stand is then bolted to the floor using a mounting system which is attached to the floor using concrete anchors which have a female thread. The importance of using female thread anchors is that they leave no tripping hazards above the floor when not in use like a stud would. These anchors are glued into place and have a design tensile load limit of 13,000lbf. There are six of these bolts to mount the stand to the floor. A disadvantage of bolting the tube to the floor is that new bolt anchors are required for each inclination angle of the tube. The stand was also modified to have a wider distance between the two towers which will allow it to hold the tube in place at a 90° angle but required a heavier connecting pin which the tube rests on (fig. 3.20).This design should prove to be very advantageous at high inclination angles in future experiments.

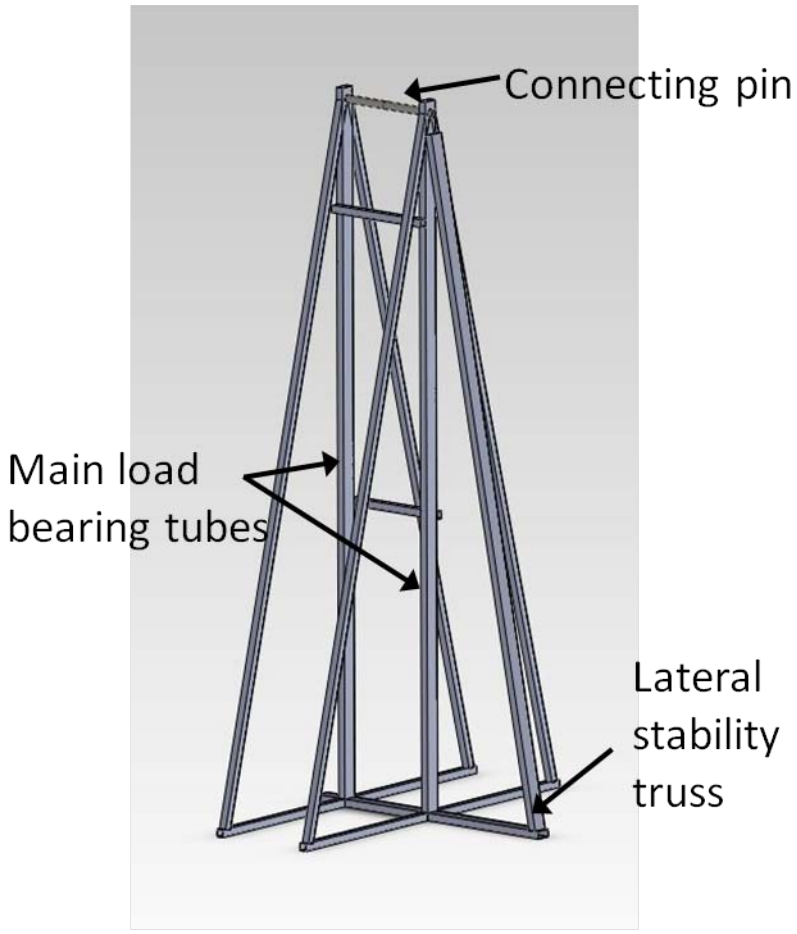

Figure 3.20: Solidworks model of the shock tube support stand.

4 EXPERIMENTAL WORK

The following chapter will cover the experimental portion of the Authors research. It is taken in part from a paper that has been submitted for review and is laid out into sections describing experimental facility capabilities, the experimental methods, the initial condition repeatability, and finally the experiments that have been completed using the facility. The experimental results will be divided into two major sections which examine the interface qualitatively and quantitatively. Experimental results will be expanded upon using a simulation run of the experimental conditions. Comparisons of the experimental and simulation results will provide some experimental verification of the results shown in the previous chapter.

4.1 Experimental Facility Capabilities and Features

The following section is a review of the material covered in chapter 3.0 as it pertains to the experiments reported on in this chapter. The Texas A&M University Fluids Mixing Shock Tube Facility (TAMUFMSTF) (fig. 4.1) was completed and began operation in May of 2012. The design of the shock tube began in the fall of 2009 and was performed by the author with the help of various undergraduate workers over the years (Peter Koppenberger, Sterling Debner, and Chris McDonald). Details of the shock tube design, instrumentation and experimental verification of its capabilities are presented in the appendices.

The TAMUFMSTF is a variable inclination, modular construction shock tube with an 11.5cm internal cross section. The internal length of the shock tube is approximately 8.7m, while the support structure is approximately 9.75m in length. The

tube can be pivoted about its base from horizontal (0°) to fully vertical (90°). It was designed to support incident shock strengths of up to Mach 3.0 into air at atmospheric conditions. The pivoting mass of the shock tube is approximately 20kN and it is bolted to an isolated concrete slab with a weight of about 45kN, which aids in resisting the vibrations induced by the shockwave and its reflections. The shock tube was constructed with a support beam and a modular reconfigurable design to allow for the greatest flexibility for future experiments. The major segments can be removed and reassembled on the beam to allow for upward or downward firing shocks (shocks from light to heavy or heavy to light gasses), or sections can be removed to shorten the tube for different experiments. The tube is moved into place by use of an overhead crane and is supported during operation by a ~6m tall steel tube stand bolted to the floor.

Figure 4.1: The Texas A&M Shock tube facility. Left: the shock tube inclined at 60 degrees, Top Right: the shock tube at approximately 30 degrees inclination, Bottom Right: Schematic of the shock tube with sections labeled. In the Picture: Mr. Chris McDonald and Mr. David Reilly (undergraduate students).

The shock tube was designed to perform up to 50 experiments per day. The ability to reach high Mach numbers while allowing optical diagnostics is a rare feature among RMI shock tube facilities. The ability to perform 50 experiments per day is even rarer. This ability is important because most RMI experiments performed to date lack statistical certainty due to low number of trials. By running up to 50 experiments a day the TAMU facility will be able to generate statistically converged data sets.

The TAMUFMSTF consists of three major sections; the driver, driven, and test section. The driver section is the high pressure chamber which is separated from the driven section by the diaphragm. This section is charged with the driver gas to a high pressure just short of the static rupture pressure of the diaphragm. A boost valve with a 15ms opening time is used to discharge high pressure (2000psi) into the driver section to rupture the diaphragm within 300ms. This releases the driver high pressure mass into the driven section to form the shock wave. The driver section is constructed of 1020 DOM tubing with a 6.25 inch inside diameter and 0.5" thick walls. The driver was designed to withstand pressures of over 2000psi.

The driver interfaces to the driven section through the hydraulic diaphragm loader. The hydraulic diaphragm loader was designed by the Sturtevant lab at Cal Tech in the 1980s. It was given to the Texas A&M advanced fluid mixing lab by the Wisconsin Shock Tube Lab. The diaphragm loader consists of a hydraulic ram designed to clamp a diaphragm in place and an "X" shaped knife edge (fig. 4.2) which cuts the diaphragm during its rupture. Hydraulic return rams were added to the design to speed up the diaphragm reload times. Most RMI shock tubes use a diaphragm loading technique which is time consuming, but the TAMU facility allows diaphragms to be changed in under 2 minutes which greatly the turnaround time for each experiment.

Figure 4.2: Image of the hydraulic diaphragm loader knife edge.

The driven section functions to allow the compression waves released from the driver time to coalesce into a well formed planar shock wave. This is necessary to ensure the acceleration of the interface is uniform and impulsive. The driven section is constructed of 3 extruded stainless steel tubes (two seven foot pieces and a two foot piece) with a 4.5 inch square cross section and 3/8 inch filleted corners. The walls are 0.75 inches thick. These pieces were also designed by the Sturtevant group at Cal Tech and were donated to the TAMU advanced fluid mixing lab by the Wisconsin shock tube lab.

The purpose of the test section is to create the interface and provide optical access from mixing measurements. The test section consists of three smaller sections (fig. 4.3); the interface creation section, the test section and the blank section. The test

sections were designed with a bolted construction of 2 inch thick heat treated 4140 steel to allow for large windows capable of surviving the stresses induced by the high strength shock waves. This bolted configuration also allows the test sections to be reconfigured for different measurement techniques which require different window orientations. The test section can use up to 6 overlapping windows, each with a 4.5”x6” viewable area, which provide a total viewing length of 1.5m and a maximum continuously visible length of 0.6m. The windows are the weakest part of the test section and were designed to withstand pressures of 12MPa, which is the anticipated reshock pressure for the high Mach number experiments.

The interface creation section and the test section were both designed with interface suction ports to facilitate interface creation in both sections. This allows for greater flexibility when reconfiguring the tube for reshock experiments. This also allows two interfaces to be created in the same experiment allowing for three fluid interfaces to be studied in the future. The ports were located for interface angles of 30, 45 and 60 degrees, but addition interface port selection permutations exist at higher and lower inclination angles as well. These ports allow for the heavy and light gases to be continuously vented from the interface to minimize diffusion.

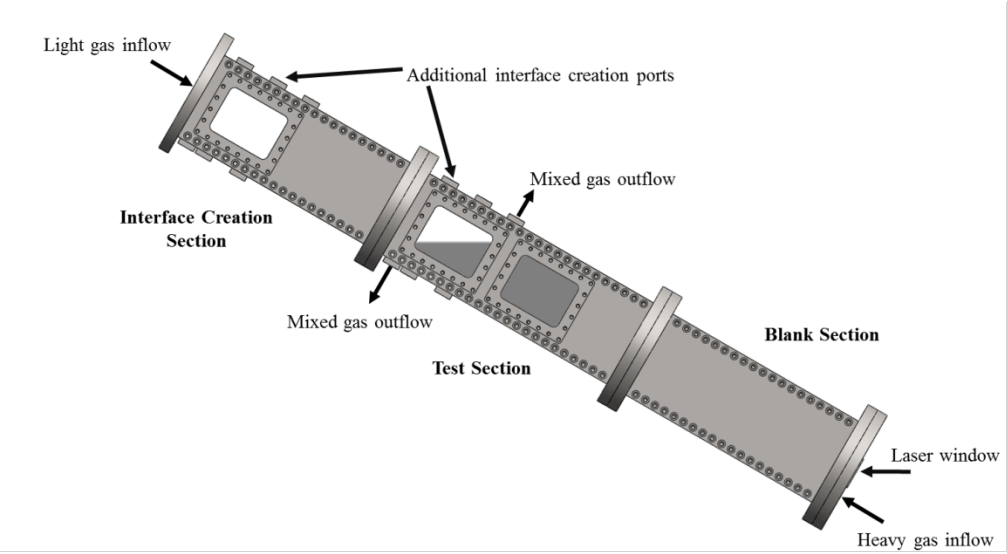

Figure 4.3: Test section design.

The shock tube is supported by wide flange I-beam (W12x40) to allow for sections to be removed from the tube while it is inclined and to carry a portion of the load generated by the shock reflection and diaphragm breaking. The I-beam also provides a mounting point for additional hardware like the driver return winch. The tube is connected to the ground through a pivot assembly. The pivot assembly is constructed of 20”x12” ASTM A500 rectangular tubes with a wall thickness of 0.5”. This assembly uses a 4.25” diameter DOM tube as the pivot, and is attached to a 4’ cubed cement shock isolation block using 24 M20 bolts which run the full depth of the isolation block.

The shock tube is controlled using a LABVIEW program running with a PXIe-6368 multifunction DAQ. The DAQ allows both analogue and digital input and output, and has a sampling rate of two million samples per channel per second. The card also has four 32 bit counter timers to allow for precise control of the valve and camera timing

up to a rate of 100MHz. The control system acquires static measurement data from 2 static pressure transducers in the driver and driven section, as well as a third static pressure transducer which monitors the boost tank pressure. The system is also capable of monitoring 4 thermocouples to obtain measurements of the initial conditions. The LABVIEW program can monitor up to 8 dynamic pressure transducers at a rate of 2MS/ch/s. Two dynamic pressure transducers are installed in the driven section to detect and record the speed of the incident shock. Additional dynamic pressure transducers will be added to the tube later to monitor the reshock pressure and the pressures in the test sections. Using the four counter timers on the DAQ card the shock tube control program precisely times the firing of the two PLIF and two PIV lasers with a resolution of 10ns. The program uses the analog signal from the driven section dynamic pressure transducers to detect the incident shock then delays a precise amount of time before triggering each of the laser pulses. Two external timing control modules can be used to time additional cameras, and to set the delay time between laser pulses for the PIV images.

The PIV laser system consists of two TSI Inc. Powerview 1.4 MP cameras that have a short frame straddling time designed for PIV imaging. The lenses are equipped with filters which block low wavelength frequencies from the PLIF system. These cameras can each take two pictures in rapid succession for PIV measurements. The camera shutters remain open during the experiment and only the CCD is activated when the lasers are fired then it turns off before the next camera's laser pulses are fired. The room is darkened so that there is very little ambient light available. This means the CCD

exposure will be limited to the length of time during which the laser is on, approximately 5ns. The timing of the two PIV images is controlled by the laser pulse timing. The CCD on each camera rapidly turns cycles between two sets of photoreceptors between images. A dual cavity Nano PIV Litron laser is used which can create the two laser pulses needed for PIV in rapid succession. It is a class IV laser with a maximum output of 800 mJ, a 4 ns pulse duration, and a wavelength of 1064/532 nm. The seed particles necessary for PIV imaging are created by a Peasoup fog machine, which creates 0.2-0.3 μm glycerin fog particles using a high pressure inert gas as a pump. The PIV laser system provides ample power at 532 nm as seen in the example image of a fogged interface shown in figure 4.4.

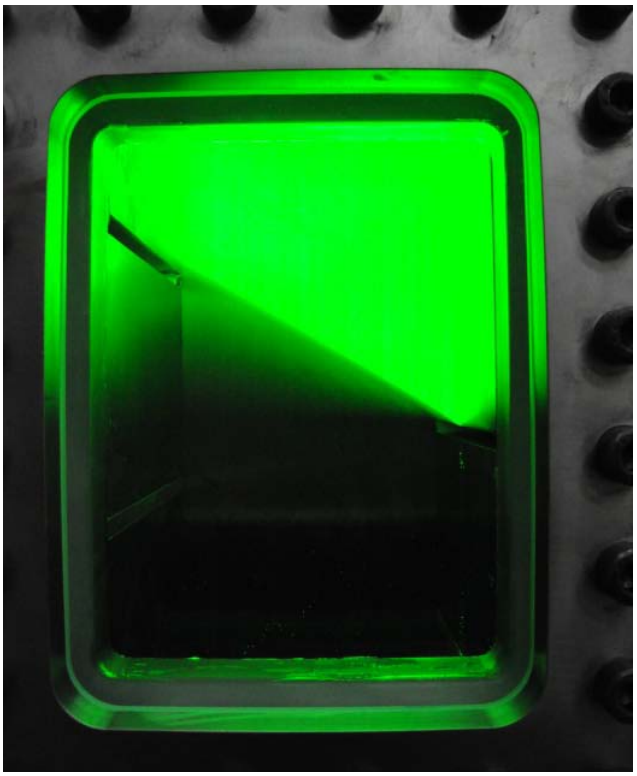

Figure 4.4: Mie scattering signal from a fogged interface using the PIV laser system.

The PLIF system used two TSI Inc. Powerview Plus 2 MP cameras. These cameras are equipped with notch filters that blocks the 532nm light from the PIV system. The lasers are illuminated by a dual cavity New Wave Research Gemini PIV laser capable of providing 200mJ per pulse at 532/nm or ~30mJ per pulse at 266nm. This system can simultaneously generate PIV and PLIF light frequencies (532 and 266nm respectively). The PLIF system can be supplemented by an older but higher power Quanta-Ray laser that can produce ~55mJ per pulse at 266nm. The PLIF system uses an acetone seeding system which seeds the light gas with acetone vapor. Acetone

vapor will absorb light frequencies near 266nm and fluoresce at a frequency near 330nm. While 330nm is ultraviolet light and cannot be seen by the human eye, the PLIF camera can pick up this wavelength. The fluoresced light contains some visible light and so it can be seen at very low intensities by the human eye as a purple glow. The PLIF signal from the acetone is a much weaker signal and requires camera lenses with large apertures (f/1.2). This signal decays rapidly with distance in to the acetone field as the laser power is absorbed by acetone molecules. Figure 4.5 shows a PLIF image of the shock wave passing through the interface at early times.

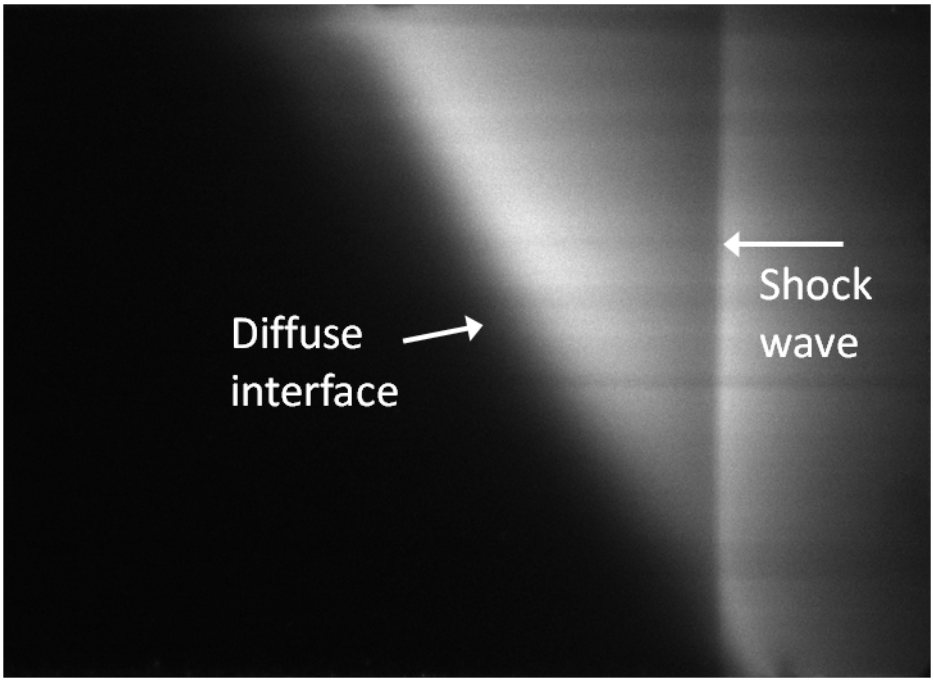

Figure 4.5: PLIF image of the shock wave passing through the interface. The shock wave can be seen as the discontinuity to the right of the interface.

A fast framing video camera can also be used to obtain Mie scattering images where the incident light is reflected off of seed particles. The video camera is capable of taking 7500 frames per second at 1MP or up to one million frames per second at a reduced resolution. To use this method the PIV system fog generator is run at a higher flow rate making a dense fog in the light gas. A continuous laser will then be used to illuminate the interface constantly for the video camera to obtain its images.

The cameras used for the PLIF and PIV systems are mounted on a rail and thread plate system attached to the shock tube (Fig. 4.6). This mounting system was built to reduce the camera positioning errors inherent in repositioning the cameras. It was desired that the camera mounting system travel with the inclination of the shock tube so the camera angle would always match the window inclination. This would also allow for the cameras to be position while the tube was down on the ground and then raised with the tube to its target inclination. Using lenses with 55mm focal lengths the cameras were required to be approximately 1m from the exterior surface of the target window. This distance would require the cameras to be mounted on a lm lever arm from the tube that could result in unacceptable vibration or variation in position. To get around this the camera were mounted at a 90° angle to the tube using a high quality aluminum mirror. These mirrors also allowed fine positioning adjustments to be made using positioning screws which adjusted the angle of the mirrors. The camera thread plate was mounted to rails which allowed the thread plate to be relocated to different windows. The position of the thread plate was set using a positioning arm which set the position of the plat base using the window flanges to within ±.050".

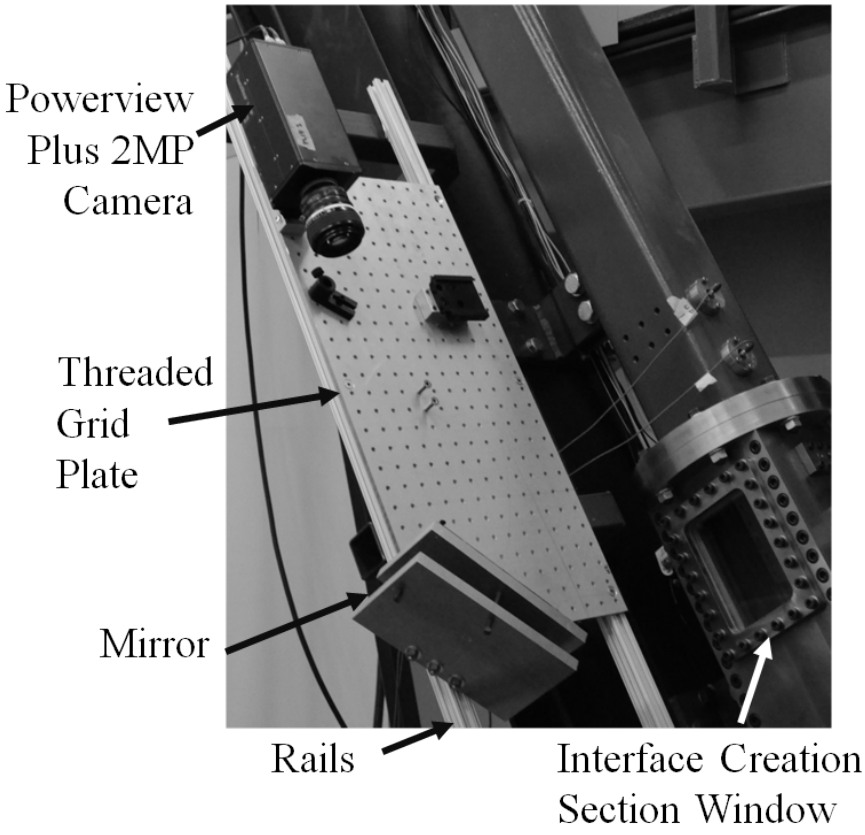

Figure 4.6: Camera mounting system.

The laser sheet for the PLIF and PIV systems was introduced to the tube via a small slit window in the lower boundary of the tube. This window was composed of fused silica to allow the passage of 266nm light. The lasers were mounted on the floor which required the usage of a mirror to reflect the beam into the tube at the inclination angle. The beam was focused using a spherical converging lens and a cylindrical diverging lens. Using various focal lengths these two lens could provide a beam that was fully diverged just as it entered the field of view for the target window and at minimum thickness.

4.2 Experimental Methods

The experiments in this work were run primarily with a N_2 over CO_2 interface (A~0.23) but some results will be shown for a He over CO_2 interface as well. The discussion and description of the procedures will assume the interface is N_2 over CO_2, but these procedures are similar to those used for the He over CO_2 interface. These gasses were selected for their moderate Atwood number (0.23), their availability from gas suppliers, and the fact that their refractive indexes were relatively similar (N_2~408kg/m^2-s, CO_2 ~480kg/m^2-s before shock, and N_2~1000kg/m^2-s, CO_2 ~1200kg/m^2-s after shock). An incident shock strength of Mach 1.55, and an inclination angle of 60° were used in all experiments reported in this dissertation. The inclination angle of the tube was set by using the overhead crane to raise the tube to the correct angle. The tube stand was then installed to hold the shock tube at the prescribed angle, and after releasing the shock tube from the crane the angle was again measured. A digital inclinometer with an accuracy of +/-0.05° was used to measure the angle and was calibrated before each use.

Before filling the tube the cameras and lasers are calibrated for imaging in the windows to be imaged. A calibration block is inserted into the tube at each image location which is used to focus the cameras and check their alignment. The focal lengths of the laser sheet lenses are changed for each window location to get the maximum laser power and the minimum sheet thickness. The laser alignment is then checked inside the tube using a calibration target. After calibration is performed for the cameras and lasers,

a series of images of the interface are then taken as the tube is filled with seeded gas to check the image quality and seed density.

The Mie scattering technique was used in this work to visualize the fluid interface in the tube and for acquiring PIV images sets as well. The light gas was seeded with fog particles using the fog equipment described in the previous section. This fog was mixed with the nitrogen in an external sealed container with a volume which was large (~8ft^3) relative to the volume of nitrogen contained in the shock tube. This box contained a stirring device to aid in mixing the fog and the nitrogen before it entered the tube. The fog density was controlled by using mass flow controllers to limit the flow rate of gas through the fog machine. The N_2 and CO_2 flow rates (~8L/min and ~3L/min, respectively) were measured and set to achieve an interface with minimum diffusion while not having any visible sheer. The tube was then allowed to fill for 20 to 30 minutes to achieve a uniform fog seeding in the nitrogen.

The incident Mach number target was Mach 1.5 but was limited by the diaphragm material and thickness availability. The diaphragm material chosen for these experiments, including the He interface, was a polycarbonate sheet with a thickness of 0.030 inches. This diaphragm had a dynamic rupture pressure of approximately 102psi which resulted in a Mach 1.55 incident shock wave into atmospheric pressure nitrogen. For each experiment, the driver section was pressurized to 70 psi initially to keep the diaphragm just short of a static failure. To fire the shock wave, a precise sequence of valve activation was executed using the LABVIEW program. The fill valves were first shut to allow the interface to settle and the initial shock tube pressure (approximately

0.3psig) to decrease. After 100ms, the boost valve is activated and interface suction valves are closed. The boost valve opens fully in under 30ms and the pressure rises to 102psi, rupturing the diaphragm, within 400ms of the valve activation. At 500ms after boost valve activation the valve is shut off, and is fully closed within 50ms.

The incident shock is formed in the driven section and its speed is then measured using two dynamic pressure transducers placed in the driven section just upstream of the interface creation section. The speed was found based on the time at which each transducer read the shock pressure rise and the distance between the two transducers. Pressure measurements from the dynamic pressure transducers are checked and compared for each experiment and show a steep pressure gradient with a rise time of less than 5μs. Images of the incident shock wave using the Mie scattering technique also show a well formed planar shock wave (Fig. 4.7) .The pressure rise recorded by the dynamic pressure transducers is also used to trigger counter timers in the LabVIEW hardware which are used to trigger the lasers and cameras at times when the interface will be visible to the cameras through their respective windows.

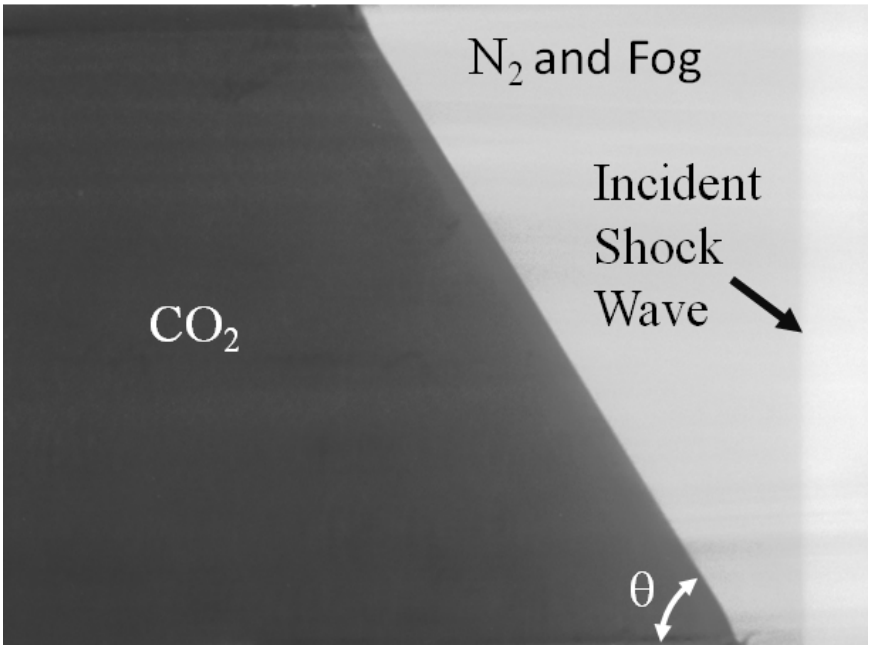

Figure 4.7: Mie scattering image of the shock wave and interface just before interaction.

After each experiment, the tube is vented to atmosphere and the diaphragm exchanged for a new one. The windows are inspected for fog condensation buildup and are cleaned. The lower laser window of the tube is also cleaned of any fog condensate. Data and images are processed before running the next shock wave to ensure that the tube is properly functioning.

4.3 Repeatability and Quantification of Initial Conditions

One of the advantages of the inclined interface shock tube facility, as discussed before, is that it produces highly repeatable initial conditions but, as with any experiment, it is subject to some variation in conditions from run to run. While initial condition variations have been discussed little in the past literature, they are important

for ensemble averaged data sets that we will use. The variations in initial conditions will be quantified to show the strengths of the inclined interface shock tube facility for obtaining statistically converged data sets. The departure of the interface from the ideal inclined interface RMI will also be discussed. To highlight the variations in initial conditions, eight Mie scattering images were obtained at a time of 10μs after shock interaction with the interface. These images were used to produce a coefficient of variation plot, figure 4.8. The coefficient of variation highlights areas where the standard deviation is high relative to the average. It can be seen in figure 4.8 that the highest coefficient of variation is due to the interface position which varies up to 1.4mm in these runs. The shock position variation can also be seen as an area of slightly elevated coefficient of variation which is in agreement with our dynamic pressure transducer data which shows a typical variation in shock speed of ±2m/s from ~540m/s to ~544m/s with a standard deviation of 2.3m/s over 100+ runs.

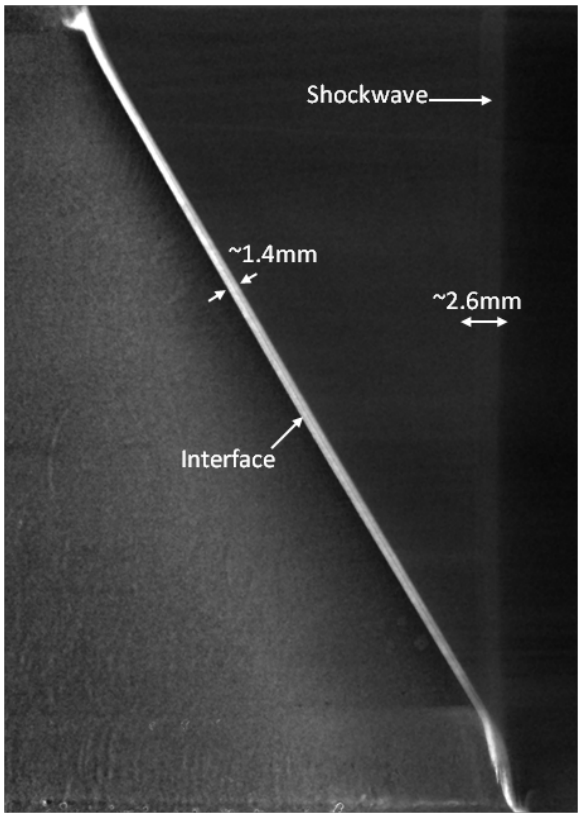

Figure 4.8: Coefficient of variation of Mie scattering image intensity from eight experimental runs at t=0.01ms after shock interaction.

One reason for the variation in interface position, shown by figure 4.9, is that the interface departs from the perfect 60° inclination during the time it takes for the driver diaphragm to rupture and the shock to reach the interface. This time can be limited to reduce the interface drift during this time, but some departure from the 60° angle is always present. To highlight this drift, a run with a high drift period was imaged just before the shock wave reached the interface. This image was processed to highlight its departure from the 60° inclination plane and is shown in figure 4.9. In figure 4.9c, areas of black (white) show where the interface rose above (below) the inclination plane. In

this worst case scenario, it can be seen that the interface can rise or fall ~1mm, while typical values are much lower. A small spike at the lower suction slot is also apparent and is created by an air hammer effect of the valve closing. A small amount of curvature is also created at the interface edges as the velocity vectors of the exiting gas align to the suction slots which are perpendicular to the tube walls. This effect can be minimized by decreasing the gas flow rates, but low flow rates also allow for longer residence times at the interface and a larger diffusion thickness. Figure 4.10 shows PIV vectors obtained at the interface before an experiment. These vectors show velocities of up to 1.7cm/s at the interface, and a low velocity back circulation at the edges of the interface. The effect of the interface velocities on the RMI are negligible since they are five orders of magnitude smaller than the post shock interface velocity (~240m/s). The departures from the perfect inclination plane can be minimized by controlling flow rates, minimizing drift time, and by improvements in the suction slot design which will be implemented in future runs.

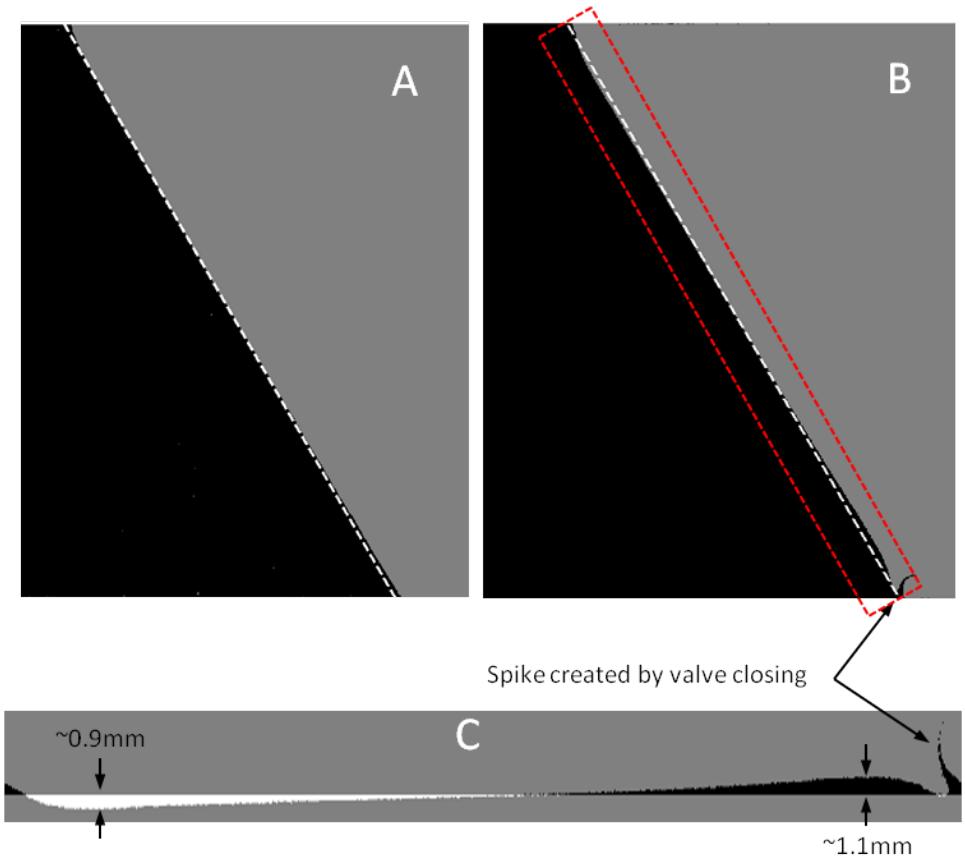

Figure 4.9: Deviations in the experimental interface from the ideal planar case. (A) the interface position with the suction valves open, (B) the interface position with the suction valves closed after being allowed the maximum drift time before shock interaction, (C) a close up of the interface highlighting its departure from a 60° plane.

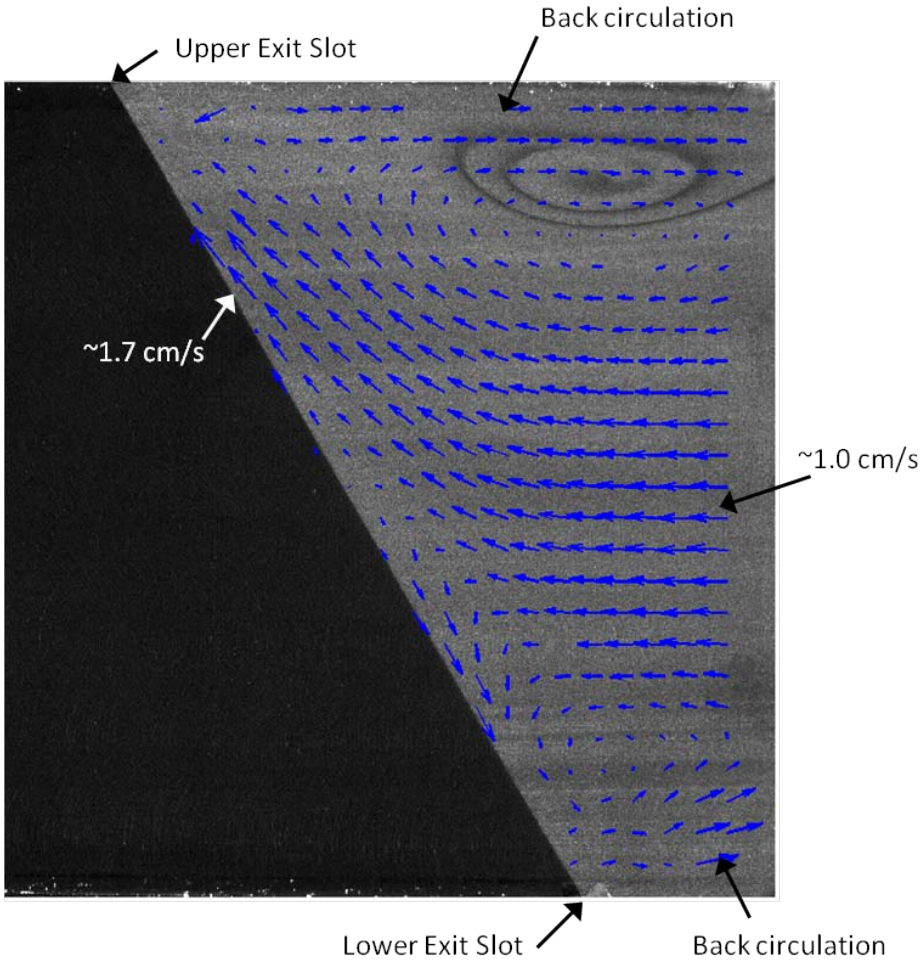

Figure 4.10: Velocity vectors at the interface before shock interaction obtained using PIV.

The interface diffusion thickness was quantified using Mie scattering images taken just before the shock interaction. A line of pixel intensities normal to the interface and extending approximately 25mm to either side was taken to measure the diffusion thickness. To smooth the random fluctuations in the data, the data was average with 30 lines to each side. The pixel intensities showed a linear trend coupled with an error function trend at the interface. The linear trend is created by the accumulation of light scattered by adjacent fog particles. When the linear trend was removed from the data, the error function could then be fitted and used to determine the 1-99% concentrations of fogged nitrogen. This showed a diffusion thickness of approximately 1.2mm (Fig. 4.11). As mentioned above, this diffusion thickness can be decreased by increasing the gas flow rates, but if the velocities are too high they may have an effect on the resulting RMI formation.

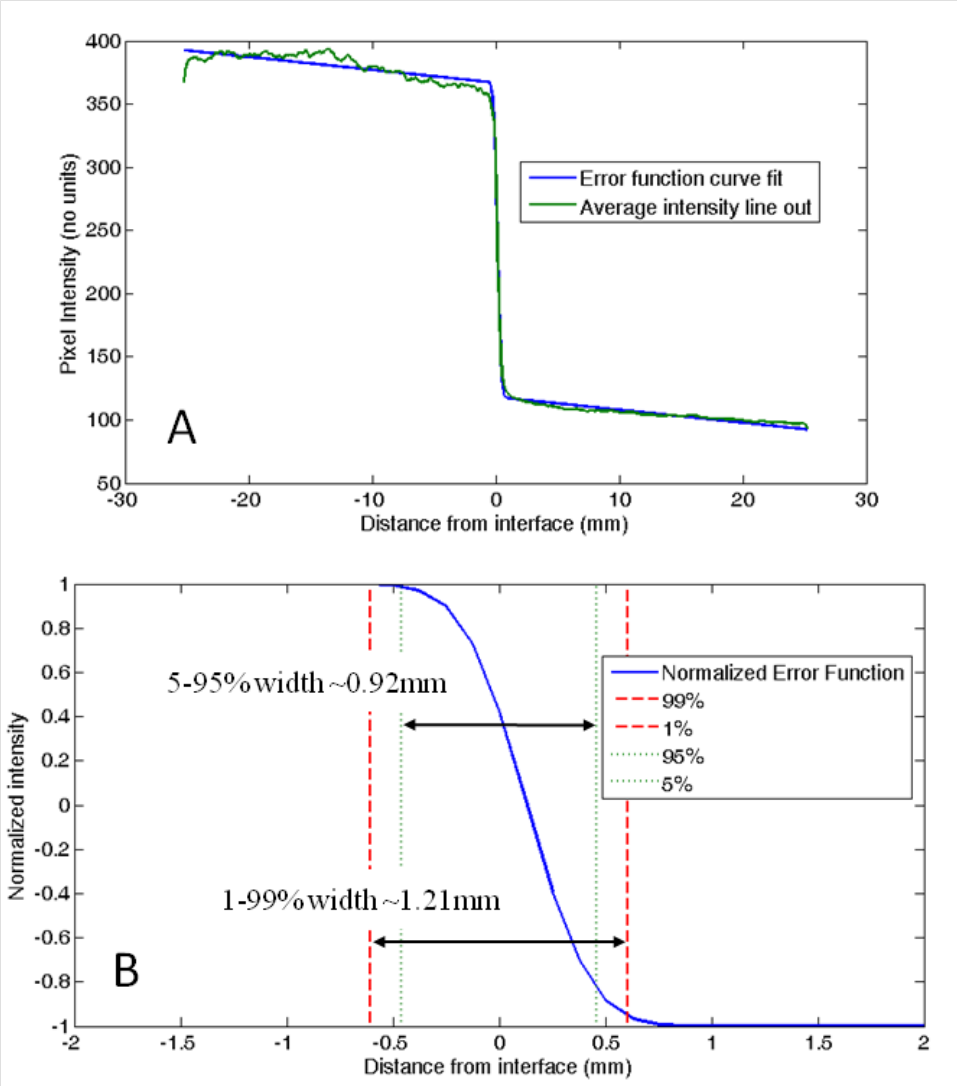

Figure 4.11: Interface diffusion width measurements. (A) Pixel intensities plotted from an average of 61 lines of data across the interface showing a linearly increasing error function fitted to the data. (B) The error function fitted to the data showing the 1-99% concentration of fogged nitrogen.

4.4 Qualitative Examination of the Interface Evolution

Having examined the initial conditions for the inclined interface RMI and the repeatability of these conditions, the interface evolution will now be examined in a qualitative manner. Figure 4.12 shows a time series of images obtained using the Mie scattering technique. These images were processed to normalize the images intensities and to remove background noise. The times measured are from the moment the shock wave first intersects the interface. At time 0.01ms, the shock wave is apparent as a jump in the fog Mie scattering intensity. At the next time (t=0.36ms), the interface is still entirely in the visible portion of the first window. A bright spot of fog at the lower wall suction slot is also visible. This bright spot is created by the shock interaction with the suction slot which re-suspends condensed fog fluid (glycerin) which had collected in the slot. This spot does not enter the field of view again until reshock occurs, but is a deleterious effect which will be mitigated later by improved suction slot design. Also at this time, two inflections in the interface curvature can be seen developing. Later, at time 1.19ms, these inflections have increased in number and amplitude as the vorticity imparted by the RMI is beginning to shape the interface. A small spike preceding what will become the main vortex is also evident at this time but dies out later as it merges with the boundary layer.

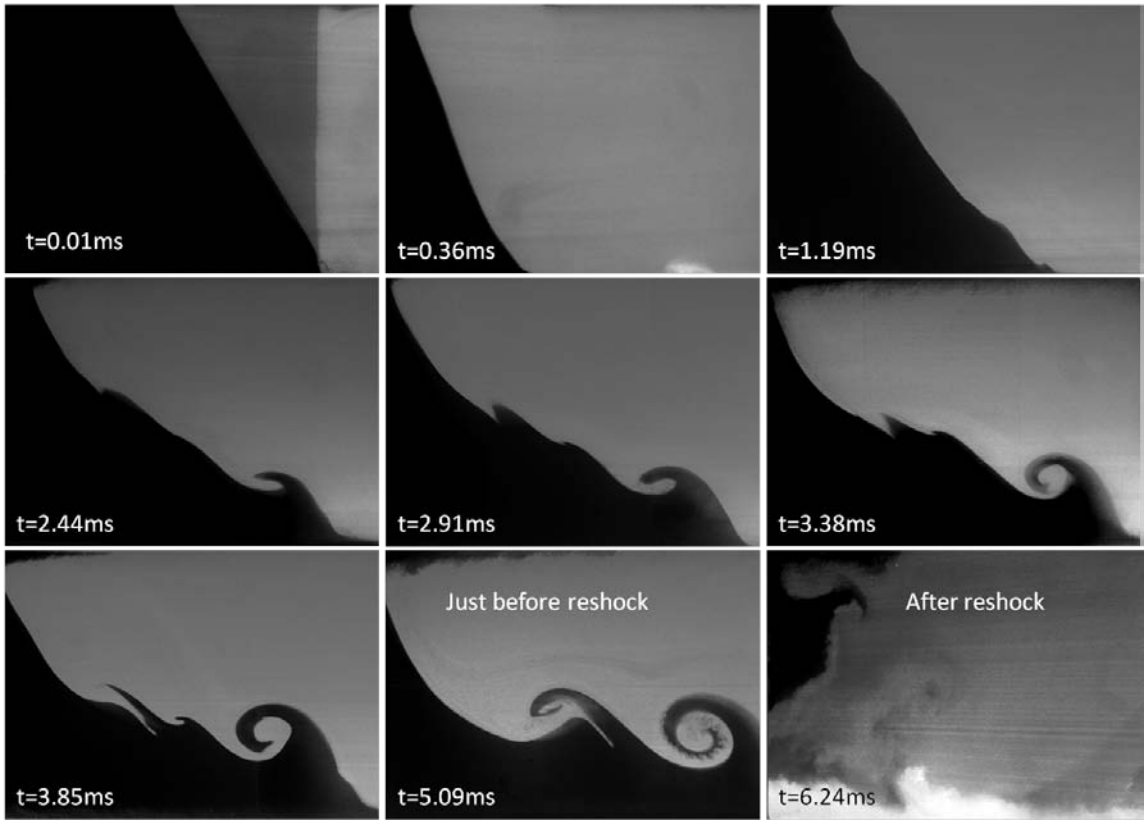

Figure 4.12: Time series of Mie scattering images of the inclined interface RMI before reshock.

At time 2.44ms, the primary vortex is now prominent and two small vortices (the secondary and tertiary vortices) can also be seen developing from the inflections seen at earlier times. At times 2.91 and 3.38ms, the secondary and tertiary vortices can be seen developing and merging. By time 3.85ms, these vortices are on top of each other and by time 5.09ms they have fully merged. At time 3.38ms, the upper boundary layer has become fully visible. This feature is always present in the flow but its visibility varies in the images due to the fog concentrations and image normalization procedures used. At time 3.85ms, another inflection is visible at the tip of the spike. This feature may be a

"forking" of the spike as seen in other simulations [57] coupled with a growing boundary layer but this feature has little time to evolve before reshock occurs at approximately 5.64ms. At time 5.09ms, many smaller Kelvin-Helmholtz vortices can be seen developing on the primary vortex. These features are induced by the strong shear which exists in this feature between the CO_2 and N_2. Figure 4.13 shows a close up of the features. These features have not been resolved in simulations of the inclined interface as of yet.

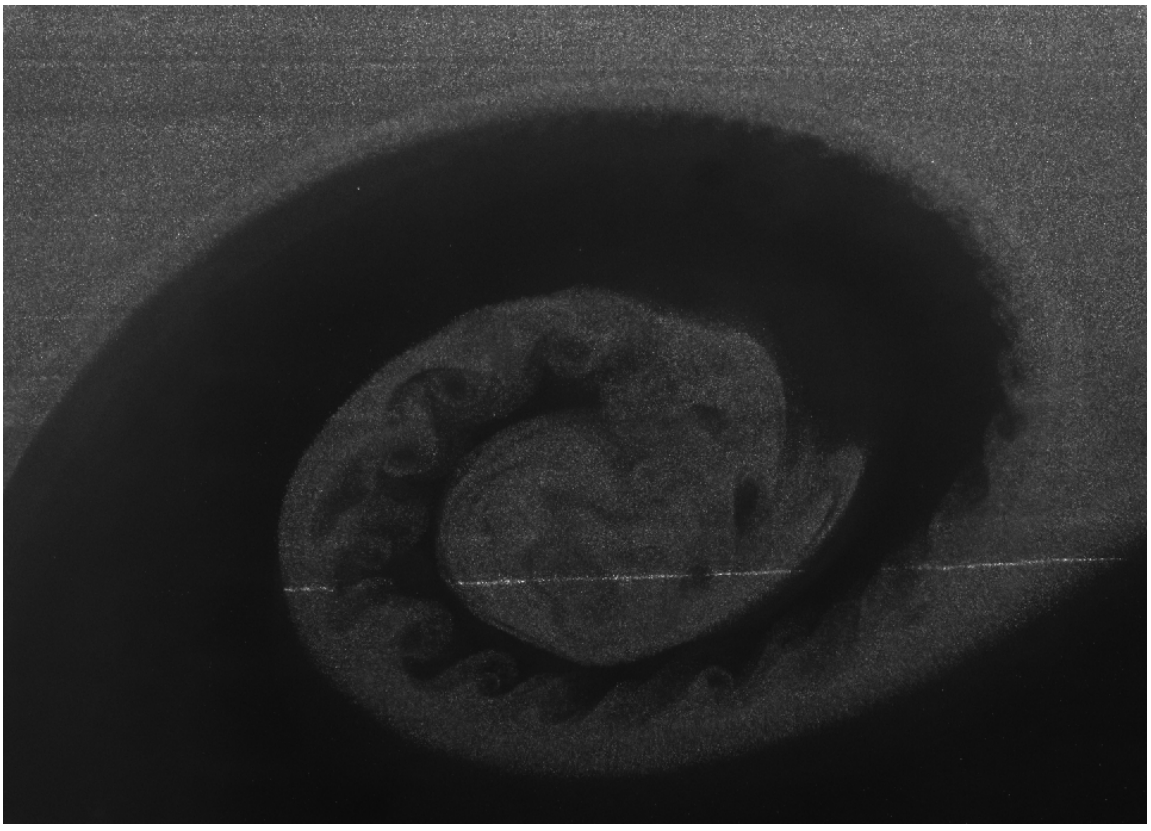

Figure 4.13: Close up Mie scattering image of the primary vortex with secondary KH vortices at t=5.09ms after shock interaction.

The final image in figure 4.12 (t=6.24ms) shows the interface approximately 0.6ms after the incident shock wave has reflected from the bottom of the tube and reintersected the interface, this time moving from the heavy gas to the light gas. The process of reshock inverts the interface where now the former spike region containing the vortices has been pushed to an area just out of the frame of view while the bubble region has been inverted and now resembles a spike structure.

The process of reshock on the interface greatly increases its mixing and accelerates its decay into a turbulent state. It is common in many application of the RMI for 2 or more shocks to intersect the interface. These problems present a much more complex flow field which provides a greater challenge for computation codes. The decay of the ordered flow into turbulence is also of great interest as it is still unknown how long the interface maintains memory of its initial conditions. For these reason the N_2 over CO_2 interface experiments were extended to late times after reshock. One key feature of the reshock process which is helpful to an experimentalist is that is brings the bulk velocity of the interface to zero. That is the interface will continue mixing and contain large fluctuations in velocity but the average speed will be zero. This allows the interface to be imaged at many times from the view field of one window. For these experiments the reshock wave speed was found to be ~224 m/s in the lab frame of reference with a standard deviation of 2.8 m/s over 100+ experiments. The reshock velocity is directed against the shocked gas flowing down the tube, which has a speed of ~240 m/s. This gives the reshock wave a relative velocity of ~464 m/s.

The effects of reshock can be seen in the figure 4.14 which shows a time series of Mie scattering images for the reshocked interface. At 5.64ms the reshock wave can be seen travelling back up the tube towards the driver. The previously well organized spike structure seen at 5.09ms is now being compressed and sheared by a velocity gradient which now has the gas in the upper portion of the tube (previously considered the bubble structure) traveling upstream while the fluid near the lower wall continues to travel downstream. A post reshock spike structure can be seen already beginning to develop at this time in the upper region of the interface. As time progresses the pre-reshock coherent spike structure breaks down into smaller structures do to vortex stretching created by the numerous secondary RMI structures which develop. At 7.04 ms it leaves the field of view having moved downstream towards the bottom of the tube. At many times before this time the structure is difficult to see because it has broken down and mixed with fogged fluid leaving it obscured by the boundary layer cloud which developed from the bottom wall.

This boundary layer cloud is believed to be a deleterious effect of foreign particulates and fog fluid which has been deposited on the lower wall, stirred up by the boundary layer, and then traveled with interface downstream propagating out from the wall with time. Following this hypothesis the most stringent cleaning standards were applied, yet the boundary layer cloud remains.

At later times the post reshock spike structure is seen to grow into a well organized structure. The boundaries of this structure have a much lower contrast than the pre-reshock structures. This is because the spike is surrounded by smaller structures

which are still working to mix the two fluids. A strong vortex can be seen within the fogged nitrogen area in images where the fog seeding was more heterogeneous like the image at 6.84ms. This vortex is coupled to the shearing of the pre and post reshock spikes. This structure was not found in simulations and may be a feature unique to a 3D flow field.

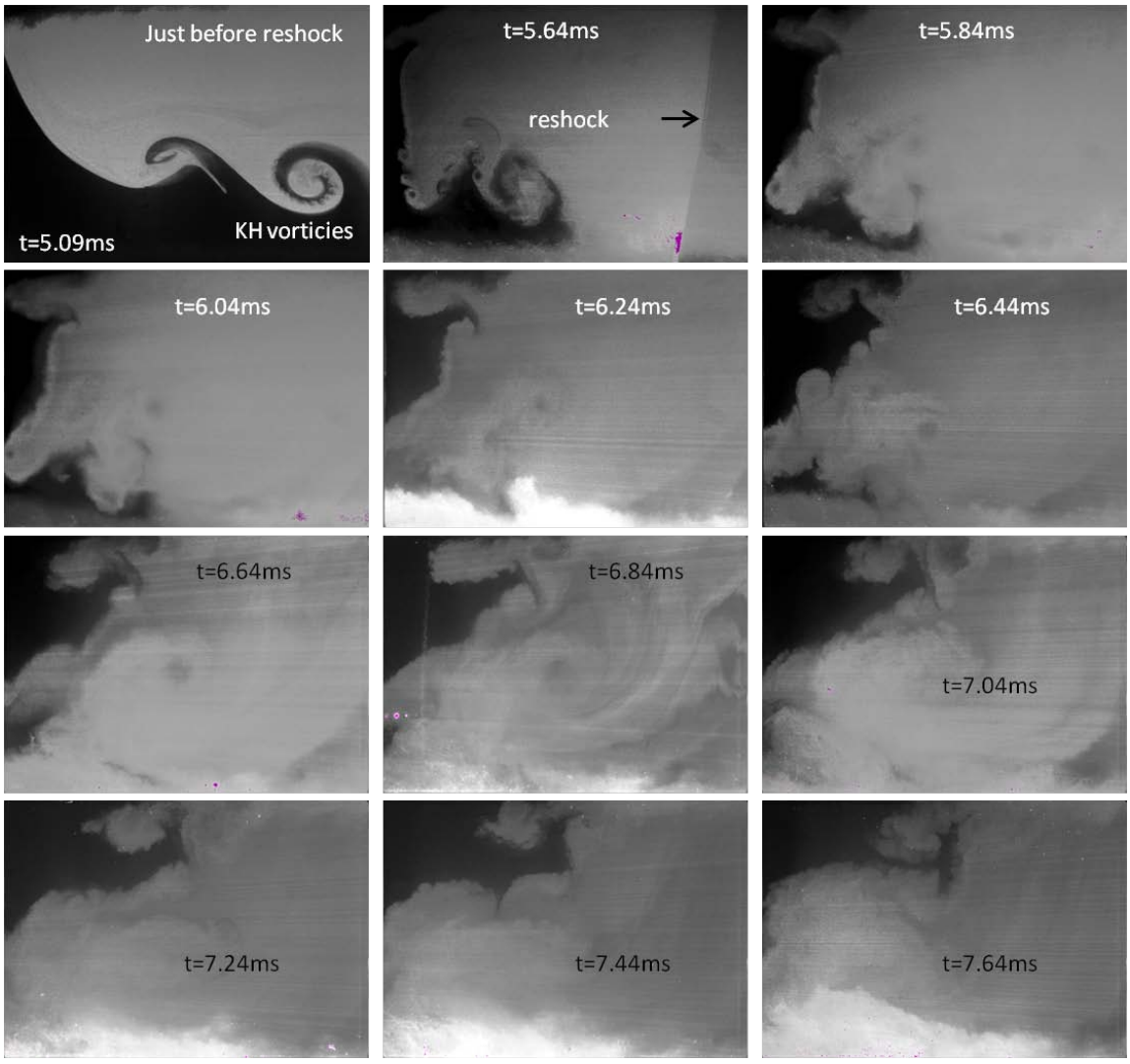

Figure 4.14: Time series of Mie scattering images of the inclined interface RMI after reshock.

A simulation study was performed to provide additional insight into the experimental results and to provide a means for comparison of the computation work in the previous chapter to the experimental work of this chapter. The simulation of the experiments was performed using the ARES code, described in section 2.1. The ARES simulation was run with initial conditions similar those of the inclined interface study (Fig. 2.4). The viscosity, species diffusion, and enthalpy diffusion models were used, and an initial diffusion thickness of 1mm was used based on the experimental interface thickness found in section 4.3A. The effects of the suction slots were not modeled. Figure 4.15 shows a time series of images from the ARES simulation where the images are framed to match the position of the windows in the shock tube. That is, a simulation image at one time is centered to match the experimental image position at that same time. These images plot a fog simulation variable which approximates the fog density based on species concentration and pressure. It is immediately clear from this figure that the simulation resolved the large structures well, including predicting the formation of multiple secondary vortices, but upon closer inspection key differences are found. Most notable of these differences is that the interface is longer and moving faster in the simulation. Also, the vortex merging that takes place in the experiments is not apparent in the simulation images.

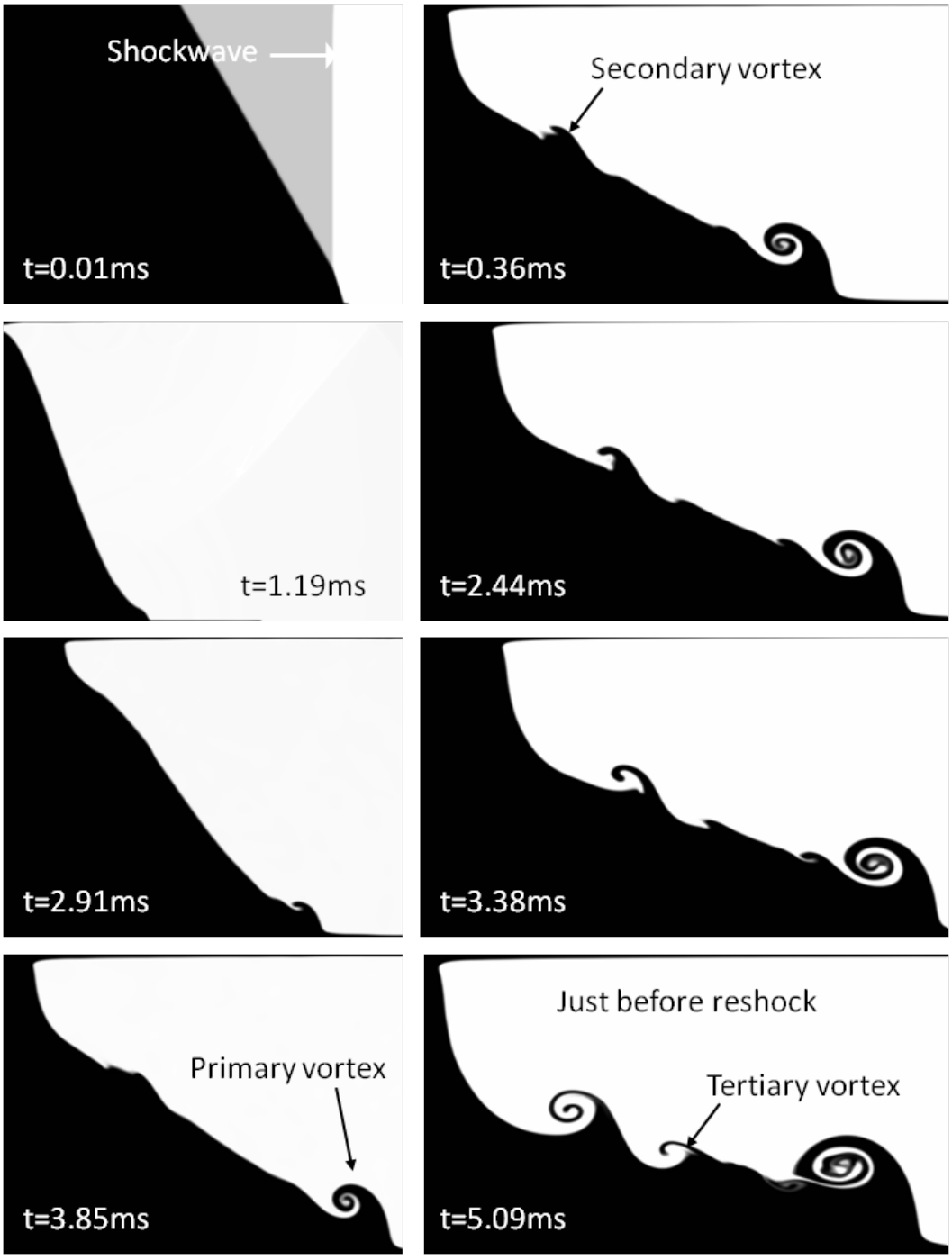

Figure 4.15: Time series of simulation images before reshock. These images plot a fog simulation variable which is dependent on species concentration and pressure.

`Figure 4.16 shows a side by side comparison of experimental and simulation images at three times. At 0.36ms the simulation interface position is already ahead (downstream) of the experiments. This comparison also shows that the vortices develop differently in the simulation. At 2.91 ms the wisps of CO_2 remain well defined as they are entrained in the vortices. The experiments show a much more blunt edge to the CO_2 which is being pulled into the primary vortex. The image resolution would be sufficient to show the type of structure shown in the simulation primary vortex, but this feature is absent. This is likely an effect of diffusion damping in the experiments that was not correctly modeled in the simulation. At this time the development of secondary RMI vortices is apparent in both the experiments and simulation, but the simulation is showing an additional inflection point which develops in to a small fourth vortex structure at 5.09ms.

At 5.09 ms the failure of the secondary and tertiary vortices to merge is apparent. The number of vortices developed and their trajectories is believed to be more dependent on the initial conditions. As seen before the experimental interface is not an ideal plane but has some perturbation near the walls as the flow attempts to turn parallel to the suction slot sides. These initial inflections in the interface could be responsible for the differences in the vortices development in the simulations. The differences in the interface velocity and growth rate could partially attributed to the effects of the suction slots. It is believed that these slots could diminish the energy that is imparted to the interface by the incident shock by allowing the edges of the incident shock to escape into the slots rather than transmit through the interface.

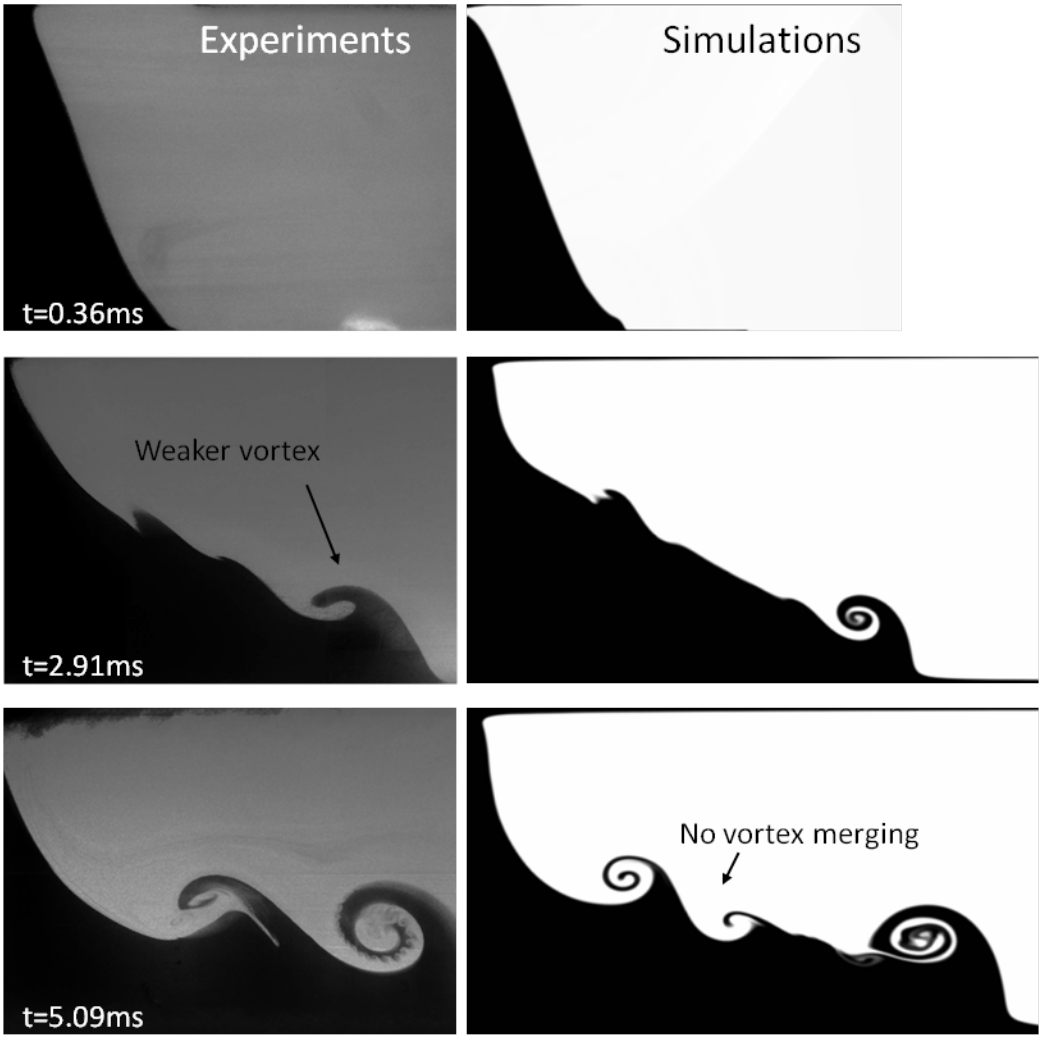

Figure 4.16: Comparison of experiments and simulation at 3 times. Mie scattering images are shown for the experiments (left), and simulated fog concentrations are shown for the simulation images (right).

Figure 4.17 shows a comparison of images from the experiment and simulation at times after reshock. The experimental images show one well defined spike structure that forms from the inversion of the interface after reshock. The simulation shows many more structures being formed with well defined vortex cores. The spike feature found in the

experiments is represented in the simulation and can be seen at late times (t=7.64ms) as a broader region of CO_2 projection out into the N_2. Here the limits of 2D simulations are apparent as the well organized structures seen in the simulation are not found in the experiments. This is likely an effect of the inability of the vorticity to extend into a third dimension. This explains the well formed vortex cores seen in the simulation vorticity plots.

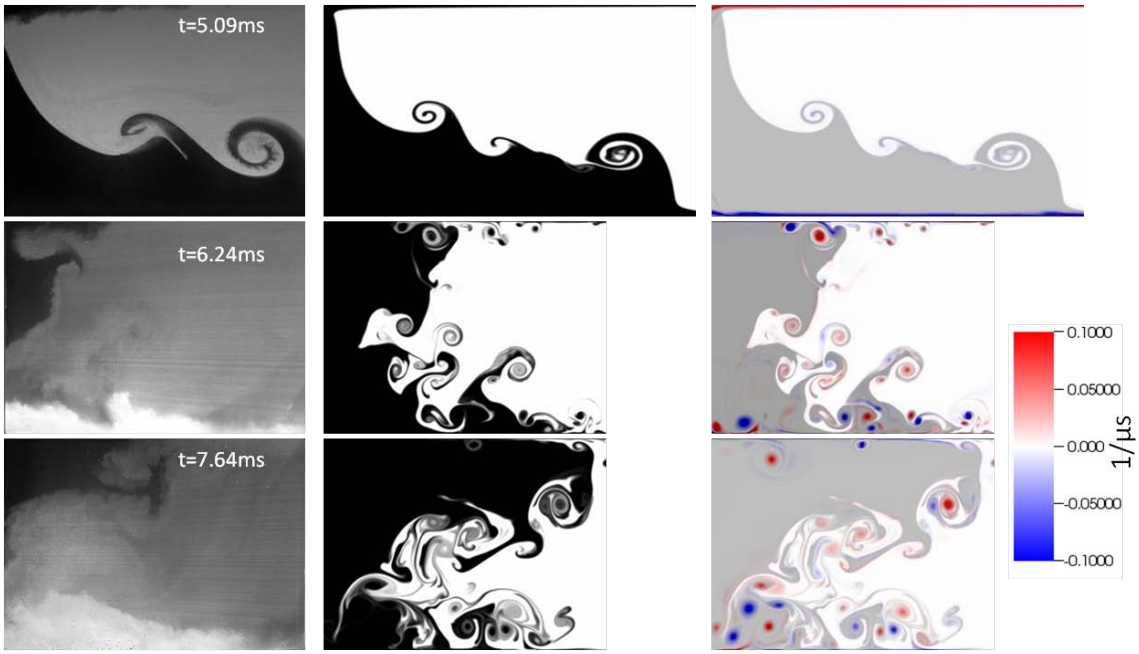

Figure 4.17: Comparison of reshock experiments and simulation at 3 times. Mie scattering images are shown for the experiments (left), simulated fog concentrations (middle), and vorticity plots with species concentrations shown in grey (right) are shown for the simulation images.

4.6 Quantitative Results and Comparison to Simulations

Having examined and compared the experimental and simulation data using qualitative measures, some quantitative measures will now be explored. The first of these measures will be the interface mixing width measurements. The interface mixing width is an integral measurement which has a lower sensitivity to the differences in initial conditions between the simulation and experiments. To measure the mixing width it will be defined by the 5-95% contours of the fogged nitrogen. This is the method used in the previous work by the author [115] presented in section 2.3. The scaling method presented in this section will also be used to scale the experimental data and compare it with simulation data. The 5% and 95% contours were found using the Mie scattering images shown in figure 4.12. These images were processed further to identify the interface gradient and divide the image into a binary field showing each pixel as N_2 or CO_2. The average intensity along the y direction was taken for each x location to determine when the flow field contained 5% and 95% CO_2. A sample image showing the 5% and 95% contours found using the method just described is shown in figure 4.18.

Figure 4.18: Sample Mie scattering image processed to find the 5% and 95% contours shown by the blue lines at 3.38ms.

To enable comparisons to the previous simulations performed by the author and to future experiments at different Atwood numbers, Mach numbers and inclination angles, the mixing width and time were non-dimensionalized using the scaling method developed in the author's previous work (section 2.3.3, eqns. 33-37). A brief recap of the method is presented below. The non-dimensional time is offset by the time at which the initial compression of the interface by the incident shock wave and its transmitted boundary reflection is complete. The time and mixing width were nondimensionalized using the transmitted wave speed and the effective wave length. This is the wavelength that would be required for each inclination angle if the amplitudes were held constant. The required wave speeds were predicted using 1D gas dynamics.

Figure 4.19 shows the nondimensional experimental mixing widths plotted with data from the simulation of the experiment and data from the parametric study presented in section 2.3. Error bars are plotted using the error estimated from image processing and from run-to-run variations. The image processing error is an estimation of the error in identifying the interface based on variations in image processing which occur due to the requirement for human input, and is near 1% for all data points. The run to run variation error was estimated using data from three runs at various times and was estimated to increase linearly from ~3.5% at t=1.19ms to ~5% at t=5.45ms. For the mixing width measurement taken at 5.45ms, the interface mixing width exceeded the visible field of the window and so measurements were estimated using images from just before and after 5.45ms where the downstream and upstream limits of the mixing width were visible. These measurements were combined using the position of the primary vortex as a reference. The error of this process was also estimated and contributed to the much larger error in this measurement.

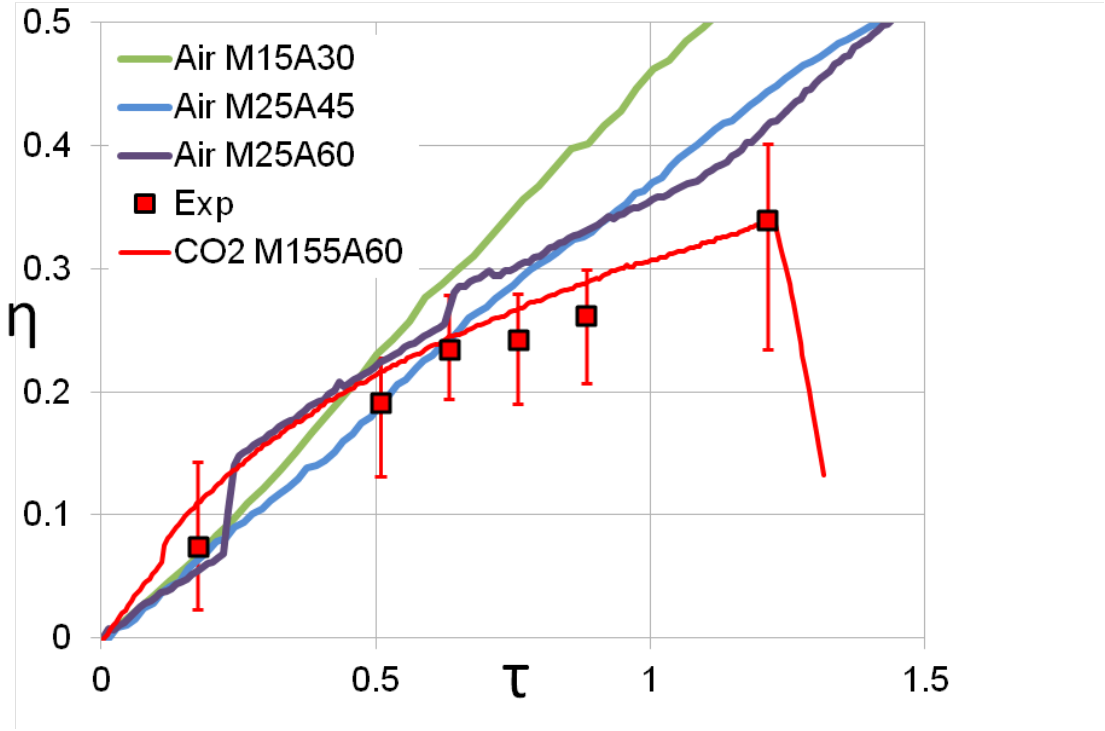

Figure 4.19: Non-dimensional mixing width data for the experiment and simulations. The experimental data contains error bars which estimate the error for run to run variations and for image processing error.

The measurements shown here exhibit a linear trend at early times and an asymptotic trend at late times as exhibited by the computational parametric study data. The simulation data for the experimental case is shown by the redline and agrees well with the experiment data. The early time linear trend can also be seen to share a common slope with the data presented from the computational parametric study. This suggests that a common nondimensional mixing width growth rate exists for cases with different Mach numbers, inclination angles, and Atwood numbers. A theoretical model for this common growth rate will be sought in future works beyond this dissertation. The

agreement between the experiment and its simulation shows that the mixing width is insensitive to the small variations in the initial conditions and boundary conditions between the two. The late time asymptotic behavior of the experimental data is a feature that is seen for the computational parametric study data sets at later nondimensional times (Fig. 4.20). The departure of the growth rate from the initial common linear trend seems to be dependent on the energy imparted on the interface by the incident shock wave. This asymptotic behavior has been reported in published works as the RMI enters a new growth regime but has not been examine for the case of an initially non-linear interface as used here.

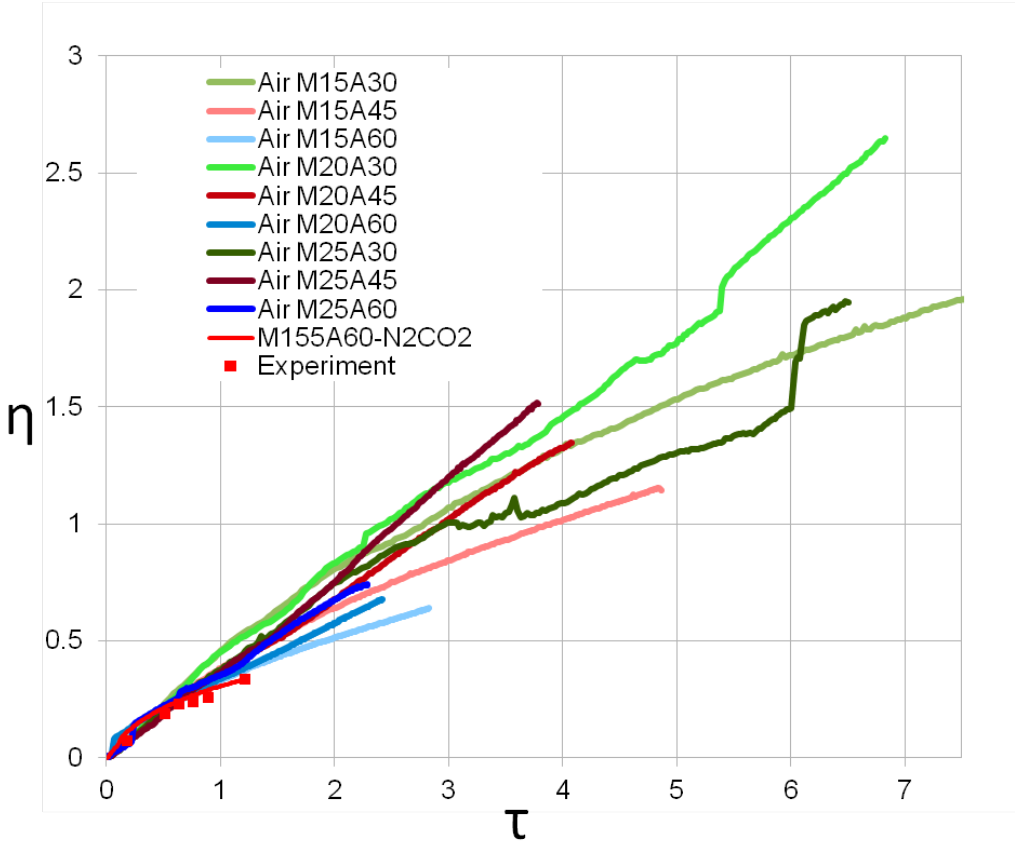

Figure 4.20: Non-dimensional mixing width data for the experiment and simulations to late times were the asymptotic behavior of the growth rate is visible.

Additional quantitative data was obtained from the experiments in the form of 2D velocity vectors made using the particle imaging velocimetry technique. The PIV cameras and equipment are described in section 4.1. Fog droplets were used as the PIV particles and a time of 2μs between PIV images was applied to obtain velocity vectors in the flow field which was traveling at a bulk velocity predicted by 1D gas dynamics to be ~240m/s. The vectors were calculated using the TSI software Insight3G with a recursive Nyquist grid, Fast Fourier Transform (FFT) correlation and Gaussian mask. The vectors

obtained had a relatively high confidence level with a signal to noise pass ratio of 2.0. The bulk velocity was subtracted from the vectors to show the relative motion of the flow field. Figure 4.21 shows these vectors plotted at 5.09ms after shock interaction. The vectors are plotted on top of a processed PIV image where only 1 out of every 9 of the approximately 12,000 vectors obtained are plotted. Figure 4.22 shows vectors obtained for the primary vortex using a reduced field of view to achieve a higher resolution.

The short time interval between images was needed to account for the high velocity in the x direction (direction of travel of the incident shock) but left the y direction velocity vectors susceptible to noise. This can be mitigated somewhat in the future by using a feature in the PIV software which searches for correlations at a distance based on the bulk velocity. This would allow a larger time interval to be used at the expense of obtaining vectors near the upstream and downstream edges of the field of view.

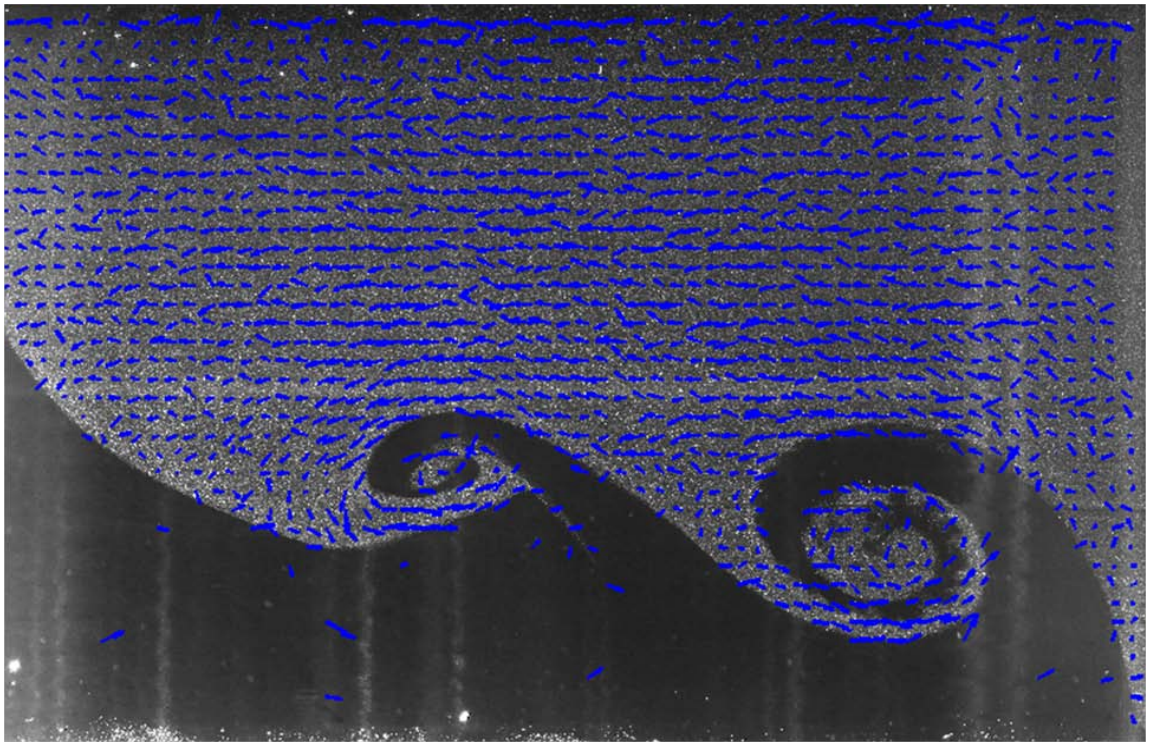

Figure 4.21: Velocity vectors obtained from PIV with the bulk fluid velocity removed of ran image resolution of 96μm/pix. These vectors are plotted on top of one of the PIV image frames.

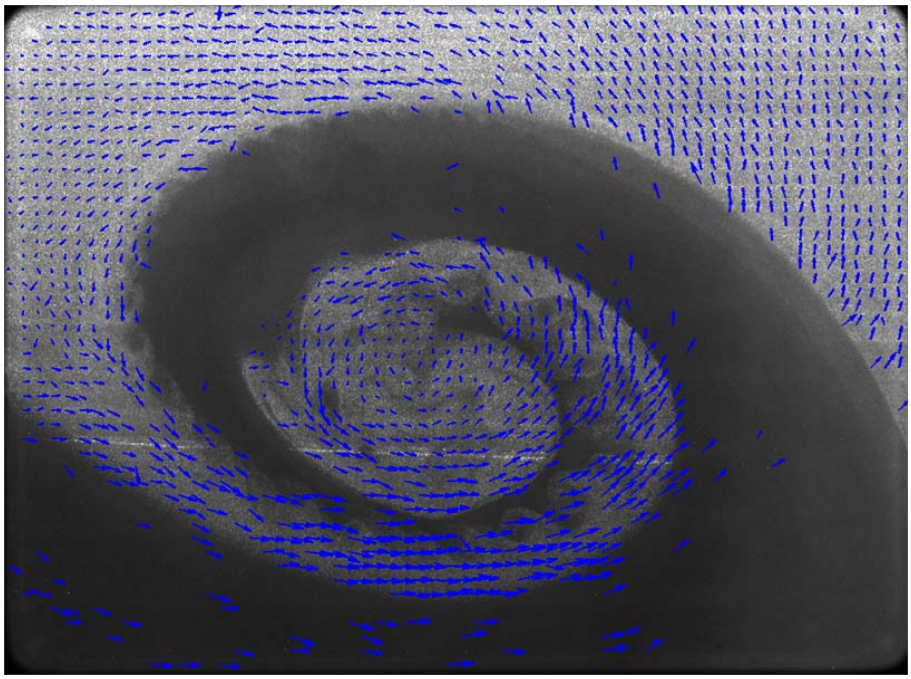

Figure 4.22: High resolution (39μm/pix) velocity vectors obtained from PIV with the bulk fluid velocity removed for the primary voprtex. These vectors are plotted on top of one of the PIV image frames.

The vorticity was plotted by taking the curl of the 2D velocity field. Obtaining numerical derivatives was complicated due to the somewhat noisy vector field. Missing values were first interpolated where nearby points were available. To obtain more accurate numerical derivatives, the vector field was then smoothed using a median filter with a 19 by 19 bin size. The derivatives were then found using central difference method, and combined to find the vorticity field. The vorticity field was again smoothed using a 3 by 3 median filter for the purpose of plotting only. Figure 4.23 shows the vorticity field found in the simulation compared to the experiment. The experiment shows a well organized vortex core in the primary vortex, and a strong linear region of vorticity where the secondary and tertiary vortices are merging. The simulation vorticity

plot shows two well organized cores in the secondary and tertiary vortices with no merging. The simulation image shows the full extents of the shock tube including the boundary layer which show up as strong vorticity layer due to their high shear. The experimental image is cropped to remove some of the boundary layers from the field of view. Despite this, the top boundary layer can be seen encroaching on the core of the flow but the lower boundary layer remains unseen since there is a lower seeding level is CO_2.

Figure 4.24 shows a comparison of the vorticity in the simulation and a close up high resolution data set from the experiment. The experiment shows a well defined vortex core with some regionally high pockets of negative vorticity along the interface possibly due to the KH structures being picked up. Localized spots of positive vorticity were picked up by the occasional vectors found in the CO_2, which was unseeded in this experiment, but these are likely numerical artifacts of the relatively few points available for numerical differentiation. The simulation vorticity is less interesting as the KH features were not resolved in the simulation. A fourth minor vortex is visible as a region of strong vorticity just to the left of the primary vortex. It is also notable that the frame dimensions are the same in both the simulation and experiment images, and so it would appear that the primary vortex is more compressed in the y direction in the simulation than it is in the experiments. This is possibly an effect of the spike growth rate difference between the simulation and experiment.

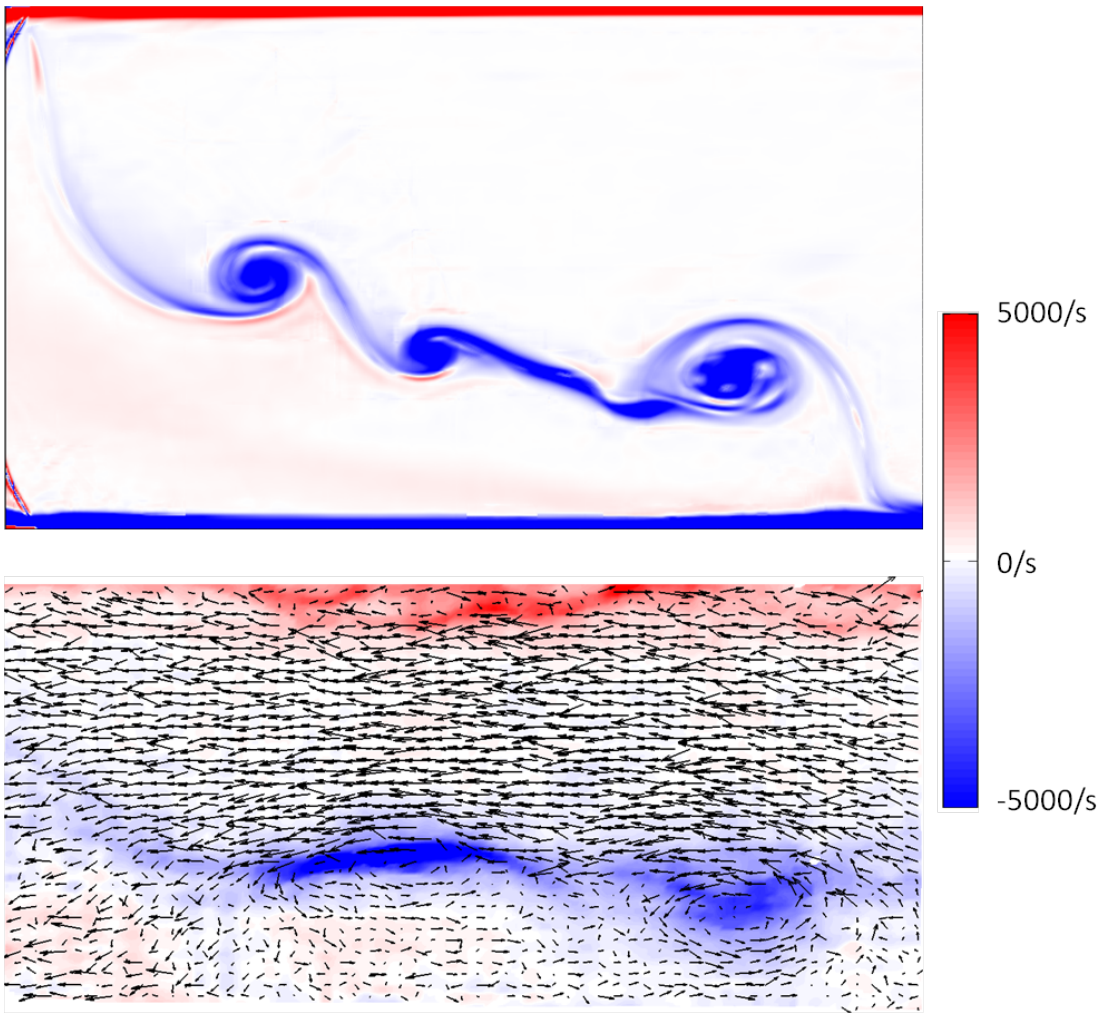

Figure 4.23: Comparison of vorticity field found from the simulation (top) and experiments (bottom). A sample of the PIV vectors used to calculate the vorticity field is shown in the experimental image.

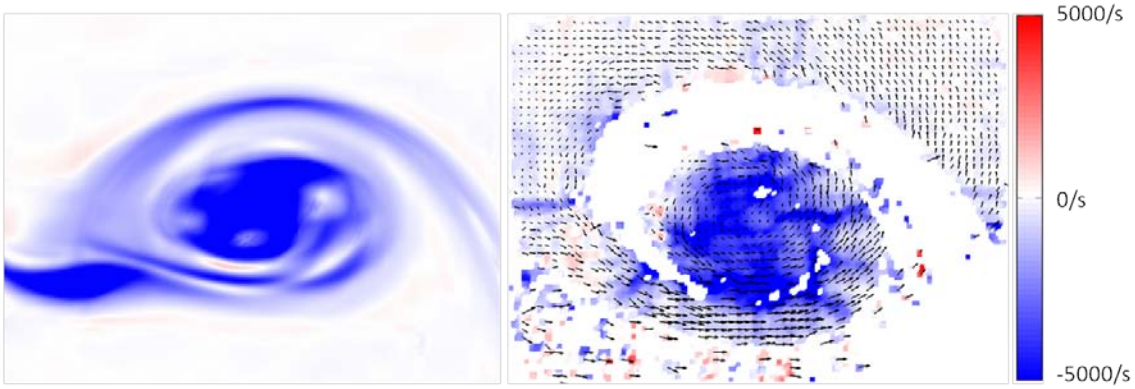

Figure 4.24: Comparison of vorticity field found from the simulation (left) and a high resolution experimental image (right). A sample of the PIV vectors used to calculate the vorticity field is shown in the experimental image.

5 SUMMARY AND CONCLUSIONS

5.1 Motivation Summarized

The need for clean sustainable energy can be linked to most of the major problems facing our world today and in the future. To meet this need scientists from around the world have sought to develop fusion power as a clean, seemingly endless power source to drive our world economy. The American government has supported this effort in many ways including building the largest inertial confinement fusion (ICF) experiment in the world, the National Ignition Facility (NIF). Inertial confinement fusion is one of the most studied paths to achieving reliable energy production from fusion. The NIF uses the largest laser system in the world to compress a fusion fuel target to the densities and temperatures required for hydrogen atoms to fuse into helium, and release a great amount of energy. It is in the process of this compression that hydrodynamic instabilities develop which mix the high density fuel core with lower density or all together inert material and reduce the fusion yield to a point that prevents the economic viability of fusion power.

The Richtmyer-Meshokov instability coupled with other instabilities is responsible for this mixing and reduction in the fusion yield. It is difficult to obtain extensive data regarding these instabilities during the NIF experiments due to the difficulties in imaging these instabilities during such a short scales. The size of the fuel pellet is in the mm range, and the resolution associated with the x-ray diagnostics is not sufficient to decouple the different stages in this process. For this reason computer simulations are used extensively to interpret and predict NIF experiments. Validating

and improving these simulations is paramount in the success of fusion power. These simulations can be validated against simpler experiments performed at larger length scales and lower energy scales with a subset of the physics involved in the ICF experiments. These simplified experiments can provide a greater diversity in measurements and higher resolution data. Numerous versions of these experiments have been developed for studying the RMI and validating RMI simulations, but the need for more diverse measurements and initial conditions, with higher resolution statistically significant data remains. The objective of this work has been to add to these previous experimental methods a new approach, studied through experiments and simulations both, which couples diverse measurement types at high resolution with highly repeatable initial conditions that precisely control the strength of the RMI.

Previous work has sought to study the strength and behavior of the instability based on the pressure gradient strength, and the density gradient strength. These parameters are represented as the incident shock wave Mach number (eqn. 13), and the Atwood number (eqn. 21). The RMI evolves from a misalignment of these two terms generated by the interaction of a shock wave with fluid interface, as seen in the baroclinic term of the vorticity equation (eqn. 10). An additional parameter is visible in this equation which controls the development of the RMI, the strength of the cross product, or the degree of misalignment between the two gradients. The new approach seeks to take advantage of this additional parameter by reducing the interface perturbation to a simple flat misaligned interface and to control the inclination angle thereby controlling the cross product of the density and pressure gradients, and the

strength of the Richtmyer-Meshkov instability. This method has been termed the inclined interface RMI.

5.2 New Scaling Method for Inclined Interface RMI

The combination of both experimental and computational work provides a unique view point which allows an experimentalist, such as the Author, to understand what data is needed most from experiments and how to adapt and change experiments to parallel the development of faster and more power computational codes. It this fact that motivated the computational work reported on in this dissertation. The parametric computational work was begun to explore the behavior of the inclined interface RMI starting in with a non-linear regime perturbation. From the qualitative results of the computation parametric study it can be seen that the inclination angle, incident Mach number, and gas pair properties have a strong effect on the development of the interface. The mixing region is capable of separating into an area of high mixing and a more homogenous region of heavy fluid with little to no mixing.

The linear growth rate of the mixing width is predicted poorly using the Richtmyer impulsive model adapted for the inclined interface. The Richtmyer impulsive model struggles to collapse the data from different inclination angles. A new non-linear regime mixing width model was proposed that collapses the mixing width data for initially non-linear perturbations for all parameters sets well at early times for. The new model uses the 1-d wave speeds for the incident shockwave and the interface reflected, wall reflected, transmitted shockwave to predict the end of the initial nonlinear growth. The characteristic velocity for the new model was the 1-d transmitted wave speed

instead of the interface jump velocity used in the Richtmyer impulsive model. Future work will seek to define the interface mixing width better and to explore the divergence between the interface angles at later times. This is the first known attempt to scale data for a RMI which began in the nonlinear regime, and the first method to scale data for an inclined interface.

5.3 Linear to Non-linear Regime Transition

The parametric study was extended to examine the inclined interface RMI starting with a linear regime perturbation and to examine the effects of reshock on the linear and nonlinear initial perturbation cases. The non-linear case was seen to generate two distinct flow field regions; a mixing region where vorticity increases surface area for diffusion between the fluids, and low mixing more homogeneous region termed the slug region where little vorticity is created. The linear case did not develop the mixing region and maintained a well-organized region spike structure. After reshock, these regions loose organization and the unmixed SF_6 regions become the primary regions for vorticity production and mixing.

Scaled mixing width plots showed that the non-linear perturbation cases collapse to a single non-dimensional growth rate while the linear perturbation cases have different growth rates that do not collapse to the same non-dimensional growth rate as the linear cases or each other. The reshock mixing width data was scaled using the same method with a different time offset to bring the various cases to a common origin after reshock. This scaled data showed there was some agreement between both linear and nonlinear cases at early non-dimensional times, but that at late times the growth rates of all cases

diverged and there was no distinction between the growth rates of the two cases. Mix mass plots showed that the increased vorticity from reshock greatly increased the mix mass and that the rate of increase in mix mass for both cases is similar after reshock.

Due to the asymmetric nature of the inclined interface Richtmyer-Meshkov instability it was seen through graphs of the circulation that the vorticity deposited by the incident shock is initially negative, while the vorticity deposited by the reshock reversed the direction of circulation to be positive. The onset of reshock greatly increased the number of vorticies in the flow field initially. At late times these vorticies combined and were reduced in strength, as seen from the decay of the circulation for both cases. By examining the circulation production terms it was seen that the vorticity was produced primarily by the baroclinic and compressible stretching terms. For the linear case the production terms remained stronger at late times after reshock than they did for the non-linear case due to the more well organized flow field reducing the vorticity interaction and merging.

The scaled mixing width data showed a distinct difference in growth rates between interfaces begin in the linear and nonlinear regimes. This transition occurred near 75° or an amplitude to wavelength ratio of ~0.1. This study was extended to examine the effects of reshock on the two distinctly different evolving flow fields which different on in their initial inclination angles. This reshock study found that the interface mixing width growth rates and mix mass production were similar for both these cases after reshock. In contrast the decay rate of the post reshock vorticity was found to have different patterns for each of these cases where the nonlinear case displayed a faster

power law trend decay and the linear case displayed a slower linear trend decay. This study suggests that while in integral measures such as mixing width the memory of initial conditions seems to have been forgotten its effect remains on vorticity scale dependent feature such as enstrophy, and circulation.

5.4 Power Law Decay of Shock Wave Perturbations

Additional computational studies were undertaken which did not focus on the inclined interface perturbation method but instead sought to answer additional questions about the effect of shock wave perturbations using sine wave type perturbations. The results presented in this computational study show that the power law decay method, in the form of $A = B * S^E$, can be used to describe the decay of the perturbations present on the shock wave created when it encounters a perturbed variable density interface. The proposed model fits the data for low incident Mach numbers well while at higher mach numbers the presence of large and irregular late time oscillations of the perturbation amplitude make it hard for the power law to fit as effectively.

When the coefficients from the power law decay model are plotted versus Mach number, a distinct transition region can be seen. This region is likely to result from the transition of the post-shock SF_6 velocity from subsonic to supersonic range in the lab frame. This region separates the data into a high and low Mach number region. These regions each have their own correlation between the coefficients of the power law decay and the incident shock Mach number. At high Mach numbers, perturbations induced on the refracted shock wave will persist even at late times, and may act as a secondary source of baroclinic vorticity production in shock tube experiments after reshock.

Therefore, one needs to very careful while pursuing reshock studies for RMI at high Mach number. The end-wall should be far enough from the initial interface, which guarantees the planarity of the refracted shock wave before reaching the wall.

5.5 Construction of the New Inclined Shock Tube Facility

To complete the study of the inclined interface RMI an experimental facility was developed to provide experimental verification of the results and to provide a repeatable experiment which could be used to generate statistically significant data sets. The facility was completed in May of 2012, after the Author had spent nearly three years working on the design, fabrication and construction of the facility while also performing the computational work. Employing this new method for developing an interface perturbation, the facility is capable of generating highly repeatable initial conditions which allow for ensemble averaging of experimental data with low run to run errors. The facility is also capable of short experimental reset times, approximately 20 minutes per experiment, which allows for large numbers of experiments to be completed for statistical data sets. Inclination angles from 0 to 90°, and incident shock Mach numbers up to 3.0 can be achieved. Variations in Atwood number are generated by gas pairs for the interface which is created by co-flowing the light (heavy) gas from above (below) and allowing the diffuse interface gas to exit through slots in the shock tube wall. The facility was constructed for optical diagnostics with 8 overlapping optical diagnostic window location, and fitted with planar laser induced fluorescence and particle imaging velocimetry systems.

5.6 Inclined Interface Experiments

Initial experiments were performed as part of this work using planar laser Mie scattering and particle imaging velocimetry. These are the first experiments to be performed on a inclined interface RMI at an incident Mach number greater than 1.5. These techniques were used to find the interface mixing width growth rate and the vorticity field. These experiments were compared with simulations using initial conditions which matched the experiment. These comparisons show overall agreement with integral measures like the interface mixing width growth rate matching well. Some disagreement was found however, and reasons for the disagreement largely point to the departure of the initial conditions in the experiment from the ideal planar interface. In the experiments the initial interface exhibits some curvature at the edges due to the velocity vectors of the coflowing gases aligning themselves to be parallel with the slots. The exit slots also allow for part of the incident shock to be entrained in the slot thereby reducing the strength of the transmitted shock. The experimental effects have not been included in the simulation and therefore some disagreement is to be expected.

The variation in simulation and experimental data are not all to be attributed to deficiencies in the new facility though, as small vortical structures were resolved in experiments at late times which have never been resolved in the simulations. These structures are a function energy scales which exist below the lowest scales that could be reached in simulations, meaning that the experiments have provided data that is beyond the capability of the current simulations and can be used to push the code capabilities further in future revisions to the ARES code. The experimental data also validated the

scaling method developed based on the computational work. These experiments showed that the experimental data can be non-dimensionalized and collapsed to a linear non-dimensional growth rate which agrees well with the simulation data from varying parametric combinations of the inclined interface RMI.

5.7 Future Work

A complete parametric study of the inclined interface RMI was performed in simulations with initial experimental data provided from the new advanced fluids mixing shock tube facility to validate the results. Both the experimental and computational work to explore the inclined interface Richtmyer-Meshkov instability remains in its infancy, with many extensions to the current work just beyond the reach of Authors time of study. The ground work has been laid but 3D simulations of the inclined interface RMI remain to be performed using the ARES code. These simulations will consume enormous amount of computational resources but will provide insight into the 3d vortical effects which likely dominate the flow at late times and after reshock. The experimental facility occupied the greatest amount of the author's study and was only completed three quarters of the way through the author's PhD study, leaving the facility in a position to return great dividends in time just beyond the completion of the Author's study. Simultaneous PLIF and PIV diagnostics have been developed and will soon yield simultaneous density and velocity fields for the inclined interface experiments. Initial experiments have been performed for different Atwood number combinations, inclination angles, shock wave mach numbers, and reshock conditions which have resolved the initial problems which will be encountered in modifying these parameters.

All that remains to be done now is to combine these diagnostic techniques and the parameter variations with some time to yield a vast amount of statistically converged experimental data that when combined with the 3D simulations will yield new insights into the RMI and its behavior under a wide range of initial conditions.

FUNDING ACKNOWLEDGEMENTS

I would like to thank following for providing financial support for my research:

The center for Radiative Shock Hydrodynamics (CRASH).

Lawrence Livermore National Laboratory (LLNL) and the High Energy Density Physics (HEDP) summer student program.

The National Science Foundation (NSF) research experience for undergraduates (REU) program.

The National Science Foundation (NSF) CAREER grant.

REFERENCES

[1] R. D. Richtmyer, “Taylor Instability in Shock Acceleration of Compressible Fluids,” *Comm. Pure Appl. Math.*, vol. 13, no. 2, pp. 297–319, May 1960.

[2] E. E. Meshkov, “Instability of the Interface of Two Gases Accelerated by a Shock Wave,” *Fluid Dyn.*, vol. 4, no. 5, pp. 101–104, 1972.

[3] W. Kelvin, “Hydrokinetic Solutions and Observations,” *The London, Edinburgh, and Dublin Philosophical Magazine and Journal of Science*, vol. 42, no. 281, pp. 362–377, 1871.

[4] H. von Helmholtz, “Über Discontinuierliche Flüssigkeits-Bewegungen,” *The London, Edinburgh, and Dublin Philosophical Magazine and Journal of Science*, vol. 36, no. 4, pp. 337–346, 1868.

[5] J. W. S. Rayleigh, “Investigation of the Character of the Equilibrium of an Incompressible Heavy Fluid of Variable Density,” *Proceedings of the London Mathmatical Society*, vol. 14, pp. 170–177, 1883.

[6] G. Taylor, “The Instability of Liquid Surfaces When Accelerated in a Direction Perpendicular to Their Planes.,” *Proceedings of the Royal Society of London. Series A, Mathematical and Physical Sciences*, pp. 192–196, 1950.

[7] P.G. Drazin and W.H. Reid, *Hydrodynamic Stability*, Second. Cambridge: Cambridge University Press, 2004.

[8] J. D. Anderson, *Modern Compressible Flow with Historical Perspective*, Second. New York: McGraw-Hill, 1990.

[9] D. Ranjan, J. Oakley, and R. Bonazza, “Shock-Bubble Interactions,” *Annu. Rev. Fluid Mech.*, vol. 43, no. 1, pp. 117–140, 2011.

[10] R. G. Jahn, “The Refraction of Shock Waves at a Gaseous Interface,” *Journal of Fluid Mechanics*, vol. 1, no. 05, pp. 457–489, 1956.

[11] L. F. Henderson, “The Refraction of a Plane Shock Wave at a Gas Interface,” *J. Fluid Mech*, vol. 26, no. part 3, pp. 607–637, 1966.

[12] A. M. Abd-el -Fattah and L. F. Henderson, “Shock Waves at a Slow-Fast Gas Interface,” *Journal of Fluid Mechanics*, vol. 89, no. 01, pp. 79–95, 1978.

[13] A. M. Abd–El–Fattah, L. F. Henderson, and A. Lozzi, “Precursor Shock Waves at a Slow—Fast Gas Interface,” *Journal of Fluid Mechanics*, vol. 76, no. 01, pp. 157–176, 1976.

[14] A. M. Abd-El-Fattah and L. F. Henderson, “Shock Waves at a Fast-Slow Gas Interface,” *Journal of Fluid Mechanics*, vol. 86, no. 01, pp. 15–32, 2006.

[15] N. J. Zabusky, “Vortex Paradigm for Accelerated Inhomogeneous Flows: Visiometrics for the Rayleigh-Taylor and Richtmyer-Meshkov Environments,” *Annu. Rev. Fluid Mech.*, vol. 31, no. 1, pp. 495–536, 1999.

[16] R. Samtaney and N. J. Zabusky, “On Shock Polar Analysis and Analytical Expressions for Vorticity Deposition in Shock-Accelerated Density-Stratified Interfaces,” *Phys. Fluids A*, vol. 5, no. 6, 1993.

[17] K. A. Meyer and P. J. Blewett, “Numerical Investigation of the Stability of a Shock-Accelerated Interface between Two Fluids,” *Phys. Fluids*, vol. 15, no. 5, p. 753, 1972.

[18] G. Fraley, “Rayleigh–Taylor Stability for a Normal Shock Wave–Density Discontinuity Interaction | Phys. Fluids (1958-1988) - Physics of Fluids,” *Physics of Fluids*, vol. 29, no. 2, p. 376, 1985.

[19] J. G. Wouchuk and K. Nishihara, “Asymptotic Growth in the Linear Richtmyer-Meshkov Instability,” *Physics of Plasmas*, vol. 4, no. 4, pp. 1028–1038, 1997.

[20] J. G. Wouchuk and K. Nishihara, “Linear Perturbation Growth at a Shocked Interface,” *Physics of Plasmas*, vol. 3, no. 10, pp. 3761–3776, 1996.

[21] J. Wouchuk, “Growth rate of the Linear Richtmyer-Meshkov Instability when a Shock is Reflected,” *Phys. Rev. E*, vol. 63, no. 5, Apr. 2001.

[22] M. Vandenboomgaerde, C. M\ügler, and S. Gauthier, “Impulsive Model for the Richtmyer-Meshkov Instability,” *Physical Review E*, vol. 58, no. 2, pp. 1874–1882, 1998.

[23] B. Motl, J. Oakley, D. Ranjan, C. Weber, M. Anderson, and R. Bonazza, “Experimental Validation of a Richtmyer–Meshkov Scaling Law Over Large Density Ratio and Shock Strength Ranges,” *Phys. Fluids*, vol. 21, p. 126102, 2009.

[24] M. Brouillette and B. Sturtevant, “Experiments on the Richtmyer–Meshkov Instability: Small-Scale Perturbations on a Plane Interface,” *Phys. Fluids A-Fluid*, vol. 5, no. 4, pp. 916–930, 1993.

[25] A. Aleshin, E. Gamalii, S. Zaytsev, E. Lazareva, and I. Lebo, “Nonlinear and transitional Stages in the Onset Of The Richtmyer–Meshkov Instability,” *Soviet Technical Physics Letters*, vol. 14, pp. 466–68, 1988.

[26] M. Brouillette, “The Richtmyer-Meshkov Instability,” *Annu Rev Fluid Mech*, vol. 34, no. 1, pp. 445–468, 2002.

[27] Q. Zhang and S. I. Sohn, “An Analytical Nonlinear Theory of Richtmyer-Meshkov Instability,” *Physics Letters A*, vol. 212, no. 3, pp. 149–155, 1996.

[28] A. L. Velikovich and G. Dimonte, “Nonlinear perturbation Theory of the Incompressible Richtmyer-Meshkov Instability,” *Physical review letters*, vol. 76, no. 17, pp. 3112–3115, 1996.

[29] R. L. Holmes, G. Dimonte, B. Fryxell, M. L. Gittings, J. W. Grove, M. Schneider, D. H. Sharp, A. L. Velikovich, R. P. Weaver, and Q. Zhang, “Richtmyer–Meshkov Instability Growth: Experiment, Simulation and Theory,” *Journal of Fluid Mechanics*, vol. 389, pp. 55–79, Jun. 1999.

[30] J. Hecht, U. Alon, and D. Shvarts, “Potential Flow Models of Rayleigh–Taylor and Richtmyer–Meshkov Bubble Fronts,” *Physics of fluids*, vol. 6, p. 4019, 1994.

[31] U. Alon, J. Hecht, D. Ofer, and D. Shvarts, “Power Laws And Similarity Of Rayleigh-Taylor and Richtmyer-Meshkov Mixing Fronts at All Density Ratios,” *Physical review letters*, vol. 74, no. 4, pp. 534–537, 1995.

[32] O. Sadot, L. Erez, U. Alon, D. Oron, L. A. Levin, G. Erez, G. Ben-Dor, and D. Shvarts, “Study of Nonlinear Evolution of Single-Mode and Two-Bubble Interaction Under Richtmyer-Meshkov Instability,” *Physical review letters*, vol. 80, no. 8, pp. 1654–1657, 1998.

[33] B. Thornber, D. Drikakis, D. L. Youngs, and R. J. R. Williams, “The Influence of Initial Conditions on Turbulent Mixing Due to Richtmyer-Meshkov Instability,” *J. Fluid Mech.*, vol. 654, pp. 99–139, 2010.

[34] B. Thornber, D. Drikakis, D. L. Youngs, and R. J. R. Williams, “Physics of the Single-Shocked and Reshocked Richtmyer–Meshkov Instability,” *Journal of Turbulence*, vol. 13, p. N10, Jan. 2012.

[35] J. M. Soures, R. L. McCrory, C. P. Verdon, A. Babushkin, R. E. Bahr, T. R. Boehly, R. Boni, D. K. Bradley, D. L. Brown, R. S. Craxton, J. A. Delettrez, W. R. Donaldson, R. Epstein, P. A. Jaanimagi, S. D. Jacobs, K. Kearney, R. L. Keck, J. H. Kelly, T. J. Kessler, R. L. Kremens, J. P. Knauer, S. A. Kumpan, S. A. Letzring, D. J. Lonobile, S. J. Loucks, L. D. Lund, F. J. Marshall, P. W. McKenty, D. D. Meyerhofer, S. F. B. Morse, A. Okishev, S. Papernov, G. Pien, W. Seka, R. Short, M. J. Shoup, M. Skeldon, S. Skupsky, A. W. Schmid, D. J. Smith, S. Swales, M. Wittman, and B. Yaakobi, “Direct-Drive Laser-Fusion Experiments with the OMEGA, 60-Beam, >40 kJ, Ultraviolet Laser System,” *Physics of Plasmas*, vol. 3, no. 5, p. 2108, 1996.

[36] H. F. Robey, J. O. Kane, B. A. Remington, R. P. Drake, O. A. Hurricane, H. Louis, R. J. Wallace, J. Knauer, P. Keiter, D. Arnett, and D. D. Ryutov, "An Experimental Testbed for the Study of Hydrodynamic Issues in Supernovae," *Phys. Plasmas*, vol. 8, no. 5, p. 2446, 2001.

[37] E. I. Moses and C. R. Wuest, "The National Ignition Facility: Laser Performance and First Experiments," *Fusion Science and Technology*, vol. 47, no. 3, 2005.

[38] H. Robey, P. Celliers, J. Kline, A. Mackinnon, T. Boehly, O. Landen, J. Eggert, D. Hicks, S. Le Pape, D. Farley, M. Bowers, K. Krauter, D. Munro, O. Jones, J. Milovich, D. Clark, B. Spears, R. Town, S. Haan, S. Dixit, M. Schneider, E. Dewald, K. Widmann, J. Moody, T. Döppner, H. Radousky, A. Nikroo, J. Kroll, A. Hamza, J. Horner, S. Bhandarkar, E. Dzenitis, E. Alger, E. Giraldez, C. Castro, K. Moreno, C. Haynam, K. LaFortune, C. Widmayer, M. Shaw, K. Jancaitis, T. Parham, D. Holunga, C. Walters, B. Haid, T. Malsbury, D. Trummer, K. Coffee, B. Burr, L. Berzins, C. Choate, S. Brereton, S. Azevedo, H. Chandrasekaran, S. Glenzer, J. Caggiano, J. Knauer, J. Frenje, D. Casey, M. Gatu Johnson, F. Séguin, B. Young, M. Edwards, B. Van Wonterghem, J. Kilkenny, B. MacGowan, J. Atherton, J. Lindl, D. Meyerhofer, and E. Moses, "Precision Shock Tuning on the National Ignition Facility," *Physical Review Letters*, vol. 108, no. 21, May 2012.

[39] Y. Aglitskiy, A. Velikovich, M. Karasik, V. Serlin, C. Pawley, A. Schmitt, S. Obenschain, A. Mostovych, J. Gardner, and N. Metzler, "Direct Observation of Mass Oscillations Due to Ablative Richtmyer-Meshkov Instability in Plastic Targets," *Physical Review Letters*, vol. 87, no. 26, Dec. 2001.

[40] J. Kane, R. P. Drake, and B. A. Remington, "An evaluation Of The Richtmyer-Meshkov Instability in Supernova Remnant Formation," *Astrophys. J.*, vol. 511, pp. 335–340, 1999.

[41] S. Dutta, J. Glimm, J. W. Grove, D. H. Sharp, and Y. Zhang, "Spherical Richtmyer-Meshkov instability for axisymmetric flow," *Mathematics and Computers in Simulation*, vol. 65, no. 4–5, pp. 417–430, May 2004.

[42] M. J. Grosskopf, R. P. Drake, C. C. Kuranz, A. R. Miles, J. F. Hansen, T. Plewa, N. Hearn, D. Arnett, and J. C. Wheeler, "Modeling of Multi-Interface, Diverging, Hydrodynamic Experiments for the National Ignition Facility," *Astrophysics and Space Science*, vol. 322, no. 1–4, pp. 57–63, Dec. 2008.

[43] K. O. Mikaelian, "Rayleigh-Taylor and Richtmyer-Meshkov Instabilities and Mixing In Stratified Spherical Shells," *Physical Review A*, vol. 42, no. 6, p. 3400, 1990.

[44] M. H. Anderson, B. P. Puranik, J. G. Oakley, P. W. Brooks, and R. Bonazza, "Shock Tube Investigation of Hydrodynamic Issues Related yo Inertial Confinement Fusion," *Shock Waves*, vol. 10, no. 5, pp. 377–387, 2000.

[45] B. Blue, S. Weber, S. Glendinning, N. Lanier, D. Woods, M. Bono, S. Dixit, C. Haynam, J. Holder, D. Kalantar, B. MacGowan, A. Nikitin, V. Rekow, B. Van Wonterghem, E. Moses, P. Stry, B. Wilde, W. Hsing, and H. Robey, "Experimental Investigation of High-Mach-Number 3D Hydrodynamic Jets at the National Ignition Facility," *Physical Review Letters*, vol. 94, no. 9, Mar. 2005.

[46] C. C. Kuranz, R. P. Drake, E. C. Harding, M. J. Grosskopf, H. F. Robey, B. A. Remington, M. J. Edwards, A. R. Miles, T. S. Perry, B. E. Blue, T. Plewa, N. C. Hearn, J. P. Knauer, D. Arnett, and D. R. Leibrandt, "Two-Dimensional Blast-Wave-Driven Rayleigh-Taylor Instability: Experiment and Simulation," *The Astrophysical Journal*, vol. 696, no. 1, pp. 749–759, May 2009.

[47] A. R. Miles, B. Blue, M. J. Edwards, J. A. Greenough, J. F. Hansen, H. F. Robey, R. P. Drake, C. Kuranz, and D. R. Leibrandt, "Transition to Turbulence and Effect of Initial Conditions on Three-Dimensional Compressible Mixing in Planar Blast-Wave-Driven Systems," *Phys. Plasmas*, vol. 12, no. 5, p. 056317, 2005.

[48] E. Harding, J. Hansen, O. Hurricane, R. Drake, H. Robey, C. Kuranz, B. Remington, M. Bono, M. Grosskopf, and R. Gillespie, "Observation of a Kelvin-Helmholtz Instability in a High-Energy-Density Plasma on the Omega Laser," *Physical Review Letters*, vol. 103, no. 4, Jul. 2009.

[49] P. R. Chapman and J. W. Jacobs, "Experiments on the Three-Dimensional Incompressible Richtmyer-Meshkov Instability," *Phys. Fluids*, vol. 18, p. 074101, 2006.

[50] C. E. Niederhaus and J. W. Jacobs, "Experimental Study of the Richtmyer–Meshkov Instability of Incompressible Fluids," *Journal of Fluid Mechanics*, vol. 485, pp. 243–277, May 2003.

[51] J. W. Jacobs and I. Catton, "Three-Dimensional Rayleigh-Taylor Instability Part 2. Experiment," *Journal of Fluid Mechanics*, vol. 187, no. 187, pp. 353–371, 1988.

[52] K. I. Read, "Experimental Investigation of Turbulent Mixing by Rayleigh-Taylor Instability," *Physica D: Nonlinear Phenomena*, vol. 12, no. 1–3, pp. 45–58, 1984.

[53] G. Dimonte and M. Schneider, "Turbulent Rayleigh-Taylor Instability Experiments with Variable Acceleration," *Physical Review E*, vol. 54, no. 4, p. 3740, 1996.

[54] N. Yamashita and J. W. Jacobs, “The Experimental Study of Rayleigh-Taylor Instability using a Linear Induction Motor Accelerator,” in *Bulletin of the American Physical Society*, Minneapolis, Minnesota, 2009, vol. 54.

[55] D. J. Hill, C. Pantano, and D. I. Pullin, “Large-Eddy Simulation and Multiscale Modelling of a Richtmyer–Meshkov Instability with Reshock,” *J. Fluid Mech.*, vol. 557, p. 29, Jun. 2006.

[56] M. Latini, O. Schilling, and W. S. Don, “Effects of WENO Flux Reconstruction Order and Spatial Resolution on Reshocked Two-Dimensional Richtmyer–Meshkov Instability,” *Journal of Computational Physics*, vol. 221, no. 2, pp. 805–836, Feb. 2007.

[57] C. Bailie, J. A. McFarland, J. A. Greenough, and D. Ranjan, “Effect of Incident Shock Wave Strength on the Decay of Richtmyer–Meshkov Instability-Introduced Perturbations in the Refracted Shock Wave,” *Shock Waves*, Jun. 2012.

[58] M. Vetter and B. Sturtevant, “Experiments on the Richtmyer-Meshkov Instability of an Air/SF 6 Interface,” *Shock Waves*, vol. 4, no. 5, pp. 247–252, 1995.

[59] L. Erez, O. Sadot, D. Oron, G. Erez, L. A. Levin, D. Shvarts, and G. Ben-Dor, “Study of the Membrane Effect on Turbulent Mixing Measurements in Shock Tubes,” *Shock Waves*, vol. 10, no. 4, pp. 241–251, 2000.

[60] A. I. Abakumov, V. Y. Fadeev, S. I. Kholkin, E. E. Meshkov, V. V. Nikiforov, P. N. Nizovtzev, N. N. Sadilov, S. K. Sobolev, V. A. Tilkunov, V. O. Tochilin, and others, “Studies of Film Effects on the Turbulent Mixing Zone Evolution in Shock Tube Experiments,” in *Proceedings of the Fifth International Workshop on Compressible Turbulent Mixing, edited by R. Young, J. Glimm, and B. Boston (World Scientific, Singapore, 1996)*, p. 118.

[61] L Houas and I Chemouni, “Experimental Investigation of Richtmyer-Meshkov Instability in Shock Tube,” *Physics of Fluids*, vol. 8, no. 2, p. 614, 1996.

[62] Y. A. Kucherenko, A. V. Pavlenko, O. E. Shestachenko, S. I. Balabin, A. P. Pylaev, and A. A. Tyaktev, “Measurement of Spectral Characteristics of the Turbulent Mixing Zone,” *Journal of Applied Mechanics and Technical Physics*, vol. 51, no. 3, pp. 299–307, 2010.

[63] A N Aleshin, S. G. Zaitsev, and E. V. Lazareva, “Damping of Perturbations at a Shock Front in the Presence of a Richtmyer-Meshkov Instability,” *Sov. Tech. Phys. Lett.*, vol. 17, no. 14, pp. 493–496, 1991.

[64] J. H. J. Niederhaus, J. A. Greenough, J. G. Oakley, D. Ranjan, M. H. Anderson, and R. Bonazza, "A Computational Parameter Study for the Three-Dimensional Shock–Bubble Interaction," *J. Fluid Mech.*, vol. 594, Dec. 2007.

[65] J. H. J. Niederhaus, D. Ranjan, J. G. Oakley, M. H. Anderson, J. A. Greenough, and R. Bonazza, "Computations in 3D for Shock-Induced Distortion of a Light Spherical Gas Inhomogeneity," *Shock Waves*, vol. 28, pp. 1169–1174, 2009.

[66] N. Haehn, C. Weber, J. Oakley, M. Anderson, D. Ranjan, and R. Bonazza, "Experimental investigation of a Twice-Shocked Spherical Gas Inhomogeneity with Particle Image Velocimetry," *Shock Waves*, vol. 21, no. 3, pp. 225–231, Feb. 2011.

[67] D. Ranjan, M. Anderson, J. Oakley, and R. Bonazza, "Experimental Investigation of a Strongly Shocked Gas Bubble," *Phys. Rev. Lett.*, vol. 94, no. 18, p. 184507, 2005.

[68] D. Ranjan, J. Niederhaus, B. Motl, M. Anderson, J. Oakley, and R. Bonazza, "Experimental Investigation of Primary and Secondary Features in High-Mach-Number Shock-Bubble Interaction," *Phys. Rev. Lett.*, vol. 98, no. 2, p. 024502, Jan. 2007.

[69] D. Ranjan, J. H. J. Niederhaus, J. G. Oakley, M. H. Anderson, J. A. Greenough, and R. Bonazza, "Experimental and Numerical Investigation Of Shock-Induced Distortion of a Spherical Gas Inhomogeneity," *Physica Scripta*, vol. 2008, p. 014020, 2008.

[70] R. Bonazza and B. Sturtevant, "X-Ray Measurements of Growth Rates at a Gas Interface Accelerated by Shock Waves," *Physics of Fluids*, vol. 8, no. 9, pp. 2496–2512, 1996.

[71] S. B. Dalziel, "Rayleigh-Taylor Instability: Experiments with Image Analysis," *Dynamics of Atmospheres and Oceans*, vol. 20, no. 1–2, pp. 127–153, 1993.

[72] J. W. Jacobs and S. B. Dalziel, "Rayleigh–Taylor Instability in Complex Stratifications," *Journal of Fluid Mechanics*, vol. 542, no. -1, p. 251, Oct. 2005.

[73] J. W. Jacobs, "Shock-Induced Mixing of a Light-Gas Cylinder," *Journal of Fluid Mechanics*, vol. 234, pp. 629–649, 1992.

[74] J. J. Quirk and S. Karni, "On the Dynamics of a Shock–Bubble Interaction," *Journal of Fluid Mechanics*, vol. 318, no. -1, p. 129, Apr. 2006.

[75] A. Bagabir and D. Drikakis, "Mach Number Effects on Shock-Bubble Interaction," *Shock Waves*, vol. 11, no. 3, pp. 209–218, 2001.

[76] C. Tomkins, K. Prestridge, P. Rightley, M. Marr-Lyon, P. Vorobieff, and R. Benjamin, "A Quantitative Study of the Interaction of Two Richtmyer–Meshkov-Unstable Gas Cylinders," *Physics of Fluids*, vol. 15, no. 4, p. 986, 2003.

[77] S. Balasubramanian, G. C. Orlicz, K. P. Prestridge, and B. J. Balakumar, "Experimental Study of Initial Condition Dependence on Richtmyer-Meshkov Instability in the Presence of Reshock," *Physics of Fluids*, vol. 24, no. 3, p. 034103, 2012.

[78] K. Prestridge, P. Vorobieff, P. M. Rightley, and R. F. Benjamin, "Validation of an Instability Growth Model Using Particle Image Velocimetry Measurements," *Phys. Rev. Lett.*, vol. 84, no. 19, pp. 4353–4356, 2000.

[79] K. O. Mikaelian, "Numerical Simulations of Richtmyer–Meshkov Instabilities In Finite-Thickness Fluid Layers," *Physics of Fluids*, vol. 8, no. 5, pp. 1269–1292, 1996.

[80] B. D. Collins and J. W. Jacobs, "PLIF Flow Visualization and Measurements of the Richtmyer–Meshkov Instability of an Air/SF6 Interface," *Journal of Fluid Mechanics*, vol. 464, Aug. 2002.

[81] O. Schilling, M. Latini, and W. Don, "Physics of Reshock and Mixing in Single-Mode Richtmyer-Meshkov Instability," *Phys. Rev. E*, vol. 76, no. 2, p. 026319, Aug. 2007.

[82] V. V. Krivets, C. C. Long, J. W. Jacobs, and J. A. Greenough, "Shock Tube Experiments and Numerical Simulation of the Single Mode Three-Dimensional Richtmyer-Meshkov Instability," in *26th International Symposium on Shock Waves*, Gottingen, Germany, 2009, vol. 2, pp. 1205–1210.

[83] C. C. Long, V. V. Krivets, J. A. Greenough, and J. W. Jacobs, "Shock Tube Experiments and Numerical Simulation of the Single Mode Three-Dimensional Richtmyer-Meshkov Instability," *Physics of Fluids*, vol. 21, p. 114104, 2009.

[84] C. Weber, N. Haehn, J. Oakley, D. Rothamer, and R. Bonazza, "Turbulent Mixing Measurements in the Richtmyer-Meshkov Instability," *Physics of Fluids*, vol. 24, no. 7, p. 074105, 2012.

[85] J. F. Haas, "Experiments and Simulations on Shock Waves in Non-Homogeneous Gases," in *Proceedings of the 19th International Symposium on Shock Waves*, Marseille, France, 1993, vol. 4, pp. 27–36.

[86] B. Sturtevant, "Rayleigh-Taylor Instability in Compressible Fluids," in *16th International Symposium on Shock Tubes and Waves*, Aachen, West Germany, 1987, pp. 89–100.

[87] R. Samtaney and N. J. Zabusky, "Circulation Deposition on Shock-Accelerated Planar and Curved Density-Stratified Interfaces: Models and scaling laws," *Journal of Fluid Mechanics*, vol. 269, pp. 45–78, 1994.

[88] S. Zhang, G. Peng, and N. J. Zabusky, "Vortex Dynamics and Baroclinically Forced Inhomogeneous Turbulence for Shock—Planar Heavy Curtain Interactions," *J. of Turbulence*, vol. 6, 2005.

[89] K. O. Mikaelian, "Richtmyer–Meshkov Instability of Arbitrary Shapes," *Phys. Fluids*, vol. 17, no. 3, p. 034101, 2005.

[90] Smith, A.V., Holder, D.A., Barton, C.J., Morris, A.P., and Youngs, D.L., "Shock Tube Experiments on Richtmyer–Meshkov Instability Across a Chevron Profiled Interface," presented at the 8th International Workshop on The Physics of Compressible Turbulent Mixing,, Pasedena, CA, 09-Dec-2001.

[91] D. Arnett, "The Fole of Mixing in Astrophysics," *The Astrophysical Journal Supplement Series*, vol. 127, p. 213, 2000.

[92] J. Krebs and W. Hillebrandt, "The Interaction of Supernova Shockfronts and Nearby Interstellar Clouds," *Astronomy and Astrophysics*, vol. 128, no. 2, pp. 411–419, 1983.

[93] R. I. Klein, C. F. McKee, and P. Colella, "On the Hydrodynamic Interaction of Shock Waves with Interstellar Clouds. 1: Nonradiative Shocks in Small Clouds," *The Astrophysical Journal*, vol. 420, pp. 213–236, 1994.

[94] R. I. Klein, K. S. Budil, T. S. Perry, and D. R. Bach, "Interaction of Supernova Remnants with Interstellar Clouds: From the Nova Laser to the Galaxy," *The Astrophysical Journal Supplement Series*, vol. 127, p. 379, 2000.

[95] R. I. Klein, K. S. Budil, T. S. Perry, and D. R. Bach, "The Interaction of Supernova Remnants with Interstellar Clouds: Experiments on the NOVA Laser," *The Astrophysical Journal*, vol. 583, p. 245, 2003.

[96] R. P. Drake, J. J. Carroll III, K. Estabrook, S. G. Glendinning, B. A. Remington, R. Wallace, and R. McCray, "Development of a Laboratory Environment to Test Modelsof Supernova Remnant Formation," *The Astrophysical Journal Letters*, vol. 500, p. L157, 1998.

[97] J. Kane, D. Arnett, B. A. Remington, S. G. Glendinning, G. Bazan, R. P. Drake, and B. A. Fryxell, "Supernova Experiments on the Nova Laser," *The Astrophysical Journal Supplement Series*, vol. 127, p. 365, 2000.

[98] F. E. Marble, E. E. Zukoski, J. W. Jacobs, G. J. Hendricks, and I. A. Waitz, "Shock Enhancement and Control of Hypersonic Mixing and Combustion," American Institute of Aeronautics and Astronautics, Orlando, FL, AIAA 90-1981, Jul. 1990.

[99] J. Yang, T. Kubota, and E. E. Zukoski, "Applications of Shock-Induced Mixing to Supersonic Combustion," *AIAA Journal*, vol. 31, no. 5, pp. 854–862, 1993.

[100] F. Houwing, A. Bishop, M. Gaston, J. Fox, P. Danehy, and N. Mudford, "Simulated-Fuel-Jet/Shock-Wave Interaction," in *Proceedings of the 23rd International Symposium on Shock Waves*, Fort Worth, Texas, 2001, pp. 1074–1080.

[101] M. Delius, "Medical Applications and Bioeffects of Extracorporeal Shock Waves," *Shock waves*, vol. 4, no. 2, pp. 55–72, 1994.

[102] M. Delius, F. Ueberle, and W. Eisenmenger, "Extracorporeal Shock Waves Act by Shock Wave-Gas Bubble Interaction," *Ultrasound in medicine & biology*, vol. 24, no. 7, pp. 1055–1059, 1998.

[103] J. Lindl, "Development of the Indirect-Drive Approach to Inertial Confinement Fusion and the Target Physics Basis for Ignition and Gain," *Physics of Plasmas*, vol. 2, no. 11, p. 3933, 1995.

[104] J. D. Lindl, R. L. McCrory, E. M. Campbell, and others, "Progress Toward Ignition and Burn Propagation in Inertial Confinement Fusion," *Phys. Today*, vol. 45, no. 9, p. 32, 1992.

[105] G. Dimonte, D. L. Youngs, A. Dimits, S. Weber, M. Marinak, S. Wunsch, C. Garasi, A. Robinson, M. J. Andrews, P. Ramaprabhu, A. C. Calder, B. Fryxell, J. Biello, L. Dursi, P. MacNeice, K. Olson, P. Ricker, R. Rosner, F. Timmes, H. Tufo, Y.-N. Young, and M. Zingale, "A Comparative Study of the Turbulent Rayleigh–Taylor Instability Using High-Resolution Three-Dimensional Numerical Simulations: The Alpha-Group Collaboration," *Physics of Fluids*, vol. 16, no. 5, p. 1668, 2004.

[106] W. J. Rider, E. Love, M. K. Wong, O. E. Strack, S. V. Petney, and D. A. Labreche, "Adaptive Methods for Multi-Material ALE Hydrodynamics," *International Journal for Numerical Methods in Fluids*, vol. 65, no. 11–12, pp. 1325–1337, 2011.

[107] J. Donea, A. Huerta, J. P. Ponthot, and A. Rodríguez-Ferran, "Arbitrary Lagrangian–Eulerian Methods," *Encyclopedia of Computational Mechanics*. Wiley Online Library, 2004.

[108] M. L. Wilkins, “Calculation of Elastic Plastic Flow,” University of California Lawrence Radiation Labratory, UCRL-7322, Apr. 1963.

[109] T. V. Kolev and R. N. Rieben, “A Tensor Artificial Viscosity Using a Finite Element Approach,” *J. Comput. Phys.*, vol. 228, no. 22, pp. 8336–8366, 2009.

[110] R. W. Sharp and R. T. Barton, “HEMP Advection Model,” Lawrence Livermore Laboratory, UCID-17809, Jan. 1981.

[111] R. Morgan, R. Aure, J. D. Stockero, J. A. Greenough, W. Cabot, O. Likhatchev, and J. W. Jacobs, “On the Late-Time Growth of the 2D Richtmyer-Meshkov Instability in Shock Tube Experiments,” *J. Fluid Mechanics*, vol. In Press, 2012.

[112] E. R. Gilliland, “Diffusion Coefficients in Gaseous Systems,” *Industrial and Engineering Chemistry*, vol. 26, no. 6, pp. 681–685, Jun. 1934.

[113] B. Poling, J. Prausbitz, and J. O’Connell, *The Properties of Gases and Liquids*, 5th ed. McGraw-Hill, 2000.

[114] A. W. Cook, “Enthalpy Diffusion in Multicomponent Flows,” *Physics of Fluids*, vol. 21, no. 5, p. 055109, 2009.

[115] J. McFarland, J. Greenough, and D. Ranjan, “Computational Parametric Study of a Richtmyer-Meshkov Instability for an Inclined Interface,” *Phys. Rev. E*, vol. 84, no. 2, p. 026303, Aug. 2011.

[116] K. H. . Winkler, J. W. Chalmers, S. W. Hodson, P. R. Woodward, and N. J. Zabusky, “A Numérica! Laboratory,” *Physics Today*, vol. 40, no. 10, p. 28, 1987.

[117] W. H. Cabot and A. W. Cook, “Reynolds Number Effects on Rayleigh–Taylor Instability with Possible Implications for Type Ia Supernovae,” *Nat Phys*, vol. 2, no. 8, pp. 562–568, Jul. 2006.

[118] J. A. McFarland, J. A. Greenough, and D. Ranjan, “Investigation of the Initial Perturbation Amplitude for the Inclined Interface Richtmyer-Meshkov Instability,” *Physica Scripta*, vol. Turbulent Mixing and Beyond, in-press.

[119] C. Tomkins, S. Kumar, G. Orlicz, and K. Prestridge, “An Experimental Investigation of Mixing Mechanisms in Shock-Accelerated Flow,” *J. Fluid Mech.*, vol. 611, Aug. 2008.

[120] A. N. Aleshin, E. I. Chebotareve, V. V. Krivets, E. V. Lazareva, S. V. Sergeev, S. N. Titov, and S. Zaytsev, “Investigation of Evolution of Interface After its Interaction with Shock Waves,” International Institute for Applied Physics and High Technology, Moscow, Russia, 02-96 and 06-96, 1996.

[121] P. Koppenberger, “Shock Tube Design,” Texas A&M University, College Station, Tx, 2010.

[122] A. Lozano, “Laser-Excited Luminescent Tracers for Planar Concentration Measurements in Gaseous Jets,” Stanford University, 1992.

APPENDIX A: INSTRUMENTATION AND CONTROL OF THE SHOCK TUBE

A.1 Control Valves

The shock tube facility uses many solenoid actuated and manual valves to control the flow of gasses in the tube to set up initial conditions and to initialize the shock valve itself. The gas fill system originates at several gas cylinders ordered from gas suppliers. There are five gas cylinder required for the current set up, one for the driver fill gas, one to act as the driver boost tank, one each for the light and heavy driven fill gasses, and another to supply gas to the fog seeding system. The driven fill cylinders and the fog seeding system cylinder are reduced to lower pressures first using pressure regulators. The driver fill tank is used to replenish the gas in the boost tank between experiments and is actuated using a manual ball valve. The boost tank is connected directly to solenoid actuated valves for filling the driver and rupturing the diaphragm. The driven fill gases are metered using mass flow controllers with 0.02 L/m resolution. These mass flow controllers were produced by MKS Instruments, Inc. and use an external control unit with a user input set point to maintain the flow rates of the fill gasses and the fog gas.

The final level of valves that all shock tube gasses pass through are solenoid actuated valves which are controlled using the LabVIEW program and NI hard ware described later in this section. The driver fill gas travels through a steel pipe to the top of the shock tube where it is then diverted to two different valves that enter the driver. The first of these valves is the slow fill valve which is capable of relatively low flow rates and can support up to 2000psi. This valve is used to fill the driver to a pressure which is

near but lower than the static rupture pressure of the diaphragm in use. The other valve which allows the driver fill gas to enter the tube is the driver boost valve. This valve was designed for very high flow rates at pressures up to 7500psi. This valve is used to push the driver pressure to the dynamic rupture pressure of the diaphragm quickly. After exiting the mass flow controllers the driven fill gasses enter solenoid control valves at the top and bottom of the tube for the light and heavy fill gasses respectively. These valves are used to shut down the flow of gas to the tube just before the shock wave is initiated. Once the gasses are in the tube they are allowed to meet at the interface plane and exit through slots to atmosphere. The exit flow of these gases through the slots is controlled by another pair of solenoid valves which are used to terminated the flow and seat the tube before the shock wave is initiated. The fog gas flows directly from the mass flow controller to the gas driven Pea Soup, Inc. fog machine discussed in greater detail later. The fogged gas exiting the fog machine is combined back with either the heavy or light gasses before entering the tube. An addition solenoid valve is used on the tube to protect the low pressure range driven static pressure transducer (SPT) from the shock wave pressures. This valve is not used for flowing of gasses but merely for preventing the shock pressure from reaching the driven SPT.

One more set of control valves is present on the shock tube which control the hydraulic pump and the hydraulic diaphragm loader. One valve is used to control the flow of shop air to the hydraulic pump. This hydraulic pump uses the air pressure to pump hydraulic fluid to a pressure of up to 5800psi. This fluid is routed to the hydraulic diaphragm loader through a manifold of valves (fig. A.1). These valves are redirected

together to allow fluid to flow into the main hydraulic ram and out of the return rams to pressurize the hydraulic diaphragm loader or to allow fluid out of the main ram, and into the return rams to release the diaphragm. The fluid which is forced out of the rams is collected and cleaned before being used to refill the hydraulic pump reservoir periodically.

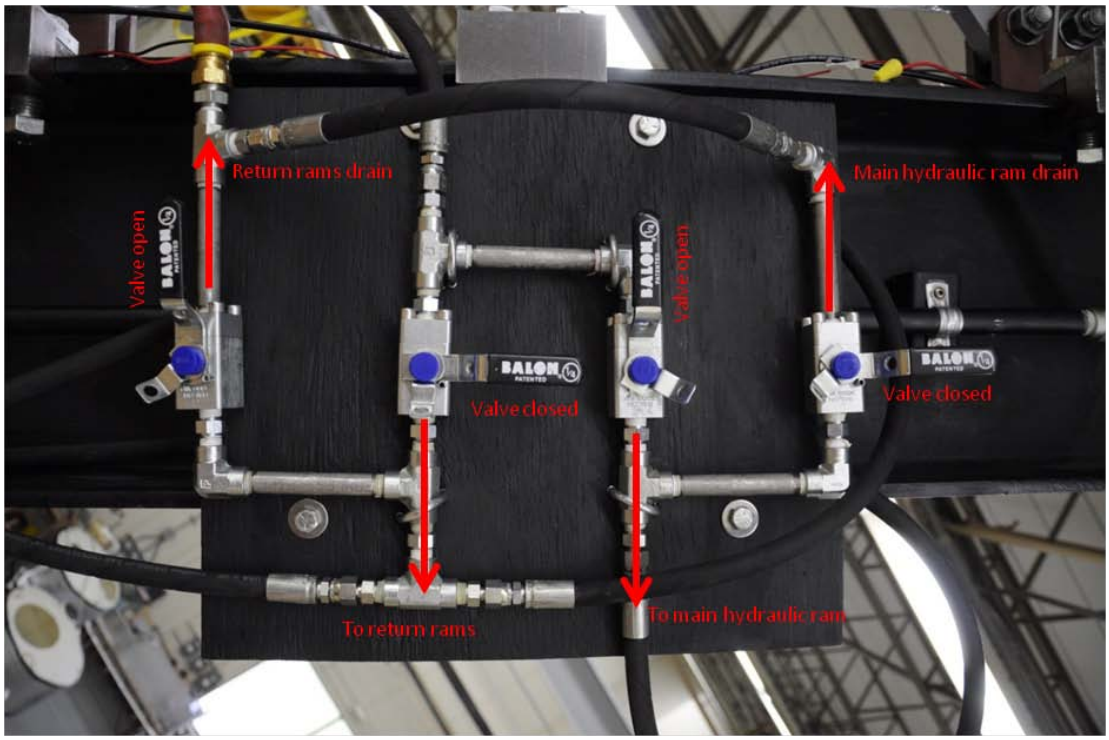

Figure A.1: Hydraulic diaphragm loader valve manifold.

A.2 Data Acquisition Instrumentation

The shock tube facility requires two distinct levels of instrumentation, one which measures the static state and conditions before an experiment and another which measures the dynamic quantities during an experimental run. Static measurements of the

initial conditions can be taken at a rate of 10Hz or less, while the dynamic quantities are measure at rates of up to 2MHz. The static instrumentation consists of static pressure transducers and thermocouples in the driver and driven sections. The location are illustrated in figure A.2. The driver static pressure transducer is designed for pressures up to 2000psi and is protected by a pressure snubber to protect it from the dynamic loads of the shock wave pressure. Despite this snubber this static pressure transducer registers the pressures of the shock wave well with only a small decrease in accuracy and temporal resolution. The driven pressure transducer is designed to read lower near atmospheric pressures and has a range of 30psig. To protect this pressure transducer from the shock pressures it uses a pressure snubber and a solenoid valve which closes before the shock is fired. An additional static pressure transducer is used to read the pressure in the boost tank. Three thermo couples are located on the tube, one in the driver, and one each at the top and bottom of the driven sections for registering the incoming temperatures of the light and heavy gases. One other thermocouple is used to read the temperature of the acetone seeding bath.

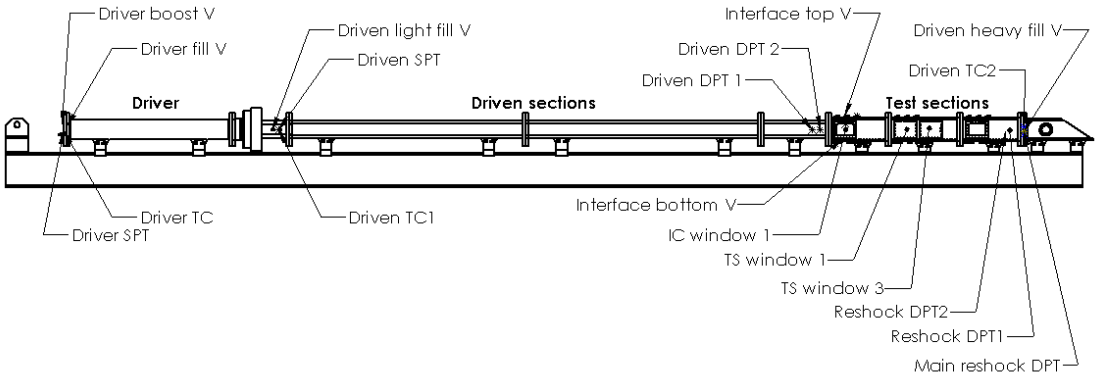

Figure A.2: Solidworks drawing of the shock tube with instrumentation and valve locations labeled.

The dynamic instrumentation system consists of five PCB Piezotronics, Inc. piezoelectric pressure transducers. These pressure transducers use a capacitive type measure that is capable of reading pressure changes at extremely high rates. Because they are capacitive type devices their signal decays with time and so they are only capable of reading dynamic changes in pressure, not steady pressures. These devices run to one of two signal conditioning devices which are used to change the signal into a voltage signal which can be read by the data acquisition hardware.

A.3 Optical Measurement System

The shock tube was designed primarily to acquire optical measurements of the interface to get 2D velocity and density fields. The optical access windows were discussed in the shock tube design section. Now the laser and camera systems will be discussed in detail in this section. Two primary methods for visualizing the interface are used in the shock tube, planar laser Mie scattering (PLMS) and planar laser induced fluorescence (PLIF). The Mie scattering technique is used for both simple interface

visualization, where one gas is marked by Mie scattering fog particles, and for particle imaging velocimetry (PIV).

PLIF works by striking a tracer molecule with a laser wavelength which excites an electron in the molecule to a higher state, which then re-emits energy in the form of light at a longer wavelength when it decays back down to its ground state. The fluorescence of molecules is dependent on the incident wavelength of light and the molecule properties. Many gases have been examined and evaluated as fluorescence tracer molecules. Many of these were reported on by Lozano in his thesis [122]. This work showed that given the laser technology available, in which only certain wavelengths of light may be produced at high powers, the best tracer molecule available was acetone. Acetone has a peak absorption of light at 275nm, and fluoresces with a broad band from 350 to 600nm with a peak near 450nm. The peak absorption is near the fourth harmonic of an Nd:YAG laser, 266nm.

Mie scattering is the effect of spherical particles scattering light which is incident upon them. Any spherical particle which has a different refractive index than the gas surrounding it can be used to provide a Mie scattering signal. Any wavelength of laser light could be used theoretically, but given the sensitivity of cameras to different wavelengths, and the power of the Nd:YAG laser at its various harmonics, 532nm light is the best choice. Mie scattering is used for visualization in the shock tube experiments by mixing tracer droplets of glycerin fog. This fog is generated by a fog machine which heats the fluid to vaporization then allows it to rapidly nucleate into small particles as it

is cooled. The particles generated by the pea soup fog machine used for these experiments are specified to be between 0.2 and 0.3μm.

Particle imaging velocimetry uses the illumination of tracer particles, in this case by Mie scattering, in two different images taken a short time apart to calculate a velocity field. This is an extension of particle tracking velocimetry where a single particle can be followed from one frame to the next, and then using its displacement vector and the frame straddling time the velocity vector can be found. For PIV a whole field of particles is used and the individual particles can no longer be tracked since one cannot be distinguished from another. Instead patterns in the tracking particle dispersals are found and statistically correlated to similar patterns in the next frame. The size of the integration area for these patterns determines the resolution of the vector field found. A smaller area allows for a higher density of vectors to be found but with a lower confidence.

The laser illumination for these two techniques can be provided by multiple lasers. The primary laser used for both these techniques is a dual cavity New Wave Research Gemini NdYAG PIV laser capable of providing 200mJ per pulse at 532nm and ~30mJ per pulse at 266nm simultaneously. Each cavity of this laser system can be fired at a rate of close to 20Hz, and the delay between the two cavities can be set using a laser synchronizer to as low as 500ns. While this laser system is capable of providing both required wavelengths simultaneously, it has been found that the 266nm light is not supplied in sufficient strength to acquire strong acetone PLIF signals. For this reason the laser system can be supplemented by a single cavity Quantaray NdYAG laser which is

capable of providing 60mJ per pulse at 266nm. This laser is an older system and its beam quality is somewhat lower, but sufficient for PLIF measurements. The Quanta ray laser is capable of a repetition rate of 15Hz.

The timing and power of NdYAG lasers running in Q-switch mode can be controlled by setting the delay between the flash lamp charging and the Q-switch activation. The flash lamp must be activated some time before the laser is fired to pump the laser medium. This laser medium reaches an optimal level of energy where it is said to be saturated. When the Q-switch is activated this pumped energy is used for optical amplification to generate the laser beam. The time between the flash lamp activation and the Q-switch activation will determine the power of the laser beam up to its maximum discharge energy when the laser beam has been optically saturated. By firing the Q-switch before or after the laser medium has been saturated the power is reduced. The time of these activations can be controlled by the laser with lower accuracy or by an external laser synchronizer device as is used for these experiments.

These lasers are directed from a laser table placed on the ground (fig. A.3) to the interior of the shock tube using multiple optical components to adjust the laser plane width and height for various experimental configurations. At the minimum a spherical plano-convex converging lens and a cylindrical plano-concave lens are required to adjust the width and height of the beam. The alignment of the beam from the horizontal path aligned with the floor to the angled path aligned with the shock tube at its inclination angle requires the use of a laser mirror which is capable of functioning with high

reflectivity at a wide range of angles. This is a more complicated set of requirements than it seems at first.

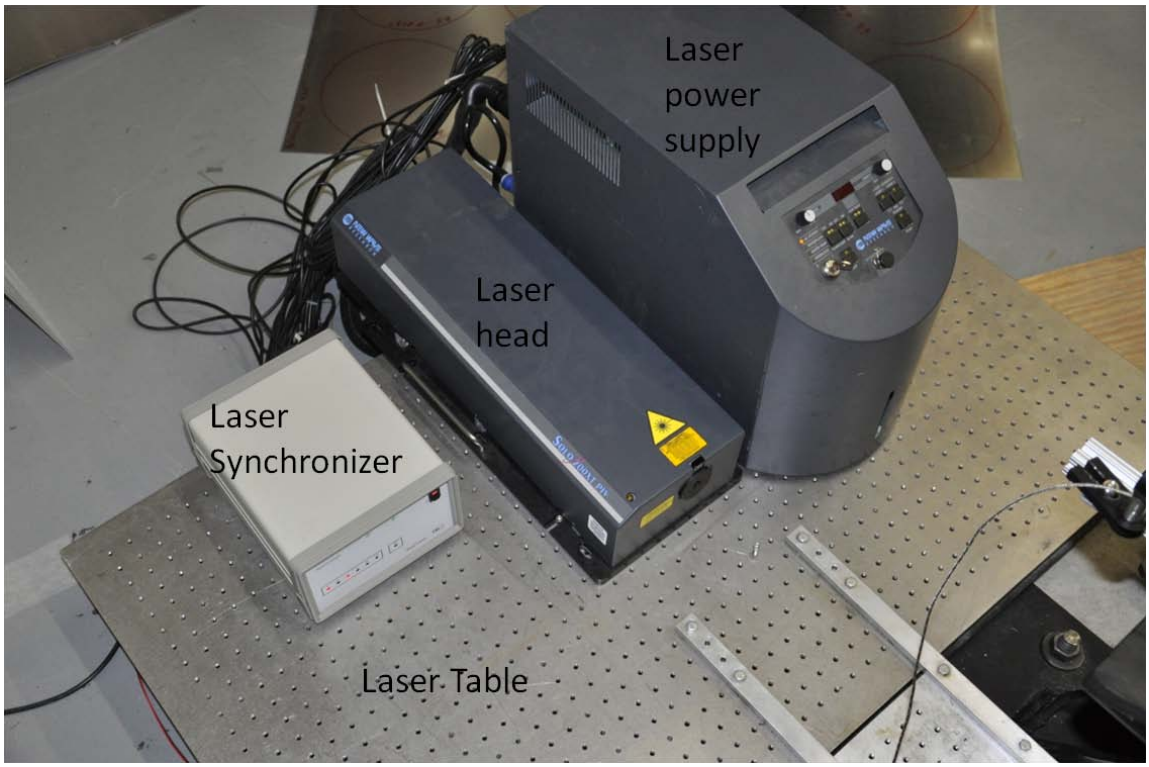

Figure A.3: Laser mounted on the laser table below the shock tube.

For running with the 266nm wavelength only an aluminum metallic mirror can be used which reflects over 80% at all the angles required for the shock tube experiments. This mirror is capable of reflecting all wavelengths of laser light required but is not capable of handling the energy flux of the 532nm laser which has nearly six times more energy per pulse than the 266nm. For the 532nm wavelength a laser line mirror optimized for 532nm light at a 45° incidence angle can be used with a reflectance of 80% or greater at all the required angles. No mirror has been found which can reflect

both the required wavelengths for simultaneous PLIF and PIV measurements at the required angles. Various methods have been employed to get around this limit. One method has been to expand the 532nm laser beam so that it has a lower energy flux and the aluminum mirror can be used, but this method has high beam energy losses. Another method is to use the Quantaray laser to generate the 266nm laser separately, and then allow each wavelength to reflect off of its ideal mirror and combine the beams before entering the tube. The ideal method for using both beams has yet to be developed though.

Two sets of cameras are available for imaging the interface using the Planar Laser Induced Mie Scattering PLIMS or PLIF techniques. Each of these camera designs has been optimized for PLIF or PIV, and so they will be referred to by the optimized imaging technique although they have been used for a wide range of techniques. The PLIF cameras are high quantum efficiency TSI, Inc. Powerview Plus 2 MP cameras. These cameras are optimized to detect the very low light levels of acetone fluorescence with little noise. The two PIV cameras are TSI Inc. Powerview 1.4 MP cameras. These cameras are designed to acquire two frames in rapid succession with frame straddling times as low as 1μs. The rapid frame straddling is accomplished by splitting one camera CCD array between two images. The first part of the array is only on for the first frame duration, then it turns off and the second part of the array is activated for the second image. These cameras can be coupled with various lenses depending on the application. For PLIF imaging a set of Nikon lenses with a 55mm focal length and maximum aperture size of f/1.2 is used. The large aperture capability of these lenses in required to

maximize the light that is received by the relatively weak fluorescence signal. For PIV imaging various lenses are used depending on the PIV image area. For taking PIV images with higher spatial resolution and smaller fields of view a Nikon macro lens is used which has a focal length of 50mm and can focus on objects as close as 0.3m from the lens. For larger fields of view many lenses can be used including Nikon lenses with 55mm focal lengths. A variety of zoom lenses with focal length from 28mm to 200mm have also been used.

The cameras are mounted on a thread plate similar to that of a laser table, which ride on rails that are connected to the shock tube support I-beam (fig. A.4). This allows the shock tube inclination to be changed without the need for repositioning the cameras. The cameras can be position in a configuration for imaging a window and then without having to realign them the whole thread plate can be moved on the rails to image a window at a different location or moved to image windows on the opposite side of the tube. Using the 55mm focal length lenses the cameras are required to be approximately three feet from the outside of the imaging windows to have a field of view which matches the window area. The use of wide angle lenses was decided against due to their optical distortion near the image edges. Since the 55mm lenses would require a long moment arm to the camera which might magnify shock tube vibration during an experiment and lower image quality, a mirror mounting system was designed which allows the camera to stay close to the tube and be placed at a 90° angle to the field of view. High quality aluminum metallic mirrors were paired with a custom designed

mirror mount which allowed the mirror angle to be adjusted using thumb screws (fig A.5).

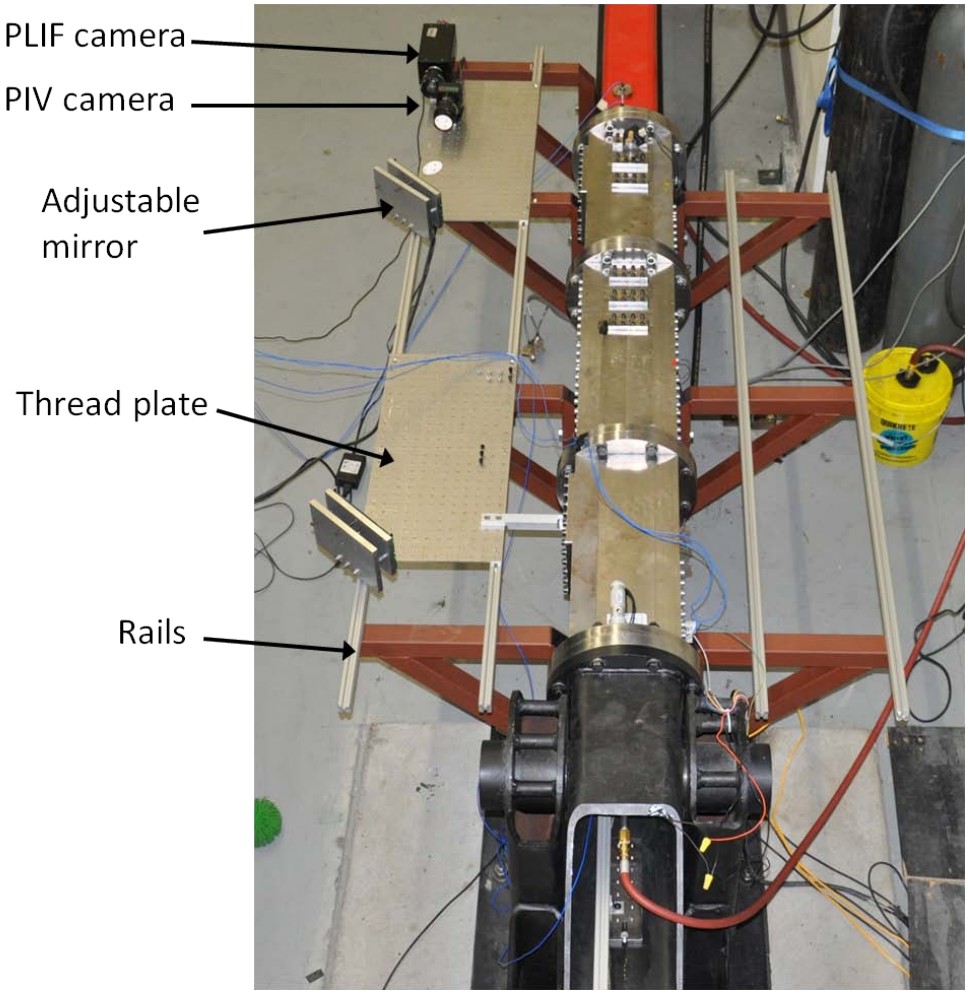

Figure A.4: Camera mounting plates with shock tube.

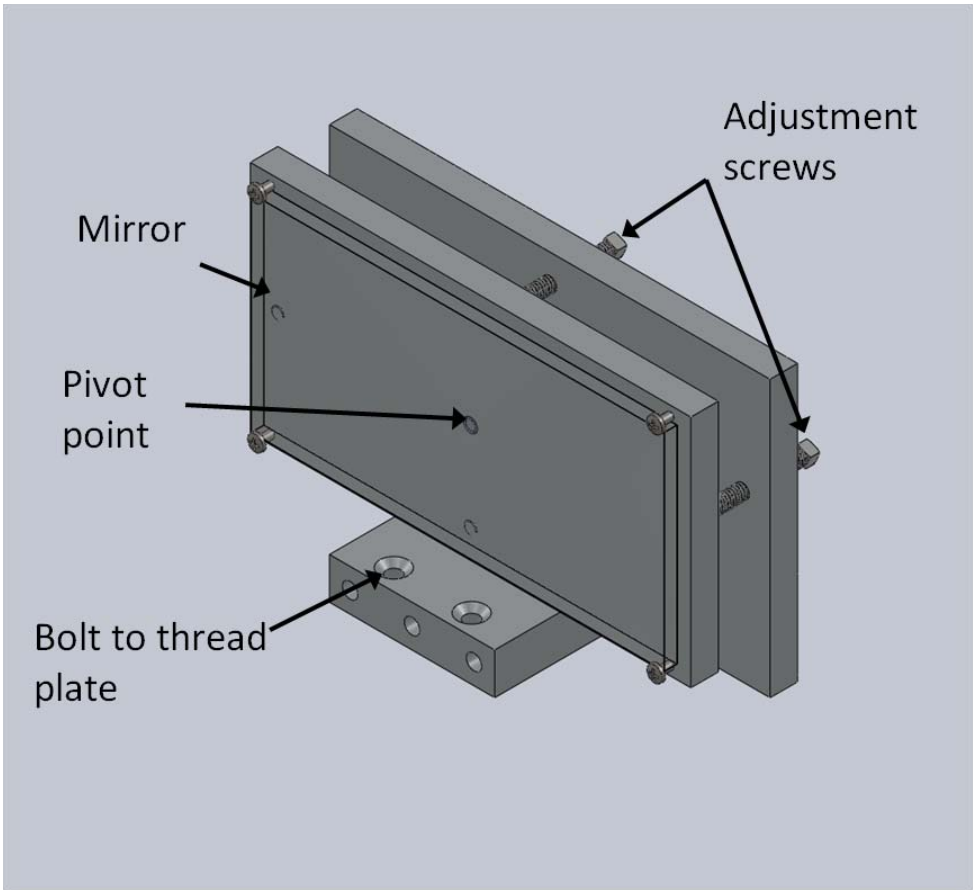

Figure A.5: Solidworks model of the adjustable mirror mount.

The cameras and laser timing are controlled using hardware from TSI, Inc. and their Insight3G program. This program must run on a 32bit Windows XP operating system and the hardware requires a high number of PCI slots so a custom computer was constructed to run them. This software is unfortunately incapable of driving more than three of the four cameras purchased so simultaneous PLIF and PIV measurements cannot be acquired in two locations without the use of a second instance of the program running on a second computer. The laser timing and power is set using a TSI, Inc. laser synchronizer which is controlled using the Insight3G software (fig A.6). This

synchronizer allows the laser timing and energy to be controlled precisely as discussed previously in this section. The software also allows the camera exposure times and durations to be controlled as well (fig A.7). Processing of the PLIF and PIV images is carried out using the software's built in tools (fig A.8). The triggering of the laser and camera systems in initiated by an external trigger which is generated by the LabVIEW program using signals from the dynamic pressure transducers.

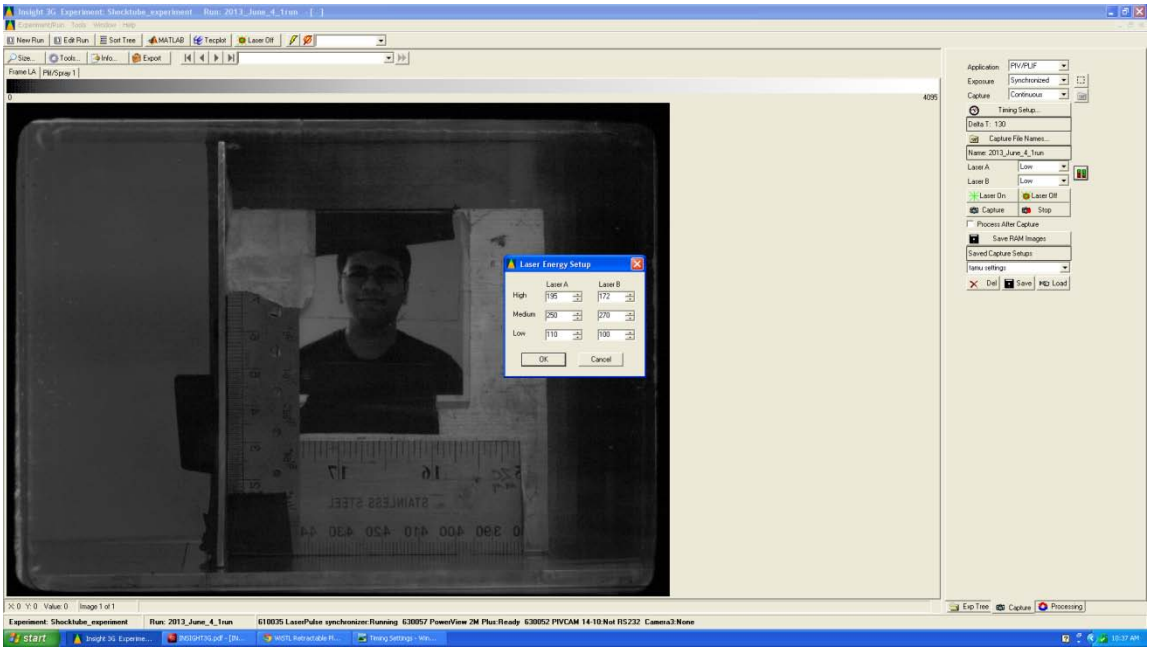

Figure A.6: TSI, Inc. Insight3G program screen shot showing the laser power settings.

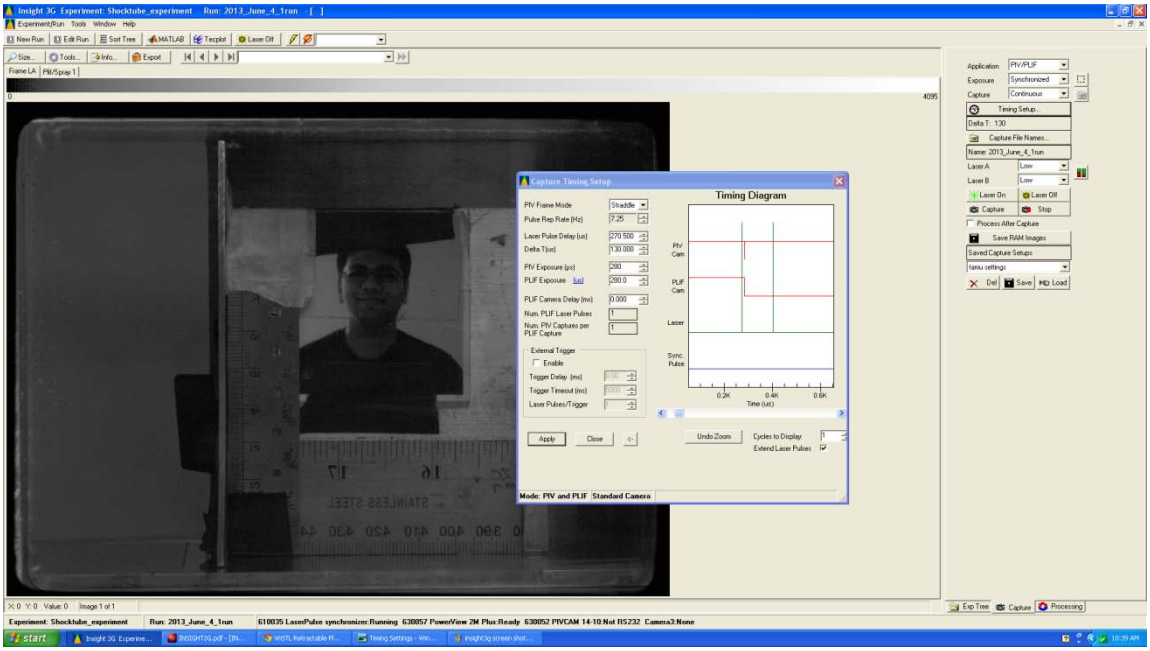

Figure A.7: TSI, Inc. Insight3G program screen shot showing the laser timing and camera exposure settings.

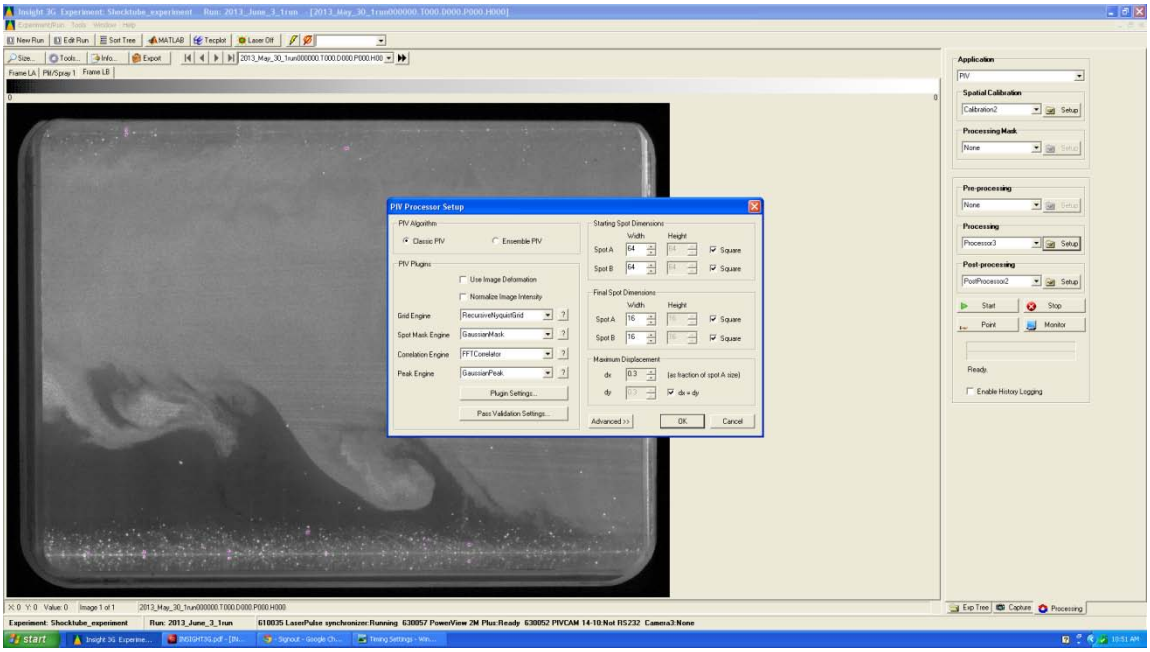

Figure A.8: TSI, Inc. Insight3G program screen shot showing the PIV processing settings.

A.4 Control Program and Hardware

The firing of shock waves, recording of data, and triggering of the optical systems is managed with a National Instruments (NI) PXIe-6368 Multifunction DAQ, and a CompactDAQ thermocouple module running with LabVIEW software. The multifunction DAQ is capable of both analog and digital input and output and has a maximum sampling rate of 2 million samples per second on up to 16 channels. These channels are used to acquire data from multiple static pressure transducers in the driver and driven sections and from piezoelectric dynamic pressure transducers installed in multiple locations to measure the shock and reshock pressures during an experiment. The dynamic pressure transducers are used for triggering of the camera and laser hardware and to trigger one of four 32-bit counter timers in the NI hardware. These counter timers are used to precisely trigger the laser and camera systems controlled by the TSI, Inc. hardware and Insight3G program. The MultifunctionDAQ is also used to control the solenoid valves on the tube for filling and firing of the shockwave as well as to control fog and acetone seeding systems. The CompactDAQ module receives data from four thermocouples mounted in the tube an in the acetone heating system. The interface of the MultifunctionDAQ and the CompactDAQ is illustrated in figure A.9 and A.10.

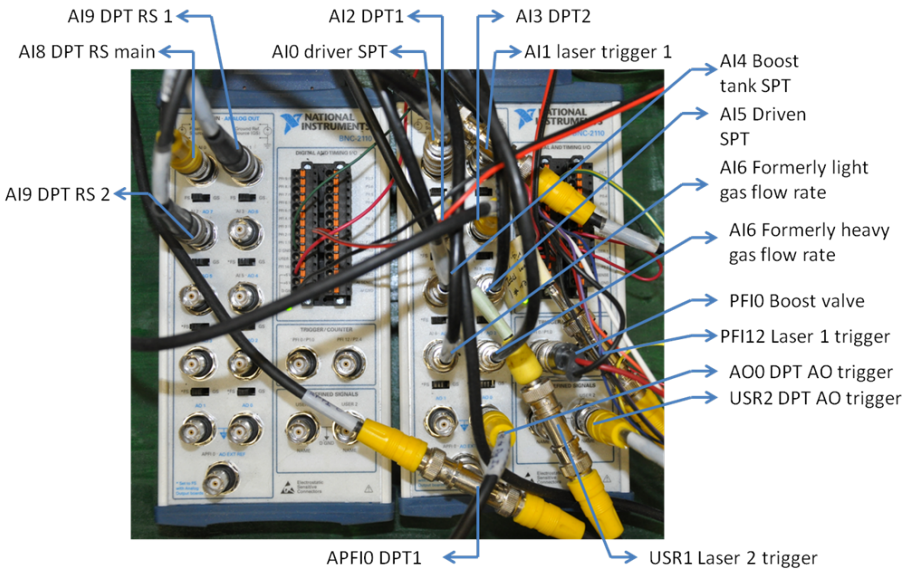

Box 1

to USR 2	PFI9/P2.1	P0.7	
	PFI8/P2.0	P0.6	
	PFI7/P1.7	P0.5	
Upper interface valve	PFI6/P1.6	P0.4	
Lower interface valve	PFI5/P1.5	P0.3	
Heavy gas fill valve	PFI4/P1.4	P0.2	
Light gas fill valve	PFI3/P1.3	P0.1	
Driven SPT valve	PFI2/P1.2	P0.0	
Driver fill valve	PFI1/P1.1	PFI13/P2.5	to USR 1
to all SSR grd	D gnd	D gnd	
to P2.1	USR2	USR1	to P2.5
Fog Machine SSR	PFI14/P2.5	PFI11/P2.3	
	+5v	PFI10/P2.2	
	+5v	AI sense	
	D gnd	AI gnd	

Box 2

	PFI9/P2.1	P0.7	
	PFI8/P2.0	P0.6	
	PFI7/P1.7	P0.5	
	PFI6/P1.6	P0.4	
	PFI5/P1.5	P0.3	
	PFI4/P1.4	P0.2	
	PFI3/P1.3	P0.1	
	PFI2/P1.2	P0.0	
	PFI1/P1.1	PFI13/P2.5	Acetone ssr
	D gnd	D gnd	Acetone ssr
	USR2	USR1	
	PFI14/P2.5	PFI11/P2.3	
sig inverter	+5v	PFI10/P2.2	
	+5v	AI sense	
sig inverter	D gnd	AI gnd	

Figure A.9: Annotated image of the Multifunction DAQ input/output blocks. The digital input/outputs are shown in two tables at the bottom of the image.

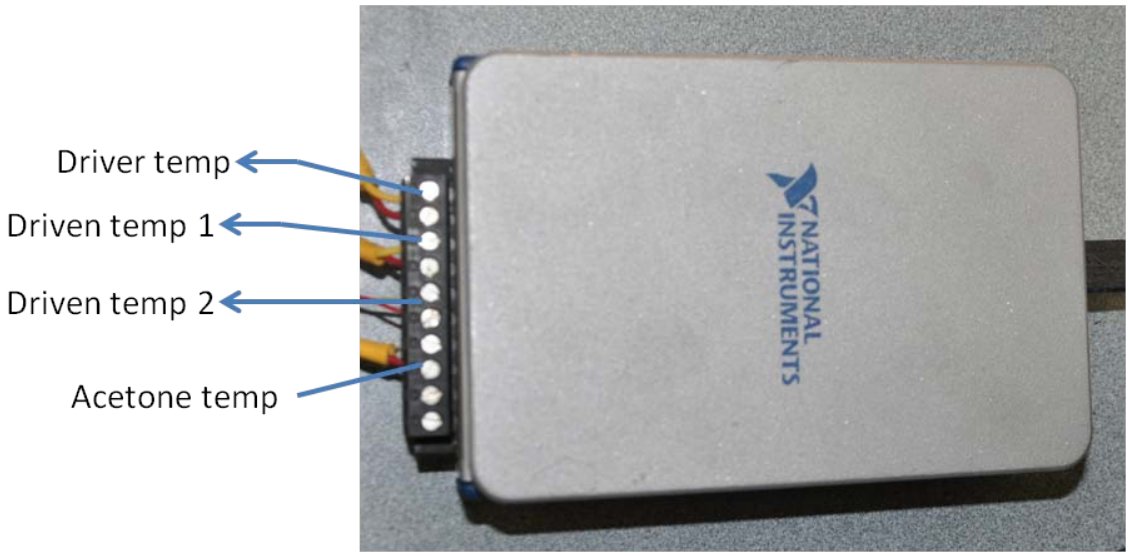

Figure A.10: Annotated image of the CompactDAQ thermocouple block.

The LabVIEW code was developed by the Author and another graduate student, Adam Hartzell, who was previously an employee and hardware engineer for National Instruments, the maker of LabVIEW. The code will be outlined in the following paragraphs and figures to explain its functioning on a basic level for future users of the shock tube facility. The front panel is shown in figures A.11 and A.12. The front panel is the basic input interface for shock tube users. It is divided into two tabs: the controls tab, and the conditions tab. The controls tab contains all the basic numerical and logical inputs as well as some simple data readings for quick reference while running the shock tube. In the top left corner is the arm system button. This button must be engaged to allow the fire shock button to appear. The color of this button will indicate whether the shock tube is in the correct condition to fire a shock. The correct condition means that the interface and fill valves are open and flowing but no other valves are open. If it is not

in the correct condition then the fire shock button will not appear and a shock wave cannot be initiated.

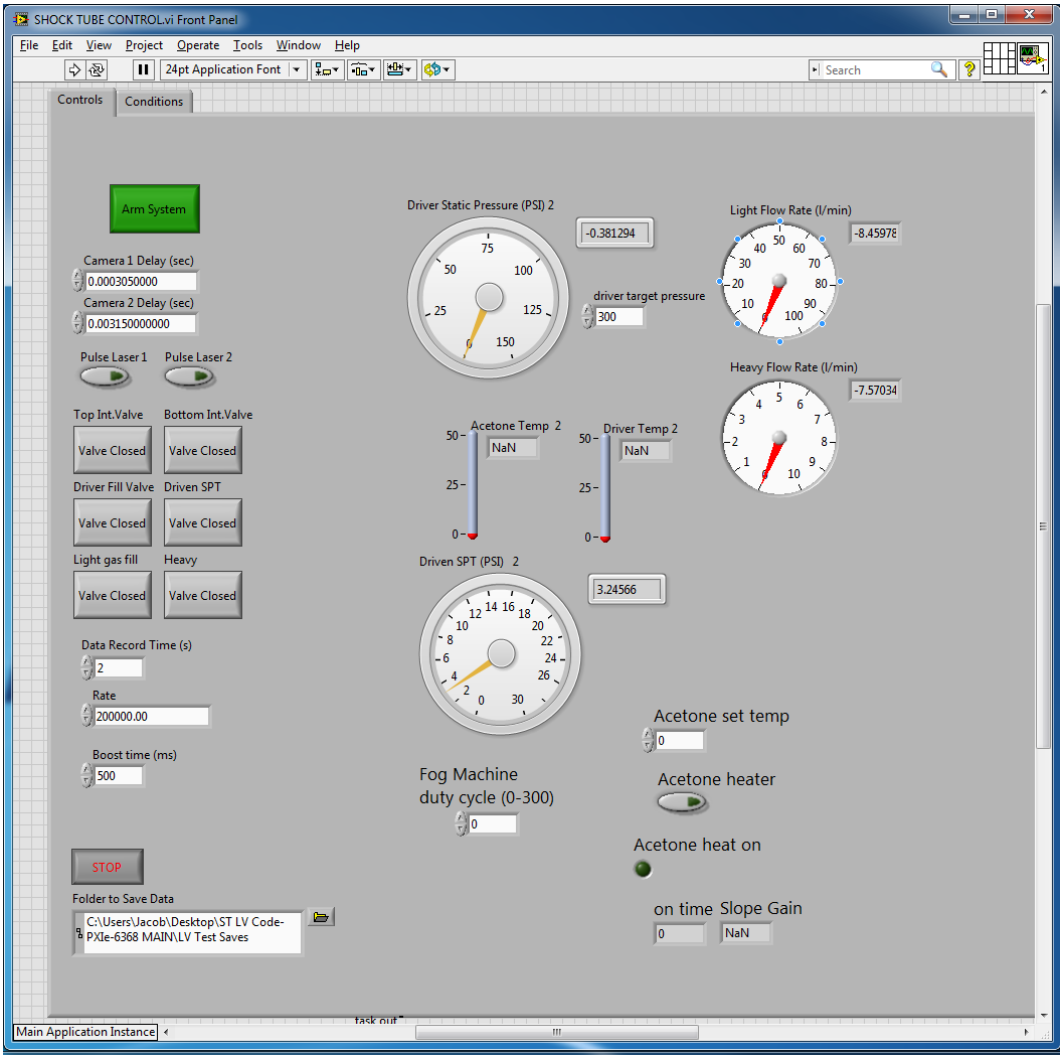

Figure A.11: LabVIEW program front panel controls tab.

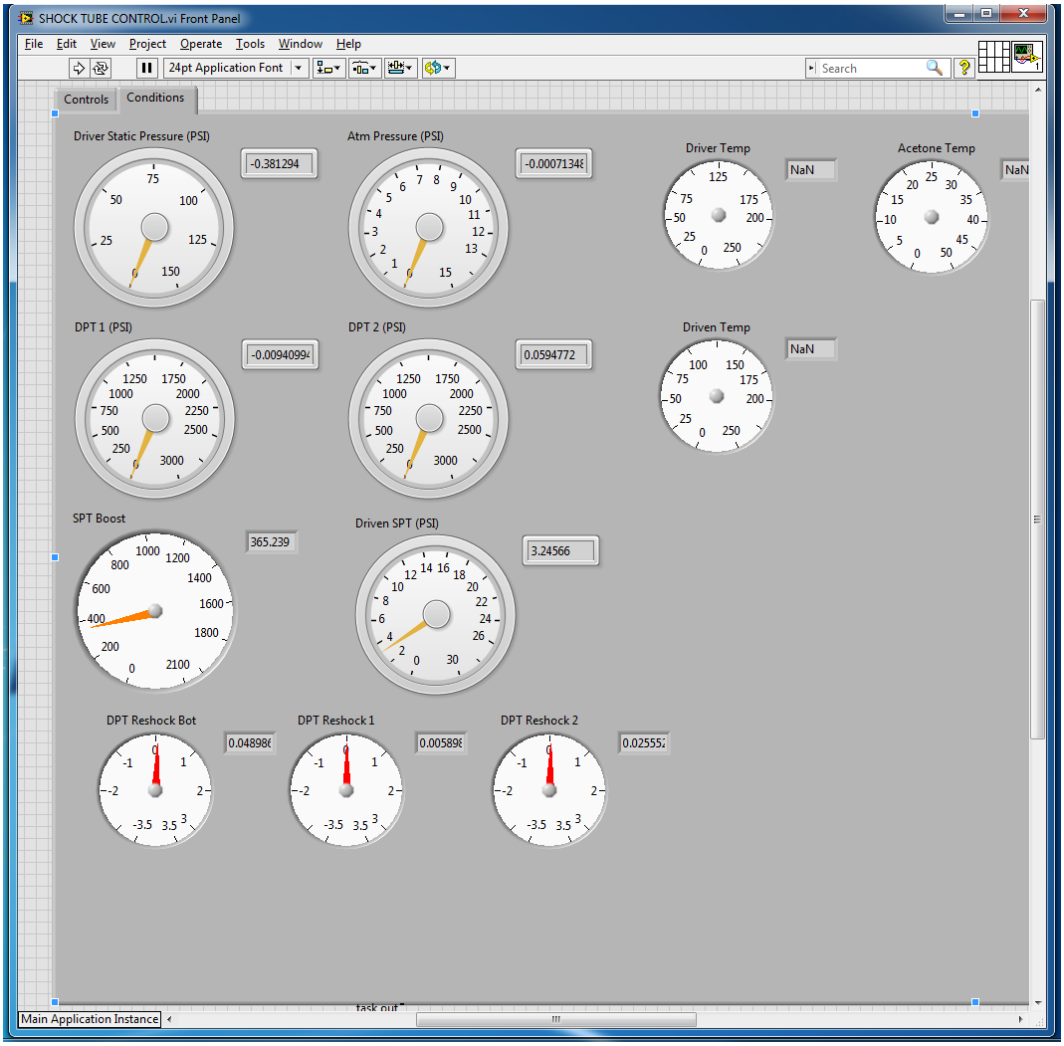

Figure A.12: LabVIEW program front panel conditions tab.

Below the arm system button are two numerical inputs which set the counter timer delays for the laser output trigger signals. In the current configuration only the camera 1 delay needs to be set as the Insight3G program and the laser synchronizer control the second laser timing. Below the camera delay inputs are two buttons which manually trigger the lasers. These are useful for testing that the laser timing is set correctly before running an experiment since they send a clone of the signal that will be

sent when the shock is fired. The valve actuation buttons are the next items on the left side. These buttons can be used to actuate the solenoid valves manually before their control is taken over by the program when a shock is fired. Below these are numerical inputs for the data record time: rate (in samples per second) and the boost valve open time. The data record rate can be set to a maximum of 2E6 samples per second. The boost valve time along with the boost tank pressure controls the volume of gas which will be added to break the diaphragm. The lowest button is the stop button which turns off all digital channels and halts the program.

Further to the right in the front panel are meters for the driver pressure and the driven pressure, along with temperature and flow rate gauges. There are three numerical inputs on this side. The driver target pressure is used to automatically shut off the fill valve when this target pressure is reached. The fog machine duty cycle can be used to set the duration the fog machine is activated if fog machine cycling is needed. Also a numerical input for the acetone temperature is located on this side of the front panel. The other numerical inputs on this side are used only to regulate control function of the acetone heater to reach the acetone temperature set point. Lastly in the lower right hand corner is the file path for where the data will be stored when a shock is fired. The file names are automatically generated. The conditions tab merely contains dial gauges for all analog input signals. This panel is useful for checking the function of these transducers before a shock is run and their data is recorded. Figure A.13 shows the indicator display VI front panel. This is a separate program which acquires data from the main VI at asynchronous rates using global variable VIs and displays it on a second

monitor. This monitor is a large 55” monitor that faces the lab area so that the condition of the tube is known to anyone in the area. This is a safety measure so that it is easily known if there is pressure in the tube or if the system is armed and a shock is impending.

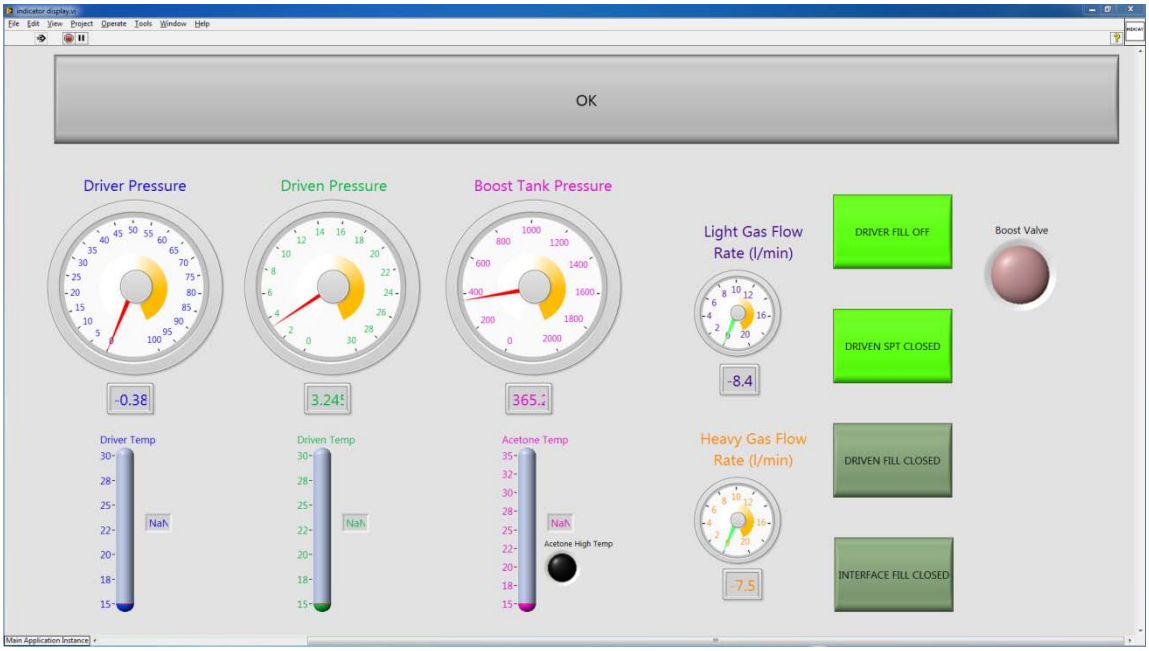

Figure A.13: LabVIEW indicator display VI front panel.

The block diagram for the main program is shown in figures A.11 through A.15. Figure A.14 shows the start up conditions for the program where the valves are all set to default conditions first. Then the indicator display VI is started and set to display on the second monitor. Figure A.15 shows the simple control loops for the manual laser triggering signals. Figure A.16 shows the valve control block and the pressure display outputs. The valve control writes to the digital output lines and must be set to certain conditions before the fire shock button becomes visible. The temperature acquisition, fog

machine cycling, and acetone temperature control loops are shown in figure A.17. All of the above function loops are stopped when the fire shock button is engaged. Only after these loops have terminated can the program move to dynamic data acquisition and control loop. This loop appears in a simple form in figure A.18 but the VIs is called in this part of the program are the most complex VIs in the shock tube control program. Also seen in figure A.18 are the defaults which are set for all digital out signals when the program is stopped.

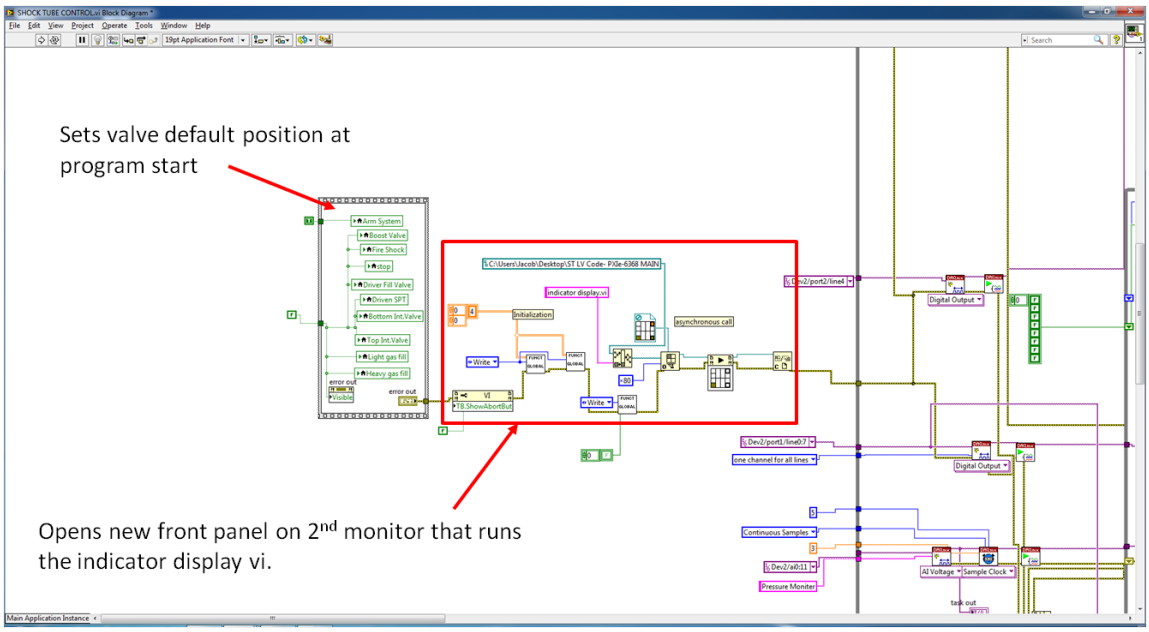

Figure A.14: LabVIEW ST control program block diagram initialization.

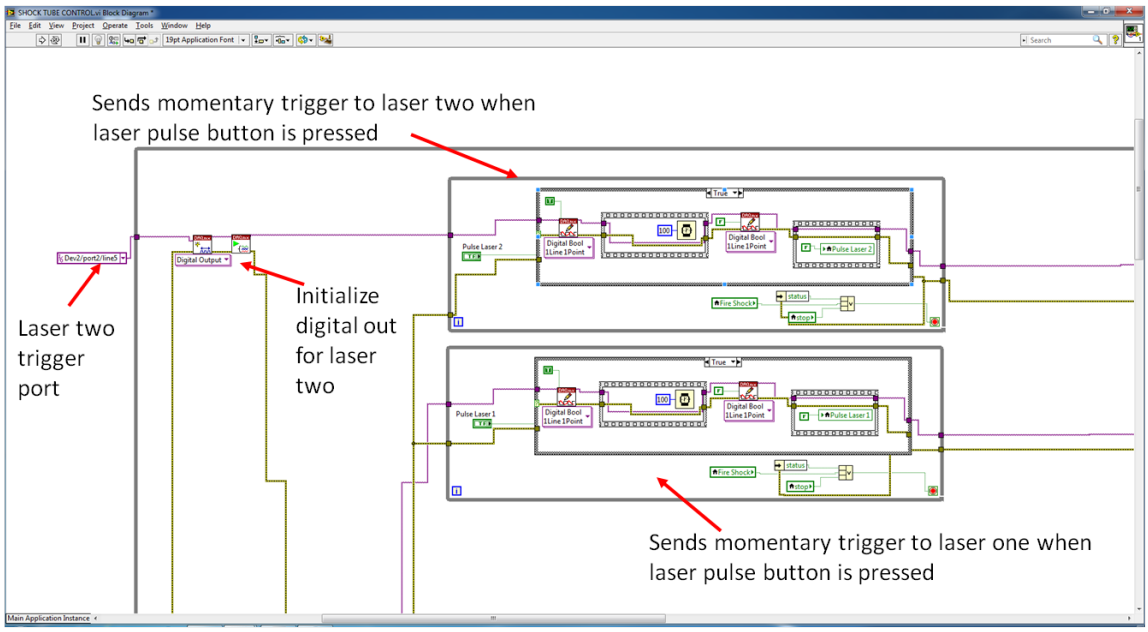

Figure A.15: LabVIEW ST control program block diagram laser test firing signals.

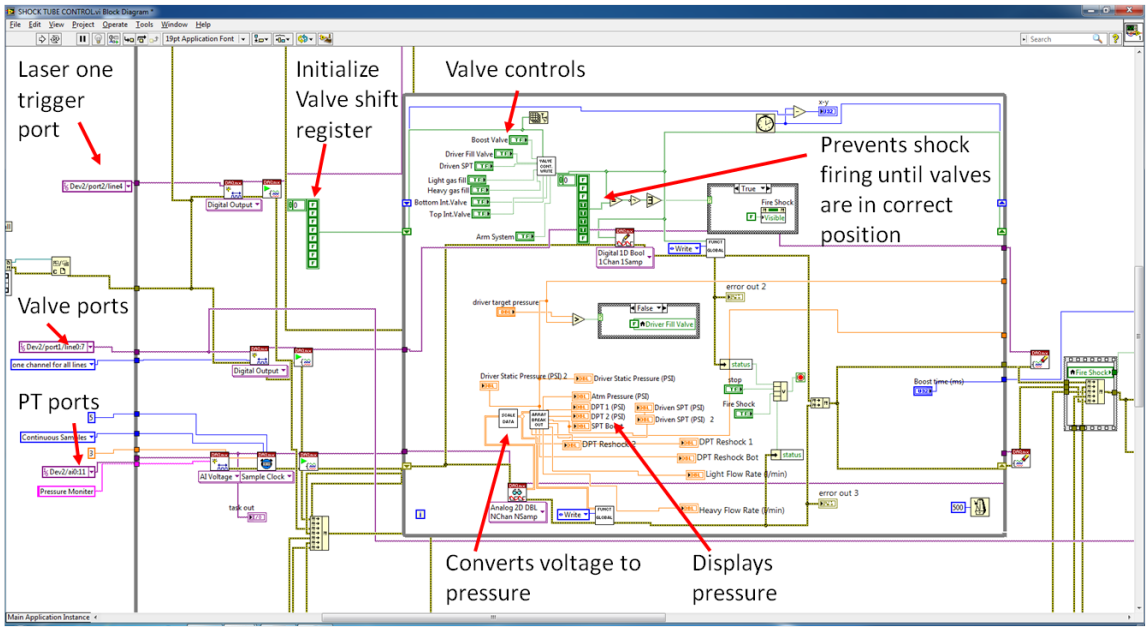

Figure A.16: LabVIEW ST control program block diagram valve control and pressure display.

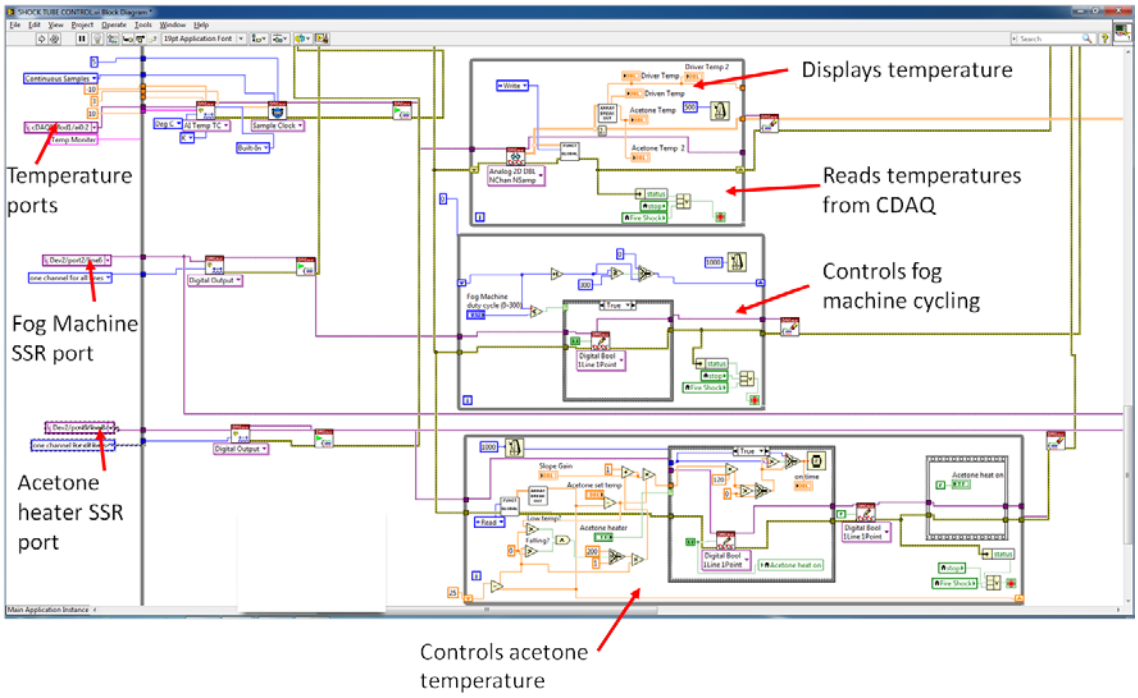

Figure A.17: LabVIEW ST control program block diagram temperature display, fog machine cycling, and acetone temperature control loops

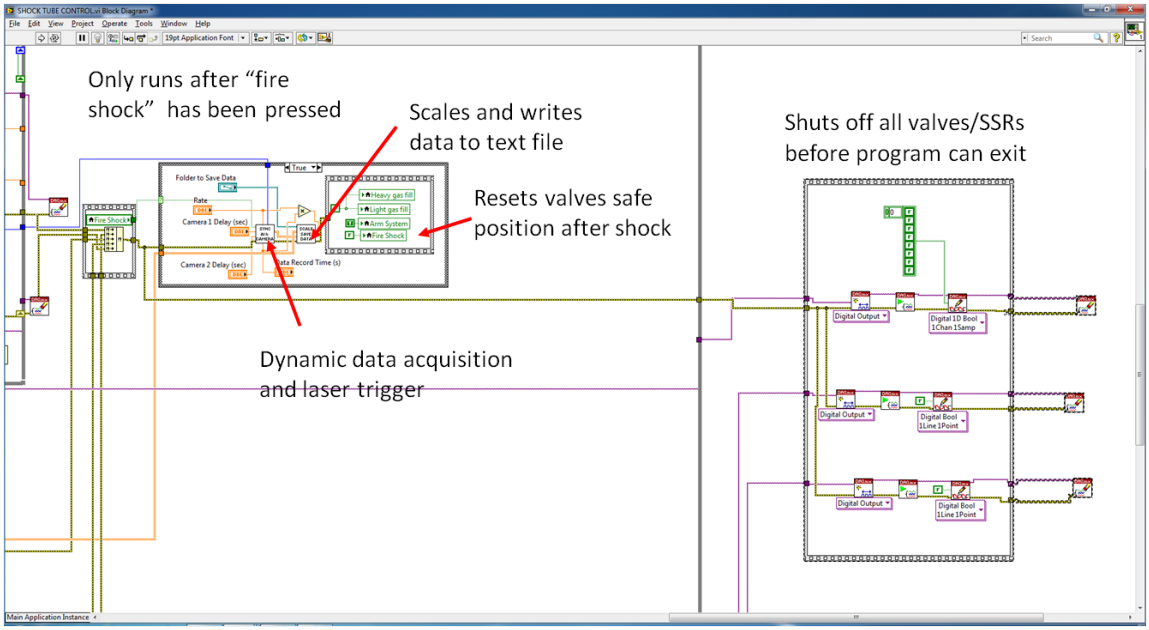

Figure A.18: LabVIEW ST control program block diagram dynamic data acquisition, camera triggering, and program closing functions.

The sync AIs (analog instruments) camera VI that is called when the fire shock button is pressed sets up the data channels to be recorded during an experiment and the trigger signal timing delays (figs. A.19 and A.20). This VI also controls the closing sequence of valves that must be executed as the boost valve is initiated. It has all valve functions wait for 200ms as the data record and camera timing function are set up on the computer before being run in the hardware. The set up of these functions is relatively slow compared to the hardware executed function as it occurs on the PC. This is why the shock firing must be delayed slightly. The fill valves and interface valves wait a set amount of time before closing while the boost valve opens immediately. This may seem out of order but even through the boost valve has opened the actual rupturing of the diaphragm will not occur for 500ms or so.

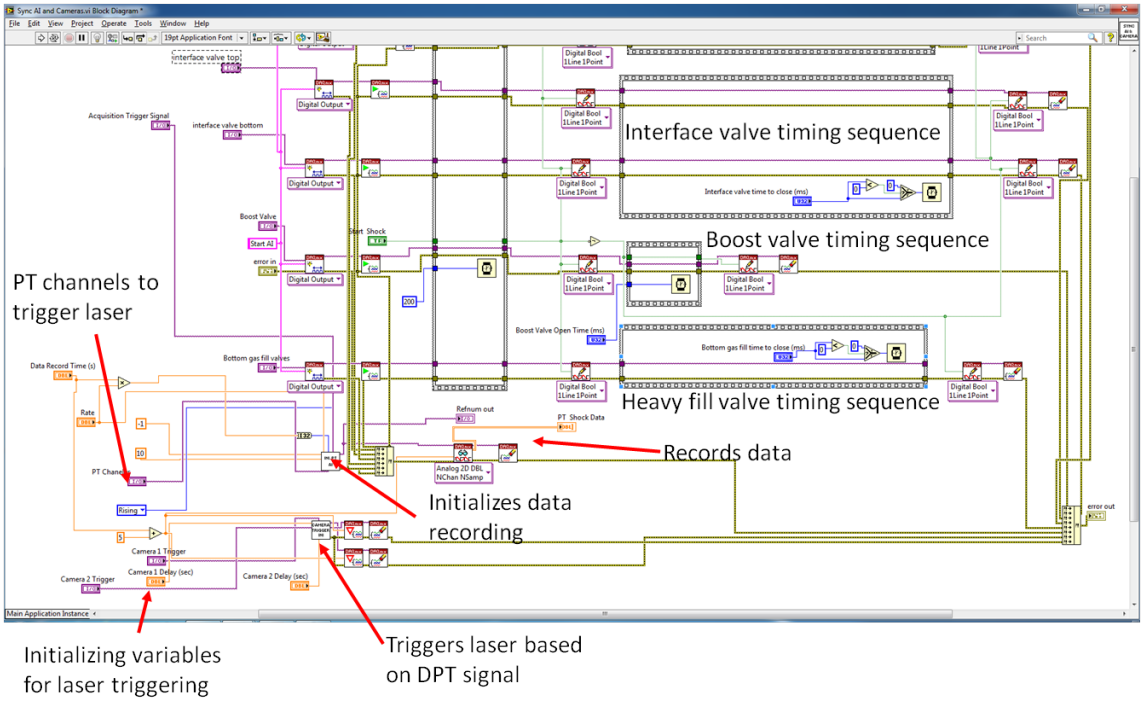

Figure A.19: LabVIEW sync AIs camera VI block diagram valve timing loops, data acquisition set up, and camera triggering.

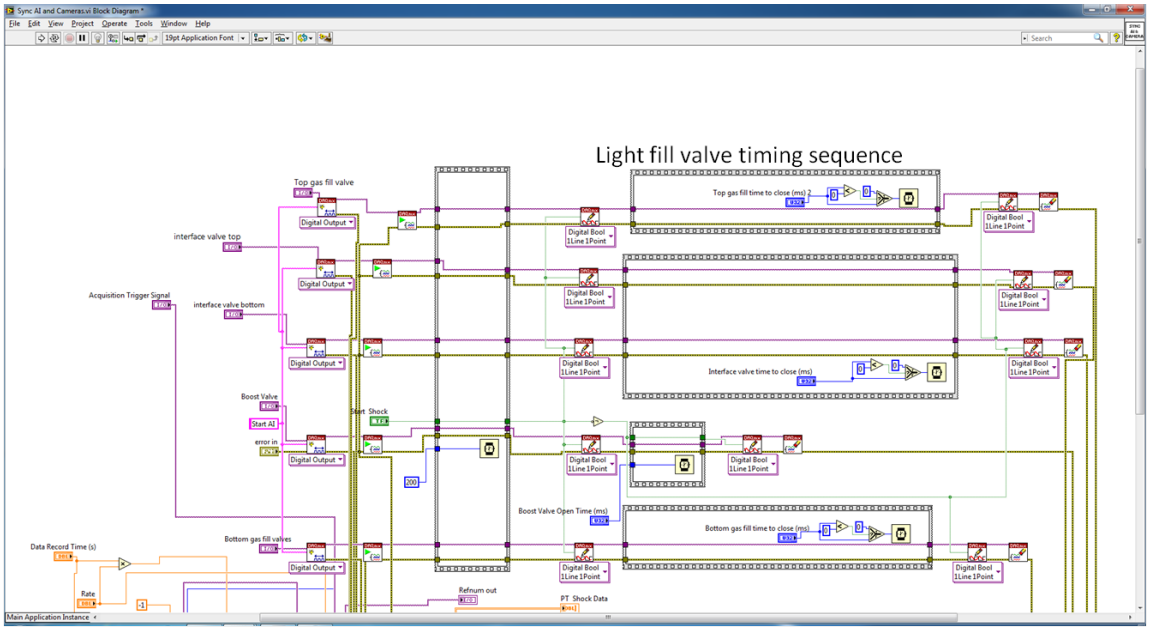

Figure A.20: LabVIEW sync AIs camera VI block diagram valve timing loops.

The laser trigger is initiates in the camera trigger VI shown in figure A.21. This VI first sets up an analog output signal which will act as a digital trigger for the counter timers. This seems like an odd way to start the counter timers, but it was found that even the internal triggering method required that a dummy analog out signal be set up. So, while this method seems inefficient it was found to be equal in efficiency to the internal triggering method and easy to trouble shoot. This analog output signal will act just like a digital signal in that it is a 5V pulse with a square wave front. This pulse is generated at the instant the DPT signal rises above 0.1V. The noise from the DPT signals is usually below 0.01V, so any rise above 0.1V will signal that a strong pressure front (the shock wave) has reached the DPT. The analog signal is then sent out and read by a digital input channel which starts two counter timers which will generate digital trigger signals at a precise delay time with a resolution of 10ns. This signal then initiates the camera and

laser hardware to activate at precise times capturing images of the interface as it enters the camera field of view.

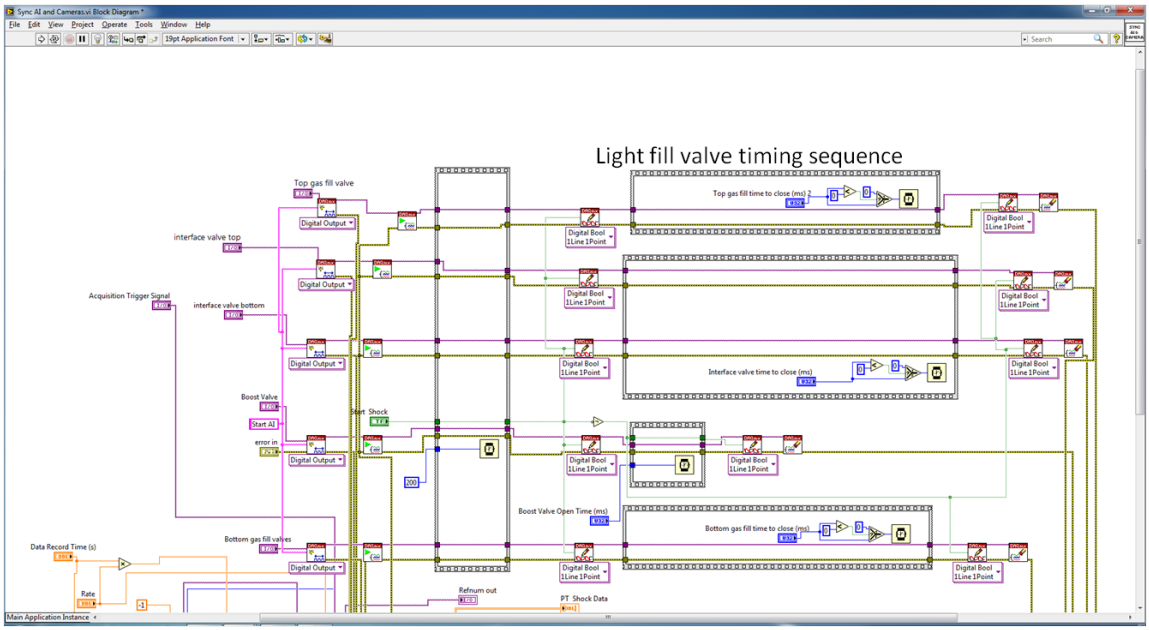

Figure A.21: LabVIEW camera trigger VI block diagram.

APPENDIX B: SHOCK TUBE OPERATING PROCEDURES

When operating the shock tube it is important to keep in mind at all times that it is located very high off the ground and composed of very heavy parts under very high pressure, meaning that there are a great deal of potential dangers when working with the shock tube. On the instrumentation and controls side there are many electrical connections which carry 120v AC power to the solenoid valves that can be electrical hazards. The laser systems also present significant risks since they operate at powers that are high enough to not only cause eye damage but to cause skin damage as well.

B.1 Setting the Inclination Angle of the Shock Tube

The shock tube is in its safest state when it is in the horizontal position resting on the ground. Raising the tube into position is a two to three person job. To raise the tube into position the crane must be used. The crane hook uses a latching mechanism to be sure it does not disengage from its load. When connecting the crane to the tube ensure that the crane hook latching mechanism is closed around the shock tube hoist pin. It is also important to ensure that the crane hook is centered between the hoist point mounting plates. As the angle of the tube rises the hook pulleys will need to travel between the two mounting plates. If the hook is not centered the pulleys will get caught on the hoist point mounting plates. Once the crane is correctly attached to the tube ensure that one person is in position to watch all the lower end of the tube for interference or wire snags as the tube is raised. The other person will raise the tube using the tethered crane control. The crane has two speeds for lifting that are engaged by pressing the “up” button lightly or heavily. Use only the slow speed when raising the

tube. Try to continuously raise the tube without stopping if possible since each time the tube is stopped its momentum cause a bounce in the cables and overhead cranes system. The north-south position of the crane must also be maintained as the tube is lifted to follow the hoist points arc. The crane trolley beam which moves from north to south can be activated while the crane hoist is lifting so the tube may be lifted continuously in an arc. Do not let the crane pull the shock tube at an angle. Keep the hook cables perpendicular to the ground.

The tube angle may be checked using the digital inclinometer. It is advised to bring the tube 0.1° above the set angle while the shock tube stand is positioned since when the tube is released from the crane to rest on the stand some small amount of settling is expected. The shock tube stand may be wheeled into place by two people. The floor bolt mounts should already be in place, so the stand will need to be carefully maneuvered around these so that it may be bolted to them when in position. If the mounts are not in place they must be bolted to the floor using grade 8 bolts torqued to 80ft-lbf. The leveling feet on the stand can be engaged to raise the stand off its wheels. Do not raise these feet any more than necessary to remove the stand load from the wheels. The floor mounts bolt to the shock tube stand using grade 9 ½" bolts which must be torque to 100ft-lbf. With these bolts in place the shock tube can then be lowered to rest on the stand.

B.2 Installing the Optical Access Windows

To install windows in the tube a strict procedure must be followed. The fused silica windows are very strong but prone to chipping and must be handled with extreme

care. Check to make sure the window hole is free of debris, the o-ring is in place and in good condition, and that there is a small amount of grease present on the surface of the window hole. Insert the window (mounted in its steel flanges) into the window hole in the test section. Run the socket head cap screws down using finger tightening only at first. The screws must be torqued down in a star pattern (fig. B.1) in three rounds of increasing torque. Start with the corners tightening to the first level of torque, 4N-m. Have a second person reach inside the tube with a feeler gauge of 0.002" thickness and insert it between the window's upper and lower edges and the shock tube walls to check that there is clearance. Repeat the feeler gauge check at each round of torque application. If at any point the feeler gauge becomes tight between the window and tube stop tightening, unload all screws, and check for an explanation. The windows will break if the clearance is not maintained as the windows are tightened into place.

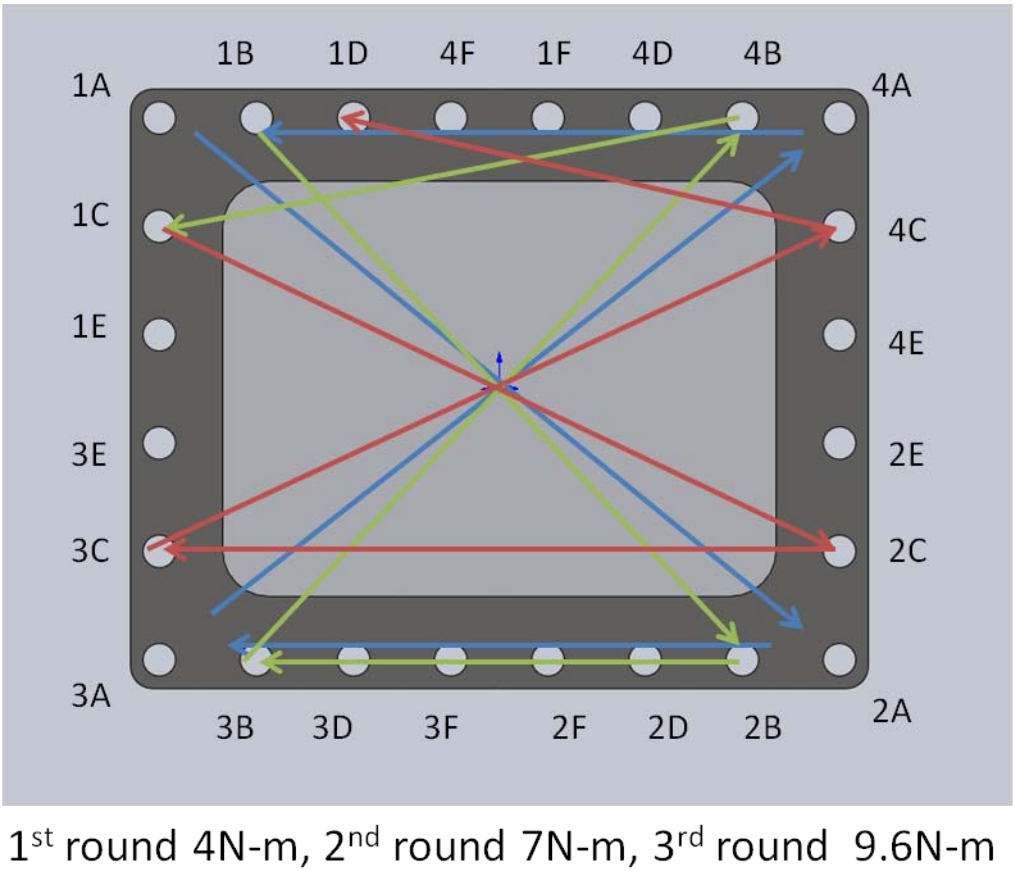

Figure B.1: Window torque pattern.

B.3 Aligning the Cameras and Laser Sheet

The camera tables can be aligned with the windows now using the feeler arms which attached to the tables (fig. B.2). These pieces of aluminum will catch the window flange edge constraining the position of the table. Loosen all bolts holding the window tables in place and attach the feeler arm. Slide the table down the rails until the arms are pressed against the window flange, and then bolt the table down to the rails tightly. Position the cameras in the proper locations, and ensure they are level with the tube using shims if necessary. Turn the cameras on and start the Insight3G program. Put the

capture mode into continuous free mode so that a continuous video of what the cameras are seeing is shown in the program. Then use the mirror adjustment screws to align the camera field of view with the window. A calibration block (fig. B.3) can be slid into the window field of view to focus on. This block must be pushed flush against the wall of the tube behind the window so that the focusing image is directly in the center of the tube. This block can be held in place by its powerful magnetic base while the tube is inclined. The focus of the camera can now be adjusted. Take and save a calibration image using Insight3G. This image can be used to calibrate the distance per pixel since the calibration block contains a ruler.

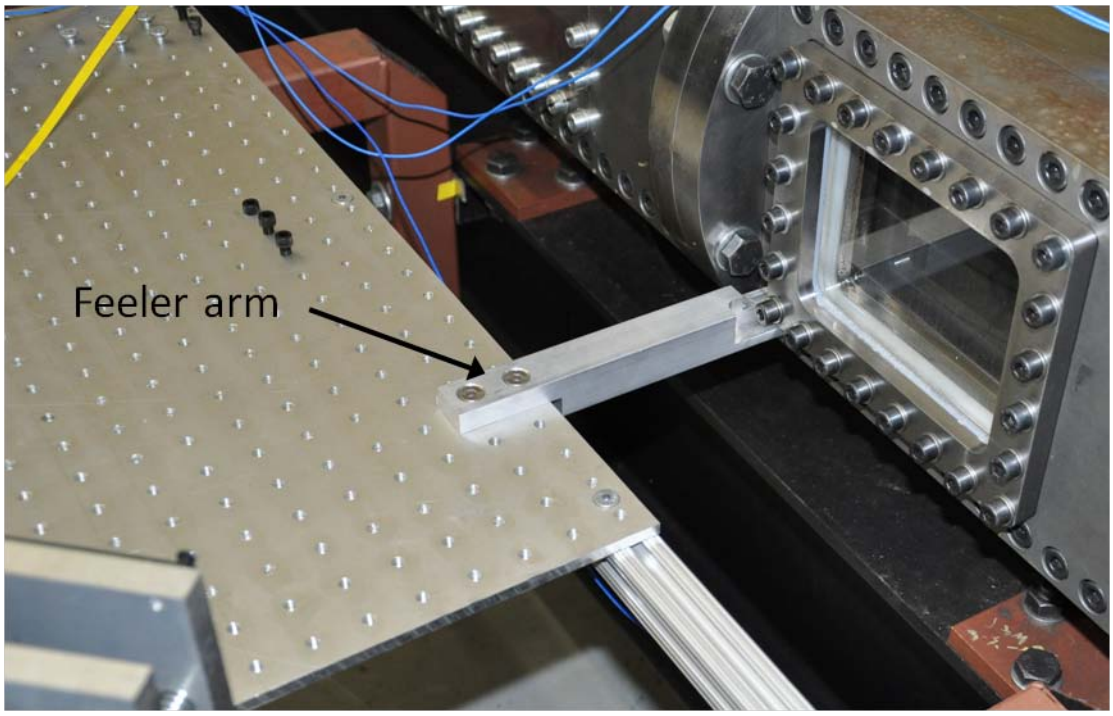

Figure B.2: Camera table feeler arm which is used to position the camera tables relative to the window position.

Figure B.3: Camera focus calibration block with a practice image of STAML PhD student Bhanesh Akula attached to focus on.

With the calibration block in place the laser sheet alignment and dimensions may also be checked. The calibration block has a targeting surface oriented at 90° to the focusing image which contains a target pattern for the laser sheet. To test the laser sheet alignment it is recommended that the laser be in continuous mode using Insight3G and that the laser power be set, in this program, to a very low level so that the beam may be viewed with a decreased risk to the human eye. If the laser sheet is not in the correct position the recommended adjustment procedure is as follows: remove the plano-concave cylindrical lens from the laser path so that only a point can be seen on the calibration block. Using the mirror align this point so that it is in the center of calibration

block. Adjust the spherical plano-convex lens or replace it with a different focal length so that the beam point on the calibration block is near its minimum size. Then check that the position of the beam as it enters the laser window at the bottom of the tube, or alternatively move the calibration block to a lower position in the tube to check that the point is still in the middle of the block. This effectively finds two points on the beam path line which defines its trajectory and ensures that it is parallel to the tube and centered. If it is not centered at both points, then the mirror position and angle must be adjusted to center it. Now place the diverging plano-concave cylindrical lens in place and check that the beam is fully diverged and still centered from top to bottom in the tube. If the beam is not fully diverged the position of the diverging lens must be changed or it must be replaced with a lens of a different focal length. Once the beam plane has been perfected, check to make sure that no parts of the beam plane are being clipped off as it passes through the laser window at the bottom of the tube. If parts of the beam are being clipped this will result in beam power loss and the lenses should be readjusted to ensure that the whole of the beam passes freely into the tube.

B.4 Setting Up the Fog and Acetone Seeding Systems

To visualize the interface with the fog seeding system the fog machine will need to be connected with the light gas using the fog settling chamber (fig. B.4). The fog machine must be turned on and allowed to warm up for approximately ten minutes before running it. The fog machine uses gas to pump the fog fluid so it must be connected to its ownt gas bottle. A mass flow controller can be used to set the mass flow rate for the gas which will control the seeding density. The pressure regulator on the

bottle should be set to ~10psi. By trial and error it has been determined that for PIV imaging a low flow rate on the order of 0.02 SLM should be used. For Mie scattering images a flow rat of closer to 1SLM can be used. Adjustments in the flow rate will take five minutes or more to manifest themselves at the interface since the shock tube fill flow rates are so low. The fog machine should then be plumbed to the fog settling chamber using a short large diameter piece of hose. Make sure that the fog machine is above the inlet to the fog box so that any condensing fog fluid will run down into the box. The box should then be connected to the light fill gas which is controlled by a separate mass flow controller. Set the pressure regulator on the bottle to less than 5psi. The light fill gas flow rate is usually set to 8.0SLM. The fog settling chamber has a pressure relief valve that will activate if the pressure in the chamber rises above 1.5psi. The fog settling chamber should then be connected to the light gas inlet solenoid valve.

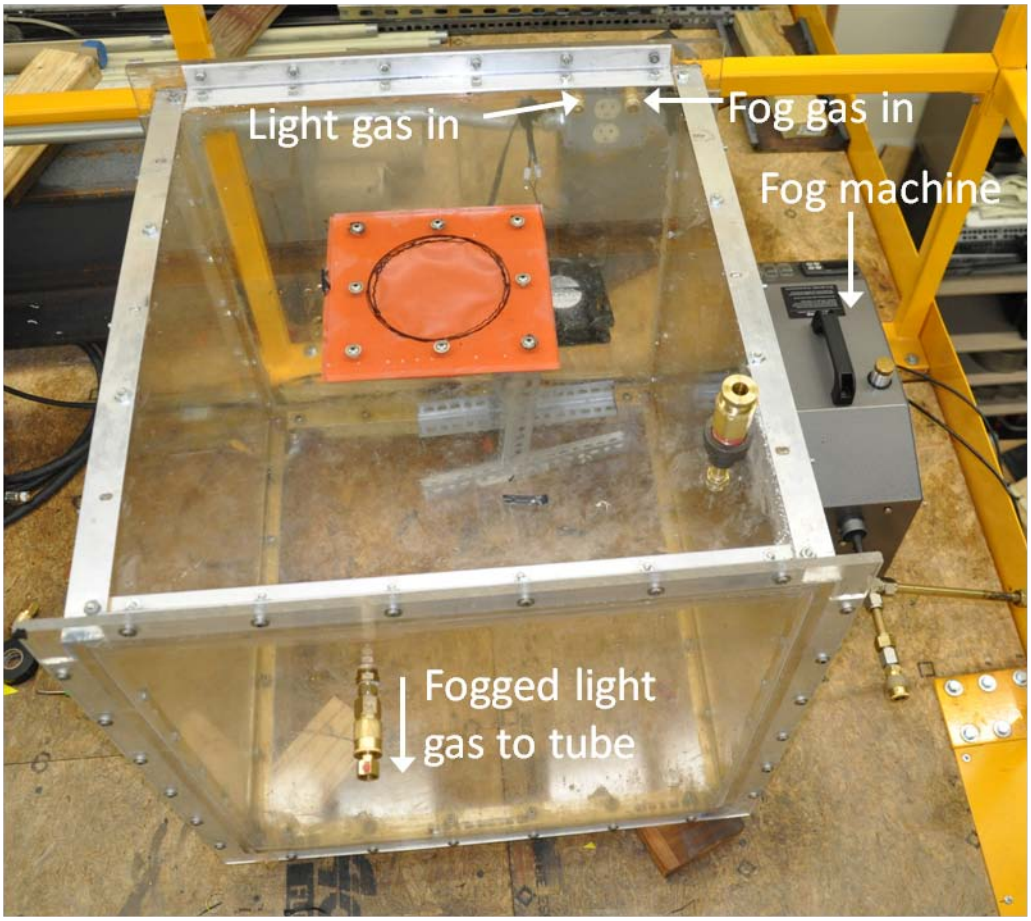

Figure B.4: Fog settling chamber and fog machine.

To run acetone PLIF experiments the light gas should be connected to the acetone bubbler (fig. B.5) after the mass flow controller. This device forces the light gas to rise through a tube of liquid acetone picking up the acetone as a vapor. The level of acetone in the bubbler should be maintained at a level well above the acetone heater core. The acetone temperature can be controlled using the LabVIEW program. It is recommended that the temperature be set to 20°C and that the temperature never be set higher than 40°C since this will result in the acetone boiling. The acetone bubbler has a protective over pressure blow off valve that will release pressure if the pressure increases

above 5 psi. The acetone bubbler outflow should then be routed directly to the light gas inflow solenoid valve. The recommended flow rate is again 8.0SLM. In the event that a simultaneous PLIF and PIV experiment is to be run the acetone bubbler should be connected in line with the light gas flow before the fog settling chamber. An inline moisture separator should be placed before the fog box to remove condensed liquid acetone so that it does not come into contact with the acrylic fog settling box. It is expected that the acetone vapor may cause some mild corrosion of the fog settling chamber with time, but this a problem that will have to be solved when it arises. The heavy gas should be routed from the gas bottle through the pressure regulator, set to 5psi or less, to the mass flow controller and then to the heavy gas inflow solenoid valve at the bottom of the tube. If desired the heavy gas can be connected to the fog seeding system in a similar method as was described for the light gas.

Figure B.5: Acetone bubbler.

B.5 Installing a Diaphragm

To install a diaphragm the return hydraulic rams must first be pressurized by switching the hydraulic manifold valves to the correct positions (fig. A.1). Then the hydraulic pump can be switched to the pressurize position. The hydraulic pump pressure can be changed if needed by raising or lowering the shop air pressure with which it is

supplied. The pump needs to be periodically refilled with hydraulic fluid as it is a one way trip for the fluid pushed into the rams. A lubricating oil is added to the inlet air consumed by the pump, and this oil level must also be replenished periodically. With the return rams pressurized the hydraulic ram collar can be removed and the driver raised using the electric wench attached to the end of the driver revealing the diaphragm contact surfaces. A new diaphragm does not need to be cut exactly as the hydraulic ram allows for a diaphragm diameter in the range of 10.5" to 11". The new diaphragm can held in place using some tape if required to maintain its position while the driver is lowered back into position. Once the driver is back in position the hydraulic ram collar can be put back into place. The hydraulic ram collar is very heavy and two people may be required to handle it safely at some shock tube inclinations. Once the collar has been latched into place the hydraulic pressure must be released from the return rams and then the hydraulic manifold valve positions can be changed. The hydraulic pump can then be activated again to pressurize the main ram.

B.6 Running an Experiment

To run an experiment the light and heavy fill valves and the interface valves must be opened. The gas regulators must all be set to the levels prescribed earlier and the mass flow controllers must be set to the right flow rates and activated. The fog machine duty cycle can be set if needed but preferably the fog machine will run constantly at the very low flow rates prescribed earlier. The driven SPT valve should also be opened so that the static pressure in the driven section can be read. The tube will need to be run like this for between 10 and 15 minutes for the interface to be properly formed. The Insight3G

program should be used during this time to take images of the interface as it develops. To set up the cameras in the Insight3G program the image exposure should be set to synchronized, and the capture mode to single. The timing set up for the cameras can then be adjusted to change the exposure duration and the time during the exposure at which the laser fires. The laser power should be set to high. This should correspond to a Q-Switch delay of ~190μs, but this setting can be changed so it should be checked as well. To acquire an image press the capture button, then in the LabVIEW program press the momentary trigger for laser one and two. The Insight3G program should then show the images. For setting up PIV imaging the timing of the camera exposures and laser firing must be set carefully. The timing mode must be set to straddle, and the pulse timing delay set to approximately 2μs for low Mach number (M~1.5) experiments. As the interface develops test images should be taken periodically until the images show a steady state has been achieved and the seeding density is uniform.

While the interface develops the laser timing should be set in the LabVIEW program based on the shock speed and the position of the cameras. The data acquisition rate and duration can also be set. It is recommended that the maximum rate of 2,000,000 samples per second be used and that the duration be 1s. Longer times will result in excessively large data files. The function of all transducers connected to the program should be checked by looking over their outputs, especially the DPTs. Make sure the DPT signal conditioners are turned on. If they are not a misfire will result and no data will be acquired from the experiment. A properly functioning DPT will register noise in the range of ±0.1psi in the LabVIEW program.

When the interface has reached it optimal conditions the driver can then be filled to a pressure which is 80% to 90% of its static rupture pressure. Set the boost tank pressure using the driver fill gas bottle and the manual valve to maintain near 500psi in the boost tank (this is for M=1.5 experiments). The solenoid driver fill valve can then be activated using the LabVIEW interface. The fill rate can be adjusted using a manual valve which is placed in line just before the fill valve at the top of the driver. The flow rate should be low enough as to avoid placing a dynamic load on the diaphragm while filling. The set point for the driver fill pressure can be set in the LabVIEW program so that the fill valve automatically shuts of when the target pressure is reached. Once the driver has been filled the experiment must be run ASAP (in less than 5min) or the diaphragm may fail statically. Ensure one last time that all transducers are functioning, that the boost tank pressure is at 500psi and that the boost tank valve is wide open, and then take a final test image of the interface. Turn off the driven SPT valve and press the arm system button. The tube is ready to fire if the "fire shock" button appears. If not, check that all solenoid valves are in the proper position. Press the capture button in Insight3G then press the fire shock button within seconds to fire the shock. The boost valve will then open and if everything was set right the tube will make a thud sound, the lasers will flash momentarily, and amazing images will appear on the Insight3G screen which reveal all the mysteries of the RMI.

After the data is saved to the hard drive which may take several seconds, the LabVIEW program will then open the interface valves to vent the tube. It is a good ideal to release the hydraulic ram pressure during this time and open the driver ASAP to speed

up the venting of the tube. The data file should then be examined using the various Matlab programs which have been created to check the diaphragm rupture pressure, the shock wave Mach number and the laser timing. The images in insight must also be saved immediately or they will be overwritten when the capture button is pressed again. The tube is now ready to be prepared for the next experiment.

Between experiments the shock tube should be cleaned of any diaphragm debris or condensed seeding fluid. The fused silica windows should be left in place if they do not need to be moved and instead the aluminum or steel window blanks should be removed to gain access to the test section interior. The bottom of the tube should be cleaned with ethanol first and then wiped down with a microfiber cloth to help remove any dust in the tube. The windows can be cleaned effectively with a commercial glass cleaner.

APPENDIX C: INITIAL EXPERIMENTS AND CAPABILITY VERIFICATION

As the shock tube was brought online several preliminary experiments and measurements were made. To determine the rupture pressure for various diaphragm design and to study how well formed the incident shock wave was, the shock tube was first operated in a horizontal configuration with no windows. Pressure traces from the dynamic pressure transducers located just upstream of the test section (fig. C.1) showed that the incident shock consisted only of one sudden rise in pressure. This meant that there were no compression waves following the shock front and that it was fully formed. The pressure traces also showed the reflected expansion waves and the reshock. Diaphragm rupture pressurewere determined by testing a suite of mylar, polycarbonate, and aluminum diaphragms with various thicknesses. It was found that polycarbonate and annealed aluminum 1100-O produced the cleanest and most predictable ruptures. A 0.040” thick poly carbonate Diaphragm was found to produce a Mach 1.7 shock wave, whereas a 0.040” thick aluminum diaphragm produced a Mach 1.85 shock wave. Higher shock strengths will be studied in later work. Heat treated aluminum was found to fail in a brittle mode and launches pieces down the shock tube. The mylar diaphragms frayed and sent small pieces down the tube as well.

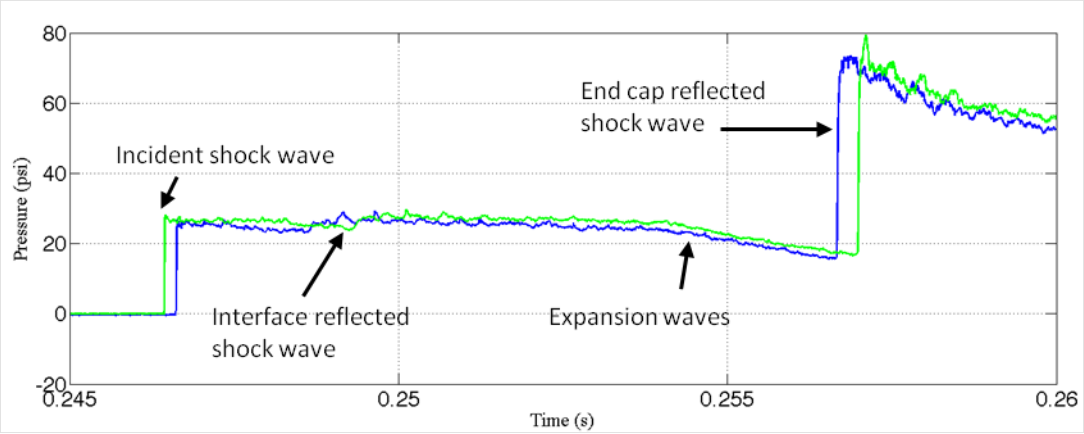

Figure C.1: Pressure data from two dynamic pressure transducers immediately upstream from the test section.

After verifying the shock wave formation the shock tube was inclined to 60°, for the first RMI experiments. For these first experiments conditions were selected to provide the cheapest and easiest to perform experiments. The gas combination was selected to be nitrogen over carbon dioxide (A~0.23) and the incident Mach number was chosen to be Mach 1.6. To image the interface Mie scattering was selected as an easier method than PIV or PLIF. The PIV fog seeding system was used to make a dense fog in the nitrogen gas. The PIV cameras and laser were used to illuminate the interface. These experiments helped to refine the valve timing and the laser timing. The boost valve duration was selected to provide just enough pressure to rupture the diaphragm, and the interface and fill valves were timed to provide the best formed interface for the experiments. It was found that the flow rate of the gases before the experiment and the orientation of the suction slots produced a curve at the edges of the interface by the slots. The effect of this curve on the RMI formation remains to be studied, but it can be reduced by closing the interface valves sooner, at the cost of greater interface diffusion.

Simulations were run in ARES for comparison to the initial experiments. These simulations were run with diffusion and viscosity models turned on. The interface diffusion thickness was set to 1cm, and a straight interface, no edge curves, was simulated. The effect of the fog on the gas properties could not be determined initially and so these effects were not included in the simulation. Figure C.2 shows a comparison of the simulations and the initial experimental results. Figure C.3 shows a higher quality image of the interface at late times. From these images it can be seen that the RMI is forming somewhat similar to what the simulations predict but it has some discrepancies. The first difference is that the experimental interface is traveling faster than the simulations predict. This is likely due to the exclusion of the fog effects from the simulations. The addition of the fog has probably changed the speed of sound in the in nitrogen and changed the incident shock strength. Another difference is that there are more vortices forming on the interface than predicted by the simulations. This could be an error created by the interface edge curving or it could be a sign that there is noise in the interface creating additional perturbation modes which form these vortices.

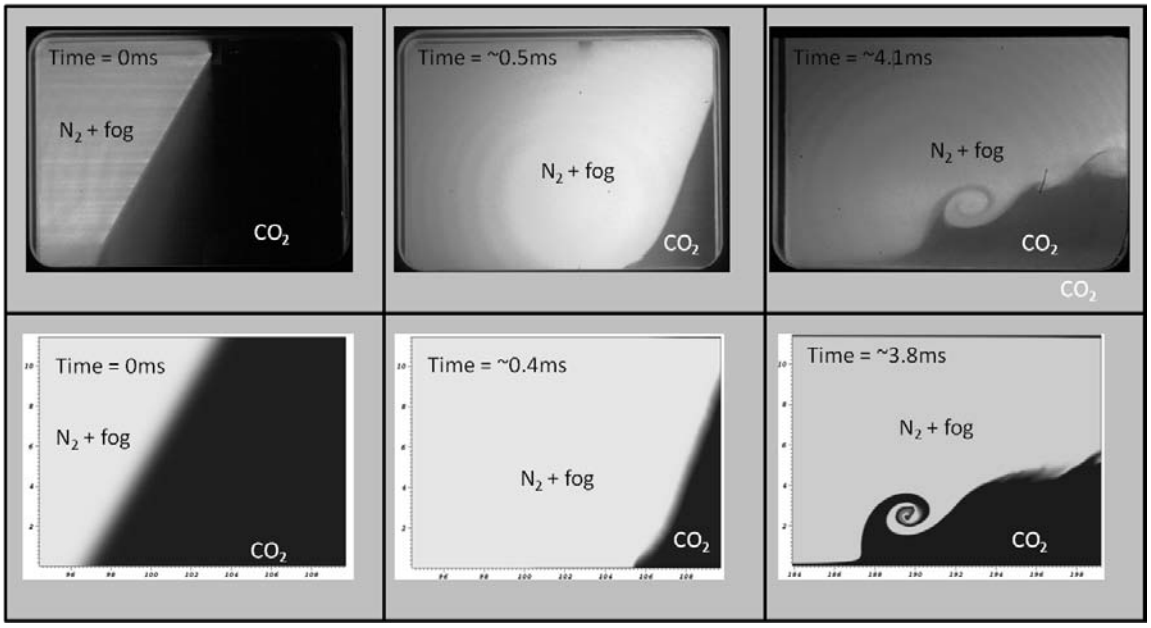

Figure C.2: Experimental and simulation images for the initial RMI experiments.

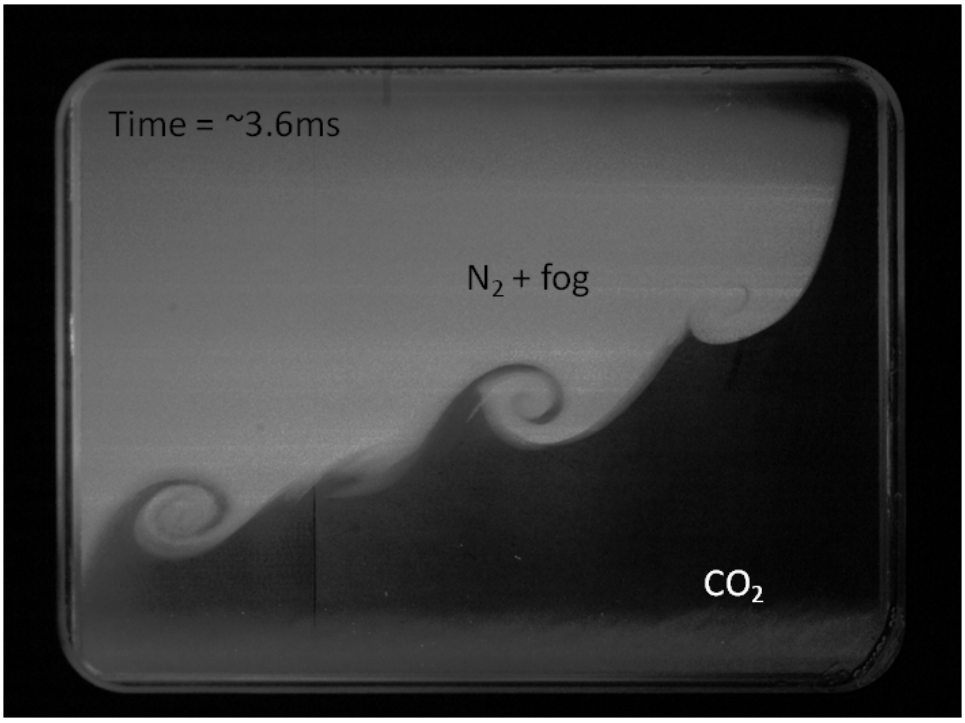

Figure C.3: Late time image of the initial RMI experiments.